

Functional dissection of a gene expression oscillator
in *C. elegans*

Inauguraldissertation

Zur Erlangung der Würde eines Doktors der Philosophie vorgelegt der
Philosophisch-Naturwissenschaftlichen Fakultät der Universität Basel

Von

Milou Wilhelmina Marcellinus Meeuse

Aus den Niederlande

2021

Originaldokument gespeichert auf dem Dokumentenserver der
Universität Basel

edoc.unibas.ch

Genehmigt von der Philosophisch-Naturwissenschaftlichen Fakultät auf
Antrag von

Prof. Dr. Erik van Nimwegen

Prof. Dr. Helge Grosshans

Prof. Dr. Andrew Oates

Basel, 19.11.2019

Prof. Dr. Martin Spiess

Dekan der Philosophisch-

Naturwissenschaftlichen Fakultät

Summary

Gene expression oscillations control diverse biological processes. One such example of gene expression oscillations, are those found for thousands of genes during *C. elegans* larval development. However, it remains unclear whether and how gene expression oscillations regulate development processes in *C. elegans*. In this work, I aimed to study the molecular architecture and the system properties of the *C. elegans* oscillator to provide insight into potential developmental functions and reveal features that are unique, as well as those that are shared among oscillators.

Here, performing temporally highly resolved mRNA-sequencing across all larval stages (L1-L4) of *C. elegans* development, we identified 3,739 genes, whose transcripts revealed high-amplitude oscillations (>2-fold from peak to trough), peaking once every larval stage with stable amplitudes, but variable periods. Oscillations appeared tightly coupled to the molts, but were absent from freshly hatched larvae, developmentally arrested dauer larvae and adults. Quantitative characterization of transitions between oscillatory and stable states of the oscillator showed that the stable states are similar to a particular phase of the oscillator, which coincided with molt exit. Given that these transitions are sensitive to food, we postulate that feeding might impact the state of the oscillator. These features appear rather unique, and hence a better understanding may help to reveal general principles of gene expression oscillators.

Our RNAPII ChIP-seq revealed rhythmic occupancy of RNAPII at the promoters of oscillating genes, suggesting that mRNA transcript oscillations arise from rhythmic transcription. Given that oscillations are coupled to the repetitive molts and that the molecular mechanisms that regulate molting are unknown, we aimed to find transcription factors important for molting and oscillations. Hence, we screened 92 transcription factors that oscillate on the mRNA level for their role in molting and identified *grh-1*, *myrf-1*, *blmp-1*, *bed-3*, *nhr-23*, *nhr-25* and *ztf-6*. We showed that oscillatory activity of GRH-1 is required for timely completion of the molt, to prevent cuticle rupturing, and for oscillatory expression of structural components of the cuticle and 'ECM regulators', among others, including *grh-1* itself. Hence, we propose GRH-1 as a putative component of the (sub-)oscillator that regulates molting. We showed that loss of BLMP-1 increased the duration of molts, affected cuticle integrity, and changed the oscillatory dynamics of a subset of genes in diverse ways. We postulate that BLMP-1 acts as factor that couples gene expression oscillations, and potentially sub-oscillators or repetitive developmental processes. In conclusion, this work provides insight into the function of the oscillator, and its system properties. Moreover we identified relevant factors, which we propose as a starting point to unravel the molecular wiring of the *C. elegans* oscillator and its functional relevance.

Contents

Summary.....	3
1. Introduction	6
1.1 Oscillations in biology: diversity and similarity.....	6
1.1.1 Circadian rhythms	7
1.1.2 Somitogenesis	10
1.1.3 Lateral root branching.....	11
1.1.4 Oscillations in lineage-specifying transcription factors.....	12
1.2 Oscillations from a theoretical point of view	13
1.2.1 Design principles of oscillators.....	13
1.2.2 Theoretical description of an oscillation in a phase plane	17
1.2.3 Bifurcations in oscillating systems	17
1.3 <i>C. elegans</i> as a model organism to study development and its timing	20
1.3.1 Embryogenesis	21
1.3.2 Molting, a repetitive feature during <i>C. elegans</i> development.....	22
1.3.3 Timing of recurring events during <i>C. elegans</i> development	27
1.4 Transcription.....	28
1.4.1 Transcriptional regulation	28
1.4.2 Transcription factors in this thesis	30
1.5 Aims for this thesis	34
2. Results.....	36
2.1 Manuscript: State transitions of a developmental oscillator	36
2.2 Rhythmic transcription of oscillating genes results from rhythmic RNAPII occupancy.....	104
2.3 Screening ‘oscillating’ transcription factors for their role in molting.....	106
2.4 Manuscript: Control of oscillatory gene expression and molting through the transcription factor GRH-1	115
2.5 Characterization of <i>myrf-1</i> , <i>nhr-25</i> , and <i>blmp-1</i>	162
3. Discussion	186
3.1 Identification of thousands of oscillating genes during <i>C. elegans</i> larval development	186
3.2 Developmental stage transitions reveal properties of the <i>C. elegans</i> oscillator.....	187
3.3 A function of the <i>C. elegans</i> oscillator in repetitive developmental processes	189
3.4 Transcript oscillations arise from rhythmic transcription	191
3.5 Finding components of the <i>C. elegans</i> oscillator.....	191
3.6 Insights into the molecular architecture of the <i>C. elegans</i> oscillator.....	193
3.7 Outlook and open questions	196

4. Methods.....	200
5. Supplement.....	206
6. References	218
7. Acknowledgements.....	231
8. Curriculum vitae.....	233

1. Introduction

1.1 Oscillations in biology: diversity and similarity

Oscillations are a common feature in biological systems. At the same time, biological oscillations diverge in many aspects, from functional relevance to the level and the timescales at which they occur. For example, predator-prey oscillations emerge at the population level and exhibit a periodicity of months or even years, whereas repetitive activation of neuronal cells occurs in the order of milliseconds.

Oscillations are characterized by repetitive fluctuations around an equilibrium over time. The maximal displacement from the equilibrium is called the amplitude and the time it takes to make one repetition is the period of the oscillation (**Figure 1.1A**). The frequency is the number of repetitions per unit of time. An oscillator is the ensemble of components, i.e. the network, which is required to generate oscillations (**Figure 1.1B**).

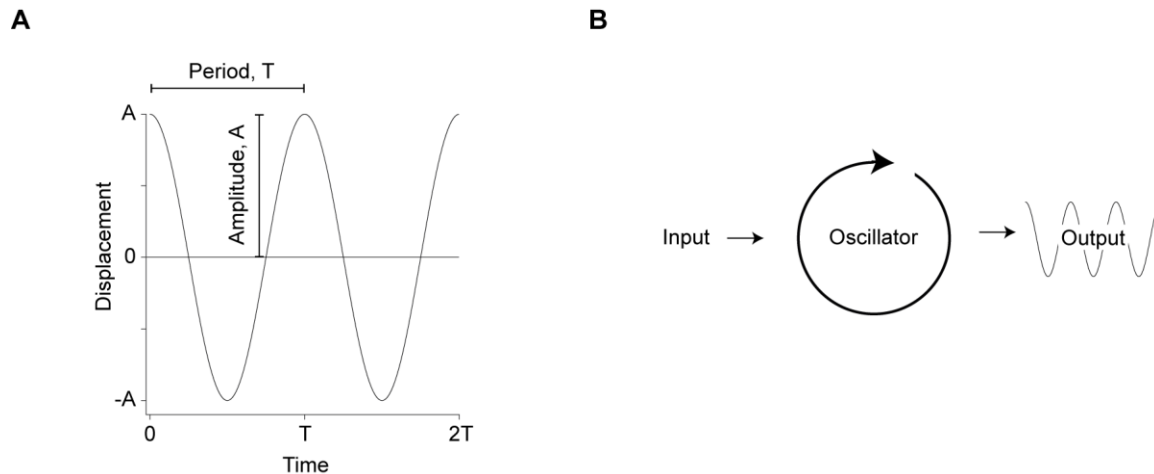


Figure 1.1: Schematic of the characteristics of an oscillation and an oscillator network

A, An oscillation is characterized by an amplitude, A , the displacement from the equilibrium and a period, T , the time to complete one repetition.

B, An oscillator comprises a network required to generate output oscillations. Some oscillators may require an input as a trigger (**section 3.7.3**) or for entrainment (**section 1.1.1**)

Functionally, oscillations can be considered as a tool to transfer information. As oscillations are characterized by an amplitude and frequency, much more information can be encoded in oscillatory compared to stationary signals. Hence, changes in the dynamics of a signal can be decoded by cells in distinct ways resulting in specific cellular responses (Purvis and Lahav, 2013). Indeed, sustained and oscillatory gene expression have been shown to promote differentiation and self-renewal respectively in

stem cells, which I further address below (**section 1.1.4**). Moreover, oscillations can serve to entrain or couple a system to other recurring processes. For example, the circadian rhythm functions to anticipate and adapt processes to repetitive environmental changes (**section 1.1.1**). Hence, the circadian oscillator keeps ‘external time’ and is often referred to as a ‘biological clock’ (Rensing et al., 2001). Besides time-keeping mechanisms, oscillators have been proposed to control events in space, as I will discuss below (**section 1.1.2**). The focus of this thesis will be on gene expression oscillators which function at the cellular and organism level, of which circadian rhythms and somitogenesis are two well-known examples (**section 1.1.1** and **section 1.1.2**). Recent progress in single cell and genomics techniques led to the discovery of new molecular oscillators, examples which I will discuss in **section 1.1.3** and **section 1.3.3**.

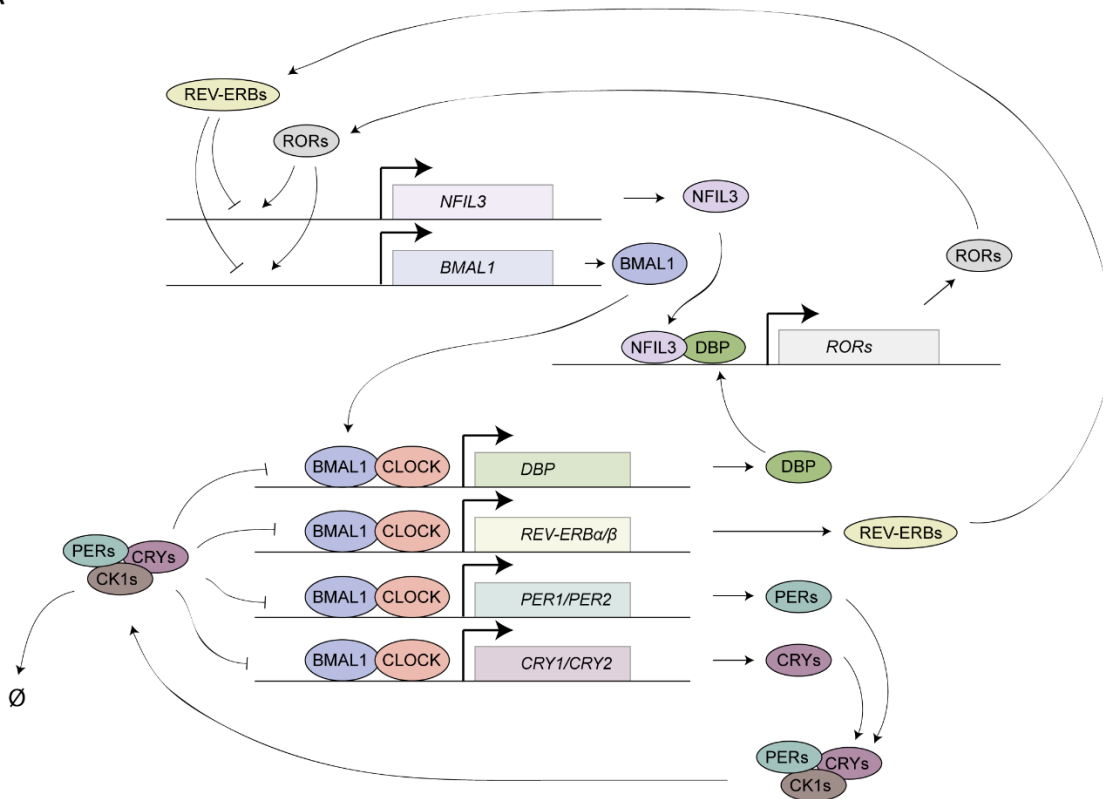
1.1.1 Circadian rhythms

The 24-hour rhythm exists in almost all, if not all, organisms. This rhythm is established by an endogenous oscillator. It synchronizes physiological and behavioral processes, such as sleep, metabolism, body temperature, and hormone release with day-night cycles. The circadian rhythm has three characteristics. First, the circadian rhythm is cell-autonomous, meaning that in the absence of external repetitive cues, a period close to 24 hours is maintained. The autonomy arises from the fact that all cells express core clock genes and can produce circadian oscillations on their own. However, different tissues control different rhythmic processes (reviewed in Dibner et al., 2010). Second, the circadian clock can be entrained by external cues, predominantly by light, but also by temperature and food. These so-called *zeitgebers* allow the endogenous oscillator to match its period with fluctuations in the environmental period, such as the light-dark cycles (Aschoff, 1960). The entrainment by light takes place as it is sensed by photo-receptors in the retina and transmitted to the neurons in the hypothalamic suprachiasmatic nucleus (SCN). These neurons function as the master circadian pacemaker to entrain clocks in other tissues of the body (reviewed in Welsh et al., 2010). The third hallmark of circadian rhythms is temperature compensation, i.e. the period of the oscillator is largely invariant over a range of physiological temperatures.

The circadian clock consists of three elements: the oscillator, the input (*zeitgebers*) and the output (rhythmic physiological processes) (**Figure 1.1B**). The circadian oscillator is driven by a transcriptional network consisting of interlocked feedback loops (reviewed in Takahashi, 2017) (**Figure 1.2A**). At the core of the clock are the transcription factors BMAL1 and CLOCK, two transcriptional activators that act as heterodimers (BMAL1-CLOCK). In contrast to BMAL1, the nuclear localization, but not the transcription, of CLOCK is controlled by the circadian rhythm (Kondratov et al., 2003; Lee et al., 2001). BMAL1-CLOCK induce the expression of the repressors PER1, PER2, PER3, CRY1 and CRY2. PER and CRY form a complex

with the serine/threonine kinases CK1 δ and CK1 ϵ , which translocates to the nucleus to repress their own transcription, allowing the mRNA levels to decrease. As PER and CRY are additionally turned-over by protein degradation, regulated by E3 ubiquitin ligase complexes, BMAL1 and CLOCK can initiate a new cycle of *PER* and *CRY* transcription. A second feedback loop induced by BMAL1 and CLOCK, is that of REV-ERB α and REV-ERB β , which leads to the repression of *BMAL1* and *NFIL3* transcription. In the third loop, CLOCK and BMAL1 drive the expression of DBP, TEF and HLF, which interact with NFIL3 to regulate the expression of RORs. In turn, RORs induce *BMAL1* and *NFIL3* transcription. The combination of the three interlocked feedback loops sets the period of the core oscillator. The transcription factors that act at the core, are also responsible for driving the expression of so-called clock-controlled genes (CCG) to generate the rhythmic output of the clock (**Figure 1.2B**).

A



B

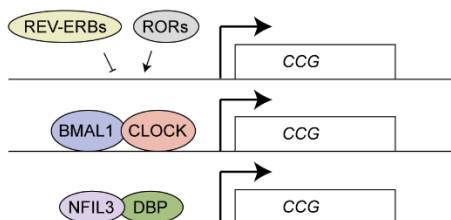


Figure 1.2: Transcriptional network of the circadian clock in mammals

A, Schematic of transcriptional network at the core of the circadian oscillator. The heterodimer BMAL1-CLOCK drives the expression of three feedback loops. i) CRYs and PERs, which form a complex with CK1, inhibit their transcription, and are degraded (\emptyset). ii) REV-ERBs, which repress *BMAL1* and *NFIL3* transcription. iii) DBP, which interact with NFIL3 to induce *RORs* expression. Based on (Takahashi, 2017)

B, Transcription factors of the core oscillator drive the expression of the clock-controlled genes (CCG), the output of the circadian clock. Based on (Takahashi, 2017)

However, the clock output does not appear to be solely driven by the rhythmic transcriptional activity of the core clock transcription factors. RNA-seq revealed that between roughly 5% and 20% of the protein-coding genes exhibit rhythmic mRNA expression in a given organ, with liver accounting for the highest percentage (Zhang et al., 2014). However, of those oscillating mRNA transcripts in the liver, only 22% were reported to arise from rhythmic transcription (Koike et al., 2012), suggesting that additional layers of post-transcriptional regulation modulate the circadian oscillations. Indeed, functions of transcriptional termination, alternative splicing, translation, miRNAs, polyadenylation and mRNA degradation in establishing circadian rhythms have been reported (reviewed in Lim and Allada, 2013).

How are differences between rhythmic production and accumulation of oscillating factors achieved? Mathematical models and experimental data have shown that increasing the stability of the product, dampens its relative amplitude and delays its peak expression (Korenčič et al., 2012; Le Martelot et al., 2012; Lück et al., 2014). On the contrary, an increase in relative amplitude and broad range of possible peak phases can be explained by rhythmic degradation (Le Martelot et al., 2012; Lück et al., 2014). The maximum amplitude occurs when production and degradation are in antiphase (Lück et al., 2014). Although there are discrepancies among studies, it has been estimated that a large fraction, ranging from 30% (Lück et al., 2014) to over 70% (Koike et al., 2012) of the liver transcriptome is affected by post-transcriptional regulation.

Among the rhythmically transcribed genes, there is not only little overlap between different tissues, but also the peak phases of the same genes are wide-spread across different tissues (Mavroudis et al., 2018; Zhang et al., 2014), suggesting that tissues-specific mechanisms are at play. Part of the phase differences has been explained by regulatory elements in the genome (Korenčič et al., 2012; Mavroudis et al., 2018), tissue-specific chromatin conformations, and tissue-specific transcription factors (Yeung et al., 2017), whereas the remainder might be explained by post-transcriptional control and systemic signals. How the tissue-specific clocks are coupled and what their functional relevance is remains to be established.

1.1.2 Somitogenesis

A key event during vertebrate embryogenesis is segmentation of the posterior-anterior axis, which will eventually give rise to the vertebrae, ribs, muscles, nerves and blood vessels. The segments, called somites, are rhythmically produced from the anterior tip of the presomitic mesoderm (PSM). At the same time, cells in the tail bud undergo cell divisions elongating the PSM at the posterior end. A mathematical model, the 'clock and wavefront' model (Cooke and Zeeman, 1976) has been suggested to drive the periodic formation of somites. The idea of this model is that an abrupt change in cellular properties is achieved when cells in a certain phase of a cellular oscillator (clock) are hit by the wavefront, which moves as the tissue grows. This converts temporal cues from an oscillator into a spatial pattern. As a consequence, the number of somites is determined by the total duration of somitogenesis and the period of the oscillator. The distance that the wavefront travels during one period of the oscillator determines the size of the somite (reviewed in Gomez and Pourquié, 2009). Hence, the combination of wavefront and clock are suggested to ensure space rather than time (Webb and Oates, 2016). Interestingly, the size and the number of somites are different between species (Gomez et al., 2008). Below I will summarize the molecular mechanisms underlying the clock and wavefront model.

1.1.2.1 The oscillator

The existence of an oscillator was supported by the identification and characterization of HAIRY1, a member of the HER family of basic helix-loop-helix (bHLH) transcription factors, in chicken embryos (Palmeirim et al., 1997). Besides the members of the HER family, factors of the Notch, Wnt and FGF signaling pathways were found to oscillate. These gene expression oscillations travel from posterior to anterior, and arrests at the anterior of the PSM. This process is repeated with every formation of a somite (reviewed in Oates et al., 2012). I will summarize the molecular mechanism of the segmentation oscillator in zebrafish and mice below (as reviewed in Dequéant and Pourquié, 2008).

In zebrafish, oscillations in *Her1* and *Her7* have been shown to arise from a negative feedback loop, in which they directly inhibit their own transcription. The *Her1*-*Her7* oscillator is thought to be coupled to, and induce, oscillations of the Notch ligand, important for synchronizing the oscillator in neighboring cells. Moreover, the *Her1*-*Her7* oscillator requires *Hes6*, which is regulated by FGF signaling. Indeed and consistent with the Clock and Wavefront model, mutations in *hes6* (Schröter et al., 2012), and the Notch signaling network (Herrgen et al., 2010) resulted in an increased period and segment length in zebrafish, without affecting growth of the PSM. Although the *Her1*-*Her7* oscillator requires other pathways for its function, it has been suggested to be the core oscillator in zebrafish.

In mice, Hes7, Hes1, Hes5 and Hey2 function similar to Her1-Her7 oscillator in zebrafish. In contrast to zebrafish, additional factors of the Notch pathway and factors of the FGF and Wnt signaling pathways also oscillate in mice. These oscillators appear to functionally coupled as the FGF and Notch pathway are connected via their interaction with Hes7 (Niwa et al., 2007), and cross-talk between Wnt and Notch signaling pathways was found to control segmentation (Sonnen et al., 2018). Thus, it is the collective oscillatory behavior of these pathways that is thought to control the periodicity of somitogenesis in mice.

1.1.2.2 The wavefront

The finding that gradients of FGF, Wnt and Retinoic acid (RA) exist along the PSM (reviewed in Aulehla and Pourquié, 2010), provided support for the wavefront model. FGF and Wnt levels are highest in the posterior end, and decline towards the anterior end of the PSM (Aulehla et al., 2003; Dubrulle et al., 2001). In contrast, reporter experiments suggest that RA is produced in the somites and decreases towards the posterior end (Niederreither et al., 1997; Rossant et al., 1991). Hence, opposing gradients are established. Whereas high levels of Wnt and FGF signaling are thought to ensure that cells stay in an undifferentiated state, high levels of RA and low levels of Wnt and FGF promote a developmental switch in the anterior end of the PSM (reviewed in Aulehla and Pourquié, 2010). The wavefront, a threshold at the anterior is thought to prime cells to respond to signaling of the segmentation clock. As a consequence, the expression of MESP genes is induced in repetitive manner, which determines the initial boundaries where the future segments will form (Saga et al., 1997). Finally, the cells undergo mesenchymal-epithelial transition to eventually form differentiated somites.

1.1.3 Lateral root branching

Plants also exhibit rhythmic formation of modules. Branching of the shoots and lateral roots of plants occurs in a repetitive manner. Whereas shoots form a phyllotactic (spiral) pattern, roots are produced laterally and repetitively along the growing axis. Recently, a *DR5::LUC* reporter construct was found to oscillate in a region close to the root tip and mark evenly spaced sites which later develop into new lateral roots, the so-called pre-branch sites (Moreno-Risueno et al., 2010). Oscillations were not limited to that of the reporter, instead two sets of roughly 2000 and 1400 genes oscillated in antiphase. Mutants of rhythmically expressed transcription factors revealed defects in number and spacing of branches, suggesting that transcription factors regulate rhythmic priming of pre-branch sites (Moreno-Risueno et al., 2010). Although growth of the primary root and the spacing of pre-branch sites is sensitive to changes in temperature, the number of pre-branch sites remained largely unchanged, suggesting that the process is temperature compensated. Hence, the authors concluded that positioning

of pre-branch sites at evenly spaced intervals is controlled by an autonomous oscillator (Moreno-Risueno et al., 2010). However, alternative hypotheses, e.g. tissue-level modulations in auxin levels and Turing-type periodic patterning, have been suggested to control lateral root branching in plants (Laskowski and Tusscher, 2017). Although auxin is a key regulator of lateral root formation, exogenous auxin fluctuations were not sufficient for the formation of pre-branch sites (Moreno-Risueno et al., 2010). However, the amplitude of the oscillations appeared to be controlled by auxin levels in the tip of the root and a local auxin source is required for the formation of lateral roots (Xuan et al., 2015). These observations suggest that although auxin does not appear to be the predominant driver, it contributes to and likely feeds into the oscillator.

1.1.4 Oscillations in lineage-specifying transcription factors

In the previous sections, I described oscillators that act to drive repetitive processes in time and space at the tissue and organism level. However, recent studies using time-lapse imaging of single cells expressing fluorescent reporters revealed that oscillations in genetic networks can also result in different cellular states rather than rhythmic outcomes (reviewed in Isomura and Kageyama, 2014; Levine et al., 2013; Purvis and Lahav, 2013). One such a distinct cellular outcome is the ability of stem cells to differentiate into different cell types. Indeed, the transcription factor Nanog fluctuates in embryonic stem cells. Although loss of Nanog did not affect the proliferative capacity, it predisposed stem cells to commit to differentiation (Chambers et al., 2007). Similarly, the transcription factor Hes1 has been found to oscillate in neural progenitor cells (Shimojo et al., 2008) and embryonic stem cells (Kobayashi et al., 2009). Stem cells expressing high and low levels of Hes1 were prone to adopting mesodermal and neuronal fate respectively. Hence, Hes1 oscillations in embryonic stem cells are thought to sustain the ability to give rise to different cell fate choices (Kobayashi et al., 2009). A recent study by Imayoshi et al. showed that together with Hes1, oscillatory expression of the transcription factors Olig2 and Ascl1 maintained neuronal progenitor cells in a proliferative and multipotent state. Upon induced differentiation towards neurons, astrocytes and oligodendrocytes, oscillations ceased and the expression of one factor, Ascl1, Hes1 and Olig2 respectively, was predominantly upregulated. However, sustained high expression was not sufficient to determine cell fate choices (Imayoshi et al., 2013). Hence, it seems likely that the expression dynamics of lineage-specifying transcription factors offer cells an opportunity to adopt multiple cell fates, depending on environmental conditions. How binary responses can arise from oscillatory gene networks will be discussed below (**section 1.2.1**).

1.2 Oscillations from a theoretical point of view

To understand the molecular mechanisms that drive an oscillator, it is not only important to identify its components and how they are wired, but also to describe the network from a theoretical perspective. Especially because it is not straightforward how interactions within the network give rise to the dynamic behavior of its components. On the one hand, this requires analysis tools that can extract and quantify the characteristics of oscillatory signals. On the other hand, mathematical models that can describe the characteristics of oscillatory networks are needed. Here, I will describe the design principles that are required (**section 1.2.1**) for a network to generate oscillations, and some of theoretical tools that are used to describe oscillations (**section 1.2.2** and **section 1.2.3**).

1.2.1 Design principles of oscillators

To understand the requirements for a system to oscillate, I consider a simple one-gene network in which an mRNA is transcribed from a gene and translated into a protein (**Figure 1.3A**). As mentioned above, a prerequisite of a component to exhibit oscillations is sufficient instability of mRNA and protein (\emptyset in **Figure 1.3A**). Here, I will discuss the design principles of oscillators as previously described (Novák and Tyson, 2008).

1.2.1.1 A negative feedback loop

The first design principle of an oscillator is a negative feedback loop. In our case, the protein represses its own transcription (**Figure 1.3B**, Negative autoregulation). When protein levels are high, production is lower than degradation, allowing protein levels to drop. As protein levels decrease, repression is released and mRNA and protein levels rise again. Indeed, at the core of the circadian and the segmentation oscillators are negative feedback loops (**section 1.1.1** and **section 1.1.2**). However, a negative feedback on its own is not sufficient to generate oscillations. Hence, the system might initially reveal fluctuations, but mRNA and protein levels will soon reach a steady state, in which the rate of production and degradation are equal (Alon, 2007).

1.2.1.2 Sufficiently large time delays

The second design principle is a sufficiently large time delay. Hence, the production at a given time depends on the protein concentration in the past. This allows the system to overshoot and undershoot the steady state. In the simple network that I describe here, time delay represents the time it takes for transcription, post-transcriptional processes, translation, and nuclear localization to occur. These time delays are considered to be in the order of seconds to minutes. Indeed, in a mathematical model of *Hes1* and *Her7* oscillations driven by a negative auto-regulatory feedback loop, a transcriptional delay was

sufficient to generate a period of 30 minutes, which is close to the period observed in zebrafish somitogenesis (Lewis, 2003). However, longer periods (90-120 min) as observed in mouse and chick somitogenesis could not be achieved without changing the parameters (Lewis, 2003). Hence, the time delay must be sufficiently large to match these periods. This can be achieved by introducing additional slow steps. Indeed, PER undergoes multiple slow post-translational modifications before being transported back to the nucleus (reviewed in Hirano et al., 2016). Alternatively, sufficiently large time delays can be obtained by adding genes to our simple model, resulting in a two-gene network (**Figure 1.3C**), or a multi-gene network. Accordingly, the core circadian oscillator does not comprise a one-gene network, but consists of three interlocked feedback loops with numerous genes involved (**section 1.1.1**). These examples show that design principles predicted by mathematical models occur in biology.

Besides slow steps and addition of components, a third way to introduce delays is by adding a positive feedback loop (**Figure 1.3C**). In a one-component network with a positive feedback loop (**Figure 1.3B**), the production rate is low, when levels are low. Only when levels are sufficiently high, production increases rapidly. Hence, the response time of positive feedback loops is larger than that of negative feedback loops and simple regulation (**Figure 1.3B**). Thus, positive feedback loops can generate a delay (Alon, 2007).

In a two-gene system, gene A (activator) induces the expression of gene R (repressor), which inhibits the expression of gene A. Additionally, gene A induces its own expression (**Figure 1.3C**). Three different versions of repression by R have been described: transcriptional repression, sequestration of A by R, and repression by degradation (Purcell et al., 2010). Although the dynamics resulting from these networks might differ, the general principles are the same. When levels of A are high, A will be repressed by R. The levels of A initially reduce gradually, but suddenly A switches to low levels (undershooting) due to the delayed positive feedback. Once A is low, repression is released and A gradually increases. At some point the delayed positive feedback loop kicks in, switching A to high levels (overshooting). When certain design principles are met, e.g. degradation and translation rates of A are larger compared to R (a design principle I will discuss below) (Guantes and Poyatos, 2006), this system can reveal self-sustained oscillations. The initial slow accumulation of A followed by the rapid increase in A characterizes so-called relaxation oscillators. Moreover, the network I describe here can reveal bistability (Ferrell, 2002). A bistable system can alternate between two different states, a state in which levels of A are low (**Figure 1.3D, i**) and one in which levels of A are high (**Figure 1.3D, iii**), but it cannot stay in an intermediate state (**Figure 1.3D, ii, iv**). Indeed, the cell cycle oscillator, consisting of a negative and positive feedback loop, has revealed bistability *in vivo* (Pomerening et al., 2003). Although the network I describe here can be bistable,

bistability is not assured and other network topologies can also be bistable (Ferrell, 2002). Moreover and in contrast to a 'negative-only' oscillator, 'combined negative and positive' oscillators revealed less variable amplitudes for changes in its frequency in mathematical models (Tsai et al., 2008) and synthetic oscillators (Stricker et al., 2008). Tunability and robustness can be of particular importance for biological oscillators that act in a range of environmental conditions (Tsai et al., 2008).

1.2.1.3 Non-linearity

Third, the design of the oscillator often reveals non-linear reaction steps. Novak and Tyson (Novák and Tyson, 2008) described four examples of non-linearity. (i) Assembly of multiple components that subsequently act as a complex, for example multimeric transcription factor complexes that binds to a single site at the DNA. (ii) Binding of multiple factors to different sites and acting in a cooperative fashion. (iii) Modification, such as phosphorylation, of a protein at multiple sites. (iv) Sequestration of an activator by a repressor, e.g. a stoichiometric inhibitor that binds a regulatory protein to form an inactive complex. All these examples exhibit sigmoidal-shaped reaction curves that help generating oscillations.

1.2.1.4 Balanced reaction rates

Finally, and as already mentioned in the second requirement, the rates of the different steps must be balanced to generate oscillations. For example, the timescale of degradation must be slower than that of production, and the time delay must be larger than the timescale of degradation. If production were to be slower than degradation, levels of the product cannot rise. If degradation were to be slower than the negative feedback loop, repression cannot be released. Hence, a network will only oscillate when the timescales of the different steps are matched accordingly (Novák and Tyson, 2008).

1.2.1.5 Conclusion on design principles

To summarize, genetic oscillations can be generated in a network that comprises nonlinear negative feedback loops with sufficiently long delays and fast decay rates, which are balanced accordingly. Indeed, the design principles described here have been observed in for example the circadian clock (**section 1.1.1**), somitogenesis (**section 1.1.2**) and the cell cycle of *Xenopus* eggs (Pomerening et al., 2003), indicating their functional relevance. Mathematical models (reviewed in Purcell et al., 2010) and synthetic oscillators (Elowitz and Leibler, 2000) have revealed that other network motifs are also capable of generating oscillations. However, whether and to what extent these networks exists *in vivo* remains to be investigated.

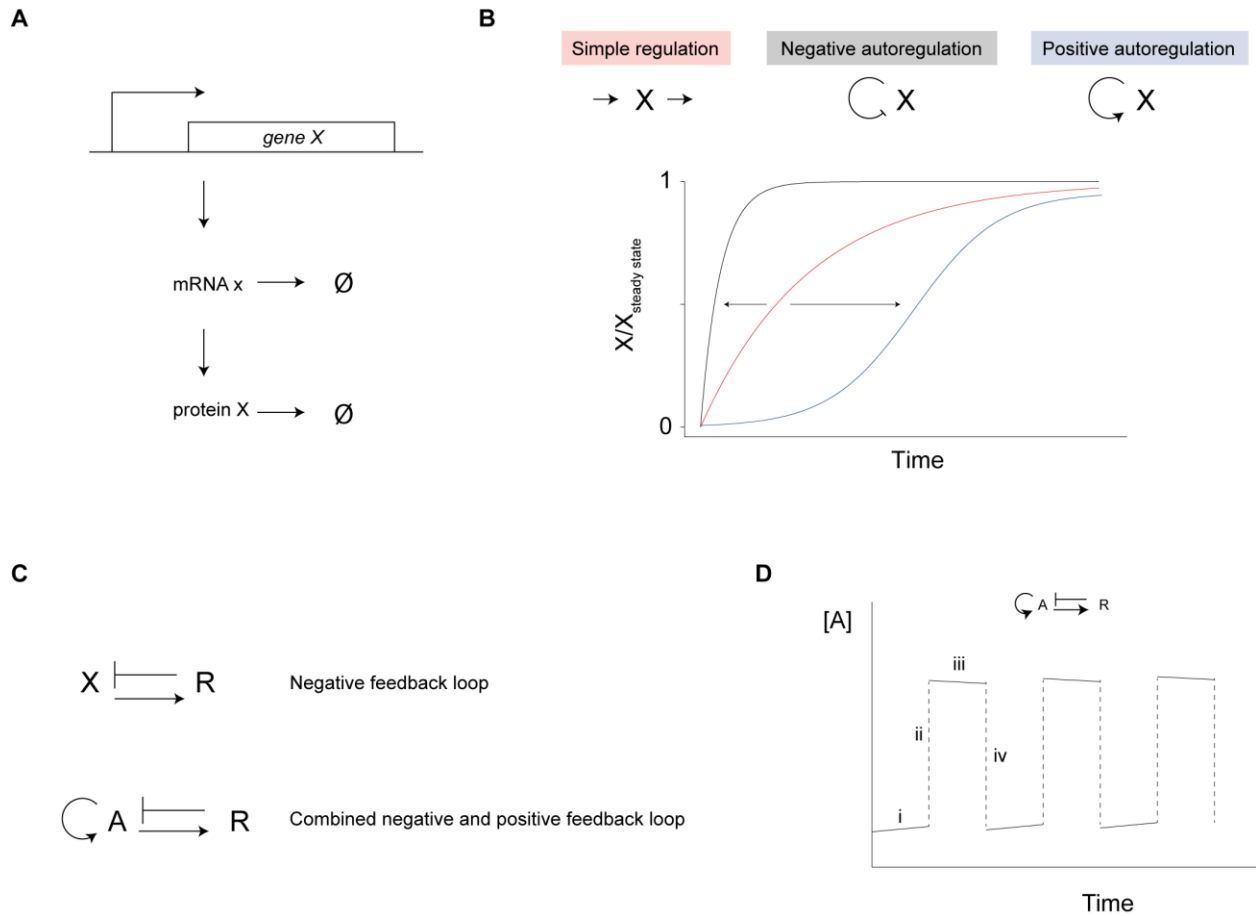


Figure 1.3: Network motifs and bistability

A, Schematic representation of a one-gene network. Gene x is transcribed in mRNA x which is degraded (\emptyset). mRNA is translated into protein which is degraded (\emptyset).

B, Overview of one-gene network motifs and their dynamics. Dynamics are represented in a cartoon showing how the concentration of X over the concentration of X at steady state changes over time. Simple regulation (as in A, red), negative autoregulation (black) and positive autoregulation (blue) are indicated. In negative autoregulation, the product of gene X inhibits its own transcription, and dynamics are faster compared to simple regulation (arrow). In positive autoregulation, the product of gene X induces its own transcription and dynamics are delayed compared to simple regulation (arrow). Based on (Alon, 2007)

C, Overview of two-gene network motifs. In a negative feedback loop only model, the product of gene X induces the expression of repressor R, which inhibits the production of X. In a combined negative and positive feedback loop, activator A additionally induces its own expression.

D, Cartoon of bistability. Dynamics of the levels of A over time in the combined negative and positive feedback network. Levels of A increase gradually (i), and subsequently shoot up when the positive feedback kicks in (ii), R inhibits A gradually and slowly (iii), and subsequently levels of A drop rapidly when the positive feedback loop becomes active (iv). Note that low (i) and high (iii) states exist, but no intermediate states. Based on (Tsai et al., 2008).

1.2.2 Theoretical description of an oscillation in a phase plane

To visualize how an oscillator behaves, a geometrical representation in a so-called phase plane can be made. Here, I will describe the phase plane of a genetic network consisting of two genes, X and Y (based on Strogatz, 2015, chapter 2 and chapter 5). The axes of a phase plane represent the levels of the X and Y respectively (**Figure 1.4A**). The phase plane is filled with arrows, which have a certain length and a certain direction. The arrows indicate how the system evolves over time, given the initial conditions, X_0 and Y_0 . Each point in the phase plane can serve as an initial condition. Hence, when choosing X_0 and Y_0 in the phase plane and following the arrow that leaves from that point (X_0, Y_0) , and the subsequent arrows, one will observe a trajectory through the phase plane. Depending on the initial conditions, the system can exhibit very different paths in phase plane (**Figure 1.4A**).

Trajectories can converge to a point (attractor) or diverge from one point (repeller) (Strogatz, 2015, chapter 2). These so-called fixed points lack an arrow, hence the system will stay in this point and does not change anymore over time. A fixed point is called stable when a small change in the levels of A or B results in the return of the system to the fixed point (**Figure 1.4B**). A stable fixed point is represented with a closed dot. In contrast, when a small perturbation in A or B prevents the system from returning, the fixed point is called unstable. An unstable fixed point is represented with an open dot. For certain systems, some trajectories might never converge, i.e. they tend to infinity.

For certain systems, the trajectories can form closed loops. A closed loop in a phase plane implies oscillations, as the system returns to the same point after travelling through the phase plane. A special case of a closed loop is a limit cycle (Strogatz, 2015, chapter 7), for which the neighboring trajectories spiral toward or away from the closed loop. Similar to fixed points, the terminology stable and unstable also applies for limit cycles. A limit cycle is stable if all neighboring trajectories approach the limit cycle (**Figure 1.4C**). Hence, the oscillations are self-sustained. A limit cycle is unstable if neighboring trajectories spiral away from the limit cycle. Stable states are represented in a solid line and unstable states with a dotted line. For higher dimensional systems, i.e. systems with more than 2 genes, the geometrical representation becomes more complicated and additional types of trajectories are possible.

1.2.3 Bifurcations in oscillating systems

Above I have presented a theoretical representation of how a given system changes over time. However, the existence of fixed points and limit cycles and their topology depends on the interactions and the parameters of the network. In fact, a system can show different qualitative behaviors for different parameter values (Strogatz, 2015, chapter 3 and chapter 8). A bifurcation is the transition between these

different qualitative behaviors when one or more of the parameters, the so-called bifurcation parameters, are varied. Bifurcation points are the parameter values at which these transitions occur. Hence, bifurcations can be used to describe changes in oscillatory behavior, e.g. transitions from a stable into an oscillatory state and vice versa. Here, I will describe some of the so-called codimension-1 bifurcations, i.e. only one bifurcation parameter is necessary for a bifurcation to take place. An overview of possible codimension-1 bifurcations has been described before (Izhikevich, 2000; Saggio et al., 2017; Strogatz, 2015). Here, I will summarize the characteristics of the following codimension-1 bifurcations: the supercritical Hopf bifurcation, the subcritical Hopf bifurcation, the Saddle Node bifurcation and the SNIC bifurcation. Higher order codimension bifurcations are beyond the scope of this thesis.

A well-known example of a bifurcation is a supercritical Hopf bifurcation (**Figure 1.4D**). Below a certain parameter value, the system is in a steady state (a fixed point) and the amplitude is zero. However, as the parameter value increases and reaches the bifurcation point, the fixed point becomes unstable and a stable limit cycle emerges. Hence, the system starts oscillating. Upon further increase of the parameter value, the amplitude of the limit cycle increases. Transitions of supercritical Hopf bifurcations are characterized by stable periods but gradually changing amplitudes. Hence, when the systems transitions from an oscillating to a stable state it reveals damped oscillations.

Similar to the supercritical Hopf bifurcation, the subcritical Hopf bifurcation has a stable fixed point (**Figure 1.4D**). However, and in contrast to the supercritical Hopf bifurcation, the stable fixed point is surrounded by an unstable limit cycle, which is in turn surrounded by a stable limit cycle (Izhikevich, 2000). As the parameter value increases, the fixed point loses its stability and the unstable limit cycle decreases and resolves, causing the system to jump to the stable limit cycle. Compared to the supercritical Hopf bifurcation, oscillations with a less gradual onset and relatively large amplitudes are observed in a subcritical Hopf bifurcation.

In contrast to the Hopf bifurcations, a Saddle Node bifurcation is characterized by pairs of fixed points with different stabilities that emerge or disappear when the bifurcation parameter is changed (**Figure 1.4D**). A special case of the Saddle Node bifurcation is the Saddle Node on Invariant Circle (SNIC) bifurcation. In contrast to the Saddle Node bifurcation, the pair of fixed points emerge or disappear on a closed trajectory. When the pair of fixed points disappear (also referred to as collided fixed point, **Figure 1.4D**) a stable limit cycle emerges, i.e. the system starts oscillating. When the pair of fixed point emerge, the closed trajectory is disrupted, i.e. oscillations are lost. As the system is already on a closed trajectory, the stable state can be referred to as quiescent, i.e. it is arrested at a certain point of the cycle. Hence,

the transition from an oscillatory state to a stable state during a SNIC bifurcation is characterized by a sudden offset of oscillations with invariant amplitudes, and a slowing down of the period. Similar characteristics are observed when the system transitions from a stable to an oscillatory state.

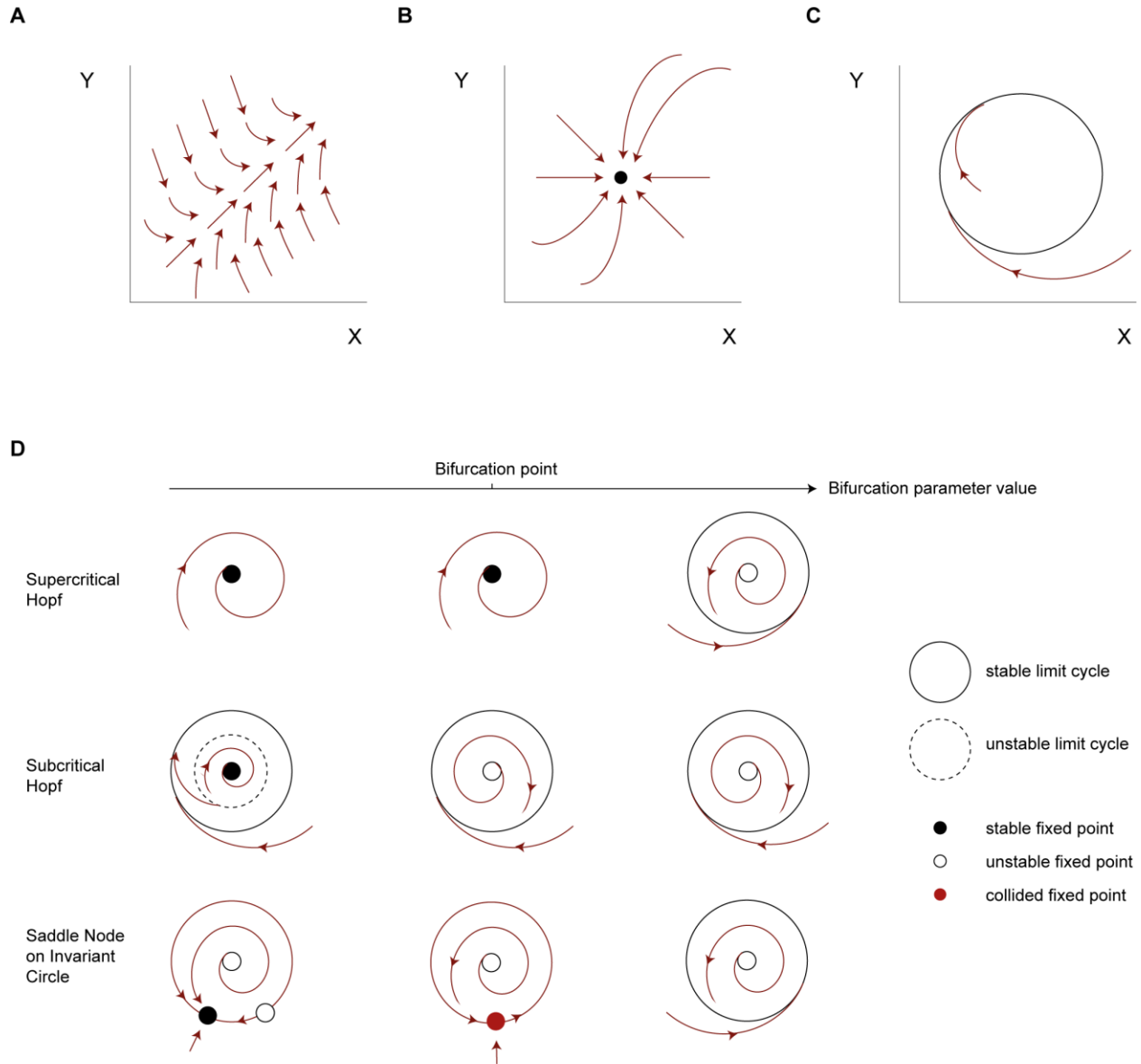


Figure 1.4: Phase planes and bifurcations

A, B, C, Cartoon of an arbitrary system in a phase plane. Arrows indicate how an arbitrary system evolves over time. B, Stable fixed and attractive point. C, Stable limit cycle.

D, Examples of how an arbitrary system changes when the bifurcation parameter is varied. At the bifurcation point, a qualitative change in the behavior of the systems occurs. Phase planes for supercritical Hopf, subcritical Hopf and Saddle Node on Invariant circle bifurcations are shown. Based on (Izhikevich, 2000; Saggio et al., 2017)

In summary, a system exhibits self-sustained oscillations only in a certain range of parameter values, depending on the network design and its parameters. Indeed, theoretical modelling and experimental data of the p53 oscillating network revealed that adding a positive feedback loop to negative feedback oscillator changed the bifurcation diagram from a supercritical Hopf to a SNIC bifurcation (Mönke et al., 2017). Hence, investigating the bifurcations of an oscillating system will help to unravel its architecture.

1.3 C. elegans as a model organism to study development and its timing

Caenorhabditis elegans is a free-living, non-parasitic roundworm of 1 mm in length and is found worldwide in rotten organic material, rich in nutrients and micro-organisms. In the lab, animals are maintained on agar plates or liquid cultures containing *Escherichia coli* bacteria as food source, at temperatures ranging from ~12°C to ~25°C. *C. elegans* has two sexual forms: self-fertilizing hermaphrodites, and males, which arise spontaneously with a frequency of about one in thousand. Self-fertilization results in the generation of genetically identical off-spring, whereas male mating allows the exchange of genetic material (reviewed in Corsi et al., 2015).

The life-cycle consists of embryogenesis (**section 1.3.1**), four larval stages (L1-L4), and an adult stage, which together takes roughly 2.5 days at 25°C from egg until egg-laying adults. The larval stages are separated by molts, in which animals renew their exoskeleton, the cuticle. Under unfavorable conditions, e.g. absence of food, high temperature, or overcrowding, L1 animals can develop into L2d stage and subsequently into a developmentally arrested state, called dauer diapause (Cassada and Russell, 1975), which they can survive for months.

Upon hatching, L1 larvae contain 558 nuclei, which increases to 959 somatic nuclei in adult hermaphrodites. Despite the small number of cells, *C. elegans* features many organs, including nervous system, muscles, intestine, epidermis, and gonad. However, it lacks a respiratory and circulatory system and more specialized digestive organs. Given its transparency and its invariant number and fate of somatic cells, all cell divisions and cell fates in *C. elegans* have been mapped (Kimble and Hirsh, 1979; Sulston and Horvitz, 1977; Sulston et al., 1983). As a result, the first so-called heterochronic genes, which control the timing of stage-specific events relative to other developmental events, could be identified (Ambros and Horvitz, 1984). Subsequent genetic studies facilitated the identification and characterization of molecular pathways involved in development. Thus, *C. elegans* has emerged as a popular model to study developmental biology.

Precise timing of events is crucial for the development of an organism. The developmental stages of *C. elegans* can be considered repetitive as well as linear. For example, the molts are repeated at the end of every stage (**section 1.3.2**), but at the same time stage-specific events occur. Hence, it seems likely that timing of larval development comprises two distinct but interacting mechanisms. A cyclical time keeping mechanism that ensures timing of repetitive events (**section 1.3.3**) and a linear time keeping mechanism that times the sequence of stage-specific events. Thus, besides studying developmental processes as such, *C. elegans* is also a powerful model to their timing.

1.3.1 Embryogenesis

Embryogenesis of *C. elegans* takes about 840 min (14 hours) at 22°C (the timing of events in this chapter is based on (Hall et al.), **Figure 1.5**). During fertilization, when the haploid oocyte and haploid sperm fuse, a diploid single cell embryo arises. Fertilization is followed by multiple rounds of cell divisions (proliferation), which have been fully mapped (Sulston et al., 1983), and spatial relocation (gastrulation). Early proliferation of the single-cell embryo takes place in the hermaphrodite uterus, from 0 to 150 min post-fertilization, and is characterized by a series of asymmetric divisions, during which the principle axes of the body plan are set-up. The asymmetric divisions result in six founder cells that differ in cell fate. They undergo further divisions and eventually give rise to partially overlapping tissue types. At approximately 30-cell stage, eggs are laid and additional proliferation events continue to occur from 150 to 350 min post-fertilization. At the same time (100 to 350 min), gastrulation takes place, i.e. cells start to move and internalize, leading to separation of ectoderm, endoderm and mesoderm precursor cells.

During morphogenesis, cells become terminally differentiated, and the shape of the animal is determined, which is largely dominated by the epidermis (Chisholm and Hardin, 2005). The major epidermal cells are already generated around 280 min post-fertilization. Soon after, they start to express the junction protein AJM-1 (McMahon et al., 2001), and the epidermal sheath, an apical extracellular matrix (ECM) is formed. Epidermal cells in embryo undergo spatial rearrangements and morphological changes (dorsal intercalation), until eventually the embryo becomes enclosed by the epidermal sheath, a process known as epidermal enclosure. Epidermal morphogenesis is followed by elongation at 400 min post-fertilization. Elongation is characterized by lengthen the bean-shaped embryo into the shape of a worm. Tension and forces provided by the epidermal sheath is required for elongation (Priess and Hirsh, 1986; Vuong-Brender et al., 2017a). Leucine-rich repeat proteins LET-4, and EGG-6 (Mancuso et al., 2012), and the conserved structural proteins (Jovine et al., 2005), so-called zona pellucida domain proteins FBN-1/Fibrillin (Kelley et al., 2015), NOAH-1 and NOAH-2 (Vuong-Brender et al., 2017b) are implicated in elongation. Quickening is

the final stage before hatching and starts at 550 minutes when the first coordinated movements of the worm (3-fold stage) are observed within the egg. Although the first ECM structures arise during the early stages of morphogenesis, the synthesis of the first larval cuticle only occurs at roughly 700 min, not long before the worm hatches at 840 min post-fertilization.

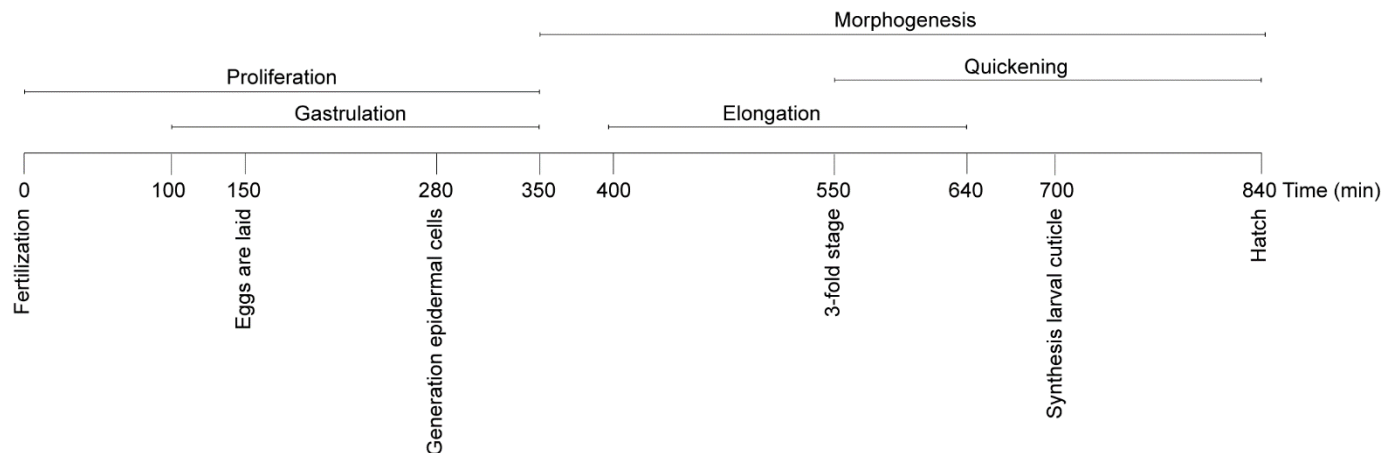


Figure 1.5: Timeline of developmental stages during embryogenesis

Timing of events during embryogenesis in minutes. Time refers to developmental time after fertilization at 20-22°C. Specific events during embryogenesis are indicated below and specific stages of embryogenesis are indicated above timeline. Based on (Hall et al., 2017).

1.3.2 Molting, a repetitive feature during *C. elegans* development

Besides stage-specific processes, a hallmark of *C. elegans* larval development is repetitive molting at the end of each larval stage. Molting is characterized by a period of behavioral quiescence (lethargus), during which the worm replaces its old cuticle, a complex extracellular matrix (ECM), for a new one. I will discuss the structural basis of the cuticle, the different events during molting (apolysis, cuticle synthesis and ecdysis) and their regulation in further detail below.

1.3.2.1 Cuticle structure

The cuticle of *C. elegans* is an apical multi-layered ECM (**Figure 1.6**), most of which is synthesized by the underlying epidermis. The cuticle is connected with the epidermis and the underlying basement membrane through bundles of filaments, called fibrous organelles. Features on the surface of the cuticle include protruding longitudinal ridges, called alae, found in L1 larvae, dauer larvae and adults, and circumferential furrows, called annuli, found in all stages (Cox et al., 1981a). Besides the external cuticle, cuticles which are directly covering the internal epithelial cells are observed in the openings of the animal,

i.e. buccal cavity, pharynx, vulva, rectum, excretory duct and excretory pore (reviewed in Lažetić and Fay, 2017).

The internal cuticles have a simple structure and except for the pharyngeal cuticle which contains chitins (George-Raizen et al., 2014; Veronico et al., 2001), the other internal cuticles consist predominantly of collagen (Gill et al., 2016). In contrast, the external cuticle comprises multiple layers (**Figure 1.6**): the surface coat, the epicuticle and the cortical, medial and basal zones (Cox et al., 1981b). Although the overall structure is very similar between worms in different developmental stages, there are stage-specific features, e.g. larva lack the medial zone in their cuticle (Cox et al., 1981a). Whereas the main component of the cortical, medial and basal zone are proteins, the surface coat and the epicuticle consist of carbohydrates and lipids respectively. Although little is known, the surface coat is thought to protect against pathogens and the epicuticle is thought to serve as a hydrophobic barrier. The outermost layer of the cortical zone differs from the underlying zones as it mostly contains non-collagen proteins, such as cuticlins. Interestingly, non-collagen proteins FBN-1, NOAH-1 and NOAH-2, implicated in the epidermal sheath, the embryonic ECM, are also found in the cuticle of larvae (Frand et al., 2005). Collagen-like proteins are the most predominant components of the external cuticle, and are mainly found in the cortical, medial and basal zones. Although some collagens are stage-specific, numerous collagens appear to be incorporated into the cuticle in every larval stage. Back in 1981, Cox and colleagues revealed that synthesis of cuticle components was increased during the molt compared to the intermolt (Cox et al., 1981c). Indeed, later work reported that the expression of several genes encoding structural components of the cuticle peaks four times during development (Frand et al., 2005; Johnstone and Barry, 1996; McMahon et al., 2003). However, how their rhythmic expression is regulated remains unclear.

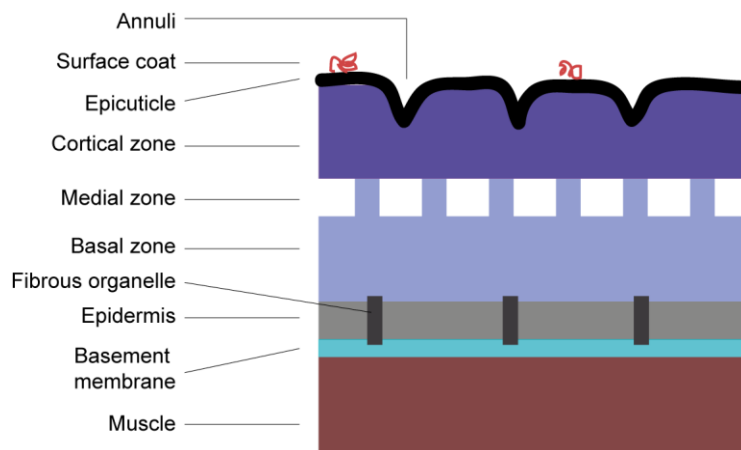


Figure 1.6: Structure of the *C. elegans* cuticle and the underlying tissues

Longitudinal cross-section of the adult cuticle. The five layers of the cuticle, i.e. surface coat, epicuticle, cortical zone, medial zone, and basal zone, are indicated. The underlying tissues include the epidermis, the basement membrane and the muscles. Based on (Lažetić and Fay, 2017a; Page and Johnstone, 2007).

1.3.2.2 Collagen structure and synthesis

The *C. elegans* cuticular collagens are encoded by roughly 170 genes (*C. elegans* Sequencing Consortium, 1998). The structure is characterized by a helical domain and a collagenous domain flanked by three cysteine-rich regions. The collagenous domain consists of 37 to 43 Gly-X-Y triplets, with X and Y often being proline and 4-hydroxyproline residues. Classification of cuticular collagens in 5 groups is based on structural similarity, i.e. on the number of interruptions in the Gly-X-Y repeats (Teuscher et al., 2019). Despite extensive genetic screens, mutants of numerous cuticular collagens do not exhibit obvious phenotypes. Thus, it seems likely that the function of at least some cuticular collagens are partially redundant. Whether functional redundancy occurs within or across classes remains to be established. Nevertheless, mutants of some 20 cuticular collagen genes have revealed phenotypes, which fall in the following groups: dumpy (Dpy, short and fat), roller (Rol, helically twisted), Blister (Bli, blistering of the cuticle), squat (Sqt, short and twisted), ray abnormal (Ram) and long (Lon) (reviewed in Page and Johnstone, 2007).

Although little is known about the synthesis of cuticular collagen in *C. elegans*, it seems likely that the process is similar to that of collagen in mammals (reviewed in Page and Johnstone, 2007). The first step in collagen synthesis is the hydroxylation of the prolines in the Gly-X-Y repeats, which is required for proper folding. This process occurs co-transcriptionally, takes place in the endoplasmic reticulum and is catalyzed by prolyl 4-hydroxylase. In *C. elegans*, *dpy-18* encodes for one of the subunits of prolyl 4-hydroxylase (Winter and Page, 2000). Next, disulfide bonds between monomers are formed by protein disulfide isomerase, followed by trimerization by peptidyl prolyl cis-trans isomerases. Trimers are exported from the ER, which is thought to be facilitated by SEC-23 a component of secretory vesicles (Roberts et al., 2003). BLI-4 (Thacker et al., 1995) and DPY-31 (Novelli et al., 2004) are required for the removal of N-terminal and C-terminal peptides respectively. The final step in collagen synthesis involves the crosslinking of multiple trimers by a hydrogen peroxide-generating NADPH dual oxidase enzyme BLI-3 (Edens et al., 2001) and a heme peroxidase MLT-7 (Thein et al., 2009).

1.3.2.3 Molting stages

The molting stages have been described in detail by Singh and coworkers (Singh and Sulston, 1978), and I will summarize them here. The onset of molting is characterized by lethargus, a stage of quiescence in which movements strongly decrease, with a burst of locomotion once in a while. Pumping is also gradually reduced and the mouth becomes sealed with a plug, preventing the animal from feeding. Before the new cuticle can be synthesized, the current cuticle needs to be detached from the underlying epidermis, a process called apolysis. Detachment starts at the head, followed by the tail and finally the old cuticle is released from the central body region. At the same time, animals exhibit rotations around the longitudinal axis, which is thought to facilitate apolysis. After synthesis of the new cuticle, the old one can be shed, a process called ecdysis. The pharynx as well as the complete body of the worm start to make spontaneous movements and the old cuticle becomes inflated at the head region. The pharyngeal lining and the cuticle break, and the plug is expelled, although the order of these events can differ among animals. Finally, the worm crawls out of the cuticle and resumes feeding.

Although the molting is a fundamental process in the development of *C. elegans*, insight into its regulators has remained limited. Genetic screens have identified several potentially important factors (Frand et al., 2005; Kamath et al., 2003). Their mutant phenotypes include: complete encasement, trapping in the cuticle with partial detachment, a corset or string around the mid body and an old cuticle that remains attached to the tail (reviewed in Lažetić and Fay, 2017). Although most molting phenotypes appear as shedding defects, apolysis or cuticle synthesis can be affected as well, but defects only become phenotypically visible during ecdysis. These phenotypes indicated a role of certain proteases, protease inhibitors, reductases, and endocrine regulators (further discussed below) in remodeling of the *C. elegans* cuticle (Frand et al., 2005; reviewed in Lažetić and Fay, 2017). For example, the proteases NAS-36, NAS-37 and CPZ-1 are implicated in the degradation of the old cuticle, as mutants fail to release the cuticle in the central body. The expression of these proteins peaks during the molt, particularly in the epidermis. Moreover, NAS-37 and CPZ-1 were found to accumulate in the cuticle (Davis et al., 2004; Hashmi et al., 2004; Suzuki et al., 2004).

1.3.2.4 Regulation of molting

Molting is a highly complex, animal-wide process, which involves behavioral changes, neuronal aspects and potentially other events, such as metabolism, to faithfully renew the cuticle. Hence, not only control of epidermal remodeling as such, but also the coordination with other processes appears essential for molting (Lažetić and Fay, 2017a). However, the molecular mechanisms that drive molting in *C. elegans* are currently unknown. In *Drosophila melanogaster*, the steroid hormone ecdysone is the master regulator of

molting (reviewed in Yamanaka et al., 2013). Once produced by the prothoracic gland, ecdysone is converted to its active form, 20-hydroxyecdysone (20E). 20E binds to its nuclear receptor to initiate the transcription of a cascade of transcription factors, which in turn induces transcriptional responses that promote molting and morphogenesis. The nuclear hormone receptor DHR3 which is responsive to 20E signaling, and its downstream target, the nuclear hormone receptor β FTZ-F1, have orthologues in *C. elegans*, NHR-23 (Kostrouchova et al., 1998) and NHR-25 (Gissendanner and Sluder, 2000) respectively (**section 1.4.2.1**). These and several other nuclear hormone receptors are implicated in molting (reviewed in Antebi, 2006). Although *C. elegans* lacks ecdysone and its receptor, sterol signaling is indispensable for development and molting: as cholesterol deprivation caused developmental arrest (Merris et al., 2003) and failure to shed the cuticle. A similar phenotype has been observed in mutants of *lrp-1*, a low density lipoprotein receptor (Yochem et al., 1999). Whether and how molting in *C. elegans* is regulated by steroid hormones and which steroid hormones are involved remains to be established.

Besides nuclear hormone receptors, another signaling pathway that may be important for molting is the hedgehog-patched signaling pathway. Hedgehog (Hh) is a ligand secreted from a signal producing cell that binds its receptor Patched (Ptc) on a signal receiving cell. This interaction releases the latent activity of Smoothed (Smo), which in turn promotes the transcription factor, Cubitus interruptus (Ci), to shuttle to the nucleus and induce the expression of Hh targets (reviewed in Bürglin and Kuwabara, 2006). In *Drosophila* and vertebrates, Hedgehog signaling is important for cell patterning, fate, survival and proliferation during development (reviewed in Briscoe and Théron, 2013). The Hh signaling pathway in *C. elegans* has diverged, as the *C. elegans* genome lacks genes encoding for Hh or the downstream effector Smo (*C. elegans* Sequencing Consortium, 1998), but Hh-related genes are considerably expanded to over sixty (Aspöck et al., 1999). Moreover, the *C. elegans* genome encodes for two *ptc* homologs, one *ptc*-pseudogene, two dispatched and 24 *ptc*-related genes (*ptr*) (Kuwabara et al., 2000). As RNAi against Hh-related, *ptr* and *ptc* genes revealed molting phenotypes, among others, a role in molting has been postulated (Zugasti et al., 2005). Indeed, expression patterns of Hh signaling genes are predominantly, but not limited to, the hypodermis or epithelial derived cells (reviewed in Bürglin and Kuwabara, 2006). Numerous of them exhibit cyclical expression with each of the molts (Hao et al., 2006; Hendriks et al., 2014). Interestingly, *ptc* in *C. elegans* and other species contain sterol sensing domains and Hh is modified by cholesterol. Moreover, cholesterol is not required for Hh signaling, but it does affect its potency and signaling activity (reviewed in Kuwabara and Labouesse, 2002). Given the requirement of sterols in *C. elegans* development, it seems likely that Hh-related genes play a role in sterol-mediated signaling during molting.

1.3.3 Timing of recurring events during *C. elegans* development

Using genome-wide gene expression studies, we and others have identified large-scale mRNA level oscillations during *C. elegans* larval development (Hendriks et al., 2014; Kim et al., 2013). Thousands of genes, hereafter referred to as ‘oscillating’ genes, are affected and their expression changes are more than 2-fold from peak to trough. The oscillations share an 8-hr period at 25°C, which resembles the larval stage durations. Moreover, the periodicity of molting and the oscillation period both increase when worms are grown at lower temperatures, i.e. they are not temperature compensated. Hence, a connection between molting and oscillations is likely (Kim et al., 2013). Indeed, previous work reported rhythmic expression of several genes encoding structural components of the cuticle (Frand et al., 2005; Johnstone and Barry, 1996; McMahan et al., 2003), and our global analyses showed that these genes were strongly enriched among ‘oscillating’ genes (Hendriks et al., 2014). However, the peak phase distribution of the oscillations is wide-spread, i.e. the expression of various genes peaks outside of the molt. This suggests that the function of gene expression oscillations is not limited to molting, but more likely functions to coordinate and time numerous developmental events.

Mechanistically, it seems possible that transcript oscillations arise from rhythmic transcription, as mRNA level oscillations were preceded by rhythmic pre-mRNA accumulation (Hendriks et al., 2014). Indeed, unpublished data from our lab revealed that the expression of destabilized GFP driven from the promoter of several ‘oscillating’ genes resembles the expression of the endogenous genes (Yannick Hauser, unpublished). We could recapitulate not only the oscillation as such, but also its phase and amplitude, indicating that the promoter sequence is sufficient for oscillatory gene expression. However, the factors that drive rhythmic transcription and the step at which rhythmic transcription is regulated (explained in more detail in **section 1.4.1**), are currently unknown.

Besides molting, another repetitive developmental event is the division and differentiation of skin progenitor cells (seam cells), although some of them occur stage-specifically (Sulston and Horvitz, 1977). Timing of seam cell divisions relative to other developmental events is controlled by the heterochronic pathway. The so-called retarded mutants of the heterochronic pathway repeat seam cell divisions and molts, whereas in the so-called precocious mutants those are skipped (Ambros and Horvitz, 1984). Moreover, exit from the molting cycle and seam cell exit from the cell cycle are some of the features that characterize the transition from larvae to adults from the skin point of view (Ambros, 1989). These studies suggest that molting and seam cell divisions are coupled. Pharmacological activation of nicotinic acetylcholine receptors resulted in uncoupling, i.e. seam cell divisions were delayed relative to the molt

in L2 stage, leading to lethality (Ruaud and Bessereau, 2006). Thus, it seems likely that molting and seam cell divisions are driven by independent but synchronized time keeping mechanisms.

1.4 Transcription

Expression of the right gene at the right time and place is crucial during development. Although regulation of gene expression occurs at many levels, the focus of this thesis is on transcriptional regulation (**section 1.4.1**). I will also discuss functions of the transcription factors that were identified through a screen in this thesis (**section 1.4.2**).

1.4.1 Transcriptional regulation

Regulation of gene expression at the level of transcription is mediated by an interplay of RNA polymerase, transcription factors, and co-factors. RNA polymerase exists in three flavors that differ in structure and associated factors: RNAPI produces the large ribosomal RNA (rRNA) precursor, RNAPII produces messenger RNA (mRNA) and non-coding RNA, and RNAPIII produces transfer RNA (tRNA) and the small rRNA (Sentenac, 1985). Here, I will describe how RNAPII transcribes mRNA in mammals, focusing on promoter recognition, transcription initiation, elongation (as reviewed in Cramer, 2019) and termination (as reviewed in Porrua and Libri, 2015). Although transcription is conserved throughout eukaryotes, some of the aspects are *C. elegans* specific, which will be pointed out below.

Transcription of mRNA is initiated at the promoter region, upstream of the transcription start site. In an inactive state, promoters are protected by nucleosomes or DNA methylation. For a gene to be transcribed, the promoter must be accessible for binding of RNAPII. Accessibility, and thus activity, of promoters is regulated by transcription factors and chromatin remodeling factors. Most of the transcription factors bind open chromatin, but some can open up small stretches of closed chromatin, the so-called pioneer transcription factors. As different families of transcription factors recognize different DNA sequences, this allows for some degree of specificity (further discussed below). In contrast, the binding site for RNAPII is more, although not completely, uniform among promoters (Smale and Kadonaga, 2003). Once the promoter is accessible, RNAPII together with associated initiation factors bind as a pre-initiation complex (PIC) to the promoter sequence. In contrast to mammals, the core promoter elements in *C. elegans* have been difficult to assess, as about 70% of the genes are trans-spliced to SL1 or SL2, a 22-nucleotide sequence (Blumenthal, 2018). Opening of the two DNA strands by PIC requires recruitment of the DNA translocase XPB. Next, transcription initiation is facilitated by the so-called Mediator complex, which promotes the phosphorylation of Serine-5 in the repeats of the C-terminal domain (CTD) of RNAPII by CDK7, required for elongation. Once initiated, RNAPII can pause after roughly 50 base pairs downstream

of the promoter, mediated by the factors DSIF and NELF. Pause-release and the transition into active elongation is regulated by P-TEFb which phosphorylates DSIF, NELF and Serine-2 of the CTD of RNAPII. In contrast to mammals, NELF is not encoded by the *C. elegans* genome (*C. elegans* Sequencing Consortium, 1998) and hence, pausing downstream of the promoter is not commonly observed during larval development (Baugh et al., 2009; Maxwell et al., 2014). As RNAPII slides along the DNA, a nascent transcript is synthesized. Once the polyadenylation signal (PAS) is transcribed, the nascent transcript is cleaved a few nucleotides downstream of PAS and subsequently adenosine nucleotides are added. The exact mechanism of how RNAPII is released from the DNA remains unclear. Two models have currently been proposed. In the one model conformational changes in the elongation complex are proposed to destabilize the complex (allosteric model). In the other model, an 5'-3' exonuclease degrades the nascent RNA after cleavage leading to dislocation of the elongation complex (torpedo model) (reviewed in Porrua and Libri, 2015).

Although the basics of transcription are generic, specificity is required to give rise to distinct cellular behaviors and different cell types during development. How is specificity achieved? The accessibility of chromatin and the presence of transcription factor binding motifs in the promoter region alone fail to fully explain transcriptional activity. Moreover, transcription factors of the same family often have similar transcription factor binding motifs, but have distinct targets (reviewed in Biggin, 2011). Indeed, additional layers of regulation at each step of the transcription cycle are known to control the transcriptional output. For example, numerous transcription factors bind not only to the DNA in the promoter region, but also interact with more distant DNA sequences, called enhancers. Another level of complexity is achieved by the interaction of monomeric transcription factors that act cooperatively to regulate gene expression as homodimers, heterodimers or even multi-mers (reviewed in Todeschini et al., 2014). Dimerization has been observed in particular for nuclear hormone receptors (reviewed in Forman and Samuels, 1990), a specific class of transcription factors, of which I will discuss some examples below (**section 1.4.2.1**). Finally, signaling pathways that modify transcription factor activity post-translationally are important to transduce internal and external cues and thus allow temporal control of gene expression (reviewed in Benayoun and Veitia, 2009). Clearly, transcriptional regulation is complex and characterization of transcription factors, their functioning and architecture will help to better understand how gene expression is regulated.

1.4.2 Transcription factors in this thesis

The work I present in this thesis focuses on the transcription factors NHR-23, NHR-25, GRH-1, BLMP-1, MYRF-1. This section will describe the function and relevance of these transcription factors.

1.4.2.1 *nhr-23* and *nhr-25*

NHR-23 and NHR-25 belong to a family of 284 nuclear hormone receptors (NHR) encoded in the *C. elegans* genome (reviewed in Antebi, 2006). NHRs are transcription factors, which often act as homo- or heterodimers (reviewed in Forman and Samuels, 1990). Many of the NHRs require lipophilic ligands for their activity, while for other NHRs the ligands are unknown or unidentified. Moreover, the mechanisms of action of numerous vertebrate NHRs and some *C. elegans* NHRs are well characterized (reviewed in Antebi, 2006). However, the biological function of the majority of the 284 NHRs in *C. elegans* is poorly understood or completely unknown.

nhr-23 is the orthologue (Kostrouchova et al., 1998) of *Drosophila* Dhr3, an ecdysone-response gene involved in molting and morphogenesis, and mammalian ROR α , regulator of oscillatory expression of Bmal-1, the second feedback loop in the circadian rhythm. Although *nhr-23* is uniformly expressed in early embryos, expression becomes restricted to epidermal cells once they are born during embryogenesis and expression continues during larval stages (Kostrouchova et al., 1998). *nhr-23(RNAi)* causes a Dpy phenotype, larval arrest, embryonic lethality, and cuticle shedding defects, mostly constrictions (Kostrouchova et al., 1998). As molting defects could be induced at every molt, NHR-23 seems to be required for every molt (Kostrouchova et al., 2001). Indeed, we and others showed that expression of *nhr-23* oscillates with its peak occurring during the intermolt (Gissendanner et al., 2004; Hendriks et al., 2014; Kostrouchova et al., 2001). Genome-wide expression microarrays in *nhr-23(RNAi)* animals revealed genes encoding for collagens and hedgehog-related proteins among the affected genes (Kouns et al., 2011).

nhr-25 is the orthologue (Gissendanner and Sluder, 2000) of *Drosophila* Ftz-f1, involved in molting and morphogenesis, and the mammalian Sf-1, involved in sex determination. *nhr-25* is expressed in epidermal cells from the moment they arise in embryos and expression is maintained in the epidermis during larval development (Asahina et al., 2000; Gissendanner and Sluder, 2000). *nhr-25(RNAi)* caused embryonic and larval lethality, larval arrest, and failure of vulva formation and sterility in adults. More specific phenotypes in larvae include Dpy, uncoordinated, posterior patterning defects and defects in shedding the cuticle resulting in cuticle attachment at the rectum (Asahina et al., 2000; Gissendanner and Sluder, 2000). Moreover, cell fusion defects were reported in embryonic epidermal cells, vulva cells, and its precursors (Chen et al., 2004), and seam cells (Šilhánková et al., 2005) of *nhr-23(RNAi)* animals. Clearly, NHR-25 plays

a role in epidermal development, but is also required for somatic gonad development (Asahina et al., 2000; Gissendanner and Sluder, 2000). Expression of *nhr-25* oscillates, but in contrast to *nhr-23*, the peak occurs during the molt (Gissendanner et al., 2004; Hendriks et al., 2014).

Mechanistically, *nhr-23* and *nhr-25* are at least partially controlled by the miRNAs *mir-84* and *let-7* involved in the heterochronic pathway, as *nhr-23(RNAi)* and *nhr-25(RNAi)* restored *mir-84* and *let-7* supernumerary molting phenotypes. However, regulation of *nhr-23*, but not *nhr-25* is most likely indirect as the 3'UTR of *nhr-23* lacks obvious binding sites for these miRNAs (Hayes et al., 2006). Even though the orthologue of *nhr-25*, *Ftz-f1*, is a target of the orthologue of *nhr-23*, *Dhr-3*, this interaction is not conserved in *C. elegans* (Kostrouchova et al., 2001). To date, the molecular mechanisms through which NHR-23 and NHR-25 act in the regulation of epidermal development and molting is unknown.

1.4.2.2 *grh-1*

GRH-1 belongs to the LSF/Grainyhead family of transcription factors (Venkatesan et al., 2003). The *C. elegans* and *Drosophila* genome encode one *grh* gene, whereas mammals have three Grhl genes (Grhl1-3). The first member, Grainyhead, was identified in *Drosophila* (Bray and Kafatos, 1991; Bray et al., 1989; Dynlacht et al., 1989; Johnson et al., 1989) and subsequent identification of other members showed high structural conservation in their DNA binding domain and dimerization domain (Venkatesan et al., 2003). Recently, the structure of the DNA binding domain of Grhl1 and Grhl2 has been solved and revealed their binding to the DNA consensus sequence (AACCGGTT) in a dimeric arrangement (Ming et al., 2018).

The name grainyhead is derived from the phenotypes observed in Grainyhead mutants in *Drosophila*, i.e. soft, thin and granular cuticles, some of which ruptured, resulting in cell extrusion (Bray and Kafatos, 1991; Nüsslein-Volhard et al., 1984a). Similar phenotypes have been reported for *grh-1(RNAi)* in *C. elegans* embryos (Venkatesan et al., 2003), suggesting a conserved role of Grainyhead family members in cuticle development. Indeed, *Ddc*, a Dopa decarboxylase and tyrosine hydroxylase, crucial for cross-linking components in the cuticle is a direct, but not the only, target of Grainyhead (Bray and Kafatos, 1991). Besides its role in cuticle formation, Grainyhead is important for cytoskeleton rearrangements and epidermal cell shape changes during epidermal wound healing (Bray and Kafatos, 1991; Cristo et al., 2018; Mace et al., 2005), size control of the epithelial tube (Hemphälä et al., 2003), and polarization of the adult epidermis (Lee and Adler, 2004).

Consistently, the mammalian Grhl1-3 genes are important for development and maintenance of epithelial tissues. Grhl genes are predominantly expressed in epithelial tissues and partially, but not completely functionally redundant (Auden et al., 2006). Grhl genes play a role in epithelial differentiation (Yu et al.,

2006), wound healing, eye lid closure (Boglev et al., 2011), neural tube closure (Rifat et al., 2010), and formation of hair coat (Wilanowski et al., 2008). Grhl3 directly regulates expression of transglutaminase 1, the enzyme essential for cross-linking structural components of the epidermis (Ting et al., 2005), a role analogous to that of Dopa decarboxylase (Ddc) in the cuticle of *Drosophila* (Bray and Kafatos, 1991). Grhl1 has been shown to directly regulate the expression of Desmoglein-1 (Dsg1), a desmosomal cadherin, which is a component of the intracellular junctions of the epidermis (Wilanowski et al., 2008). Grhl2 is known to directly regulate the expression of Cadherin-1 and Claudin 4, among other cell interaction genes, and its phenotypes reveal defective cell-cell junctions and impaired cell migration (Varma et al., 2012; Werth et al., 2010). In line with their role in promoting cell adhesion, loss of Grhl genes has been correlated with epithelial-mesenchymal transition (EMT) and progression of epithelial-derived cancers. In contrast, overexpression of GRHL2 has been associated with poor prognosis non-EMT-driven cancer, suggesting that *grhl2* may function not only as a tumor suppressor, but also as an oncogene (Frisch et al., 2017).

Mechanistically, binding of Grh to its DNA binding sites was found to be stable over embryonic development, whereas the expression of Grh-regulated genes was dynamic during this time (Nevil et al., 2017). Moreover, Grh is required for the opening the chromatin at enhancers in epithelial tissues, but is not sufficient to drive their gene expression (Jacobs et al., 2018). Hence, Grh has been proposed to acts as a pioneer transcription factor in developmental programs of epithelial cells. It has been postulated that the dual role of Grh, i.e. acting as a transcriptional repressor and activator, might be attributed to the ability of other transcription factors to now bind accessible DNA (Jacobs et al., 2018; Nevil et al., 2017).

Functions of the mammalian Grhl and *Drosophila* Grainyhead do not appear to be limited to the epidermis. Grainyhead family members are also expressed in neuroblasts at the end of embryogenesis (Brody and Odenwald, 2000; Johnson et al., 1989) and in proliferative post-embryonic neural precursor cells (Prokop et al., 1998). Grainyhead has been placed downstream of the Hunchback → Krüppel → Pdm → Castor cascade (Brody and Odenwald, 2000; Isshiki et al., 2001), which regulates the birth order of ganglion mother cells during asymmetric divisions of neuroblasts. In post-embryonic neuroblasts, Grainyhead is required for their mitotic activity (Almeida and Bray, 2005; Cenci and Gould, 2005).

Given that our previous study identified *grh-1* as an 'oscillating' transcription factor and *grh-1(RNAi)* embryos revealed defective cuticles, a role of GRH-1 in cuticle remodeling during larval development sounds appealing. However, the functional relevance of GRH-1 and molecular mechanisms through which it acts remain to be identified.

1.4.2.3 *blmp-1*

BLMP-1 is a transcription factor, consisting of an N-terminal SET domain, a proline rich domain and a Zn-finger C-terminal domain. BLMP-1 shares sequence similarity to the mammalian BLIMP1, a B-lymphocyte maturation factor (Turner et al., 1994), which has been implicated in epidermal terminal differentiation (Magnúsdóttir et al., 2007). BLMP-1 plays a role in distal tip cell (DTC) migration in the gonad, i.e. BLMP-1 prevents its precocious turn (Huang et al., 2014). BLMP-1 has been identified as proteolytic target of DRE-1 (Horn et al., 2014), an E3-ubiquitin ligase. *blmp-1* is potentially part of a gene regulatory network which controls DTC migration through positive feed-forward loops that involve *daf-12*, *lin-42*, *lin-29*, and *dre-1* (Chepyala et al., 2016). Besides expression in DTCs, BLMP-1 is also expressed in seam and hypodermal cells. Whereas BLMP-1 is specifically expressed in L2-L3 stage in DTCs, expression peaked during L4 stage and remained stable during the rest of development in seam and hypodermal cells (Horn et al., 2014). Although we did not quantify BLMP-1 levels, we previously observed oscillations in *blmp-1* mRNA levels (Hendriks et al., 2014). Besides its function in DTC migration, whether and how BLMP-1 is involved in regulating oscillatory gene expression is unknown. A role of BLMP-1 in regulating molting is however plausible as genes encoding for molting and cuticle factors were found to be affected in *blmp-1* mutant animals in an RNA-seq experiment (Horn et al., 2014).

1.4.2.4 *myrf-1*

myrf-1 is the *C. elegans* homolog of the transcription factor Myelin Regulatory Factor (Myrf). Myrf is expressed in the Central Nervous System, where it is required for the expression of myelin genes, myelination of oligodendrocytes (Emery et al., 2009) and maintenance of myelination in mature oligodendrocytes (Koenning et al., 2012). Even though *C. elegans* does not have myelin, its genome encodes two Myrf genes: *myrf-1* and its paralog *myrf-2*. In *C. elegans*, MYRF-1 and MYRF-2 act functionally redundant in promoting synaptic rewiring of DD neurons in L1 stage (Meng et al., 2017). Biochemical assays revealed that MYRF is an ER-associated transcription factor that frees its N-terminal region containing the DNA binding domain from the ER via auto-proteolytic cleavage (Bujalka et al., 2013; Li et al., 2013). This allows direct binding of the N-terminal product to a DNA consensus sequence, thereby inducing gene expression (Bujalka et al., 2013; Chen et al., 2018).

In *C. elegans*, *myrf-1* has also been identified in a screen for molting factors (Russel et al., 2011, here named *pqn-47*, later renamed to *myrf-1*). *myrf-1(0)* animals underwent apolysis, but failed to shed the cuticle and died trapped in the cuticle. Weaker alleles of *myrf-1* revealed supernumerary molts in adults, and heterochronic genes *lin-41*, *lin-28* and *lin-14* could suppress this phenotype (Russel et al., 2011). Therefore, interaction with the heterochronic pathway has been suggested. The transcriptional reporter

and the GFP fusion protein showed broad spatial expression patterns (Russel et al., 2011), but in contrast to our previous observation (Hendriks et al., 2014), *myrf-1* levels were not found to oscillate (Russel et al., 2011). How *myrf-1* exactly regulates molting in *C. elegans* and whether *myrf-2* shares functional redundancy in molting remains to be determined.

1.5 Aims for this thesis

Genetic oscillations are essential in regulating developmental events, such as somitogenesis in vertebrates, lateral root branching in plants and cell fate decisions. Our previous identification of oscillations affecting thousands of genes during *C. elegans* development (Hendriks et al., 2014), provide a new system to study the role of gene expression oscillations, their architecture and design principles in the context of development. However, to date, it is not well understood whether and how oscillations drive developmental processes in *C. elegans*. Hence, I aimed to provide insight into the properties of the oscillator. Moreover, I aimed to understand whether and how oscillations are coupled to development. I sought to investigate the architecture of the oscillator and identify relevant components. Given the molting phenotypes that we identified along the way, I aimed to provide insight into the molecular mechanisms that regulate molting.

Given that the design of an oscillator determines its dynamics, we investigated how the oscillator behaved in response to perturbations and how it transitions between different states. To study such state transitions, we first investigated the gene expression patterns of oscillating genes across the *C. elegans* life cycle. After we identified distinct expression patterns of oscillating genes in embryos, freshly hatched larvae and adults, I next aimed to quantitatively describe the dynamic changes in gene expression that occur during the transitions between the developmental stages. Moreover, we took the advantage of our previous finding that oscillations appeared absent during dauer diapause (Hendriks et al., 2014), to investigate a state transition from a developmentally arrested stage. The quantitative characterization of transitions between oscillatory and stable states can provide insight into the properties of the oscillator.

Although the oscillation period resembled the larval stage durations, a quantitative analysis is currently lacking. Here, we quantified *C. elegans* developmental stage durations and gene expression oscillation periods using population-based and single animal approaches to investigate to what extent oscillations are coupled to developmental processes, such as molting. Given that molting is repetitive in its nature, one would expect that a regulatory, perhaps rhythmic, genetic network is required for timing of molting and coordination with other developmental events. However, only a few factors have been implicated in molting and the molecular mechanisms are currently unknown. Our results here suggested that mRNA

level oscillations arise from rhythmic transcription. Hence, I aimed to identify transcription factors that are important for oscillatory gene expression and molting. The characterization of such transcription factors is of interest to better understand the molecular basis of molting, the molecular wiring of the oscillator and functional relevance of the coupling between oscillations and molting.

2. Results

2.1 Manuscript: State transitions of a developmental oscillator

Gert-Jan Hendriks and Yannick Hauser performed RNA sequencing time courses. MM and YH analyzed the RNA sequencing data. MM performed and analyzed luciferase assays. Guy Bogaarts developed the graphical user interface for analyzing the luciferase data. YH acquired and analyzed the single worm imaging data. Jan Eglinger wrote the KNIME workflow for analyzing the single worm imaging. Charisios Tsiairis conceived parts of the analysis. Helge Grosshans, MM and YH conceived the project and wrote the manuscript.

Developmental function and state transitions of a gene expression oscillator in *C. elegans*

Milou W.M. Meeuse^{1,2*}, Yannick P. Hauser^{1,2*}, Gert-Jan Hendriks^{1,2}, Jan Eglinger¹, Guy Bogaarts³, Charisios Tsiairis¹, Helge Grosshans^{1,2,4}

¹ Friedrich Miescher Institute for Biomedical Research (FMI), Maulbeerstrasse 66, CH-4058 Basel.

² University of Basel, Petersplatz 1, CH-4001 Basel.

³ University Hospital, Spitalstrasse 21, CH-4031 Basel.

⁴ Corresponding Author and Lead Contact: helge.grosshans@fmi.ch.

* equal contribution.

Abstract

Gene expression oscillators can structure biological events temporally and spatially. Different biological functions benefit from distinct oscillator properties. Thus, finite developmental processes rely on oscillators that start and stop at specific times; a poorly understood behavior. Here, we have characterized a massive gene expression oscillator comprising >3,700 genes in *C. elegans* larvae. We report that oscillations initiate in embryos, arrest transiently after hatching and in response to perturbation, and cease in adults. Experimental observation of the transitions between oscillatory and non-oscillatory states at a resolution where we can identify bifurcation points reveals an oscillator operating near a Saddle Node on Invariant Cycle (SNIC) bifurcation. These findings constrain the architecture and mathematical models that can represent this oscillator. They also reveal that oscillator arrests occur reproducibly in a specific phase. Since we find oscillations to be coupled to developmental processes, including molting, this characteristic of SNIC bifurcations thus endows the oscillator with the potential to halt larval development at defined intervals, and thereby execute a developmental checkpoint function.

Introduction

Gene expression oscillations occur in many biological systems as exemplified by circadian rhythms in metabolism and behavior (Panda et al., 2002), vertebrate somitogenesis (Oates et al., 2012), plant lateral root branching (Moreno-Risueno et al., 2010), and *C. elegans* larval development (Hendriks et al., 2014). They are well-suited for timekeeping, acting as molecular clocks that can provide a temporal, and thereby also spatial, structure for biological events (Uriu, 2016). This structure may represent external time, as illustrated by circadian clocks, or provide temporal organization of internal processes without direct reference to external time, as illustrated by somitogenesis clocks (Rensing et al., 2001).

Depending on these distinct functions, oscillators require different properties. Thus, robust representation of external time requires a stable period, i.e., the oscillator has to be compensated for variations in temperature and other environmental factors. It also benefits from a phase-resetting mechanism to permit moderate realignments, if needed, to external time. Intuitively, either feature seems unlikely to benefit developmental oscillators. By contrast, because developmental processes are finite, e.g., an organism has a characteristic number of somites, developmental oscillators need a start and an end. How such changes in oscillator activity occur *in vivo*, and which oscillator features enable them, is largely unknown (Riedel-Kruse et al., 2007; Shih et al., 2015).

Here, we characterize the recently discovered '*C. elegans* oscillator' (Hendriks et al., 2014; Kim et al., 2013) at high temporal resolution and across the entire period of *C. elegans* development, from embryo to adult. The system is marked by a massive scale where ~3,700 genes exhibit transcript level oscillations that are detectable, with large, stable amplitudes and widely dispersed expression peak times (i.e., peak phases), in lysates of whole animals. For the purpose of this study, and because insufficient information exists on the identities of core oscillator versus output genes, we define the entire system of oscillating genes as 'the oscillator'. We demonstrate that the oscillations are coupled to molting, i.e., the cyclical process of new cuticle synthesis and old cuticle shedding that occurs at the end of each larval stage. We observe and characterize onset and offset of oscillations both during continuous development

and upon perturbation, and find that these changes in the state of the oscillator system (or bifurcations), occur with a sudden change in amplitude. They also occur in a characteristic oscillator phase and thus at specific, recurring intervals. Because of the phase-locking of the oscillator and molting, arrests thus always occur at the same time during larval stages, around molt exit. This time coincides with the recurring windows of activity of a checkpoint that can halt larval development in response to nutritionally poor conditions. Hence, our results indicate that the *C. elegans* oscillator functions as a developmental clock whose architecture supports a developmental checkpoint function. Indeed, the features of the bifurcations constrain oscillator architecture, excluding a simple negative-loop design, and possible parameters of mathematical models.

Results

Thousands of genes with oscillatory expression during the four larval stages

Although previous reports agreed on the wide-spread occurrence of oscillatory gene expression in *C. elegans* larvae (Grün et al., 2014; Hendriks et al., 2014; Kim et al., 2013), the published data sets were either insufficiently temporally resolved or too short to characterize oscillations across *C. elegans* larval development. Hence, to understand the extent and features of these oscillations better, including their continuity throughout development, we performed two extended time course experiments to cover the entire period of post-embryonic development plus early adulthood at hourly resolution. We extracted total RNA from populations of animals synchronized by hatching in the absence of food. The first time course (designated TC1) covered the first 15 hours of development on food at 25°C, the second time course (TC2) covered the span of 5 hours through 48 hours after plating at 25°C. [**Fig. S1A** provides a summary of all sequencing time courses analyzed in this study.] The extensive overlap facilitated fusion of these two time courses into one long time course (TC3) (**Fig. S1B**), and a pairwise-correlation plot of gene expression over time showed periodic similarity that was repeated four times (**Fig. 1A**, light-gray off-diagonals), presumably reflecting progression through the four larval stages.

The larger dataset enabled us to improve on the previous identification of genes with oscillatory expression (Hendriks et al., 2014). Using cosine wave fitting, and an amplitude cut-off of $2^{0.5}$, we classified 3,739 genes (24 % of total expressed genes) as ‘oscillating’ (i.e., rhythmically expressed) from TC2 (**Fig. 1B, S1C and Table S1; Methods**). Relative to the previous result of 2,718 oscillating genes (18.9% of total expressed genes) in mRNA expression data of L3 and L4 animals (Hendriks et al., 2014), this adds 1,240 new genes and excludes 219 of the previously annotated oscillating genes. We consider this latter group to be most likely false positives from the earlier analysis, resulting from the fact that some genes behave substantially different during L4 compared to the preceding stages as shown below.

Visual inspection of a gene expression heatmap of the fused time course (TC3; **Fig. 1C**) revealed four cycles of gene expression for the oscillating genes. Oscillations were absent during the first few hours of larval development as well as in adulthood, from ~37 hours on, and both their onset and offset appeared to occur abruptly. We will analyze these and additional features of the system and their implications in more detail in the following sections.

'Oscillating' genes are expressed in several tissues with dispersed peak phases

An examination of the calculated peak phases confirmed the visual impression that individual transcripts peaked at a wide variety of time points, irrespective of expression amplitude (**Fig. 1D**). In circadian rhythms, peak phase distributions are typically clustered into three or fewer groups when examined in a specific tissue (Koike et al., 2012; Korenčič et al., 2014). However, the identity of oscillating genes differs across cell types and tissues, and for those genes that oscillate in multiple tissues, phases can differ among tissues (Zhang et al., 2014). Hence, we wondered whether the broad peak phase distribution was a consequence of our analysis of RNA from whole animals, whereas individual tissues might exhibit a more defined phase distribution.

To understand in which tissues oscillations occur, we utilized a previous annotation of tissue-specifically expressed genes (Cao et al., 2017). 1,298, and thus a substantial minority (~35%) of oscillating genes, fell in this category for seven different tissues. They were strongly (~2.5-fold) enriched in the hypodermis (epidermis) and pharynx, and more modestly (≤ 1.5 -fold) in glia and intestine (**Fig. 1E**). By contrast, oscillating genes were greatly depleted from body wall muscle, neurons, and gonad. Hence, oscillatory gene expression occurs indeed in multiple tissues. However, although peak phase distributions deviated for each tissue to some degree from that seen for all oscillating genes, they were still widely distributed for each individual tissue (**Fig. 1F**).

We conclude that a wide dispersion of peak phases appears to be an inherent oscillator feature rather than the result of a convoluted output of multiple, tissue-specific oscillators with distinct phase preferences.

Oscillations initiate with a time lag in L1

The observation that oscillations were undetectable during the first few hours of larval development and started only after > 5 hours into L1 (**Fig. 1A, C**) surprised us. Hence, we performed a separate experiment that covered the first 24 hours of larval development (TC4). This confirmed our initial finding of a lack of oscillations during the first few hours of larval development (**Fig. 2A, B**).

To understand how oscillations initiate after the initial quiescence, we looked at individual genes and observed that the start of detectable oscillations differed for individual genes (**Fig. 2A, C**). Nonetheless, the occurrence of first peaks was globally well correlated to the peak phases calculated from data in **Fig. 1** (**Fig. 2D, E**). Moreover, the transcript levels of many genes with a late-occurring (11 – 13 hours) first peak proceeded through a trough before reaching their first peak as exemplified in **Fig. 2C** for *F11E6.3*. We conclude that initiation of larval development after hatching is accompanied by a time lag prior to transition into an oscillatory state, and that oscillations exhibit a structure of phase-locked gene expressing patterns as soon as they become detectable.

L1 larvae undergo an extended intermolt

Although the gene expression oscillations occur in the context of larval development, functional connections have been lacking. However, genes encoding cuticular components were reported to be enriched among previously identified oscillating genes (Hendriks et al., 2014; Kim et al., 2013), and Gene Ontology (GO-) term analysis of the new extended set of oscillating genes confirms that the top 12

enriched terms all linked to cuticle formation and molting, or protease activity (**Fig. 3A**). These findings, and the fact that molting is itself a rhythmic process, repeated at the end of each larval stage, suggest the possibility of a functional link between molting and gene expression oscillations.

If such a link were true, we would predict that the initial period of quiescence in the early L1 stage be accompanied by a lengthened stage, and, specifically, intermolt duration. Indeed, using a luciferase-based assay that reveals the period of behavioral quiescence, or lethargus, that is associated with the molt (**Fig. S2A-C**), others had previously reported an extended L1 relative to other larval stages (Olmedo et al., 2015). However, they reported an extension of both molt and intermolt.

As the previously used luciferase-expressing transgenic strains developed relatively slowly and with limited synchrony across animals, presumably due to their specific genetic make-up, we repeated the experiment with a newly generated a strain that expressed luciferase from a single copy integrated transgene and that developed with improved synchrony and speed (**Fig. S2D-J, Methods**). Our results confirmed that L1 was greatly extended relative to the other larval stages (**Fig. S2I**). However, in contrast to the previous findings (Olmedo et al., 2015), but consistent with our hypothesis, the differences appeared largely attributable to an extended intermolt (**Fig. S2G**). The duration of the first molt (M1) was instead comparable to that of M2 and M3 (**Fig. S2H**).

Thus, an extended first intermolt coincides with the fact that no oscillator activity can be detected by RNA sequencing during the first five hours of this larval stage. Moreover, because we performed the experiment by hatching embryos directly into food, we can conclude that the extended L1 stage is an inherent feature of *C. elegans* larval development, rather than a consequence of starvation-induced synchronization.

Development is coupled to oscillatory gene expression

The luciferase assay revealed that also the L4 stage took significantly longer than the two preceding stages, though not as long as L1 (**Fig. S2I**). In this case, both the fourth intermolt and the fourth molt were extended (**Fig. S2G,H**). As apparent from the gene expression heatmap, and quantified below, the oscillation period during L4 was also extended. Hence, grossly similar trends appeared to occur in larval stage durations and oscillation periods, determined by the luciferase assay and RNA sequencing, respectively. We considered this as further evidence for a coupling of the two processes.

To test this hypothesis explicitly, we sought to quantify the synchrony of oscillatory gene expression and developmental progression in individual animals at the same time. To this end, we established a microchamber-based time-lapse microscopy assay by adapting a previous protocol (Turek et al., 2015). In this assay, animals are hatched and grown individually in small chambers where they can be tracked and imaged while moving freely, enabling their progression through molts. Using Mos1-mediated single copy transgene integration (MosSCI) (Frøkjær-Jensen et al., 2012), we generated transgenic animals that expressed destabilized *gfp* from the promoter of *qua-1*, a highly expressed gene with a large mRNA level amplitude.

Consistent with the RNA sequencing data, we detected oscillations of the reporter with four expression peaks (**Fig. 3B**). Moreover, we observed similar rates of development as in the luciferase assays when we curated the molts (**Fig. 3C, Table S2, Methods**). The stage durations were in good agreement with the averaged oscillation period times for each cycle, obtained through a Hilbert transform of GFP intensities, for all three larval stages, L2 through L4, for which oscillations period lengths could be reliably determined (**Fig. 3D**).

Single animal imaging enabled us to ask when molts occurred relative to oscillatory gene expression, and we observed a very uniform behavior across animals (**Fig. 3B**). To quantify this relationship, we determined the gene expression phases at molt entries and exits. We obtained highly

similar values across worms within one larval stage (**Fig. 3E**), and only a minor drift when comparing phases across larval stages. Two additional reporter transgenes, based on the promoters of *dpy-9* and *F11E6.3*, which differ in peak expression phases from *qua-1* and one another, yielded similar results (**Fig. S3**).

We considered two possible interpretations of the narrow distributions of oscillation phases at molt entry and exit: first, both oscillations and development could be under independent, but precise temporal control. In this model, certain developmental events would merely coincide with specific phases of oscillations rather than being coupled to them. Therefore, variations in the periods of oscillation and development would add up, non-linearly, to the experimentally observed phase variations. Second, phase-locking of oscillatory gene expression and developmental events might result from the two processes being truly coupled and/or from one driving the other. In this case, the variations in the two periods would partially explain each other, causing a reduction in the expected phase variation relative to the first scenario (**Fig. 3F**).

To distinguish between these scenarios, we used error-propagation to calculate the expected error for two independent processes (**Methods**). Focusing on L2 and L3 stages to exclude any edge effects on period calculation by Hilbert transform, we found that this calculated error consistently exceeded the experimentally observed error (**Fig. 3G**), for all three reporter genes, for both molt entry and molt exit, and for both larval stages. Thus, our observations agree with the notion that development and oscillatory gene expression are functionally coupled (**Fig. 3H**), and potentially causally connected.

Quantification of amplitude and period behavior over time reveal characteristic systems properties

Consistent with the coupling between oscillations and development, both the last larval stage and the period of the last oscillation cycle appeared increased (**Fig. 3D**), before oscillations ceased. The characteristics of such a transition from oscillatory to non-oscillatory state, or bifurcation, can be

examined in the light of bifurcation theory. Bifurcation, that is, a qualitative change in system behavior, occurs in response to a change in one or more control parameters. Depending on the system's topology, characteristic changes of amplitude and period occur during bifurcation (**Fig. 4A**) (Izhikevich, 2000; Salvi et al., 2016; Strogatz, 2015). Thus, transition into a quiescent state through a supercritical Hopf (supH) bifurcation involves a declining, and ultimately undetectable, amplitude and a constant period. By contrast, a Saddle Node on Invariant Cycle (SNIC) bifurcation results in a declining frequency (and thus increasing period) but a stable amplitude.

Hence, to gain a better understanding of the oscillator's bifurcation, we quantified oscillation amplitudes and periods over time. To minimize variations from differences between experiments, we did this for the contiguous 5 – 48 hour time course (TC2). This enabled reliable quantification of these features for the last three oscillation cycles, C2 through C4, which begin at 14 h (C2), 20 h (C3) and 27 h (C4), respectively (**Fig. 4C**). Excluding a small set of 291 genes that exhibited unusual expression trends during the fourth larval stage, i.e., a major change in mean expression levels (**Fig. S4**) this analysis revealed a good agreement of amplitudes across stages, and in particular no indication of damping during the last cycle, C4 (**Fig. 4B**).

We used a Hilbert transform (Pikovsky et al., 2001) to quantify the period over time with high temporal resolution, i.e., at every hour of development. The mean oscillation period thus calculated was approximately seven hours during the first cycles but increased during the fourth cycle (**Fig. 4C**). This change was also apparent when we reconstructed an oscillation from the mean observed oscillation period and compared it to an oscillation with a constant period of seven hours (**Fig. 4D**).

In summary, these analyses reveal a sudden loss of oscillation upon transition to adulthood without prior amplitude damping and an oscillator that can maintain a stable amplitude in the presence of period changes. These are features of an oscillator operating near a SNIC rather than a supH bifurcation (**Fig. 4A**) (Izhikevich, 2000; Salvi et al., 2016; Strogatz, 2015).

Arrest of the oscillator in a specific phase upon transition to adulthood

SNIC and supH bifurcations differ not only in amplitude and period behavior, but also in the stable state, or fixed point, that the systems adopts. In a supH bifurcation, the system spirals from a limit cycle onto a fixed point, whereas in a SNIC bifurcation, the fixed point emerges on the limit cycle (**Fig. 5A**) (Saggio et al., 2017). In other words, a quiescent oscillator near a SNIC bifurcation adopts a state similar to that of a specific phase of the oscillator; the oscillator has become ‘arrested’. By contrast, following a supH bifurcation, the oscillator adopts a stable state that is distinct from any phase of the oscillator. Hence, if the *C. elegans* oscillator entered an arrested state through a SNIC bifurcation, the overall expression profile of the oscillating genes in the adult stage should resemble that seen at some other time point during larval development.

To test this prediction, we analyzed the correlation of oscillating gene expression for adult time points (TP \geq 37 h) to all other time points of the fused time course (TC3). (In the following, we will use “TPx” to refer to any time point ‘x’, in hours, after hatching. Technically, this is defined in our experiment as the time after plating synchronized, first larval stage animals on food.) For this analysis (illustrated in **Fig. S5**), we used the pairwise correlation matrix resulting from the oscillating gene set without the previously excluded genes that changed in expression in the L4 stage (**Fig 5B**). This provided two insights. First, correlation coefficients among adult time points all exceeded 0.8 with little change over time, confirming the high similarity of samples TP37 – 48 to one another and thus an absence of detectable oscillations. Second, in addition to one another, TP37 – 48 are particularly highly correlated to a specific time – and thus phase – of the oscillatory regime, namely TP13 and the ‘repetitive’ TP19 and TP26/27 (**Fig. 5C**, arrows). In other words, expression levels of oscillating genes in the adult resembled a specific larval oscillator phase, providing further support for a SNIC bifurcation.

Phase-specific arrest of the oscillator after hatching

We noticed that the gene expression states of TP37 – 48 also correlated well to each of TP1 – 5; i.e., the early L1 larval stage (**Fig. 5B**). To examine this further, we performed the same correlation analysis as

described above, but now for TP1 – 5. Mirroring the adult situation, correlation coefficients among all these five time points were high and exhibited little change over time, and TP1 – 5 exhibited particularly high levels of correlation to TP13 and the ‘repetitive’ TP19 and TP27 (**Fig. 5D**). These are the same larval time points to which the adult time points exhibit maximum similarity. We confirmed these two key observations when fusing the independent time course TC4 to TC2 (generating TC5; **Fig. S6**).

We conclude that also during the first five hours after plating, oscillating genes adopt a stable expression profile that resembles a specific phase of the oscillator. In other words, both the transition into the oscillatory state during L1 and out of it during L4 occur through a SNIC bifurcation. This finding indeed explains our observation (**Fig. 2**) that in L1 stage larvae, oscillations exhibit a structure of phase-locked gene expressing patterns as soon as they become detectable: the oscillator initiates from an arrested phase.

Initiation of oscillation soon after gastrulation

We wondered how the oscillator entered the arrested state observed in early larvae, i.e., what dynamics the class of larval oscillating genes exhibited in embryos. Hence, we examined single embryo gene expression data from a published time series (Hashimshony et al., 2015). When plotting the embryonic expression patterns of oscillating genes sorted by their peak phase defined in larvae, we observed a dynamic expression pattern with a striking phase signature (**Fig. 6A**). To investigate this further, we performed a correlation analysis between embryonic and larval time points (TC3) for the oscillating genes (**Fig. S7A**). When we plotted the correlation coefficients for each embryonic time point over larval time we observed two distinct behaviors (**Fig. 6B, C**), which separated at ~380 min (95%-CI: 317.6 minutes – 444.2 minutes) (**Fig. 6D; Fig. S7B**): First, from the start of embryogenesis until ~380 min, the peak of correlation occurred always for the same larval time point, but the extent of correlation increased rapidly (**Fig. 6B, D**). Second, past ~380 min of embryonic development, the peaks of correlation moved

progressively from TP14 (which we define as $0^\circ/360^\circ$ because it demarcates the end of the first and the beginning of the second oscillation cycle in the fused time course, **Fig. 1C**); towards TP19 (accordingly defined as 300°), but the extent of correlation increased only modestly (**Fig 6C, D**).

We conclude that the system adopts two distinct states during embryogenesis (**Fig. 6E**): Initially, it approaches the oscillatory regime through increasing similarity to the oscillator phase TP14/ 0° . After completion of gastrulation and around the beginning of morphogenesis/organogenesis (Hall et al., 2017), it transitions into the oscillatory state and reaches, at hatching, a phase corresponding to larval \sim TP19/ 300° , where oscillations arrest until resumption later in L1.

A shared oscillator phase for experimentally induced and naturally occurring bifurcations

The arrested states of the oscillator in both early L1 stage larvae and in adults are highly similar and resemble the oscillator state at TP19/ 300° . Therefore, we wondered whether this oscillator phase was particularly conducive to state transitions of the system in response to changes in the developmental trajectory. To test this, we examined animals that exited from dauer arrest, a diapause stage that animals enter during larval development under conditions of environmental stress such as heat, crowding, or food shortage. Using a published time course of animals released from dauer arrest after starvation (Hendriks et al., 2014), we found that their expression patterns of oscillating genes correlated highly with those of animals initiating oscillations (TC3) in the L1 stage (**Fig. 7A, B**). Additionally, gene expression patterns at 1 hour through 5 hours and at 13 hours post-dauer were highly correlated to those of the repetitive TP13, TP19 and TP26/27 during continuous development. Hence, the system state during a period of quiescence during the first five hours after placing animals on food corresponds to an arrest of the oscillation in a phase seen at TP19/ 300° of the continuous development time course.

We conclude that the system bifurcates in the same manner during continuous, unperturbed development, after hatching, and in response to a perturbation, namely starvation-induced dauer arrest.

Discussion

In this study, we have characterized biological function and behavior of the *C. elegans* larval oscillator. Our results from single animal- and population-based analyses reveal a close coupling to development, and specifically molting, and imply that processes essential for molting may not be restricted to lethargus. We have observed that oscillations are highly similar during the four cycles (**Fig. 7C, Fig. S8**). Yet, oscillations cease and (re-) initiate several times during physiological development, and similar state transitions, or bifurcations, of the system can be induced through an external perturbation (**Fig. 7C**). In particular, all non-oscillatory states correspond to an arrest of the oscillator in one specific phase. Hence, the observed bifurcations provide a conceptual model of how a developmental checkpoint can operate to halt larval development at a particular, repetitive point of development. Moreover, they constrain possible system architectures and properties as well as the choice and parametrization of mathematical models that can represent the system.

Oscillatory expression of thousands of genes

Our previous work (Hendriks et al., 2014) identified ~2,700 oscillating (i.e., rhythmically expressing) genes, a number that we now increase to 3,739 genes (24% of total expressed genes). We attribute this improved identification of oscillating genes to the fact that our present analysis focused on the L1, L2 and L3 stages, where a constant oscillation period of ~7 hours facilitates cosine wave fitting. This contrasts with the situation in the previous experiment, which used data from the L3 and L4 stages and thus, as we reveal here, a time of changing period.

Even our current estimate is conservative, i.e., the ‘non-oscillating’ genes contain genes that exhibit oscillatory expression with low amplitude or, potentially, strongly non-sinusoidal shapes. It is possible that such dynamics may play important roles for specific genes and processes and our data

provide a resource to identify these in the future. However, here we focused on genes with robust and extensive oscillations to facilitate functional dissection of the oscillator.

A developmental oscillator with functions in and beyond molting and lethargus

The physiological function of the *C. elegans* oscillator has remained unclear. Here, we have tested a possible connection with molting. By quantifying the periods of both molting and gene expression oscillations simultaneously, in the same individual animals, we revealed their high degree of similarity and showed that the two processes are more closely phase-locked than expected from mere coincidence, i.e., they are coupled. We propose that a function of the oscillator as a developmental clock provides a parsimonious explanation for the coupling, but other models remain possible, e.g., the oscillator may facilitate an efficient molting process by anticipating the time of peak demand for cuticular building blocks and other factors.

Conventionally, molting is subdivided into three distinct steps, namely apolysis (severing of connections between the cuticle and the underlying epidermis), new cuticle synthesis, and ecdysis (cuticle shedding) (Lažetić and Fay, 2017). The first two occur during, and the latter terminates, lethargus, a period of behavioral quiescence. However, we find that the temporal structure imposed by the *C. elegans* oscillator extends beyond lethargus. Our data reveal two probable causes: occurrence of processes required for molting before lethargus and a temporal organization that extends to processes unrelated to molting.

Specifically, we observed initiation of oscillations in embryos, which execute cuticle synthesis but neither apolysis nor ecdysis, at ~380 min into embryo development and thus long before the first signs of cuticle synthesis at ~600 min (Sulston et al., 1983). Instead, this time coincides with formation of an apical extracellular matrix (ECM). Although termed embryonic sheath, we find genes encoding components of this ECM, namely *sym-1*; *fbn-1*; *noah-1*; *noah-2* (Vuong-Brender et al., 2017), also

detectably expressed in larvae, and all four are required for larval molting or proper cuticle formation (Frand et al., 2005; Niwa et al., 2009). Moreover, their mRNA levels oscillate with high amplitudes, and as predicted from the embryonic data, their expression peaks long before lethargus, and in fact shortly after ecdysis, i.e., after a molt has been completed. Hence, to account for all these facts, we propose that molting involve processes that are executed long before the onset of lethargus and that include ECM remodeling.

However, even a substantially more complex molting process may fail to account for the fact that a majority of oscillating genes is phase-locked with the molt but exhibits peak expression outside the molt and lacks any obvious link to molting. We consider it plausible that robust larval development may benefit from a coordination of molting with other physiological or developmental processes, as previously postulated for skin cell proliferation (Ruaud and Bessereau, 2006). Similarly, as lethargus involves cessation of food-uptake, oscillatory gene expression may serve to anticipate this event, consistent with a large number of intestinally expressed oscillating genes. Nonetheless, even for this class, a broad dispersion of peak expression phases may suggest additional functions, yet to be uncovered. Whatever the benefit, it is evident that the oscillator imposes a temporal structure of gene expression that extends far beyond lethargus.

Oscillatory state transitions and developmental checkpoints

We have observed a loss of oscillations under three distinct conditions, in early L1 stage larvae, dauer arrested animals, and adults. The similarity of the oscillator states under all three conditions is striking and involves an arrest in the same specific phase.

Formally, for the L1 arrest, we cannot distinguish between perturbation-induced or naturally occurring arrest, as the sequencing experiments required animal synchronization by hatching animals in the absence of food, causing a transient arrest of development. However, the fact that the L1 stage is

extended also in animals hatched into food suggests that they may adopt a similar arrested state even in the presence of food, perhaps because the nutritional resources in the egg (i.e., egg yolk) have become depleted by the time that hatching occurs. In other words, synchronization of L1 animals by hatching them in the absence of food may propagate a pre-existing transient developmental and oscillator arrest.

Irrespective of this interpretation, a key feature of the arrests that we observe under different conditions is that they always occur in the same phase. This is a behavior one would predict for a repetitive developmental checkpoint. Such a checkpoint has indeed been found to operate shortly after each larval molt exit, arresting development in response to a lack of food (Schindler et al., 2014). Importantly, developmental arrest does not result from an acute shortage of resources. Rather, it is a genetically encoded, presumably adaptive, response to nutritionally poor conditions, as demonstrated by the fact that mutations in the *daf-2*/IGFR signaling pathway causes animals to continue development under the same food-depleted conditions (Baugh, 2013; Schindler et al., 2014).

Within the limits of our resolution, the phase of the arrested oscillator corresponds to the phase seen around ecdysis. Hence, oscillations and development are synchronously arrested, and we propose that signals related to food sensing, metabolism, or nutritional state of the animal help to control the state of the oscillatory system and thereby developmental progression. An oscillator operating near a SNIC bifurcation appears ideally suited to processing such information, because it acts as a signal integrator, i.e., it becomes active when a signal threshold is surpassed (Forger, 2017; Izhikevich, 2000). This contrasts with the behavior of oscillators operating near a supH bifurcation, which function as resonators, i.e., they respond most strongly to an incoming signal of a preferred frequency. Hence, both the phase-specific arrest and the integrator function as characteristics of an oscillator operating in the vicinity of a SNIC bifurcation are physiologically relevant features of this *C. elegans* oscillator.

Insights into oscillator architecture and constraints for mathematical modelling

What mechanisms determine the type and behavior of the *C. elegans* oscillator? Although the nature and wiring of the ‘core oscillator’, i.e., the machinery that drives the pervasive gene expression oscillation, remains to be established, the behavior of the oscillator that we characterized here provides clear constraints. Thus, a change in period without a noticeable change in amplitude, as seen in L4 stage larvae, is a feature of rigid oscillators (Abraham et al., 2010) that is considered incompatible with the function of a simple negative feedback loop but compatible with the operation of interlinked positive and negative feedback loops (Mönke et al., 2017; Tsai et al., 2008). This conclusion is supported by evidence from synthetic biology, where most synthetic genetic oscillators appear to operate near a supH bifurcation (Purcell et al., 2010). An exception are so-called amplified negative feedback oscillators, which operate near a SNIC bifurcation and rely on interlinked negative and positive feedback loops.

Beyond constraining possible oscillator architectures, our experimental observations will help to guide mathematical modelling of the *C. elegans* oscillator. Modelling is needed because the nonlinear dynamic behaviors of oscillators are difficult to grasp intuitively. However, it is usually difficult to ensure the relevance of a given model, because both its formulation and its parametrization determine whether oscillations occur and which behaviors the resulting oscillator model displays. Amplified negative feedback oscillators are a case in point as they can also operate near a supH bifurcation; operation near a SNIC bifurcation occurs only in a certain parameter space (Conrad et al., 2008; Guantes and Poyatos, 2006). The experimental characterization of the system’s bifurcation that we have achieved here will therefore provide crucial constraints to exclude invalid mathematical models.

We do note that mathematical models of somitogenesis clocks, inspired by mechanistic knowledge about the identity of individual oscillator components and their wiring, tend to represent oscillators operating near a supH bifurcation (Jensen et al., 2010; Webb et al., 2016). This appears consistent with observations on isolated cells *in vitro* (Webb et al., 2016). At the same time it contrasts with changes in both amplitude and period that were shown to occur in zebrafish embryos during somite

formation and prior to cessation of oscillation (Shih et al., 2015). Thus, and because an analysis of bifurcation behavior of somitogenesis clocks *in vivo* is challenging due to a complex space-dependence of oscillation features (Soroldoni et al., 2014), it remains to be answered whether and to what extent the *C. elegans* oscillator and the somitogenesis clocks share specific properties. However, whatever the answer, a comparison of the similarities and differences in behaviors, architectures and topologies will help to reveal whether and to what extent diverse developmental oscillators follow common design principles.

References:

- Abraham, U., Granada, A.E., Westermarck, P.O., Heine, M., Kramer, A., Herzog, H., 2010. Coupling governs entrainment range of circadian clocks. *Mol Syst Biol* 6, 438. <https://doi.org/10.1038/msb.2010.92>
- Au, K.F., Jiang, H., Lin, L., Xing, Y., Wong, W.H., 2010. Detection of splice junctions from paired-end RNA-seq data by SpliceMap. *Nucleic Acids Res* 38, 4570–4578. <https://doi.org/10.1093/nar/gkq211>
- Bates, D., Maechler, M., 2018. *Matrix: Sparse and Dense Matrix Classes and Methods*.
- Baugh, L.R., 2013. To grow or not to grow: nutritional control of development during *Caenorhabditis elegans* L1 arrest. *Genetics* 194, 539–555. <https://doi.org/10.1534/genetics.113.150847>
- Cao, J., Packer, J.S., Ramani, V., Cusanovich, D.A., Huynh, C., Daza, R., Qiu, X., Lee, C., Furlan, S.N., Steemers, F.J., Adey, A., Waterston, R.H., Trapnell, C., Shendure, J., 2017. Comprehensive single-cell transcriptional profiling of a multicellular organism. *Science* 357, 661–667. <https://doi.org/10.1126/science.aam8940>
- Conrad, E., Mayo, A.E., Ninfa, A.J., Forger, D.B., 2008. Rate constants rather than biochemical mechanism determine behaviour of genetic clocks. *J R Soc Interface* 5, S9–S15. <https://doi.org/10.1098/rsif.2008.0046.focus>
- Edgar, R., Domrachev, M., Lash, A.E., 2002. Gene Expression Omnibus: NCBI gene expression and hybridization array data repository. *Nucleic Acids Res* 30, 207–210. <https://doi.org/10.1093/nar/30.1.207>
- Forger, D.B., 2017. *Biological Clocks, Rhythms, and Oscillations: The Theory of Biological Timekeeping*. The MIT Press, Cambridge, Massachusetts.
- Frand, A.R., Russel, S., Ruvkun, G., 2005. Functional Genomic Analysis of *C. elegans* Molting. *PLOS Biology* 3, e312. <https://doi.org/10.1371/journal.pbio.0030312>
- Frøkjær-Jensen, C., Davis, M.W., Ailion, M., Jørgensen, E.M., 2012. Improved Mos1-mediated transgenesis in *C. elegans*. *Nat. Methods* 9, 117–118. <https://doi.org/10.1038/nmeth.1865>
- Frøkjær-Jensen, C., Davis, M.W., Hopkins, C.E., Newman, B.J., Thummel, J.M., Olesen, S.-P., Grunnet, M., Jørgensen, E.M., 2008. Single-copy insertion of transgenes in *Caenorhabditis elegans*. *Nat. Genet.* 40, 1375–1383. <https://doi.org/10.1038/ng.248>
- Gaidatzis, D., Lerch, A., Hahne, F., Stadler, M.B., 2015. QuasR: quantification and annotation of short reads in R. *Bioinformatics* 31, 1130–1132. <https://doi.org/10.1093/bioinformatics/btu781>
- Gaujoux, R., Seoighe, C., 2010. A flexible R package for nonnegative matrix factorization. *BMC Bioinformatics* 11, 367. <https://doi.org/10.1186/1471-2105-11-367>
- Gibson, D.G., Young, L., Chuang, R.-Y., Venter, J.C., Hutchison, C.A., Smith, H.O., 2009. Enzymatic assembly of DNA molecules up to several hundred kilobases. *Nat. Methods* 6, 343–345. <https://doi.org/10.1038/nmeth.1318>
- Gritti, N., Kienle, S., Filina, O., van Zon, J.S., 2016. Long-term time-lapse microscopy of *C. elegans* post-embryonic development. *Nature Communications* 7, 12500. <https://doi.org/10.1038/ncomms12500>

- Grün, D., Kirchner, M., Thierfelder, N., Stoeckius, M., Selbach, M., Rajewsky, N., 2014. Conservation of mRNA and protein expression during development of *C. elegans*. *Cell Rep* 6, 565–577. <https://doi.org/10.1016/j.celrep.2014.01.001>
- Guantes, R., Poyatos, J.F., 2006. Dynamical principles of two-component genetic oscillators. *PLoS Comput. Biol.* 2, e30. <https://doi.org/10.1371/journal.pcbi.0020030>
- Hall, D.H., Herndon, L.A., Altun, Z., 2017. Introduction to *C. elegans* Embryo Anatomy. In *WormAtlas*.
- Hashimshony, T., Feder, M., Levin, M., Hall, B.K., Yanai, I., 2015. Spatiotemporal transcriptomics reveals the evolutionary history of the endoderm germ layer. *Nature* 519, 219–222. <https://doi.org/10.1038/nature13996>
- Hendriks, G.-J., Gaidatzis, D., Aeschmann, F., Großhans, H., 2014. Extensive oscillatory gene expression during *C. elegans* larval development. *Mol. Cell* 53, 380–392. <https://doi.org/10.1016/j.molcel.2013.12.013>
- Izhikevich, E.M., 2000. Neural excitability, spiking and bursting. *Int. J. Bifurcation Chaos* 10, 1171–1266. <https://doi.org/10.1142/S0218127400000840>
- Jensen, P.B., Pedersen, L., Krishna, S., Jensen, M.H., 2010. A Wnt Oscillator Model for Somitogenesis. *Biophys J* 98, 943–950. <https://doi.org/10.1016/j.bpj.2009.11.039>
- Jones, E., Oliphant, T., Peterson, P., 2001. *SciPy: Open Source Scientific Tools for Python*.
- Kim, D., Oh, H.-S., 2018. EMD: Empirical Mode Decomposition and Hilbert Spectral Analysis.
- Kim, D. hyun, Grün, D., van Oudenaarden, A., 2013. Dampening of expression oscillations by synchronous regulation of a microRNA and its target. *Nat. Genet.* 45, 1337–1344. <https://doi.org/10.1038/ng.2763>
- Koike, N., Yoo, S.-H., Huang, H.-C., Kumar, V., Lee, C., Kim, T.-K., Takahashi, J.S., 2012. Transcriptional Architecture and Chromatin Landscape of the Core Circadian Clock in Mammals. *Science* 338, 349–354. <https://doi.org/10.1126/science.1226339>
- Korenčič, A., Košir, R., Bordyugov, G., Lehmann, R., Rozman, D., Herzog, H., 2014. Timing of circadian genes in mammalian tissues. *Sci Rep* 4, 1–9. <https://doi.org/10.1038/srep05782>
- Lagido, C., Pettitt, J., Flett, A., Glover, L.A., 2008. Bridging the phenotypic gap: Real-time assessment of mitochondrial function and metabolism of the nematode *Caenorhabditis elegans*. *BMC Physiology* 8, 7. <https://doi.org/10.1186/1472-6793-8-7>
- Lažetić, V., Fay, D.S., 2017. Molting in *C. elegans*. *Worm* 6, e1330246. <https://doi.org/10.1080/21624054.2017.1330246>
- Lebigot, E.O., n.d. *Uncertainties: a Python package for calculations with uncertainties*.
- McKinney, W., 2010. Data Structures for Statistical Computing in Python, in: *Proceedings of the 9th Python in Science Conference*. pp. 51–56.

- Mönke, G., Cristiano, E., Finzel, A., Friedrich, D., Herzel, H., Falcke, M., Loewer, A., 2017. Excitability in the p53 network mediates robust signaling with tunable activation thresholds in single cells. *Scientific Reports* 7, 46571. <https://doi.org/10.1038/srep46571>
- Moreno-Risueno, M.A., Van Norman, J.M., Moreno, A., Zhang, J., Ahnert, S.E., Benfey, P.N., 2010. Oscillating gene expression determines competence for periodic Arabidopsis root branching. *Science* 329, 1306–1311. <https://doi.org/10.1126/science.1191937>
- Niwa, R., Hada, K., Moliyama, K., Ohniwa, R.L., Tan, Y.-M., Olsson-Carter, K., Chi, W., Reinke, V., Slack, F.J., 2009. *C. elegans* sym-1 is a downstream target of the hunchback-like-1 developmental timing transcription factor. *Cell Cycle* 8, 4147–4154. <https://doi.org/10.4161/cc.8.24.10292>
- Oates, A.C., Morelli, L.G., Ares, S., 2012. Patterning embryos with oscillations: structure, function and dynamics of the vertebrate segmentation clock. *Development* 139, 625–639. <https://doi.org/10.1242/dev.063735>
- Olmedo, M., Geibel, M., Artal-Sanz, M., Merrow, M., 2015. A High-Throughput Method for the Analysis of Larval Developmental Phenotypes in *Caenorhabditis elegans*. *Genetics* 201, 443–448. <https://doi.org/10.1534/genetics.115.179242>
- Panda, S., Hogenesch, J.B., Kay, S.A., 2002. Circadian rhythms from flies to human. *Nature* 417, 329–335. <https://doi.org/10.1038/417329a>
- PANTHER Classification System, n.d.
- Pikovsky, A., Rosenblum, M., Kurths, J., 2001. *Synchronization: A universal concept in nonlinear sciences*. Cambridge University Press, Cambridge. <https://doi.org/10.1017/CBO9780511755743>
- Purcell, O., Savery, N.J., Grierson, C.S., di Bernardo, M., 2010. A comparative analysis of synthetic genetic oscillators. *J R Soc Interface* 7, 1503–1524. <https://doi.org/10.1098/rsif.2010.0183>
- R Core Team, n.d. *R: A language and environment for statistical computing*.
- Rensing, L., Meyer-Grahe, U., Ruoff, P., 2001. Biological timing and the clock metaphor: oscillatory and hourglass mechanisms. *Chronobiol. Int.* 18, 329–369.
- Riedel-Kruse, I.H., Müller, C., Oates, A.C., 2007. Synchrony dynamics during initiation, failure, and rescue of the segmentation clock. *Science* 317, 1911–1915. <https://doi.org/10.1126/science.1142538>
- Ruaud, A.-F., Bessereau, J.-L., 2006. Activation of nicotinic receptors uncouples a developmental timer from the molting timer in *C. elegans*. *Development* 133, 2211–2222. <https://doi.org/10.1242/dev.02392>
- Saggio, M.L., Spiegler, A., Bernard, C., Jirsa, V.K., 2017. Fast–Slow Bursters in the Unfolding of a High Codimension Singularity and the Ultra-slow Transitions of Classes. *J Math Neurosci* 7. <https://doi.org/10.1186/s13408-017-0050-8>
- Salvi, J.D., Ó Maoiléidigh, D., Hudspeth, A.J., 2016. Identification of Bifurcations from Observations of Noisy Biological Oscillators. *Biophys. J.* 111, 798–812. <https://doi.org/10.1016/j.bpj.2016.07.027>

- Schindler, A.J., Baugh, L.R., Sherwood, D.R., 2014. Identification of late larval stage developmental checkpoints in *Caenorhabditis elegans* regulated by insulin/IGF and steroid hormone signaling pathways. *PLoS Genet.* 10, e1004426. <https://doi.org/10.1371/journal.pgen.1004426>
- Shih, N.P., François, P., Delaune, E.A., Amacher, S.L., 2015. Dynamics of the slowing segmentation clock reveal alternating two-segment periodicity. *Development* 142, 1785–1793. <https://doi.org/10.1242/dev.119057>
- Soetaert, K., 2017. plot3D: Plotting Multi-Dimensional Data.
- Soroldoni, D., Jörg, D.J., Morelli, L.G., Richmond, D.L., Schindelin, J., Jülicher, F., Oates, A.C., 2014. Genetic oscillations. A Doppler effect in embryonic pattern formation. *Science* 345, 222–225. <https://doi.org/10.1126/science.1253089>
- Spiess, A.-N., 2018. propagate: Propagation of Uncertainty.
- Stiernagle, Theresa, n.d. Maintenance of *C. elegans* (February 11, 2006), *WormBook*, ed. The *C. elegans* Research Community, *WormBook*, doi/10.1895/wormbook.1.101.1, <http://www.wormbook.org>.
- Strogatz, S.H., 2015. *Nonlinear Dynamics and Chaos with Student Solutions Manual: Nonlinear Dynamics and Chaos: With applications To Physics, Biology, Chemistry, And Engineering (Studies in Nonlinearity)*, 2nd ed. Westview Press, Boulder, CO.
- Sueur, J., Aubin, T., Simonis, C., 2008. Seewave, a Free Modular Tool for Sound Analysis and Synthesis. *Bioacoustics* 18, 213–226. <https://doi.org/10.1080/09524622.2008.9753600>
- Sulston, J.E., Schierenberg, E., White, J.G., Thomson, J.N., 1983. The embryonic cell lineage of the nematode *Caenorhabditis elegans*. *Dev. Biol.* 100, 64–119.
- Tsai, T.Y.-C., Choi, Y.S., Ma, W., Pomerening, J.R., Tang, C., Ferrell, J.E., 2008. Robust, Tunable Biological Oscillations from Interlinked Positive and Negative Feedback Loops. *Science* 321, 126–129. <https://doi.org/10.1126/science.1156951>
- Turek, M., Besseling, J., Bringmann, H., 2015. Agarose Microchambers for Long-term Calcium Imaging of *Caenorhabditis elegans*. *J Vis Exp* e52742. <https://doi.org/10.3791/52742>
- Uriu, K., 2016. Genetic oscillators in development. *Development, Growth & Differentiation* 58, 16–30. <https://doi.org/10.1111/dgd.12262>
- Vuong-Brender, T.T.K., Ben Amar, M., Pontabry, J., Labouesse, M., 2017. The interplay of stiffness and force anisotropies drives embryo elongation. *eLife* 6, e23866. <https://doi.org/10.7554/eLife.23866>
- Webb, A.B., Lengyel, I.M., Jörg, D.J., Valentin, G., Jülicher, F., Morelli, L.G., Oates, A.C., 2016. Persistence, period and precision of autonomous cellular oscillators from the zebrafish segmentation clock. *eLife* 5, e08438. <https://doi.org/10.7554/eLife.08438>
- Zhang, R., Lahens, N.F., Ballance, H.I., Hughes, M.E., Hogenesch, J.B., 2014. A circadian gene expression atlas in mammals: implications for biology and medicine. *Proc. Natl. Acad. Sci. U.S.A.* 111, 16219–16224. <https://doi.org/10.1073/pnas.1408886111>

Acknowledgements: We thank Stephane Thiry, Kirsten Jacobeit and the FMI Functional Genomics Facility for RNA sequencing, Iskra Katic for help in generating transgenic strains, Maria Olmédo and Henrik Bringmann for introducing us to the luciferase and the single animal imaging assays, respectively, Dimos Gaidatzis and Michael Stadler for advice on computational analyses, Laurent Gelman for help with imaging, and Benjamin Towbin, Lucas Morales Moya, Prisca Liberali and Luca Giorgetti for comments on the manuscript.

Funding: M.W.M.M. is a recipient of a Boehringer Ingelheim Fonds PhD fellowship. This work is part of a project that has received funding from the European Research Council (ERC) under the European Union's Horizon 2020 research and innovation programme (Grant agreement No. 741269, to H.G.). The FMI is core-funded by the Novartis Research Foundation.

Author contributions: Gert-Jan Hendriks and Yannick Hauser performed RNA sequencing time courses. Milou Meeuse and Yannick Hauser analyzed RNA sequencing data. Milou Meeuse performed and analyzed luciferase assays. Guy Bogaarts developed the graphical user interface for the luciferase data. Yannick Hauser acquired and analyzed single worm imaging data. Jan Eglinger wrote the KNIME workflow for the single worm imaging. Charisios Tsiairis conceived parts of the analysis. Helge Großhans, Milou Meeuse and Yannick Hauser conceived the project and wrote the manuscript.

Competing interests: The authors declare no competing interests.

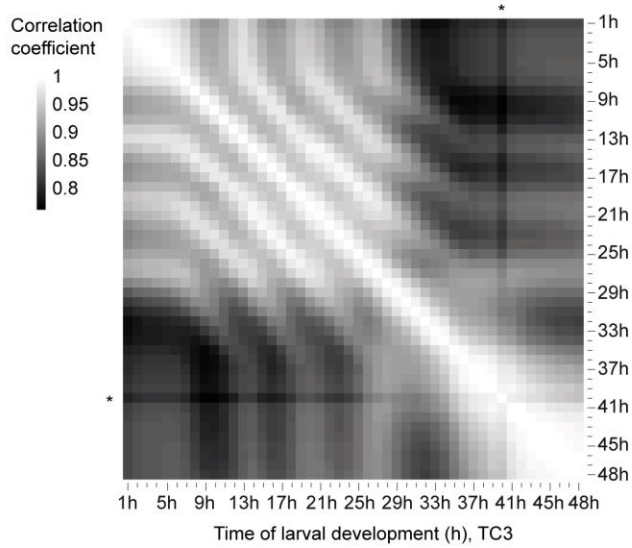
Data and materials availability: All sequencing data generated for this study have been deposited in NCBI's Gene Expression Omnibus (Edgar et al., 2002) and are accessible through GEO SuperSeries accession number GSE133576 <https://www.ncbi.nlm.nih.gov/geo/query/acc.cgi?acc=GSE133576> . A reviewer token for data access is available through the editorial office. The dauer exit time course was published previously (Hendriks et al., 2014) and is accessible through GEO Series accession number GSE52910 (<http://www.ncbi.nlm.nih.gov/geo/query/acc.cgi?acc=GSE52910>).

Published research reagents from the FMI are shared with the academic community under a Material Transfer Agreement (MTA) having terms and conditions corresponding to those of the UBMTA (Uniform Biological Material Transfer Agreement).

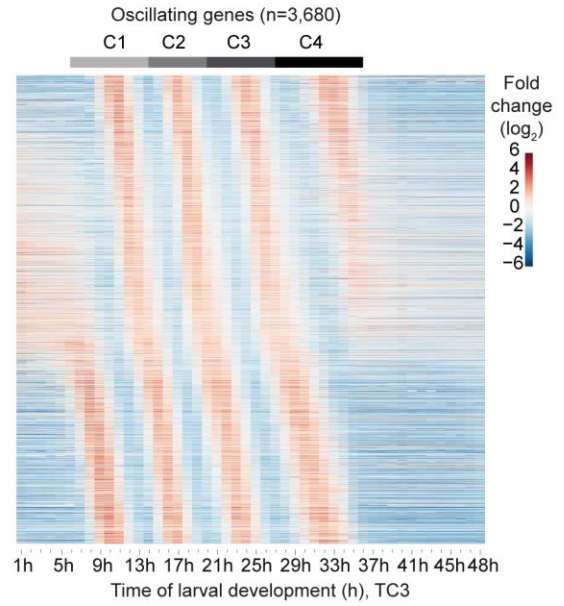
Conflict of Interests: The authors declare that they have no conflict of interest.

Figures

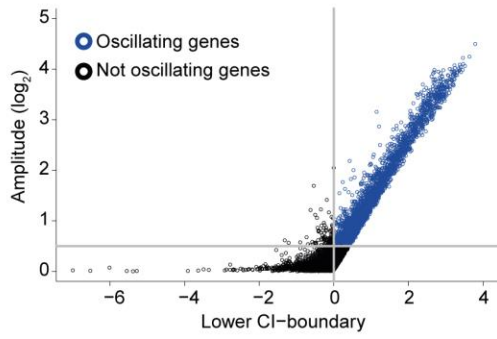
A



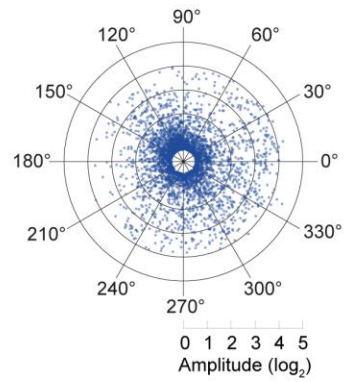
C



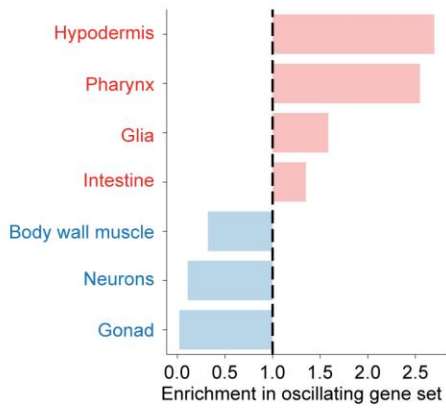
B



D



E



F

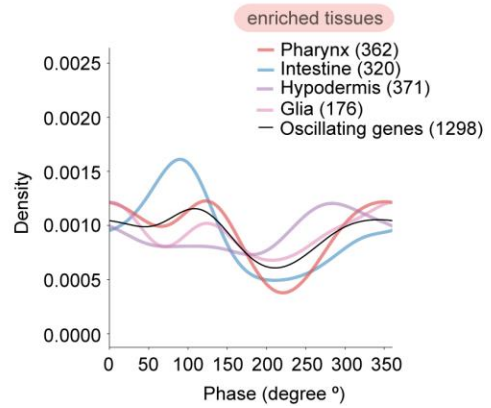


Fig 1: A massive oscillator with dispersed peak phases in several tissues

(A) Pairwise correlation plot of \log_2 -transformed gene expression patterns obtained from synchronized population of L1 stage larvae sampled and sequenced from $t = 1$ h until $t = 48$ h (TC3; a fusion of the two time courses TC1 and TC2 after 13 h; **Fig. S1A,B**). Asterisk indicates an outlier, time point $t = 40$ h.

(B) Scatter plot identifying genes with oscillatory expression (henceforth termed oscillating genes, *blue*) based on amplitude and 99% confidence interval (99%-CI) of a cosine fitting of their expression quantified in TC2 (**Methods**). A lower CI-boundary ≥ 0 , i.e. $p\text{-value} \leq 0.01$, and a $\log_2(\text{amplitude}) \geq 0.5$, which corresponds to a 2-fold change from peak to trough, were used as cut-offs. Genes below either cut-off were included in the 'not oscillating' group (*black*). **Fig. S1C** reveals gene distributions in a density scatter plot.

(C) Gene expression heatmaps of oscillating genes as classified in **Fig. 1B** and **Fig. S1C**. Oscillating genes were sorted by peak phase and mean expression per gene from $t = 7$ h to $t = 36$ h (when oscillations occur) was subtracted. $n=3,680$ as not all genes from the long time course (TC2) were detected in the early time course (TC1). Gray horizontal bars indicate the individual oscillation cycles, C1 through C4 as later determined in **Fig. S8**.

(D) Radar chart plotting amplitude (radial axis, in \log_2) over peak phase (circular axis, in degrees) as determined by cosine fitting in **Fig. 1B**.

(E) Enrichment (*red*) or depletion (*blue*) of tissues detected among oscillating genes expressed tissue-specifically relative to all tissue-specific genes using annotations derived from (Cao et al., 2017). Significance was tested using one-sided binomial tests which resulted in $p\text{-values} < 0.001$ for all tissues.

(F) Density plot of the observed peak phases of tissue-specifically expressed oscillating genes for all enriched tissues.

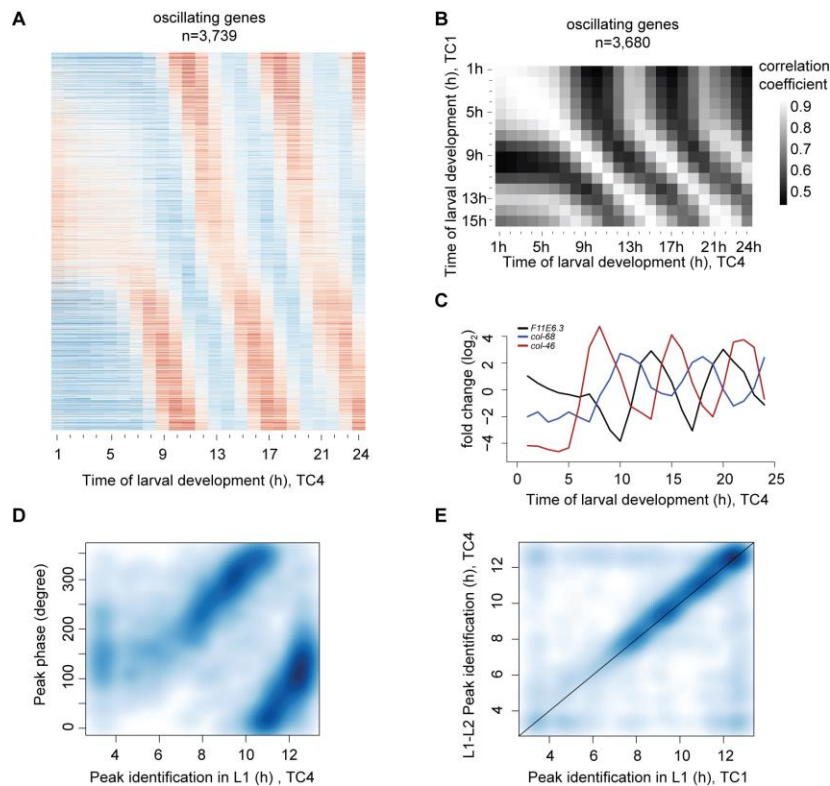


Fig 2: Oscillations start with a time lag in L1

(A) Gene expression heatmap of detectably expressed oscillating genes sampled from a separate early developmental time course (TC4; $t = 1$ h to $t = 24$ h). Genes were ranked according to their peak phase as determined in **Fig. 1**.

(B) Pairwise correlation plot of \log_2 -transformed oscillating gene expression data obtained from both early larval development time courses, TC1 and TC4.

(C) Gene expression traces of representative genes *F11E6.3*, *col-68* and *col-46*.

(D) Scatter plot of calculated oscillating gene peak phase (**Fig. 1**) over the time of occurrence of the first expression peak in L1 larvae, observed in TC4. Peak detection was performed using a spline analysis. As visual inspection did not reveal peaks in the heatmap during the first three hours, and as the first cycle ends at 13 h, we performed this analysis for $t = 3$ h to $t = 13$ h to reduce noise.

(E) Scatterplot comparing experimentally identified first peaks of gene expression (as in D) of the two early time course replicates, TC1 and TC4.

All analyses for oscillating genes identified in **Fig. 1** with detectable expression ($n=3,680$).

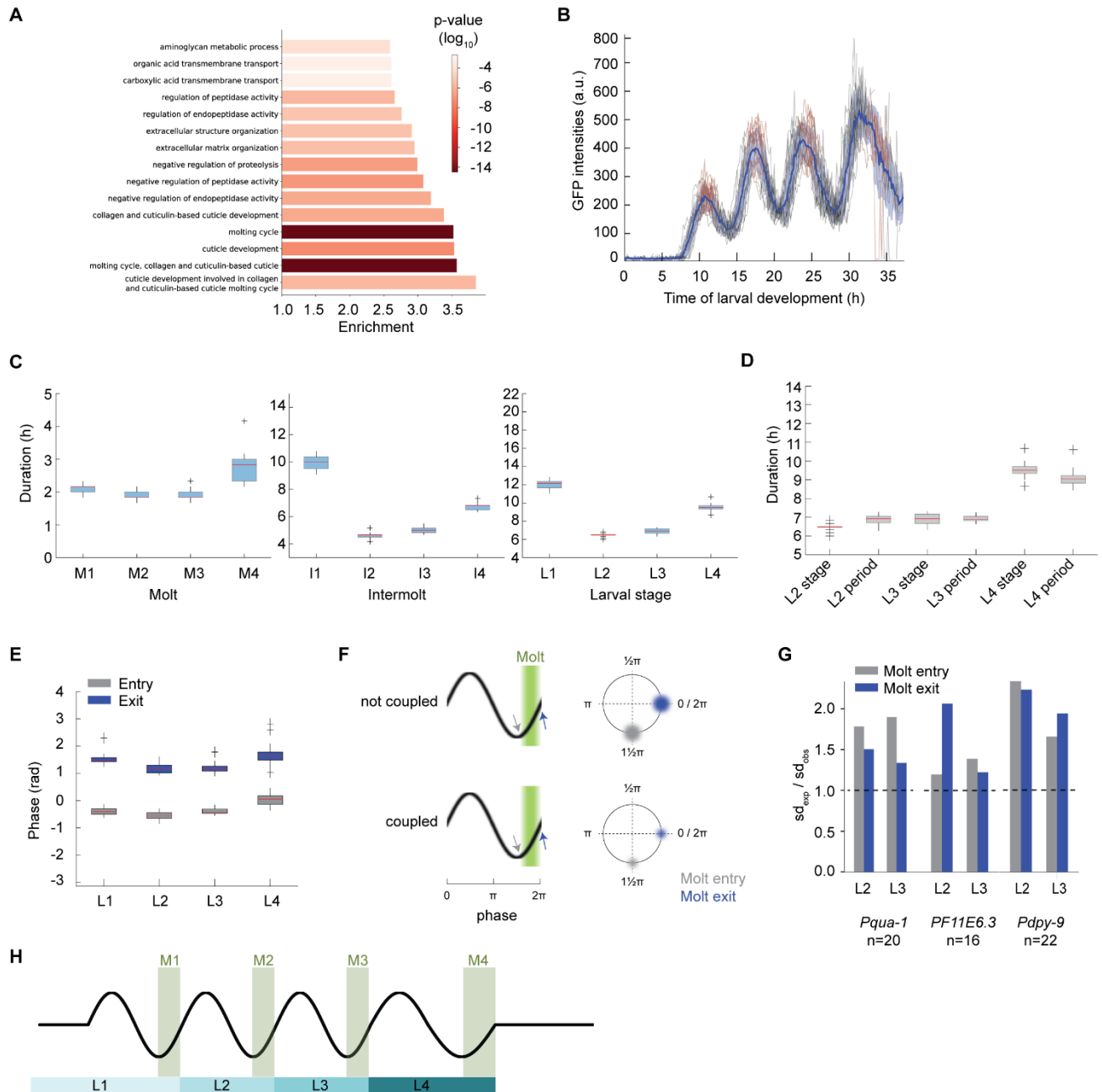


Fig 3: Oscillatory gene expression is coupled to molting

(A) GO-term enrichments for oscillating genes as classified in Fig. 1C. The top 15 enriched terms are displayed.

(B) GFP signal quantification for *Pqua-1::gfp::pest::h2b::unc-54_{3'UTR}* expressing single animals (HW2523, n=20) over larval development, starting from hatch (t = 0 h). Molts (*red*), mean intensity (*blue line*) and standard deviation across population (*shading*) are indicated.

(C), (D) Boxplots of molt, intermolt and larval stage durations (C) and of larval stage durations and period times of oscillations (D) of single animals (HW2523) developing in microchambers (n=20). In (D), L1 was excluded because of the time lag before oscillations manifest after hatching.

(E) Boxplot of phase at molt entry (start of lethargus) and molt exit (end of lethargus) separated by larval stages for single animals (HW2523) developing in microchambers (n=20)

(F) Schematic models of size of expected phase variation (radius of colored blur) at molt entry (*gray*) and molt exit (*blue*) depending on the coupling status between oscillations and molting.

(G) Barplots displaying the ratio of expected standard deviation over observed standard deviation for phase calling at either molt entry or molt exit for the indicated reporters. A dashed line indicates parity.

(H) Schematic depiction of coordination between oscillatory gene expression and development.

Boxplots in (C) – (E) extend from first to third quartile with a line at the median, outliers are indicated with a cross, whiskers show 1.5*IQR.

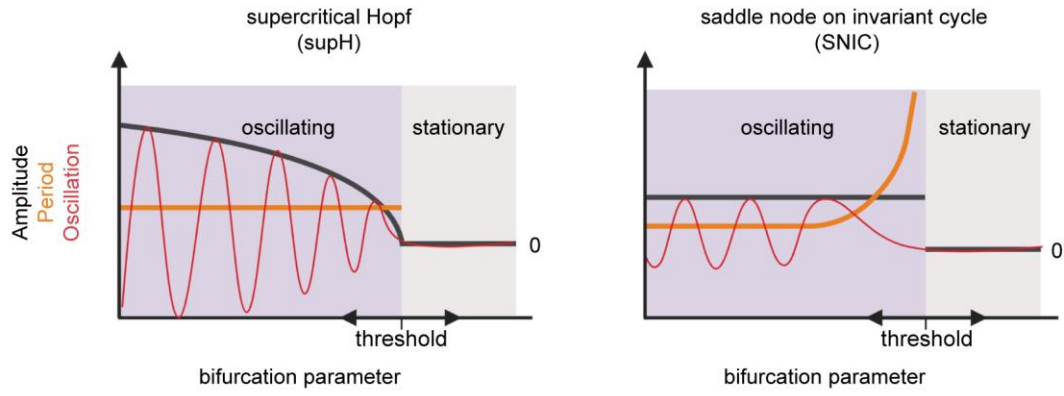
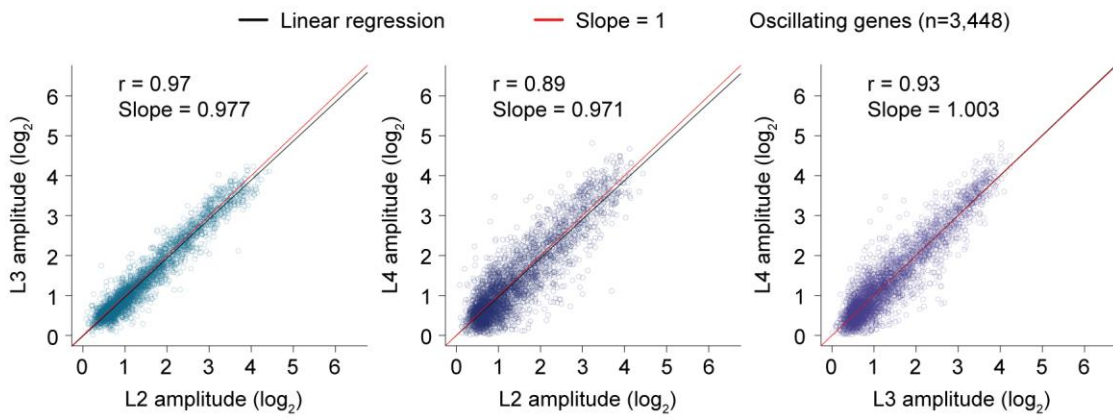
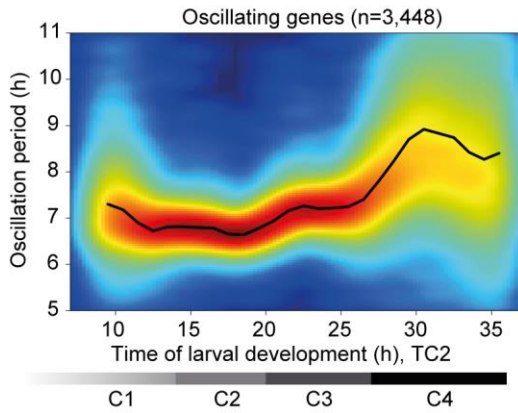
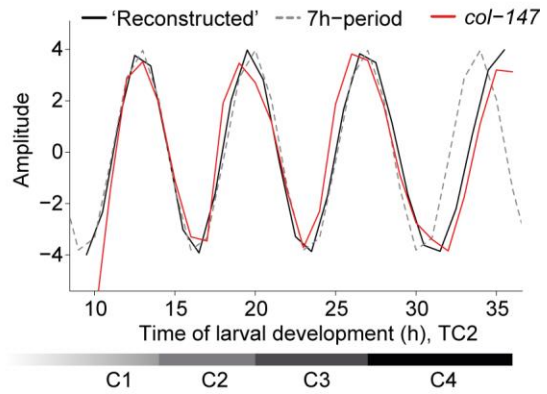
A**B****C****D**

Fig 4: Change in period without noticeable change in amplitude

(A) Schematic depiction of amplitude and period behaviors in response to a control parameter change for an oscillatory system transitioning between a quiescent (stationary) and an oscillatory state through the indicated bifurcations (created with BioRender.com). Note that transitions can occur in either direction.

(B) Amplitudes derived from cosine fitting to the individual oscillations of L2, L3 and L4 stage (TC2) plotted against each other. Pearson correlation coefficient r , slope of the linear regression (*black*) and the diagonals (slope=1; *red*) are indicated. 291 genes were excluded from oscillating genes due to altered mean expression in L4, see **Fig. S4**, i.e., $n=3,448$.

(C) Density plot showing oscillation period at every time point for each of the oscillating genes ($n=3,448$) as quantified by Hilbert transform. Mean oscillation period over all oscillating genes is shown by the black line. Horizontal gray bars indicate oscillation cycles C1 through C4 as in **Fig. 1C**.

(D) Expression changes for an oscillation with a constant 7h period (*dotted line*), and an oscillation reconstructed from the mean oscillation period in (C) (*black line*), both amplitudes set to four. The expression of a representative gene, *col-147* (mean normalized) is shown (*red line*). Horizontal gray bars indicate oscillation cycles C1 through C4 as in **Fig. 1C**.

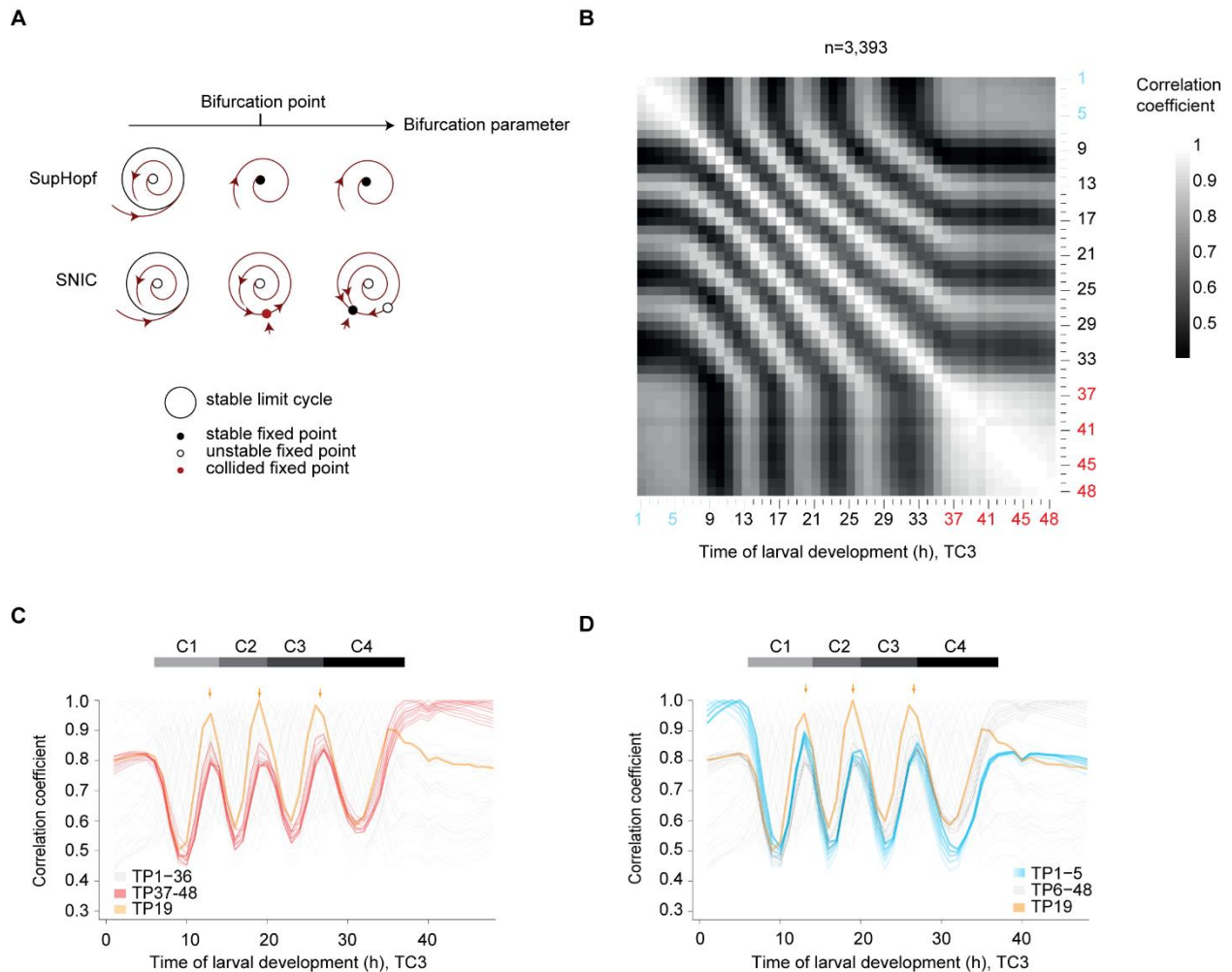


Fig 5: The oscillator is phase arrested in early L1 and adults

(A) Phase plane diagrams depicting supH and SNIC bifurcations, respectively, showing the change in qualitative behavior as the bifurcation parameter value changes (arrow). The bifurcation point, i.e. the parameter value at which the bifurcation occurs, is indicated.

(B) Pairwise correlation plot of \log_2 -transformed oscillating gene expression data obtained from TC3, i.e., the fusion of TC1 (*blue labels*) and TC2 (*black*). Genes which deviated in mean expression in L4 were excluded (**Fig. S4**), resulting in $n=3,393$ genes.

(C) Lines of correlation for TP37–48 (*red*) to all time points in the fused larval time course. Arrows indicate local correlation maxima at TP13, 19 and 26/27. Correlation traces for $TP \leq 36$ h are shown in light gray, except for TP19 (*orange*). **Fig. S5** illustrates how correlation lines were generated.

(D) Lines of correlation for TP1–5 (*blue*) and TP19 (*orange*) to all time points in the fused larval time course. Arrows indicate local correlation maxima at TP13, 19 and 26/27.

All correlations were determined by Pearson correlation. Correlation values were obtained from **Fig. 5B**.

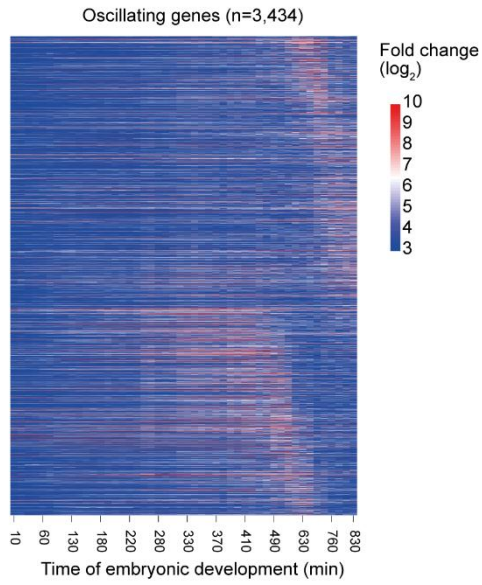
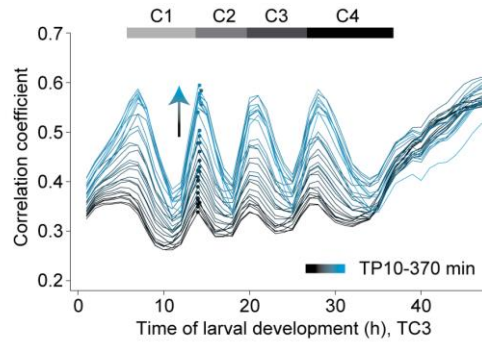
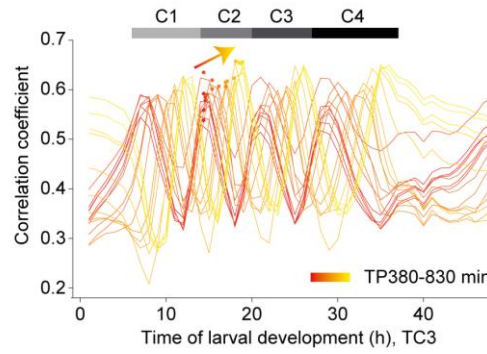
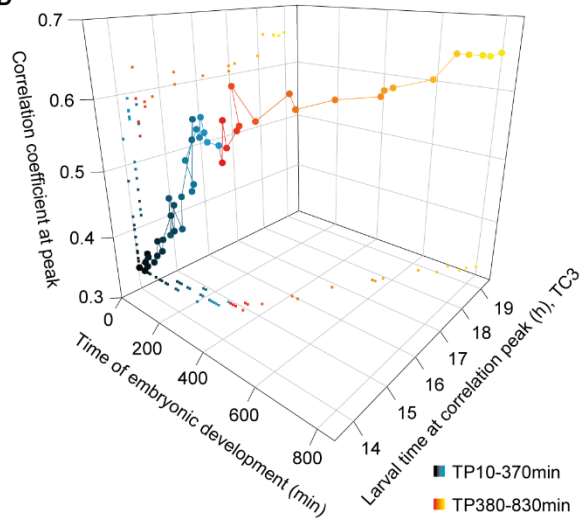
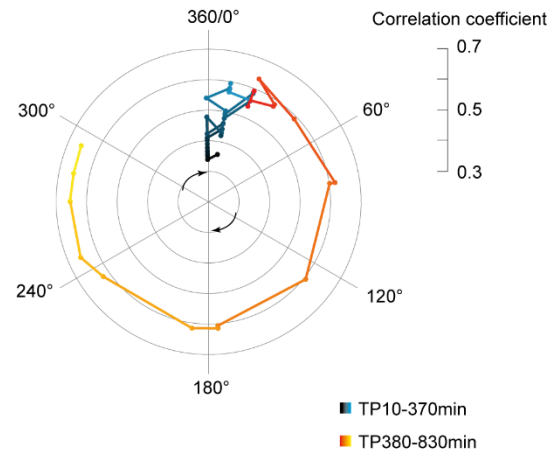
A**B****C****D****E**

Fig 6: Transition to an oscillatory state during embryogenesis

(A) Heatmap of \log_2 -transformed embryonic expression of oscillating genes, excluding L4 deviating genes, sorted by larval peak phase (defined as in **Fig. 1**).

(B, C) Pairwise correlation coefficients between embryonic and larval time points (**Fig. S7**) plotted over larval time for embryonic TP10-370 min (B, *black-blue gradient*) and TP380-830 min (C, *red-yellow gradient*), respectively. Dots represent peaks of the correlation lines after spline analysis in the second oscillation cycle (C2), arrows indicate trends. Horizontal gray bars indicate oscillation cycles C1 through C4 as in **Fig. 1C**.

(D) 3D-scatter plot of the correlation coefficient peak for each embryonic time point to the time of larval development at the second oscillation cycle (C2). Embryonic time is determined by time of sample collection, larval time by spline interpolation. Color scheme as in B and C.

(E) Polar plot of correlation coefficient peak over the time point in the second larval oscillation cycle (C2) at which the correlation peak is detected. TP14 is defined as 0° and correlates most highly to TP20, thus defined as 360° . Values are as in D; color scheme as in B and C.

All correlations were determined by Pearson correlation.

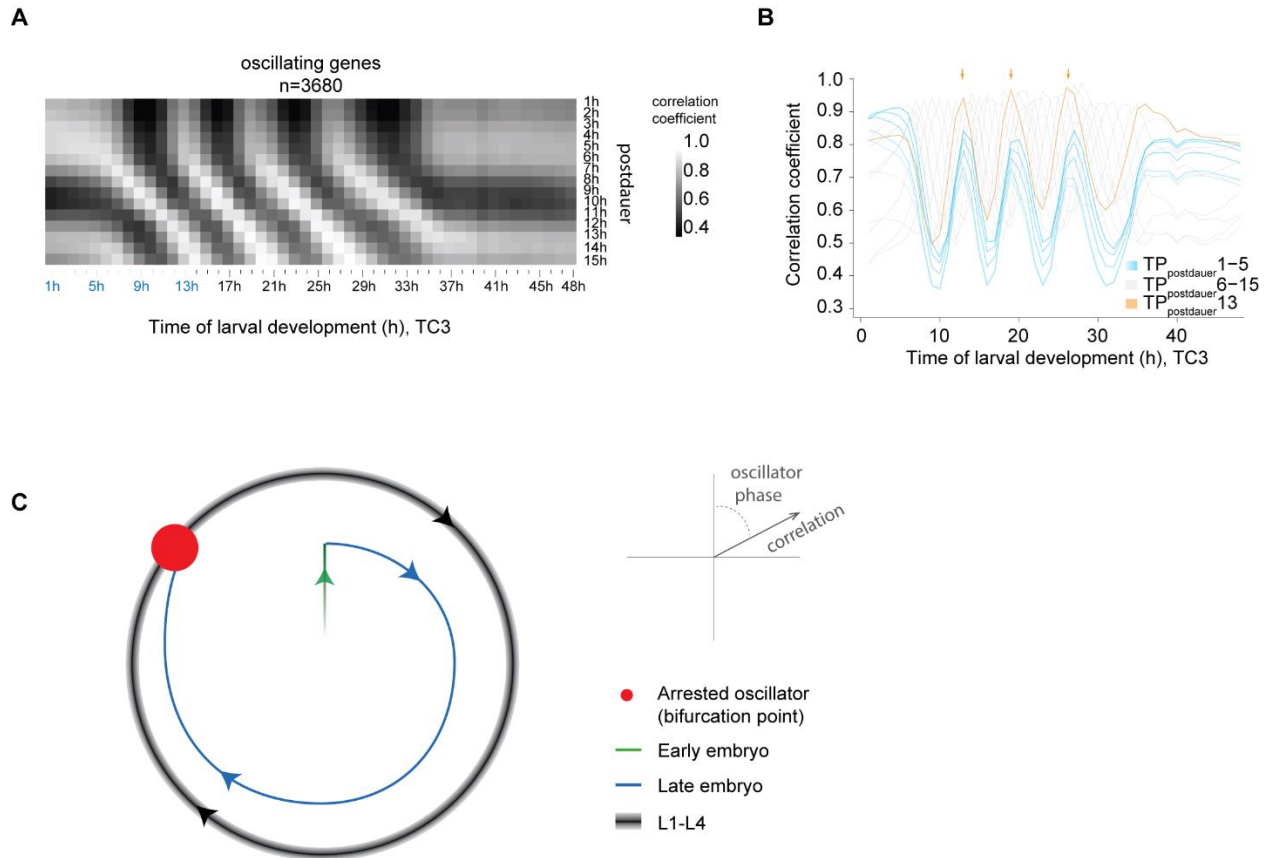


Fig 7: Re-initiation of oscillations after dauer from an arrested oscillator phase

(A) Pairwise-correlation map of \log_2 -transformed oscillatory gene expression of dauer exit samples (“postdauer”) and fused larval time course (TC3) samples.

(B) Correlation of the indicated time points after plating dauer-arrested animals on food (TP_{postdauer}) to the fused larval time course, TC3. Arrows indicate peaks of correlation to TP13/19/26.5 (300°) of TC3.

(C) Schematic depiction of behavior of the *C. elegans* oscillator from embryo to adult. A phase-specific arrest (*red dot*) is observed in hatch, early L1, young adults, and dauer-arrested animals. See Fig. S8 for additional data supporting four similar oscillation cycles during L1 through L4.

Methods

C. elegans strains

The Bristol N2 strain was used as wild type. The following transgenic strains were used:

HW1370: *EG6699; xeSi136 [F11E6.3p::gfp::h2b::pest::unc-54 3'UTR; unc-119 +] II* (this study)

HW1939: *EG6699, xeSi296 [Peft-3::luc::gfp::unc-54 3'UTR, unc-119(+)] II* (this study)

HW2523: *EG6699; xeSi437 [Pqua-1::gfp::h2b::pest::unc-54 3'UTR; unc-119 +] II* (this study)

HW2526: *EG6699; xeSi440 [Pdpy-9::gfp::h2b::pest::unc-54 3'UTR; unc-119 +] II* (this study)

PE254: *feIs5 [Psur-5::luc::gfp; rol-6(su1006)] V* (Lagido et al., 2008)

PE255: *feIs5 [Psur-5::luc::gfp; rol-6(su1006)] X* (Lagido et al., 2008)

All transcriptional reporters and luciferase constructs produced for this study were generated using Gibson assembly (Gibson et al., 2009) and the destination vector pCFJ150 (Frøkjær-Jensen et al., 2008). First a starting plasmid was generated by combining *NotI* digested pCFJ150, with either *Nhe-I::GFP-Pest-H2B* or *Nhe-I::luciferase::GFP* (adapted from pSLGCV (Lagido et al., 2008)) and ordered as codon optimized, intron containing gBlocks® Gene Fragment (Integrated DNA Technologies), and *unc-54 3'UTR* (amplified from genomic DNA) to yield pYPH0.14 and pMM001 respectively. Second, promoters consisting of either 2kb upstream of the ATG or up to the next gene were amplified from *C. elegans* genomic DNA before inserting them into *Nhe-I*-digested pYPH0.14 or pMM001. PCR primers and resulting plasmids are listed in the Table S3. Third, we obtained transgenic worms by single-copy integration into EG8079 worms, containing the universal *tTi5605* locus on chromosome II by following the published protocol for injection with low DNA concentration (Frøkjær-Jensen et al., 2012). All MosSCI strains were backcrossed at least twice.

Methods luciferase assay

Gravid adults were bleached and single embryos were transferred by pipetting into a well of a white, flat-bottom, 384-well plate (Berthold Technologies, 32505). Embryos hatched and developed in 90 µL volume containing *E. coli* OP50 (OD₆₀₀ = 0.9) diluted in S-Basal medium (Stiernagle, Theresa, n.d.), and 100 µM Firefly D-Luciferin (p.j.k., 102111). Plates were sealed with Breathe Easier sealing membrane (Diversified Biotech, BERM-2000). Luminescence was measured using a Luminometer (Berthold

Technologies, Centro XS3 LB 960) for 0.5 seconds every 10 minutes for 72 hours at 20°C in a temperature-controlled incubator and is given in arbitrary units.

Luminescence data was analyzed using an automated algorithm for molt detection on trend-corrected data as described previously (Olmedo et al., 2015), but implemented in MATLAB, and with the option to manually annotate molts in a Graphical User Interface. The hatch was identified as the first data point (starting from time point 4 to avoid edge effects) that exceeds the following value: the mean + 5*stdev of the raw luminescence of the first 20 time points.

To quantify the duration of the molts, we subtracted the time point at molt entry from the time point at molt exit. To quantify the duration of larval stages, we subtracted the time point at molt exit of the previous stage (or time point at hatch for L1) from the time point at molt exit of the current stage. The duration of the intermolt was quantified as duration of the molt subtracted from duration of the larval stage. For statistical analysis, we assumed the durations to be normally distributed and used Welch two-sample and two-sided t-test, i.e. the function ‘t.test’ of the package ‘stats’ (version 3.5.1) (R Core Team, n.d.) in R.

RNA sequencing

For RNA sequencing, synchronized L1 worms, obtained by hatching eggs in the absence of food, were cultured at 25°C and collected hourly from 1 hour until 15 hours of larval development, or 5 hours until 48 hours of larval development, for L1–L2 time course (TC1) and L1–YA time course (TC2) respectively. A replicate experiment was performed at room temperature from 1 hours until 24 hours (TC4). RNA was extracted in Tri Reagent and DNase-treated as described previously (Hendriks et al., 2014). For the TC2 and TC4, libraries were prepared using the TruSeq Illumina mRNA-seq (stranded – high input), followed by the Hiseq50 Cycle Single-end reads protocol on HiSeq2500. For the TC1, libraries were prepared using the Illumina TruSeq mRNA-Seq Sample Prep Kit (Strand-sequenced: any), followed by the Hiseq50 Cycle Single-end reads protocol on HiSeq2500.

Processing of RNA-seq data

RNA-seq data were mapped to the *C. elegans* genome using the qAlign function (splicedAlignment=TRUE) from the QuasR package (Au et al., 2010; Gaidatzis et al., 2015) in R. Gene expression was quantified using qCount function from the QuasR package in R. For TC2 and Dauer exit (Hendriks et al., 2014) time course, QuasR version 1.8.4 was used, and data was aligned to the ce10 genome using Rbowtie aligner version 1.8.0. For TC1, QuasR version 1.2.2 was used, and data was

aligned to the ce6 genome using Rbowtie aligner version 1.2.0. For TC4 (**Fig. 2**), RNA-seq data were mapped to the *C. elegans* ce10 genome using STAR with default parameters (version 2.7.0f) and reads were counted using htseq-count (version = 0.11.2).

Counts were scaled by total mapped library size for each sample. A pseudocount of 8 was added and counts were log₂-transformed. For the TC2, lowly expressed genes were excluded (maximum log₂-transformed gene expression - (log₂(gene width)-mean(log₂(gene width))) ≤ 6). This step was omitted in the early time courses because many genes start robust expressing only after 5-6 hours. Expression data of the dauer exit time course was obtained from (Hendriks et al., 2014).

Classification of genes

To classify genes, we applied cosine fitting to the log₂-transformed gene expression levels from t=10 hours until t=25 hours of developmental time (mid L1 until late L3) of TC2, when the oscillation period is most stable (**Fig. 4C**). During this time the oscillation period is approximately 7 hours, which we used as fixed period for the cosine fitting. We built a linear model as described (Hendriks et al., 2014) using cos(ωt) and -sin(ωt) as regressors (with 13 degrees of freedom). In short, a cosine curve can be represented as:

$$C * \cos(\omega t + \varphi) = A * \cos(\omega t) - B * \sin(\omega t)$$

$$\text{With } A = C * \cos(\varphi)$$

$$\text{and } B = C * \sin(\varphi)$$

From the linear regression ('lm' function of the package 'stats' in R) we obtained the coefficients A and B, and their standard errors. A and B represent the phase and the amplitude of the oscillation:

$$phase = \arctan(A, B)$$

$$amplitude = \sqrt{A^2 + B^2}$$

As the density of the genes strongly decreased around 0.5 (**Fig. S1C**) we used amplitude ≥ 0.5 as a first classifier. We propagated the standard error of the coefficients A and B to the amplitude using Taylor expansion in the 'propagate' function (expr=expression(sqrt(((A^2)+(B^2))), ntype = 'stat', do.sim=FALSE, alpha=0.01) from the package 'propagate' (version 1.0-6) (Spiess, 2018) in R. We obtained a 99% confidence interval (99%-CI) for each gene. As 99%-CI that does not include 0 is significant (p-value=0.01), we used the lower boundary (0.5%) of the CI as a second classifier. Thus, we classified genes with an amplitude ≥ 0.5 and lower CI-boundary ≥ 0 as 'oscillating' and genes with an

amplitude < 0.5 or a lower CI-boundary < 0 were classified as ‘not oscillating’ (**Fig. 1B, S1C**). Every gene thus has an amplitude and a peak phase. A peak phase of 0° is arbitrarily chosen, and thus current peak phases are expected to differ systematically from the previously assigned peak phases (Hendriks et al., 2014). To compare the peak phases of TC2 with those of the previously published L3-YA time course (TC6), we calculated the phase difference (TC2 – TC6) (**Fig. S1D, E**). We added 360° to the difference and used the modulus operator ($\%360$), to maintain the circularity within the data. The coefficient of determination, R^2 , was calculated by $1 - (SS_{res}/SS_{tot})$, in which the SS_{tot} (total sum of squares) is the sum of squares in peak phase of the L1-YA time course. SS_{res} (response sum of squares) is the sum of squares of the phase difference.

Time course fusion

In order to obtain an RNAseq time course spanning the complete larval development, we fused the L1–L2 time course (TC1, TP1 – TP15) with the L1–YA course (TC2, TP5 – TP48). To decide which time points to choose from the individual time courses, we correlated the gene expression of all genes ($n = 19,934$) of both time courses against each other using the \log_2 transformed data with a pseudocount of 8 with pearson correlation. In general, we saw good correlation between the two time courses, e.g. $TP1_{(TC1, L1-L2)}$ correlated well with $TP1_{(TC2, L1-YA)}$ etc. (**Fig. S1B**). Additionally, we could see comparable correlation values of $TP13_{(TC2, L1-YA)}$ and $TP13_{(TC1, L1-L2)}$ with $TP1-5_{(TC1, L1-L2)}$ (not shown). We concluded that $TP13_{(TC1, L1-L2)}$ and $TP13_{(TC2, L1-YA)}$ are highly similar and thus fused at this time point, i.e., combined $TP1-TP13_{(TC1, L1-L2)}$ with $TP14-TP48_{(TC2, L1-YA)}$.

Exclusion of genes based on L4 mean expression

Given that oscillating genes were identified based on gene expression in TP10-TP25, when oscillation period is most stable, some genes showed deviating behavior in the last oscillation cycle, C4. Hence, for quantification of oscillation amplitude, period and correlation, we excluded those genes. We determined the mean expression levels for each gene over time in oscillation cycles C2 (TP14-TP20), C3 (TP20-TP27) and C4 (TP27-TP36). Genes ($n=291$) were excluded if the absolute value of the difference in mean expression between L2 and L4 normalized by their mean difference exceeded 0.25, i.e.

$$\text{abs}((L2\text{meanExpr}-L4\text{meanExpr})/(0.5*(L2\text{meanExpr}+L4\text{meanExpr})))>0.25.$$

Quantification of oscillation amplitude

To quantify the oscillation amplitude for each larval stage, we split the TC2 in 4 separate cycles, roughly corresponding to the developmental stages, i.e. C1: TP6-TP14, C2: TP14-TP20, C3: TP20-TP27 and C4: TP27-TP36 developmental time. We applied cosine fitting to C2, C3 and C4 as described above to the expression of oscillating genes in TC2, excluding genes with deviating mean expression in L4 as described above. We excluded C1, because amplitudes were sometimes difficult to call reliably. We used a fixed period of 7 h for C2-C3 and 8.5 h for C4 as determined by quantification of the oscillation period (**Fig. 4C**). We applied a linear regression using the function 'lm' of the package 'stats' in R to find the relationship between the amplitudes across different stages, i.e. the slope. The correlation coefficient, r , was determined using the 'cor' function (method=pearson) of the package 'stats' in R.

Quantification of oscillation period

For a temporally resolved quantification of the oscillation period, we filtered the mean-normalized \log_2 transformed gene expression levels of oscillating genes, excluding L4 deviating genes (we selected TP5-TP39, because oscillations cease at \sim TP36 and the inclusion of 3 additional time points avoided edge effects) using a Butterworth filter ('bwfilter' function of the package 'seewave' (version 2.1.0) (Sueur et al., 2008) in R, to remove noise and trend-correct the data. The following command was used to perform the filtering: `bwfilter(data, f = 1, n = 1, from = 0.1, to = 0.2, bandpass = TRUE, listen = FALSE, output = "matrix")`. The bandpass frequency from 0.1 to 0.2 (corresponding to 10 hour and 5 hour period respectively) was selected based on the Fourier spectrum obtained after Fourier transform ('fft' function with standard parameters of the package 'stats'). As an input for the Hilbert transform we used the butterworth-filtered gene expression. The 'ifreq' function (with standard parameters from the package 'seewave') was used to calculate the instantaneous phase and frequency based on the Hilbert transform. To determine the phase progression over time we unwrapped the instantaneous phase (ranging from 0 to 2π for each oscillation) using the 'unwrap' function of the package 'EMD' (version 1.5.7) (Kim and Oh, 2018) in R. To avoid edge effects, we removed the first 4 data points (TP5-TP8) and last 3 data points (TP37-TP39) of the unwrapped phase (retaining TP9-TP36). The angular velocity is defined as the rate of phase change, which we calculated by taking the derivative of the unwrapped phase. The instantaneous period was determined by $2\pi/\text{angular velocity}$ and was plotted for each gene individually and as mean in a density plot. The mean of the instantaneous period over all oscillating genes was used to reconstruct a 'global' oscillation by taking the following command: `sin(cumsum(mean angular velocity))` and plotted

together with a 7h-period oscillation and the mean normalized expression of a representative gene, *col-147*.

Correlation analyses of RNAseq data

Log₂-transformed data was filtered for oscillating genes and then plotted in a correlation matrix using the R command `cor(data, method="pearson")`. The correlation line plots represent the correlations of selected time points to the fused full developmental time course (**Fig. S5**) and are specified in the line plot.

To reveal the highest correlations for a selected time point, we analyzed the correlation line of this time point between TP7 and TP36 (the time in which oscillations occur) using a spline analysis from Scipy (Jones et al., 2001) in python (“`from scipy.interpolate import InterpolatedUnivariateSpline`” with `k=4`) and stored the spline as variable “`spline`”. We identified peaks of the correlation line by finding the zeros of the derivative of the spline (`cr_points = spline.derivative().roots()`). The highest correlations of the respective correlation line were thus the value of the spline at the time point where the spline derivative was zero and the value was above the mean of the correlation line (`cr_vals = spline(cr_pts)` followed by `pos_index = np.argwhere(cr_vals > np.mean(data.iloc[i]))` and `peak_val = cr_vals[pos_index]`). Thus, we identified the correlation of particular time points (e.g. TP14–TP19) with their corresponding time points in the next oscillation cycle. Thereby, we were able to identify cycle time points as described in the results section. We defined the first cycle time point, e.g. TP14 of cycle 2, as 0°, and the last unique one, TP19, as 300°. TP14 (0° of cycle 2) is also 360° of cycle 1. Note that a sampling interval of 1 hour means that a TP in one cycle may correlate equally well to two adjacent TPs in another cycle, as seen for instance in the correlation of TP13 to TP26 and TP27. The spline interpolation places the peak of correlation in the middle of these time points at ~TP26.5. The spline analysis thus annotates cycle points correctly even in C4 which has an extended period.

We performed correlation analyses without mean normalization of expression data, hence correlation values cannot be negative but remain between 0 and 1. We made this decision because a correlation analysis using mean-centered data, where correlations can vary between -1 and +1, requires specific assumptions on which time points to include or exclude for mean normalization, and because it is sensitive to gene expression trends. However, we confirmed, as a proof of principle, the expected negative correlation of time points that are in antiphase when using mean-centered data (**Fig. S9**) using all oscillating genes in TC3 (n = 3680).

GO-term analysis

GO-term analysis was performed using the GO biological process complete option (GO ontology database, release 2019-02-02) from the online tool PANTHER (“PANTHER Classification System,” n.d.) (overrepresentation test, release 2019-03-08, standard settings).

Tissue specific analysis

In order to reveal if particular tissues are enriched in oscillating genes, we used single cell sequencing data from (Cao et al., 2017). In particular, we used Supplementary “Table S6: Differential expression test results for the identification of tissue-enriched genes” where each gene’s highest and second highest tissue expression and the ratio of is reported. We selected tissue specific genes based on a ratio > 5 and a q value < 0.05 (these criteria reduced the number of genes to investigate). Using this list of genes we calculated the percentage of tissues present in both, all genes and oscillating genes using the function “Counter” from “collections” in python (*labels, values = zip(*Counter(tissue_info_thr["max.tissue"]).items())*). In order to obtain the enrichment of tissues, we divided the percentage of tissue X among oscillating genes in the tissue enriched dataset by the percentage of tissue X among all genes in the tissue enriched data set and plotted the resulting values. The list of tissue specific oscillating genes was further used to investigate the peak phases within one tissue by plotting a density plot of the peak phase (from **Fig. 1**) for every tissue. As we lack data below 0 degree and above 360 degree, density values at these borders are distorted as the density is calculated over a moving window. Since we are confronted with cyclical data and thus 0 degree corresponds to 360 degree, we added and subtracted 360 degree to each phase value, thus creating data that ranged from -360 degree to 720 degree which allowed us to plot the correct density at the borders 0 and 360 degree. We used python (pandas) to plot this data using the following command:

```
data_tissue ["Phase"].plot(kind="kde", linewidth=5, alpha=0.5, bw=0.1)
```

Identification of first gene expression peaks in L1 larvae

To identify the first peak of oscillating genes, we used a spline analysis in Python (“from scipy.interpolate import InterpolatedUnivariateSpline”) from TP3 – TP13. We chose these time points to remove false positives in the beginning due to slightly higher noise for the first 2 time points as well as not to identify the second peak which occurred at \geq TP14 for some very early genes. The function used was “InterpolatedUnivariateSpline” with $k=4$. After constructing the spline, we identified the zeros of the

derivative and chose the time point value with the highest expression value and a zero derivative as the first peak time point.

Embryonic gene expression time course

Embryonic gene expression data was obtained from (Hashimshony et al., 2015), and represented precisely staged single embryos at 10 min intervals from the 4-cell stage up to muscle movement and every 10-70 min thereafter until 830 minutes. We obtained the gene count data from the Gene Expression Omnibus data base under the accession number GSE50548, for which sequencing reads were mapped to WBCel215 genome and counted against WS230 annotation.

We normalized the gene counts to the total mapped library size per sample, added a pseudocount of 8, and \log_2 -transformed the data. We selected genes according to the larval oscillating gene annotation, with L4 deviating genes excluded, and plotted their embryonic expression patterns according to peak phase in larvae. The embryonic time course was correlated to the fused larval time course (TC3) using the 'cor' function (method='pearson') of the package 'stats' in R (**Fig. S7A**). Correlation line plots were generated by plotting the correlation coefficients for each embryonic time point over larval time. To identify the peaks of the correlation lines with a resolution higher than the sampling frequency, we interpolated the correlation lines using the 'spline' function (n=240, method='fmm') of the package 'stats' in R. To call the peaks of the interpolated correlation lines, we applied the 'findpeaks' function (with nups=5, ndowns=5) of the package 'pracma' on the time points on the interpolated time points 10-185, that cover the four cycles. To find the embryonic time point at which oscillations initiate, we plotted the larval TP in cycle 2 at which the correlation peak occurred over embryonic time (**Fig. S7B**) and determined the intersection of the two linear fits, using the 'solve' function of the package 'Matrix' (version 1.2-15) (Bates and Maechler, 2018) and the 'lm' function of the package 'stats' in R respectively. To determine the 95%-CI of the x-coordinate of the intersect, the standard error of the slope a and the intercept b of the two linear fits was propagated using Taylor expansion in the 'propagate' function (expr = expression((b1-b2)/(a2-a1)), ntype = "stat", do.sim = FALSE, alpha=0.05) from the package 'propagate' in R. The pairwise correlation map was generated with the 'aheatmap' function of the package 'NMF' (version 0.21.0) (Gaujoux and Seoighe, 2010) and the 3D plot was generated with the '3Dscatter' function of the package 'plot3D' (version 1.1.1) (Soetaert, 2017) in R.

Time-lapse imaging of single animals

Single worm imaging was done by adapting a previous protocol (Turek et al., 2015), and is similar to the method reported in (Gritti et al., 2016). Specifically, we replaced the previous 3.5-cm dishes with a “sandwich-like” system: The bottom consisted of a glass cover slip onto which two silicone isolators (GRACE Bio-Labs, SKU: 666103) with a hole in the middle were placed on top of each other and glued onto the glass cover slip. We then placed single eggs inside the single OP50 containing chambers, which were made of 4.5% agarose in S-basal. The chambers including worms were then flipped 180 degree and placed onto the glass cover slip with the silicone isolators, so that worms faced the cover slip. Low melt agarose (3% in S-basal) was used to seal the agarose with the chambers to prevent drying out or drifts of the agarose chambers during imaging. The sandwich-like system was then covered with a glass slide on the top of the silicone isolators to close the system.

We used a 2x sCMOS camera model (T2) CSU_W1 Yokogawa microscope with 20x air objective, NA = 0.8 in combination with a 50 μ m disk unit to obtain images of single worms. For a high throughput, we motorized the stage positioning and the exchange between confocal and brightfield. We used a red LED light to combine brightfield with fluorescence without closing the shutter. Additionally, we used a motorized z-drive with 2 μ m step size and 23 images per z-stack. The 488nm laser power for GFP imaging was set to 70% and a binning of 2 was used.

To facilitate detection of transgene expression and oscillation, we generated reporters using the promoters of genes that exhibited high transcript levels and amplitudes, and where GFP was concentrated in the nucleus and destabilized through fusion to PEST::H2B (see strain list above). We placed embryos into chambers containing food (concentrated bacteria HT115 with L4440 vector) and imaged every worm with a z-stack in time intervals of 10 min during larval development in a room kept at ~21°C, using a double camera setting to acquire brightfield images in parallel with the fluorescent images. We exploited the availability of matching fluorescent and brightfield images to identify worms by machine learning. After identification, we flattened the worm at each time point to a single pixel line and stacked all time points from left to right, resulting in one kymograph image per worm. We then plotted background-subtracted GFP intensity values from the time of hatch ($t = 0$ h), which we identified by visual inspection of the brightfield images as the first time point when the worm exited the egg shell.

Time lapse images were analyzed using a customized KNIME workflow (**File S1**). We analyzed every worm over time using the same algorithm. First, we identified the brightest focal planes per time point by calculating the mean intensity from all focal planes per time point and selecting the focal planes that had a higher intensity than the mean. Then we maximum-projected the GFP images over Z per time point and blurred the DIC image and also max projected over Z (blurring the DIC improved the machine

learning process later on). All images per worm over time were analyzed by Ilastik machine learning in order to identify the worm in the image. The probability map from Ilastik was used to select a threshold that selected worms of a particular experiment best. (The threshold might change slightly as DIC images can look slightly different due to differences in the sample prep amongst experiments.) Using a customized ImageJ plugin, we straightened the worm. The straightened GFP worm image was then max projected over Y which resulted in a single pixel line representing the GFP intensities in a worm and after stacking up all the single pixel lines in Y direction, we obtained the kymographs. In order to remove noise coming from the head and tail regions of the worm due to inaccuracy of the machine learning, we measured mean GFP intensities per time point ranging from 20% until 80% of the worms anterior – posterior axis. For background subtraction we exploited the fact that only the nuclei were GFP positive and thus subtracted the minimum intensity value between GFP nuclei from their intensity values.

After the KNIME workflow, we imported the measured GFP intensities into Python and analyzed the traces using a butterworth filter and Hilbert transform analysis (both from Scipy (Jones et al., 2001)). We used the butterworth bandpass filter using `b, a = butter(order=1, [low,high], btype="band")` with `low=1/14` and `high=1/5`, corresponding to 14 hour and 5 hour periods respectively. We then filtered using `filtfilt(b, a, data, padtype='constant')` to linearly filter backwards and forwards.

For individual time points where the worm could not be identified by the Ilastik machine learning algorithm, we linearly interpolated (using interpolation from pandas (McKinney, 2010)) using `"pandas.series.interpolate(method = 'linear', axis =0, limit = 60, limit_direction = 'backward')"`, between the neighboring time points to obtain a continuous time series needed for the Hilbert transform analysis. Using Hilbert transform, we extracted the phase of the oscillating traces for each time point and specifically investigated the phase at molt entry and molt exit for our different reporter strains.

In order to determine time points in which worms are in lethargus, we investigated pumping behavior. As the z-stack of an individual time point gives a short representation of a moving worm, it is possible to determine whether animals pump (feeding, corresponds to intermolt) or not (lethargus / molt). Additionally to the pumping behavior, we used two further requirements that needed to be true in order to assign the lethargus time span: First, worms needed to be quiescent (not moving, and straight line) and second, a cuticle needed to be shed at the end of lethargus. Usually worms start pumping one to two time points before they shed the cuticle. This analysis was done manually with the software ImageJ, and results were recorded in an excel file, where for every time point, the worms' behavior was denoted as 1 for pumping and as 0 for non-pumping.

To determine a possible connection between oscillations and development, we applied error propagation, assuming normal distribution of the measured phases and larval stage durations. Thereby, we exploited the inherent variation of the oscillation periods and developmental rates among worms, rather than experimental perturbation, to probe for such a connection. We define the phase θ at either molt exit or entry as $\theta \equiv \frac{2\pi}{T_o} * T_d \sim (\mu, \sigma^2)$

with $T_o \sim (\mu_o, \sigma_o^2)$ being the period of oscillation and $T_d \sim (\mu_d, \sigma_d^2)$ the intermolt duration (for phase at molt entry) or larval stage duration (for phase at molt exit), resulting in a phase with mean μ and a standard deviation σ . Should the two processes be coupled as in scenario 2, we would expect

$$\sigma_{observed} < \sigma_{calculated}.$$

To calculate the phase at molt entry and molt exit with error propagation we used the “uncertainties” package (Lebigot, n.d.) in python. The larval stage duration as well as intermolt duration and period were treated as ufloat numbers, representing the distributions coming from our measurement (e.g. 7.5 +/- 0.2). These distributions were then used to calculate the expected phase at molt entry (using the intermolt duration) and molt exit (using the larval stage duration) using: $phase(err.prop) = \frac{2*\pi}{period} * larval\ stage$. This resulted in the phase being represented by an ufloat number and thus a distribution which we used for plotting after normalizing for the mean to compare the variation of the data.

Supplementary Figures and Materials

Developmental function and state transitions of a gene expression oscillator in *C. elegans*

Authors: Milou W.M. Meeuse, Yannick P. Hauser, Gert-Jan Hendriks, Jan Eglinger, Guy Bogaarts, Charisios Tsiairis, Helge Großhans*

*Correspondence to: helge.grosshans@fmi.ch.

This PDF file includes:

Figs. S1 to S9

Tables S2 to S3

Other Supplementary Materials for this manuscript include the following:

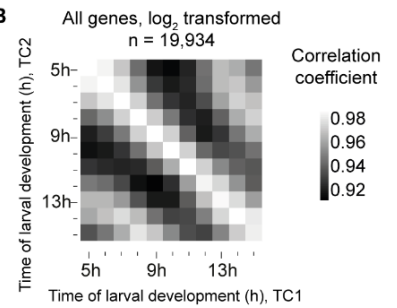
Table S1

File S1

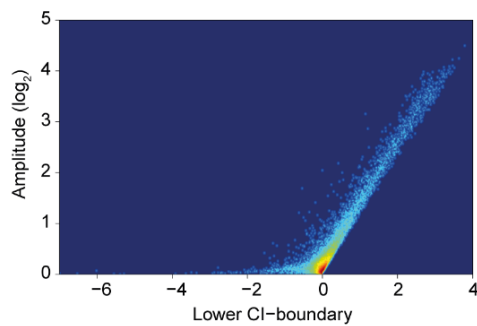
A

	Description	TP	Figure	# osc genes	# osc w/o deviating L4 genes
TC1	early larval time course, replicate 1	1-15	2	3680	NA
TC2	long developmental time course	5-48	4, S1, S4	3739	3448
TC3	TC1 (TP1-13) + TC2 (TP14-48)	1-48	1, 2, 5, 6, 7, S1, S5, S8, S9	3680	3393
TC4	early larval time course, replicate 2	1-24	2	3739	NA
TC5	TC4 (TP1-13) + TC2 (TP14-48)	1-48	S2	3739	NA
TC6	L3-YA TC from Hendriks et al, 2014	21-36	S1	2718	NA
embryo	Hashimshony et al, 2015	10-830	6, S7	3723	3434
dauer	Hendriks et al, 2014	1-15	7	3680	3393

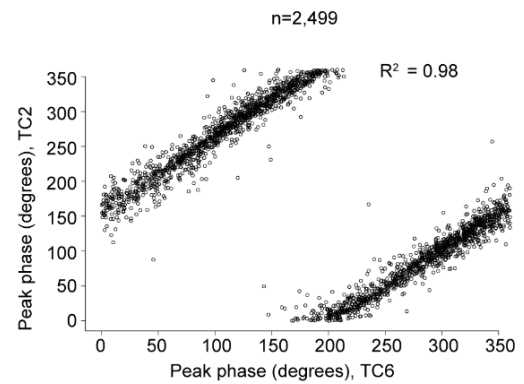
B



C



D



E

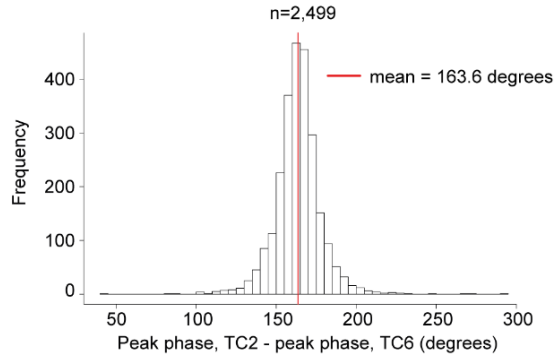


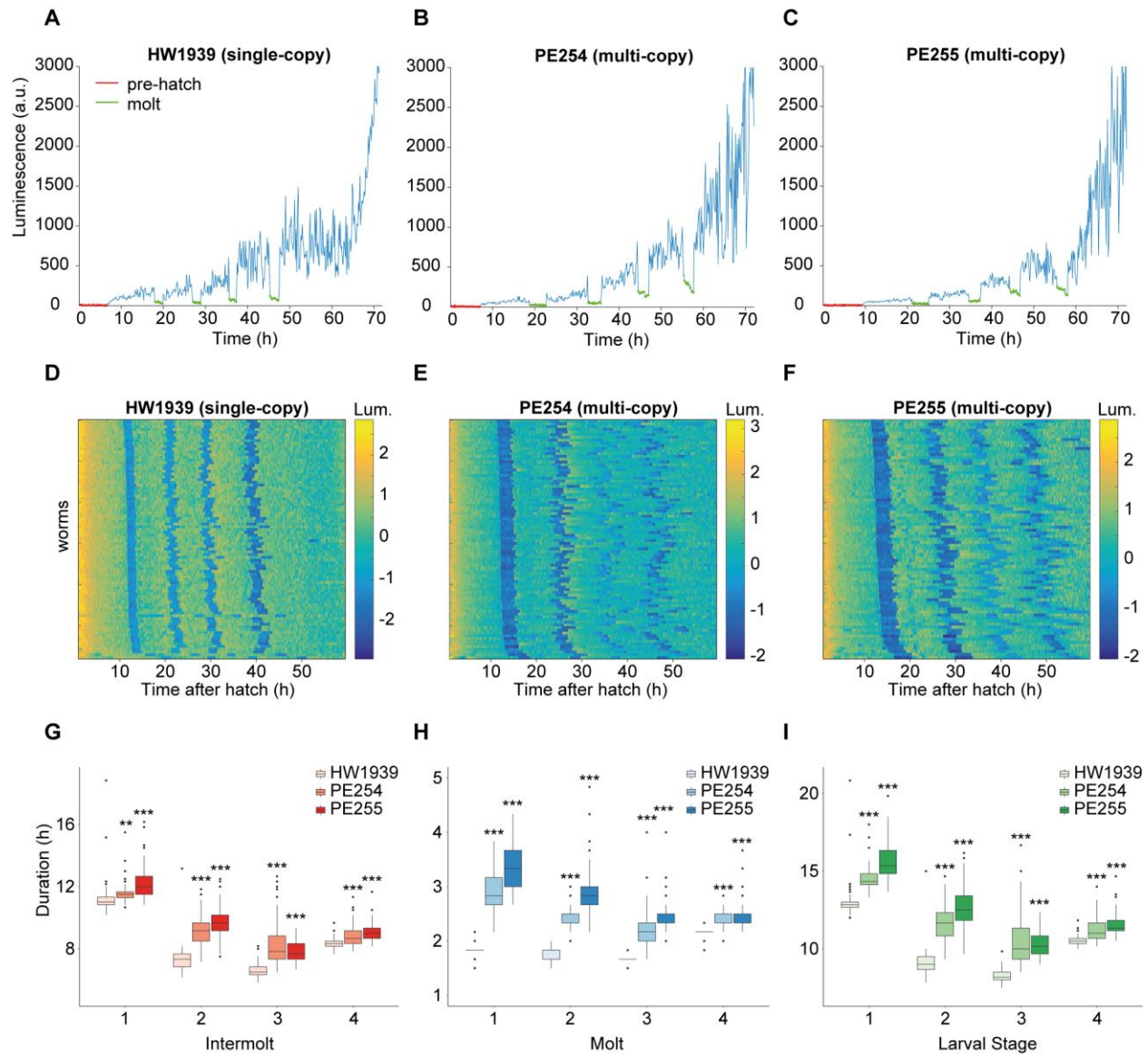
Fig. S1. Identification of 3,739 ‘oscillating’ genes

(A) Overview of time courses in this study

(B) Pairwise-correlation of \log_2 transformed count data ($n=19,934$) of the early time course (TC1) with the long developmental time course (TC2). High correlation is detected for samples that correspond to the same time points, justifying a fusion of these time courses to one continuous full developmental time course (TC3).

(C) Smooth scatter of amplitude over lower boundary of 99% confidence interval of the amplitude as determined by cosine fitting and error propagation (see **methods**, related to **Fig. 1B**).

(D, E) Scatterplot **(D)** of the peak phase of the long developmental time course (TC2) described here over the previously published L3-YA time course (TC6) (Hendriks et al., 2014). Genes that were identified as ‘oscillating’ in both time courses ($n = 2,499$) are shown. Peak phases correlate well as confirmed by the coefficient of determination, R^2 , as indicated. However, they differ systematically **(E)** because a peak phase of 0° is arbitrarily chosen. A red vertical line indicates the mean phase difference (TC2 – TC6; corrected for circularity as described in **Methods**). Note that the gene-specific peak phase calculated here and previously both also differ from the arbitrarily assigned cycle phases in **Fig. S8** and their discussion.



J

	stage 1	stage 2	stage 3	stage 4
Intermolt PE254	1.04 (p=3.28E-03)	1.26 (p=4.51E-31)	1.26 (p=3.07E-19)	1.05 (p=1.94E-08)
Intermolt PE255	1.10 (p=1.98E-10)	1.32 (p=1.39E-35)	1.19 (p=3.72E-30)	1.08 (p=2.10E-16)
Molt PE254	1.60 (p=4.92E-51)	1.40 (p=9.60E-54)	1.33 (p=2.11E-29)	1.11 (p=8.68E-23)
Molt PE255	1.84 (p=2.49E-50)	1.65 (p=3.53E-37)	1.46 (p=2.33E-38)	1.15 (p=9.74E-21)
Larval stage PE254	1.11 (p=5.20E-20)	1.28 (p=2.35E-40)	1.27 (p=1.99E-22)	1.07 (p=4.32E-14)
Larval stage PE255	1.20 (p=6.93E-31)	1.38 (p=2.97E-42)	1.25 (p=3.97E-40)	1.10 (p=8.24E-22)

Fig. S2. A strain with single-copy integrated luciferase transgene develops rapidly and synchronously

(A-C) Representative raw luminescence traces of individual animals grown at 20°C. As the egg-shell is impenetrable to luciferin, a sudden increase in luminescence at the beginning of the time course indicates hatch (pre-hatch in red). Abrupt drops and subsequent rises in luminescence specify molts (in green). The previously published strains (B, PE254; C, PE255) (Olmedo et al., 2015) express luciferase from randomly integrated multi-copy transgene arrays that carry a semi-dominant version of the cuticular collagen *rol-6* as a marker (Lagido et al., 2008). To exclude that this genetic make-up could interfere with our quantification, we integrated a luciferase transgene, driven by the strong, ubiquitous and constitutive *eft-3* promoter, into the genome through Mos1-mediated single copy integration (MosSCI) (A, HW1939).

(D-F) Heatmap per strain showing trend-corrected luminescence (Lum.) trace for one animal per horizontal line (D, Single-copy integrated HW1939 (n=86). E, Multi-copy integrated PE254 (n=88). F, Multi-copy integrated PE255 (n=79)). Hatch is set to t = 0 h and traces are sorted by time of entry into first molt. Blue indicates low luminescence and corresponds to the molts.

(G-I) Quantification of the duration of each intermolt (G), molt (H), larval stage I) for indicated strains in hours. The newly generated strain developed more rapidly and with less variability with regard to the duration of individual stages. Although the general trend in larval stage durations was shared between the different strains, i.e. L1>L4>L2&L3 (I), animals carrying the *rol-6*-marked multi-copy luciferase arrays also exhibited an extended M1 molt (H) as reported previously (Olmedo et al., 2015). This effect disappeared when using the single-copy transgene strain. Hence, the duration of molt M1 became comparable to that of M2 and M3 and lengthening of L1 is explained by lengthening of intermolt 1. Significant differences between single-copy integrated (n=86) and multi-copy integrated strains (PE254 (n=88) and PE255 (n=79)) is indicated (***) $P < 0.001$, Welch two sample, two-sided t-test). Boxplots extend from first to third quartile with a line at the median, outliers are indicated with a cross, whiskers show 1.5*IQR.

(J) Table showing fold changes of mean durations of indicated stages for PE254 and PE255 compared to HW1939 for data shown in G-I. P-values are indicated in brackets (Welch two-sample, two-sided t-test).

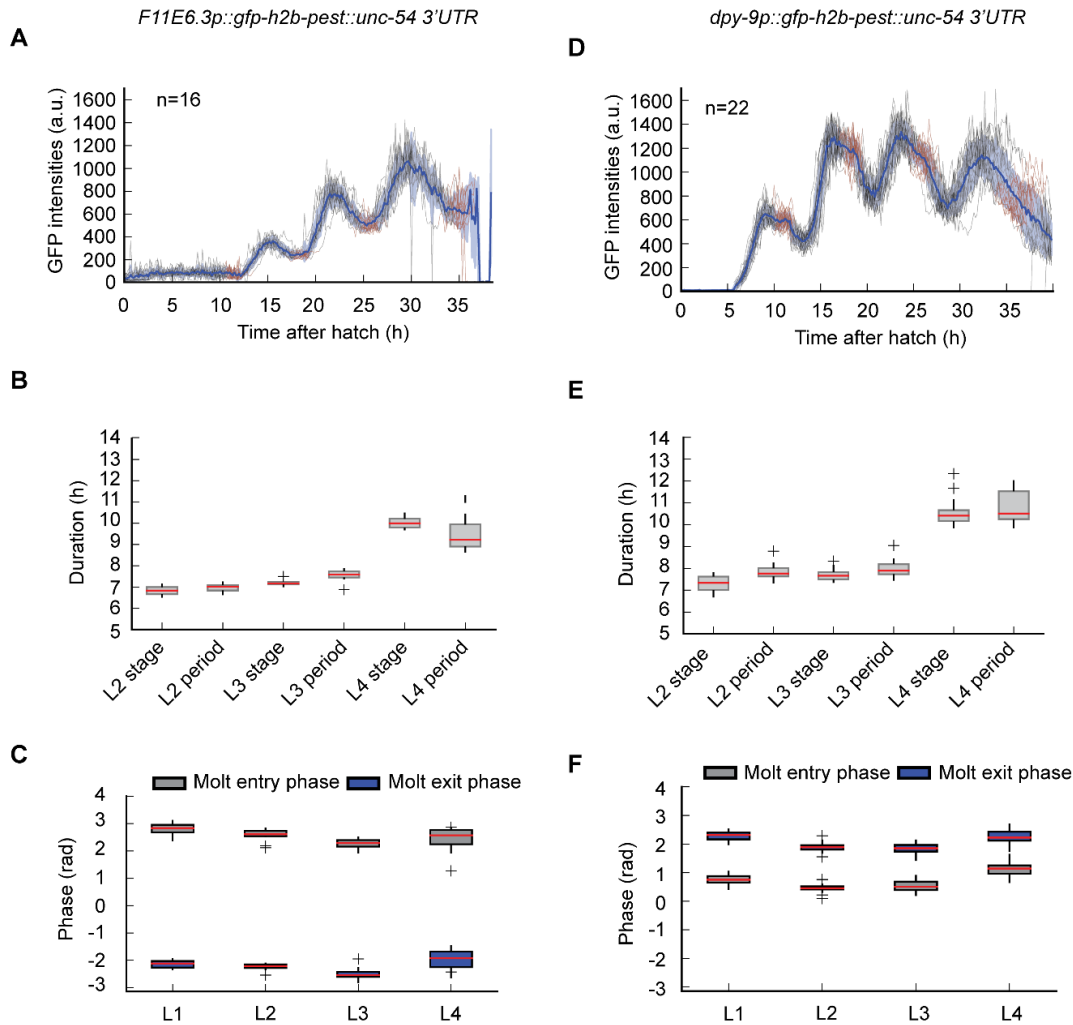


Fig. S3. Single worm imaging with two additional reporter strains confirms phase-locking of oscillations to molts independently of peak phases

(A, D) GFP quantification of single worm kymographs for the *F11E6.3* (HW1370, n=16) and the *dpy-9* (HW2526, n=22) transcriptional reporters respectively. All traces were aligned to the time of hatching, which was set to $t = 0$ h. Segments in red indicate lethargus while the blue shading indicates the standard deviation at each time point with the blue line representing the mean across worm. Only three peaks are visible for the *F11E6.3* reporter, because the assay terminated before the final rise in expression seen with RNA sequencing.

(B, E) Comparison of larval stage duration and period times of oscillations in hours for L2-L4 larval stages for *F11E6.3* and *dpy-9* transcriptional reporters respectively.

(C, F) Boxplot of expression phases at molt entry (start of lethargus) and molt exit (end of lethargus) separated by larval stages; $n = 16$ for *F11E6.3* (D) and $n = 22$ for *dpy-9* (I) transcriptional reporters.

Boxplots extend from first to third quartile with a line at the median, outliers are indicated with a cross, whiskers show $1.5 \times \text{IQR}$.

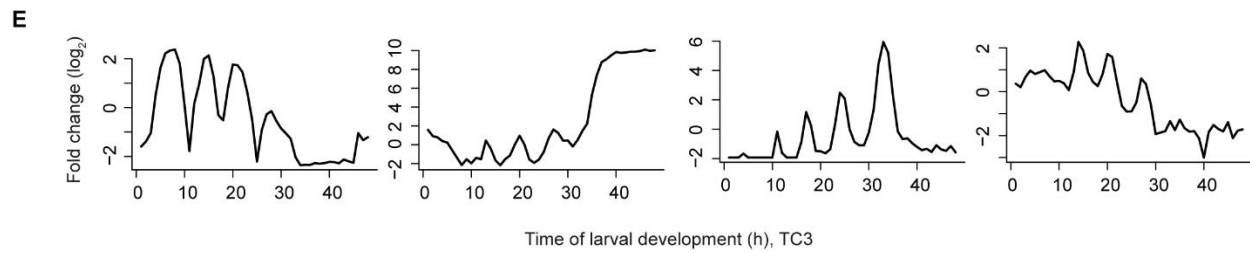
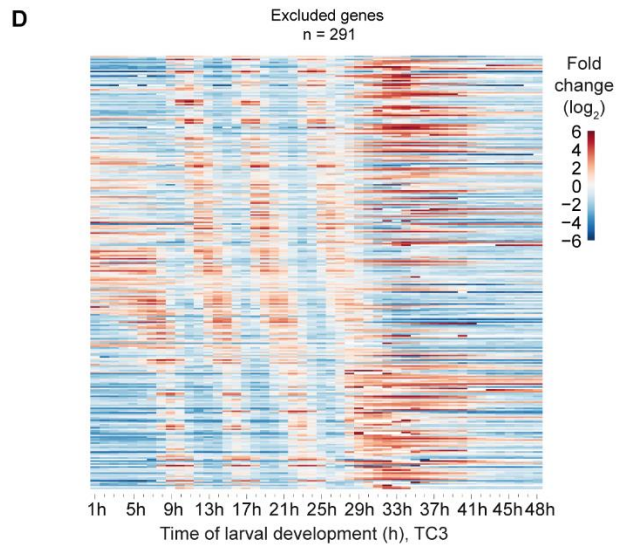
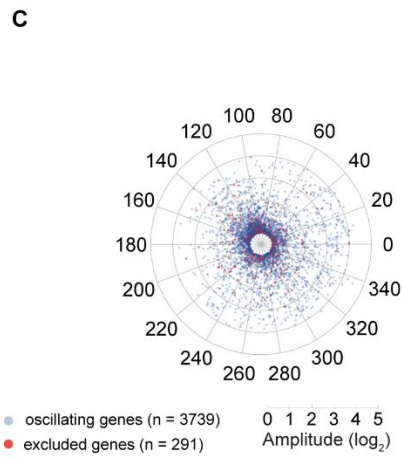
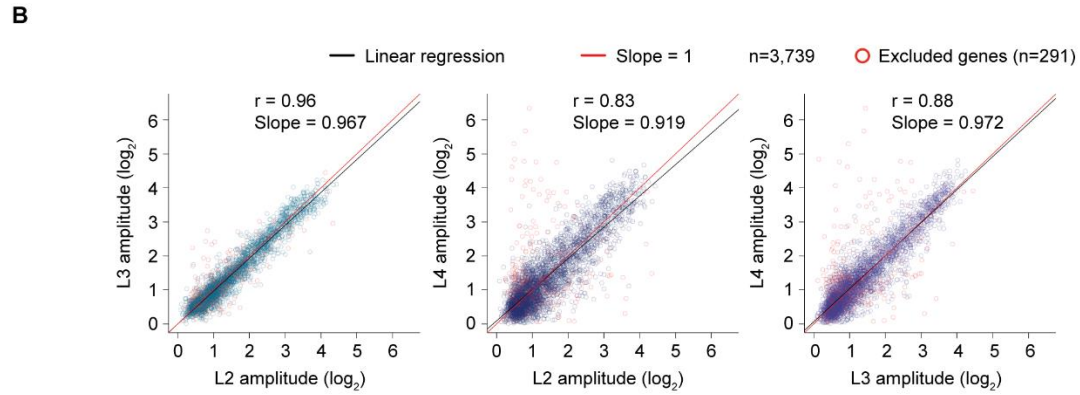
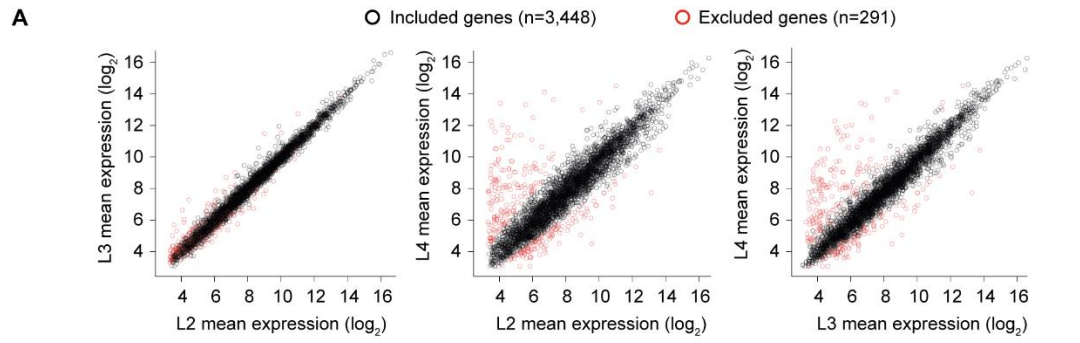


Fig. S4: Exclusion of genes based on deviating behavior in L4 stage

(A) Scatter plot showing mean expression over time in L2, L3 or L4 for each oscillating gene. Genes indicated in red were excluded based on the L2-L4 scatter plot (**Methods**).

(B) Scatter plot showing the amplitude in L2, L3 or L4 for each oscillating gene. Genes indicated in red correspond to red genes in A and were excluded from amplitude analysis in **Fig. 4**.

(C) Polar Scatterplot visualizing the amplitude and peak phase of all oscillating genes (n = 3739) in blue and the excluded oscillating genes (n = 291) in red. The excluded genes do not show a particular peak phase or amplitude preference.

(D) Gene expression heatmap of \log_2 transformed mean normalized data of the excluded oscillating genes in the fused time course TC3 (n = 291).

(E) Example gene expression of four excluded oscillatory genes that were excluded based on the L2-L4 scatter plot in (A).

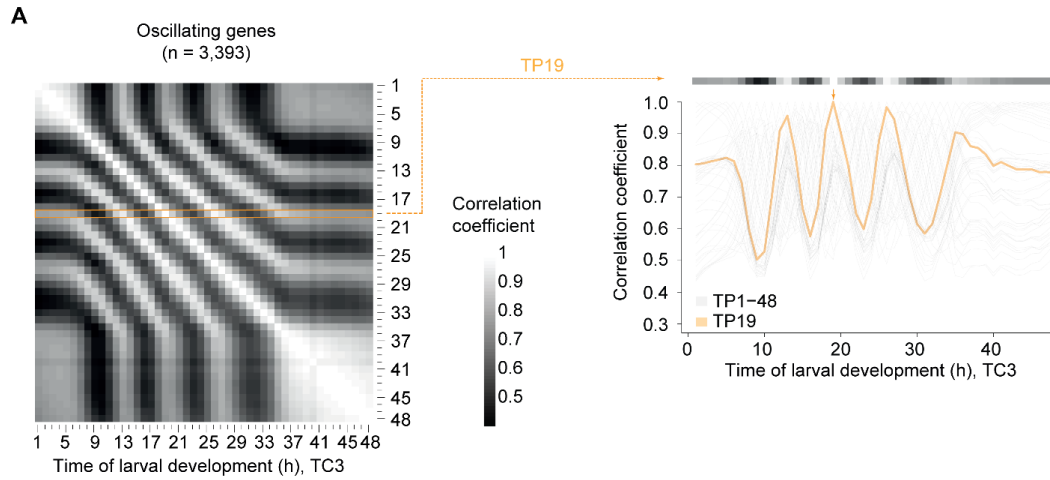


Fig. S5. Correlation line explanation

(A) Left: Pairwise-correlation plot of \log_2 -transformed oscillatory gene expression patterns without L4 deviating genes obtained from synchronized population of L1 stage larvae at 25°C (TC1, TP1 – 13) combined time points from the long developmental time course (TC2, TP14 – 48), as in **Fig. 5B** (n = 3,393). Right: The correlation of TP19 versus all other time points is plotted as a line (orange), correlation with itself at 19 hours is 1.0 (orange arrow).

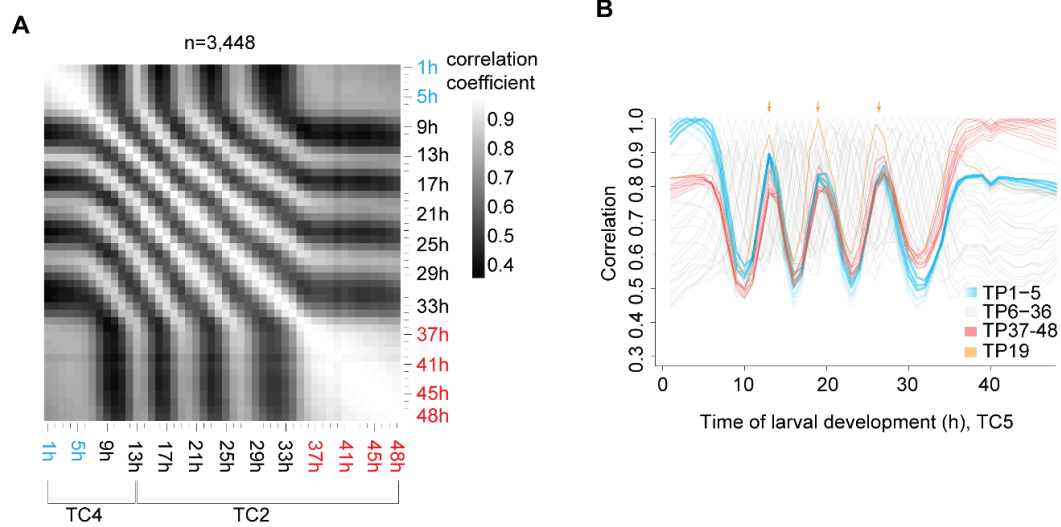


Fig. S6: Arrested phase of the oscillator is reproduced in a second RNA sequencing experiment

(A) Pairwise correlation plot of \log_2 -transformed oscillatory gene expression patterns without L4 deviating genes ($n=3,448$) from the replicate time course TC4 (TP1 – 13) fused with TP14 – 48 of the long RNA seq time course TC2 (TP14 – 48).

(B) Correlations of expression patterns for the indicated time points to all other time points of the fused time course from A. TP1 – 5 (blue) as well as the adult time points (red) correlate highly with TP13, TP19 and TP26/27 (arrows). Hence, oscillations are arrested in the same phase at the beginning and the end of the time course.

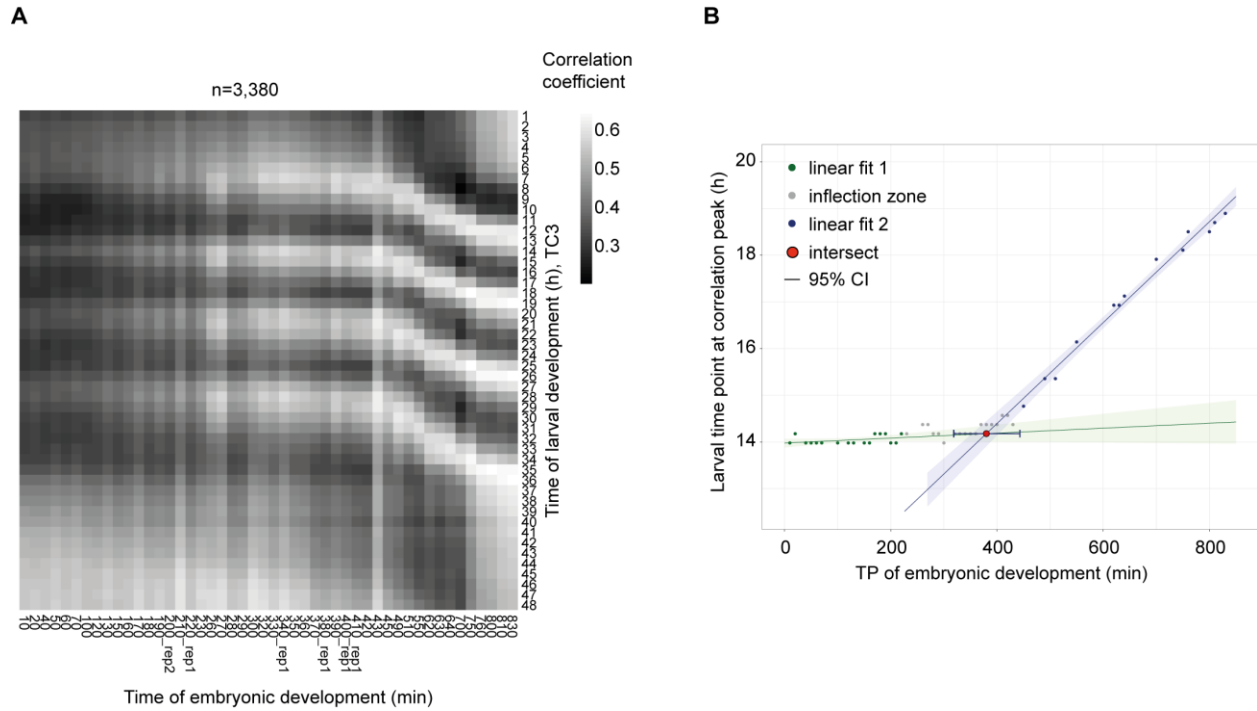


Fig. S7. Initiation of oscillations during mid-embryogenesis

(A) Pairwise correlation map of \log_2 -transformed oscillating gene counts of fused larval time course to embryonic time course (Hashimshony et al., 2015).

(B) Scatter plot showing the larval time point of the larval oscillation cycle 2 (Fig. 6) for each embryonic time point. The larval time point of the peak was determined after spline interpolation (9). Linear model 1 ($y = 5.312e-04 \cdot x + 13.98$, $p=0.098$, $R^2 = 0.162$, 16 degrees of freedom) was fitted to the data of embryonic TP10-TP230 min (in green) and linear model 2 ($y = 0.0108 \cdot x + 10.07$, $p=2.08e-11$, $R^2 = 0.985$, 11 degrees of freedom) was fitted to the data of embryonic TP450-TP830min (in blue). The embryonic time at the intersection (in red, 380.0 min (95%-CI 317.6 min – 444.2 min)) of the linear models was determined in the inflection zone, i.e. points (in grey) not used for model 1 or model 2 fit, and the 95% CI was determined by propagating the standard errors of the coefficients of the linear models (Methods).

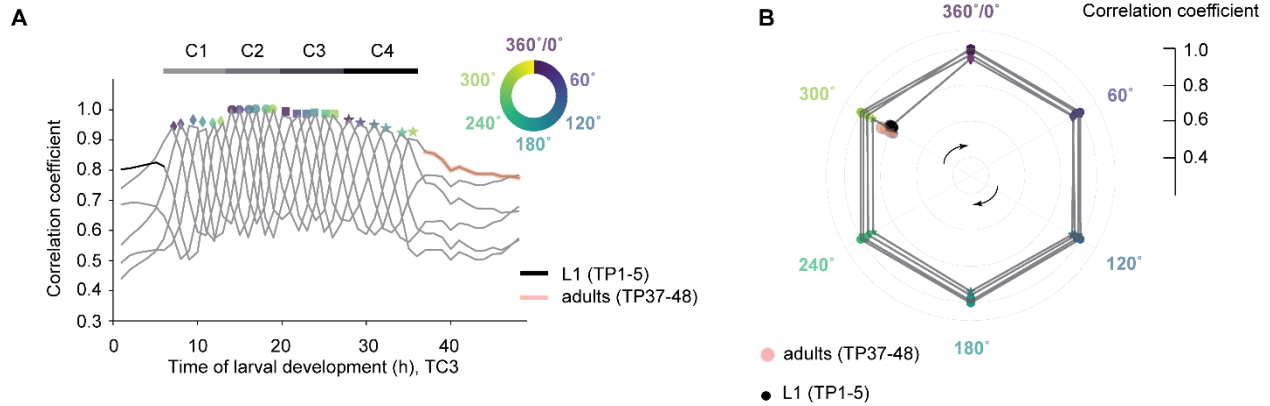


Fig. S8: Oscillations are invariant over time

The correlation analysis revealed a stably arrested oscillator state in early L1 and young adults. To explore how the oscillating state changes over time, we investigated the similarity among the four oscillation cycles, C1 through C4. Specifically, we compared oscillator states at each time point sampled during C2 to the three other cycles. By choosing C2 as a starting point, we could examine correlations to both earlier and later cycles. Because the last time point (360°) of one cycle is the first time point (0°) of the following cycle, we truncated each cycle at 300° for this analysis, to avoid an artificially inflated correlation.

Using spline interpolation and local maxima detection to determine correlation peaks (**Methods**) for each of the six time points TP14/0° through TP19/300° of C2 to the other cycles, we observed high and largely invariant values across each of the other three cycles. In other words, except for the extended period during L4, little variability occurs in oscillations across the four cycles.

(A) Correlation of cycle 2 time points (TP14–19; corresponding to 0° to 300°; marked by indicated colors) to all other time points of the fused larval time course (TC3). For the correlation analysis we used the log₂-transformed oscillating gene expression data without the L4 deviating genes. Diamonds (cycle 1), circles (cycle 2), squares (cycle 3) and stars (cycle 4) indicate correlation peak values and peak times determined by spline interpolation.

(B) Polar plot displaying correlation of cycle 2 gene expression patterns with those of the corresponding points in the other cycles. Color scheme and symbols as in B. Adult time points (red circles) and start (0° in cycle 1; orange) are placed according to correlations in A and B, respectively.

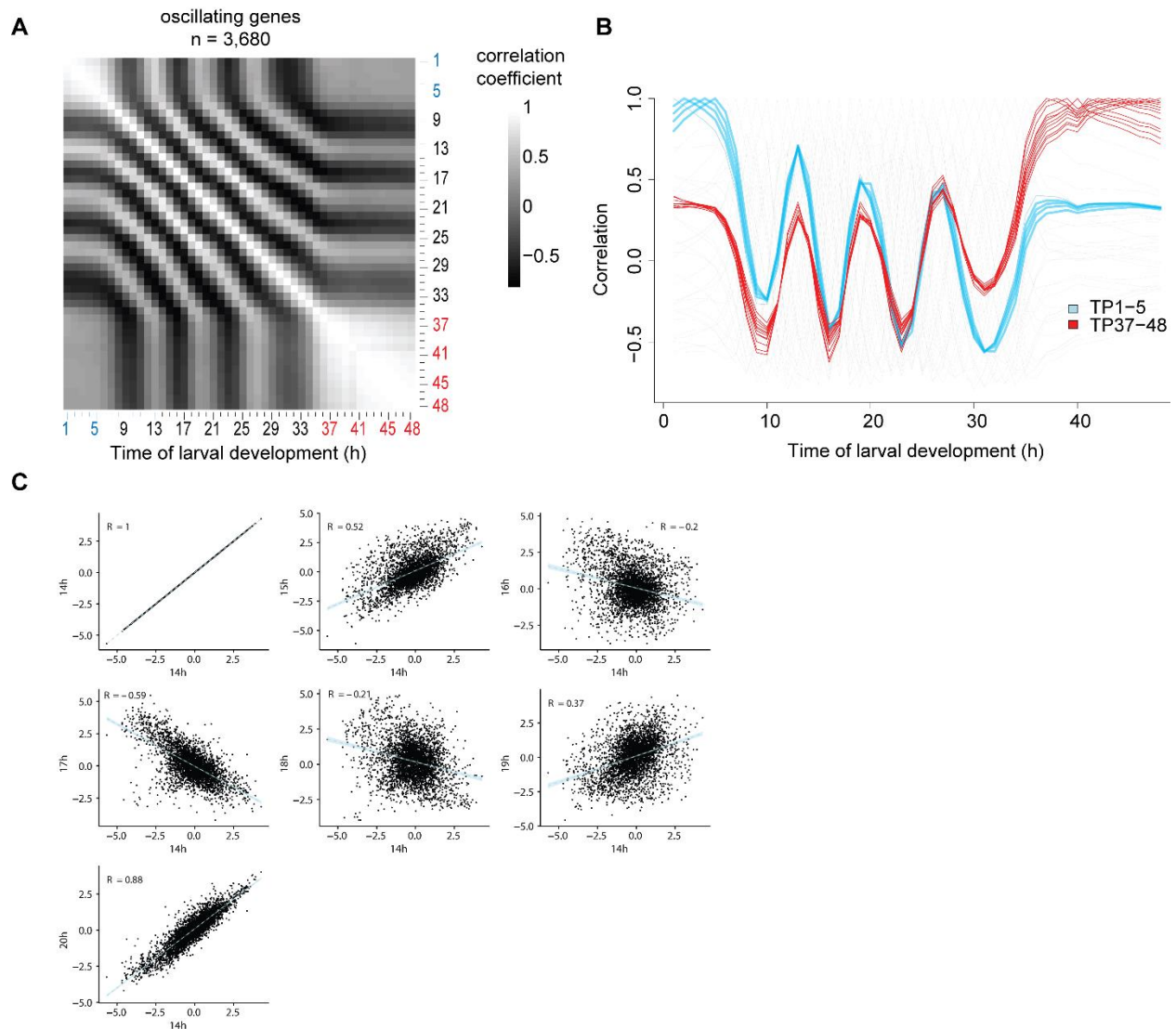


Fig. S9: Correlation analysis with mean normalized data yields qualitatively similar results to an analysis without mean normalization

(A) Pairwise correlation plot of log₂-transformed, mean normalized oscillating gene expression from the fused developmental time course (Fig 1C, n = 3,680).

(B) Correlation line plots reveal repetitive similarity of TP1 – 5 to TP13, TP19 and TP26/27. Due to mean normalization, the correlation lines oscillates around 0.

(C) Scatter plot comparing log₂-transformed, mean-normalized oscillating gene expression data of individual time points.

The Spearman correlation coefficient is indicated on the left corner and can range from anti-correlation (-1) to full correlation (+1).

Table S1. Related to Fig. 1 – Similar GO terms are enriched for the L1–YA developmental time course and the L3-YA time course

GO term enrichment for ‘GO biological process complete’ for the L1–YA developmental time course described here and the previously published L3–YA time course (Hendriks et al., 2014). Similar GO terms were enriched for both time courses.

Analysis Type:
Annotation Version and Release Date:

PANTHER
Overrepresentation Test
GO Ontology database

Released 2019-03-08
Released 2019-02-02

GO biological process complete	total # in GO	L1-YA time course				
		#	expected #	Fold Enrichment	p-value	FDR
cuticle development involved in collagen and cuticulin-based cuticle molting cycle	34	24	6.24	3.85	2.00E-06	9.79E-05
molting cycle, collagen and cuticulin-based cuticle	110	72	20.19	3.57	3.24E-15	6.89E-13
cuticle development	54	35	9.91	3.53	4.63E-08	3.21E-06
molting cycle	113	73	20.74	3.52	3.42E-15	7.04E-13
collagen and cuticulin-based cuticle development	50	31	9.18	3.38	5.43E-07	2.94E-05
negative regulation of endopeptidase activity	58	34	10.65	3.19	5.92E-07	3.18E-05
negative regulation of peptidase activity	69	39	12.67	3.08	1.35E-07	8.33E-06
negative regulation of proteolysis	71	39	13.03	2.99	2.24E-07	1.30E-05
extracellular matrix organization	59	32	10.83	2.95	3.35E-06	1.53E-04
extracellular structure organization	60	32	11.01	2.91	4.28E-06	1.91E-04
regulation of endopeptidase activity	67	34	12.3	2.76	5.54E-06	2.42E-04
regulation of peptidase activity	82	40	15.05	2.66	1.86E-06	9.18E-05
carboxylic acid transmembrane transport	46	22	8.44	2.61	5.49E-04	1.46E-02
organic acid transmembrane transport	46	22	8.44	2.61	5.49E-04	1.46E-02
aminoglycan metabolic process	63	30	11.57	2.59	6.72E-05	2.28E-03
negative regulation of hydrolase activity	85	39	15.6	2.5	8.26E-06	3.47E-04
alpha-amino acid biosynthetic process	59	27	10.83	2.49	2.37E-04	6.85E-03
endoplasmic reticulum unfolded protein response	57	26	10.46	2.48	3.37E-04	9.32E-03
innate immune response	220	100	40.39	2.48	1.40E-12	1.92E-10
immune response	222	100	40.75	2.45	1.81E-12	2.28E-10
immune system process	227	102	41.67	2.45	1.65E-12	2.17E-10
cellular amino acid biosynthetic process	63	28	11.57	2.42	2.22E-04	6.42E-03
organic acid transport	80	34	14.69	2.32	1.23E-04	3.92E-03
carboxylic acid transport	80	34	14.69	2.32	1.23E-04	3.90E-03
defense response	277	116	50.85	2.28	1.45E-12	1.94E-10
negative regulation of catalytic activity	111	46	20.38	2.26	1.14E-05	4.64E-04
cellular response to unfolded protein	70	29	12.85	2.26	4.35E-04	1.18E-02
fatty acid metabolic process	104	43	19.09	2.25	2.76E-05	1.01E-03
response to unfolded protein	74	30	13.58	2.21	5.53E-04	1.45E-02
carboxylic acid biosynthetic process	113	45	20.74	2.17	3.37E-05	1.22E-03
organic acid biosynthetic process	114	45	20.93	2.15	3.69E-05	1.32E-03
alpha-amino acid metabolic process	125	49	22.95	2.14	1.99E-05	7.57E-04
sulfur compound biosynthetic process	74	29	13.58	2.13	9.36E-04	2.34E-02
negative regulation of molecular function	123	47	22.58	2.08	4.47E-05	1.58E-03
organic anion transport	148	56	27.17	2.06	1.46E-05	5.86E-04
sodium ion transport	77	29	14.14	2.05	1.73E-03	3.93E-02
sulfur compound metabolic process	139	50	25.52	1.96	1.06E-04	3.41E-03
organic acid catabolic process	99	35	18.17	1.93	1.64E-03	3.77E-02
carboxylic acid catabolic process	99	35	18.17	1.93	1.64E-03	3.75E-02
lipid transport	94	33	17.26	1.91	2.00E-03	4.45E-02
regulation of proteolysis	145	50	26.62	1.88	2.17E-04	6.38E-03
lipid catabolic process	113	38	20.74	1.83	2.11E-03	4.59E-02
oxoacid metabolic process	380	126	69.76	1.81	3.59E-08	2.52E-06
monocarboxylic acid metabolic process	151	50	27.72	1.8	5.53E-04	1.45E-02
organic acid metabolic process	420	139	77.1	1.8	7.28E-09	6.41E-07
carboxylic acid metabolic process	345	112	63.33	1.77	4.25E-07	2.38E-05
cellular amino acid metabolic process	183	57	33.59	1.7	8.42E-04	2.12E-02
anion transport	245	75	44.98	1.67	1.77E-04	5.41E-03
lipid metabolic process	432	125	79.3	1.58	1.40E-05	5.63E-04
oxidation-reduction process	637	175	116.94	1.5	3.32E-06	1.53E-04
cellular lipid metabolic process	337	91	61.86	1.47	1.49E-03	3.46E-02
transmembrane transport	900	243	165.22	1.47	1.21E-07	7.60E-06
small molecule metabolic process	717	189	131.62	1.44	1.28E-05	5.18E-04
ion transport	698	167	128.14	1.3	2.17E-03	4.68E-02

*empty rows were present in L1-YA time course but not in L3-YA time course (Hendriks et al. 2014)

GO biological process complete	total # in GO	L3-YA time course (Hendriks et al, 2014)				
		#	expected #	Fold Enrichment	p-value	FDR
cuticle development involved in collagen and cuticulin-based cuticle molting cycle	34	22	4.52	4.87	1.21E-07	7.07E-06
molting cycle, collagen and cuticulin-based cuticle	110	67	14.62	4.58	2.33E-19	9.59E-17
cuticle development	54	30	7.18	4.18	9.14E-09	6.96E-07
molting cycle	113	68	15.01	4.53	2.03E-19	8.94E-17
collagen and cuticulin-based cuticle development	50	26	6.64	3.91	2.36E-07	1.15E-05
negative regulation of endopeptidase activity	58	29	7.71	3.76	9.26E-08	5.55E-06
negative regulation of peptidase activity	69	33	9.17	3.6	2.83E-08	1.92E-06
negative regulation of proteolysis	71	33	9.43	3.5	4.81E-08	3.06E-06
extracellular matrix organization	59	24	7.84	3.06	1.85E-05	6.42E-04
extracellular structure organization	60	24	7.97	3.01	2.31E-05	7.90E-04
regulation of endopeptidase activity	67	29	8.9	3.26	9.71E-07	4.13E-05
regulation of peptidase activity	82	34	10.9	3.12	2.61E-07	1.25E-05
carboxylic acid transmembrane transport	46	18	6.11	2.94	2.91E-04	8.04E-03
organic acid transmembrane transport	46	18	6.11	2.94	2.91E-04	8.01E-03
aminoglycan metabolic process	63	24	8.37	2.87	6.23E-05	2.02E-03
negative regulation of hydrolase activity	85	33	11.29	2.92	1.65E-06	6.87E-05
alpha-amino acid biosynthetic process*						
endoplasmic reticulum unfolded protein response	57	19	7.57	2.51	1.07E-03	2.42E-02
innate immune response	220	60	29.23	2.05	3.42E-06	1.35E-04
immune response	222	61	29.5	2.07	2.40E-06	9.73E-05
immune system process	227	62	30.16	2.06	2.04E-06	8.44E-05
cellular amino acid biosynthetic process*						
organic acid transport	80	25	10.63	2.35	6.12E-04	1.51E-02
carboxylic acid transport	80	25	10.63	2.35	6.12E-04	1.50E-02
defense response	277	71	36.81	1.93	3.01E-06	1.19E-04
negative regulation of catalytic activity	111	34	14.75	2.31	7.24E-05	2.30E-03
cellular response to unfolded protein*						
fatty acid metabolic process*						
response to unfolded protein*						
carboxylic acid biosynthetic process*						
organic acid biosynthetic process*						
alpha-amino acid metabolic process	125	33	16.61	1.99	1.07E-03	2.43E-02
sulfur compound biosynthetic process*						
negative regulation of molecular function	123	34	16.34	2.08	3.99E-04	1.07E-02
organic anion transport*						
sodium ion transport*						
sulfur compound metabolic process*						
organic acid catabolic process*						
carboxylic acid catabolic process*						
lipid transport*						
regulation of proteolysis	145	38	19.27	1.97	4.55E-04	1.16E-02
lipid catabolic process*						
oxoacid metabolic process	380	80	50.49	1.58	3.12E-04	8.51E-03
monocarboxylic acid metabolic process*						
organic acid metabolic process	420	94	55.81	1.68	1.11E-05	3.92E-04
carboxylic acid metabolic process*						
cellular amino acid metabolic process*						
anion transport*						
lipid metabolic process*						
oxidation-reduction process	637	131	84.64	1.55	1.02E-05	3.71E-04
cellular lipid metabolic process*						
transmembrane transport	900	166	119.59	1.39	1.14E-04	3.44E-03
small molecule metabolic process*						
ion transport*						
ecdysis, collagen and cuticulin-based cuticle	14	10	1.86	5.38	2.00E-04	5.76E-03
molting cycle process	14	10	1.86	5.38	2.00E-04	5.73E-03
chitin metabolic process	21	11	2.79	3.94	6.93E-04	1.69E-02
glucosamine-containing compound metabolic process	24	11	3.19	3.45	1.61E-03	3.44E-02
amino acid transmembrane transport	35	15	4.65	3.23	4.28E-04	1.10E-02
amino acid transport	45	16	5.98	2.68	1.90E-03	3.98E-02
carbohydrate derivative catabolic process	65	21	8.64	2.43	1.04E-03	2.39E-02
carbohydrate derivative metabolic process	476	95	63.25	1.5	4.56E-04	1.16E-02

Table S2. Related to Figure 3 - Larval developmental duration in single worm imaging experiments

Median durations of molts, intermolts and larval stage durations determined for single worm imaging reporter strains grown in microchambers at ~21°C ambient temperature.

Reporter	Larval stage	Median duration (h)
qua-1	I1	10
qua-1	I2	4.7
qua-1	I3	5

qua-1	I4	6.8
qua-1	M1	2.2
qua-1	M2	1.8
qua-1	M3	1.8
qua-1	M4	2.8
qua-1	L1	12.2
qua-1	L2	6.5
qua-1	L3	6.9
qua-1	L4	9.5
dpy-9	I1	10.2
dpy-9	I2	5.5
dpy-9	I3	5.6
dpy-9	I4	7.8
dpy-9	M1	2
dpy-9	M2	1.8
dpy-9	M3	2
dpy-9	M4	2.7
dpy-9	L1	12
dpy-9	L2	7.3
dpy-9	L3	7.7
dpy-9	L4	10.4
F11E6.3	I1	10.5
F11E6.3	I2	5
F11E6.3	I3	5.3
F11E6.3	I4	7.5
F11E6.3	M1	1.8
F11E6.3	M2	1.7
F11E6.3	M3	1.8
F11E6.3	M4	2.5
F11E6.3	L1	12.5
F11E6.3	L2	6.8
F11E6.3	L3	7.2
F11E6.3	L4	10

Table S3. Plasmids and primers used

Vector name	Backbone	Inserts	Primers	Primer sequence
pYPH0.14	pCFJ150	GFP::H2B::Pest	GFP-pest-H2B FW1 + Overhang	gcgtgtcaataatcactcGCTAGCATGTCTAGAC TTAGCCATGGC
			GFP-pest-H2B RV1 + Overhang	gccgatgaggagctcttattTACTTGCTGGAAGTG TACTTG
		Unc-54 3'UTR	Unc-54 3'UTR FW1 + Overhang	AGTACACTTCCAGCAAGTAAgataagagctcc gcatcg
			Unc-54 3'UTR RV1 + Overhang	Aacatatccagtcactatggaacagttatgtttggtatattggga
pYPH5	pYPH0.14	F11E6.3 promoter	F11E6.3 FW1 + Overhang	gcgtgtcaataatcactcaggaaaacctcaaattttgtaaacct
			F11E6.3 RV + Overhang	GCTAAGTCTAGACATcatggttacctaaaaatataaa gctct
pYPH69	pYPH0.14	dpy-9 promoter	dpy-9 promoter FW +OH to pYPH0.14	gcgtgtcaataatcactcgtacaatagaaaaaacgagcaat
			dpy-9 promoter RV +OH to pYPH0.14	CCATGGCTAAGTCTAGACATtctgcaataataa gtattgaaaacaaga
pYPH70	pYPH0.14	qua-1 promoter	qua-1 promoter FW +OH to pYPH0.14	gcgtgtcaataatcactcactatctttgactacacggag
			qua-1 promoter RV +OH to pYPH0.14	CCATGGCTAAGTCTAGACATcttaaatatagtt aagcatgataggat
pMM001	pCFJ150	luciferase::GFP	unc-54 3'UTR + overhang gfp	GCATGGATGAACTATACAAAgataagagctcc gcatcg
			gfp + overhang unc-54 3'UTR	gccgatgaggagctcttattTTTGTATAGTTCATCC ATGCC
			luc, piece2 + overhang piece 1	GACTACAAGgtaagtttaaacagttcggtactaactaac a
			luc, piece1 + overhang piece 2	ccgaactgttaaacctacCTTGTAGTCTTGGAG
			luc, piece1 + overhang NheI and backbone	tgtcaataatcactcGCTAGCATGGAGGACGCC AAGAA
pMM001	pCFJ150	Unc-54 3'UTR	gfp + overhang luc::spacer (piece2)	TACCGGTAGAAAAAATGAGTAAAGGAG AAGAACTTTTCACTGG
			luc::spacer (piece2) + overhang gfp	GTGAAAAGTTCTTCTCCTTTACTCATTTT TTCTACCGGTAC
pMM002	pMM001	eft-3 promoter	Peft-3 RV primer (OH to :luciferase)	ATGTTCTTGGCGTCTCCATtgagcaaagtgtt cccaac
			Peft-3 FW primer (OH to pCF150)	gcgtgtcaataatcactcGCACCTTTGGTCTTTTA TTGT

References:

Hashimshony, T., Feder, M., Levin, M., Hall, B.K., Yanai, I., 2015. Spatiotemporal transcriptomics reveals the evolutionary history of the endoderm germ layer. *Nature* 519, 219–222. <https://doi.org/10.1038/nature13996>

Hendriks, G.-J., Gaidatzis, D., Aeschmann, F., Großhans, H., 2014. Extensive oscillatory gene expression during *C. elegans* larval development. *Mol. Cell* 53, 380–392. <https://doi.org/10.1016/j.molcel.2013.12.013>

Lagido, C., Pettitt, J., Flett, A., Glover, L.A., 2008. Bridging the phenotypic gap: Real-time assessment of mitochondrial function and metabolism of the nematode *Caenorhabditis elegans*. *BMC Physiology* 8, 7. <https://doi.org/10.1186/1472-6793-8-7>

Olmedo, M., Geibel, M., Artal-Sanz, M., Merrow, M., 2015. A High-Throughput Method for the Analysis of Larval Developmental Phenotypes in *Caenorhabditis elegans*. *Genetics* 201, 443–448. <https://doi.org/10.1534/genetics.115.179242>

[end of manuscript]

2.2 Rhythmic transcription of oscillating genes results from rhythmic RNAPII occupancy

Milou Meeuse and Helge Grosshans conceived the project. MM performed the experiments, under HG's supervision. Sarah Carl and MM analyzed the data.

Our lab previously showed that oscillating mRNA levels are preceded by rhythmic pre-mRNA accumulation (Hendriks et al., 2014). However, sufficient intronic reads were detected for only ~30% of the genes that oscillate on the mRNA level and it remained possible that splicing is rhythmic. At least for a subset of genes, it seems likely that mRNA level oscillations arise from rhythmic transcription. Whether the remainder of transcript oscillation also result from rhythmic transcription and at which step of transcription this is regulated is unknown. Given that transcription can be regulated at the level of RNAPII recruitment, transcription initiation, pause release, elongation and termination, I aimed to investigate whether binding of RNA polymerase II (RNAPII) to the promoters of oscillating genes is rhythmic. To this end, we performed RNAPII chromatin immunoprecipitation coupled to sequencing (ChIP-seq) and total mRNA sequencing (mRNA-seq) on synchronized wild-type L1 larvae collected hourly from 22 hrs until 33 hrs after plating at 25°C. RNAPII ChIP-seq reads were quantified in a 1-kb window around the annotated transcription start site (TSS) serving as a proxy for temporal RNAPII promoter occupancy. We found rhythmic binding of RNAPII (**Figure 2.1**) at many of the promoters of genes previously assigned as oscillating (Meeuse et al., 2019), consistent with the idea that transcript level oscillations arise to a large extent from rhythmic transcription.

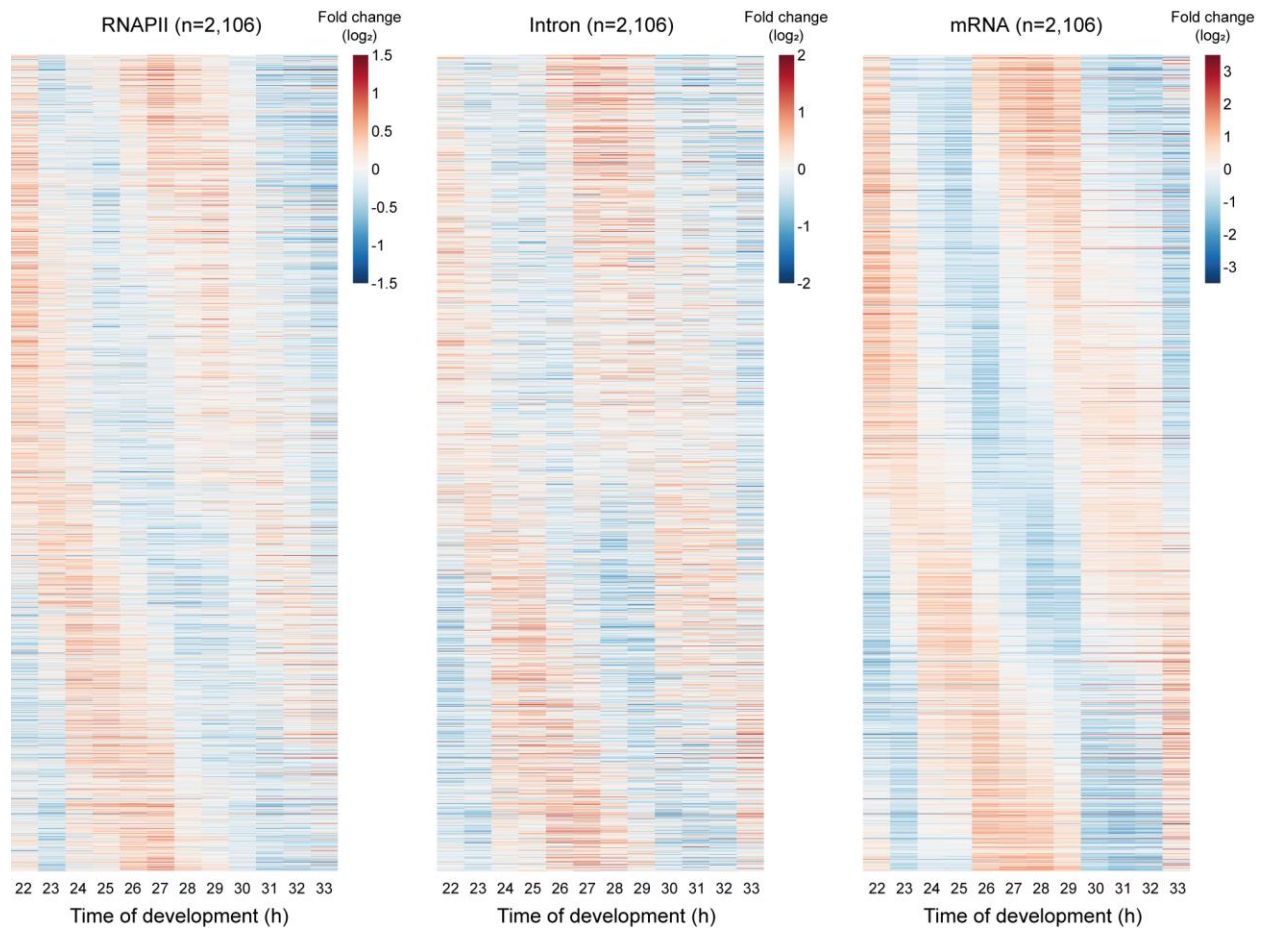


Figure 2.1: Rhythmic RNAPII occupancy at the transcription start site of oscillating genes

Heatmaps showing fold changes of RNA Polymerase II occupancy in a 1-kb window around the transcription start site (RNAPII), fold changes of intronic expression (introns) and fold changes of exonic expression (mRNA) of ‘high-confidence-oscillating’ genes (sufficiently expressed, $n=2,106$) sorted by phase as annotated previously (Meeuse et al., 2019). Synchronized wild-type L1 worms were grown at 25°C, sampled from 22 hrs until 33 hrs after plating, and followed by RNAPII ChIP-sequencing and total RNA-sequencing. Mean normalized \log_2 -transformed expression is shown.

2.3 Screening ‘oscillating’ transcription factors for their role in molting

Milou Meeuse and Helge Grosshans conceived the project. MM generated the strains, with help from Iskra Katic with the microinjections. MM performed and analyzed all the experiments, under HG’s supervision. Dimos Gaidatzis built the HSMM to automatically quantify stage durations.

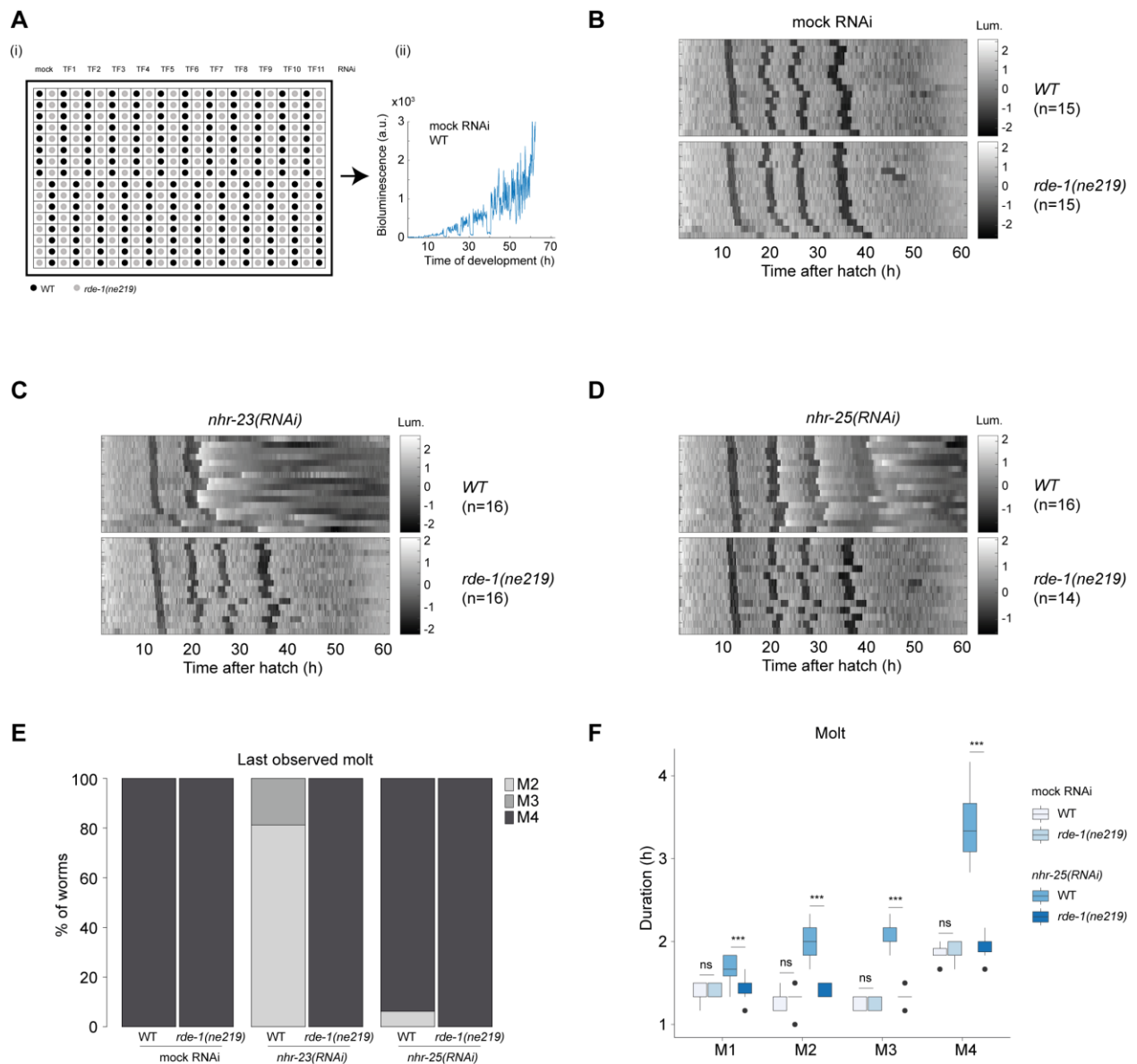
Given that our RNAPII ChIP-seq data suggests that mRNA level oscillations predominantly arise from rhythmic transcription, specifically at the level of RNAPII recruitment to the TSS, I aimed to investigate which transcription factors could regulate oscillatory gene expression. To this end, we performed an RNAi screen targeting the 92 transcription factors that oscillate themselves on the transcript level (based on our previous annotation (Hendriks et al., 2014)). Although quantification of transcript oscillations in transcription factor mutants by RNA-seq or transcriptional reporters might allow us to directly investigate the effects on oscillations globally or for a specific mRNA, respectively, they do not support high-throughput screening. Given that our quantitative analysis revealed that oscillations are tightly coupled to the molting cycles (Meeuse et al., 2019), we screened for aberrant progression or duration of developmental stages, including that of the molts.

2.3.1 RNAi screen set-up and validation

Developmental progression can be tracked at high temporal resolution, i.e. 10 minute intervals, by measuring luminescence in single worms expressing luciferase from a constitutive and ubiquitous promoter, when they are grown in the presence of D-luciferin, the substrate of luciferase (Meeuse et al., 2019; Olmedo et al., 2015) (**Figure 2.2A**). In short, the abrupt drop in luminescence during the lethargus, when larvae are in a quiescent state and do not feed, marks the entry of the molt. The subsequent sharp rise in luminescence due to resumption of feeding after animals escape from the old cuticle, characterizes the molt exit. These features allow the identification of molts during larval development and hence quantification of their duration. We cultured animals from the embryo stage until adulthood in a 384-well plate in liquid medium containing D-luciferin. Knock-down of 92 ‘oscillating’ transcription factors was achieved by feeding worms with HT115 bacteria carrying L4440 RNAi vectors. To control for effects that are unrelated to the knock-down of transcription factors, we performed the screen using a specific plate design (**Figure 2.2A**) and in a wildtype (WT) and an RNAi deficient strain (*rde-1(ne219)*). We confirmed that the WT and the RNAi-deficient strain developed with similar rates on mock RNAi (**Figure 2.2B,F,G,H**).

To validate that the RNAi deficient strain rescues the phenotype induced by RNAi in the WT strain, we used RNAi against *nhr-23* and *nhr-25*, two ‘oscillating’ transcription factors, which are known to be required for molting (Gissendanner and Sluder, 2000; Kostrouchova et al., 1998). To identify aberrant

molts, we visualized the luminescence traces of single animals in heatmaps, in which low luminescence levels correspond to dark grey and are characteristic for the molts (**Figure 2.2B,C,D**). *nhr-23(RNAi)* animals failed to complete development; only two molts were observed (**Figure 2.2C,E**). *nhr-25(RNAi)* revealed lengthening of molts and intermolts (**Figure 2.2D,F,G,H**). Both effects were completely rescued in the *rde-1(ne219)* background (**Figure 2.2C-H**), confirming that the assay works robustly. Given that RNAi by feeding is generally considered less potent compared to RNAi by microinjection, a disadvantage of our approach is that phenotypes might be weak or delayed in onset. Indeed, we observed that L1 and L2 stage were large unaffected by *nhr-23(RNAi)* and *nhr-25(RNAi)* (**Figure 2.2**).



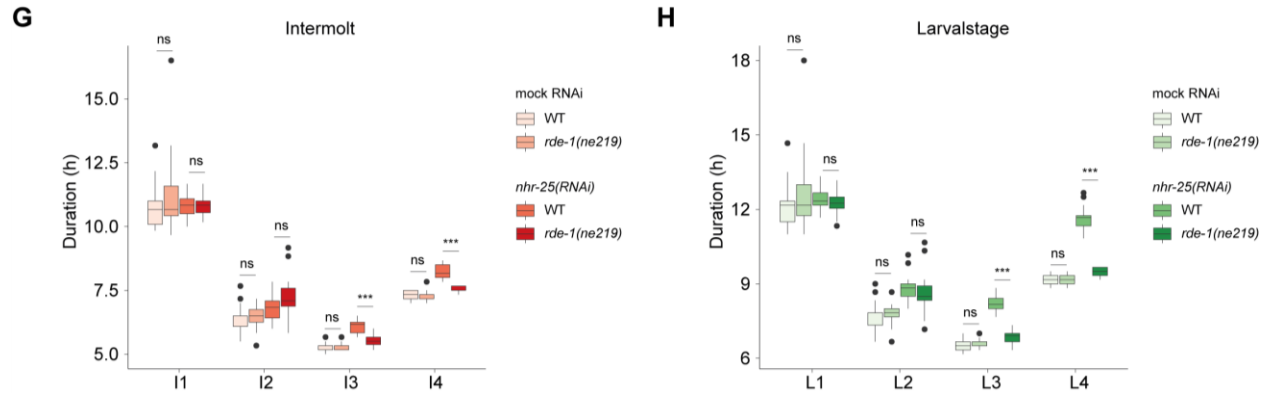


Figure 2.2: RNAi screen set-up and validation

A, (i) Schematic overview of the plate set-up of the screen. Two consecutive columns are filled with same RNAi condition. WT (in black) and RNAi deficient (*rde-1(ne219)*, in grey) animals alternate in blocks of 8 wells to avoid plate effects. (ii) Representative luminescence trace of a single WT animal on mock RNAi recorded for 72 hours. Sudden drop and subsequent rise in luminescence corresponds to molts.

B-D, Heatmaps showing trend-corrected luminescence (Lum) of WT (top) and RNAi deficient (*rde-1(ne219)*, bottom) animals expressing luciferase from the *eft-3* promoter. Single embryos were plated and cultured for 72 hrs in a temperature controlled incubator. RNAi was achieved by feeding on HT115 bacteria with L4440 vector for mock RNAi (B), *nhr-23(RNAi)* (C), and *nhr-25(RNAi)* (D). One horizontal line represents one animal. Hatch is set to $t = 0$ hours and traces are sorted by entry into the first molt. Black corresponds to low luminescence and is associated with the molt.

E, Quantification of percentage of animals in last observed molt for mock RNAi, *nhr-23(RNAi)*, and *nhr-25(RNAi)* in WT and RNAi deficient animals (*rde-1(ne219)*). Number of animals in each conditions as indicated in B-D.

F-H, Quantification of molt (F), intermolt (G) and larval stage (H) durations in WT and RNAi deficient (*rde-1(ne219)*) animals that make 4 molts grown in the presence of mock RNAi ($n=15$ and $n=15$ in WT and *rde-1(ne219)* respectively), and *nhr-25(RNAi)* ($n=16$ and $n=14$ in WT and *rde-1(ne219)* respectively). Boxes extend from first to third quartile, horizontal line indicates the median and dots indicate outliers. Significant differences between WT and *rde-1(ne219)* are indicated for each RNAi condition (** $p < 0.001$, ns: not significant, Welch two sample t-test).

2.3.2 Identification of transcription factors with strong molting phenotypes

By visual inspection of the heatmaps of the RNAi screen, we could readily identify *blmp-1*, *bed-3*, *grh-1* and *myrf-1*, and confirm *nhr-23*, *nhr-25*, which all revealed strong defects in molt progression or molt duration (**GRH-1 manuscript**). Further characterization of *blmp-1*, *grh-1* and *myrf-1*, *nhr-23*, and *nhr-25* will be discussed in **section 2.5**.

However, small differences in stage durations could not be identified by visual inspection of the heatmaps. Hence, I aimed to accurately quantify the durations of developmental stages for each of the RNAi conditions to identify subtle molting phenotypes. To this end, we exploited a method for the automatic annotation of molts in luciferase traces, which is described in further detail in the next section.

2.3.3 A Hidden Semi Markov Model to annotate molting in luciferase traces

To quantify the duration of developmental stages from the luciferase data, we annotated the molts in the luminescence traces using a Hidden Semi Markov Model (HSMM). The basis of a HSMM is a Markov Model, with some extensions that we will discuss below. A Markov Model is a stochastic model that describes a Markov Chain (**Figure 2.3A**) (tutorial Rabiner, 1989), i.e. a series of states for which the probability of each state depends only on the previous state. Thus, a Markov Model allows to make predictions about the future state based on the current state. The transitions between the states are described by transition probabilities, the probability of moving from state 1 to state 2 (a_{12}), but also the probability of staying in state 1 (a_{11}).

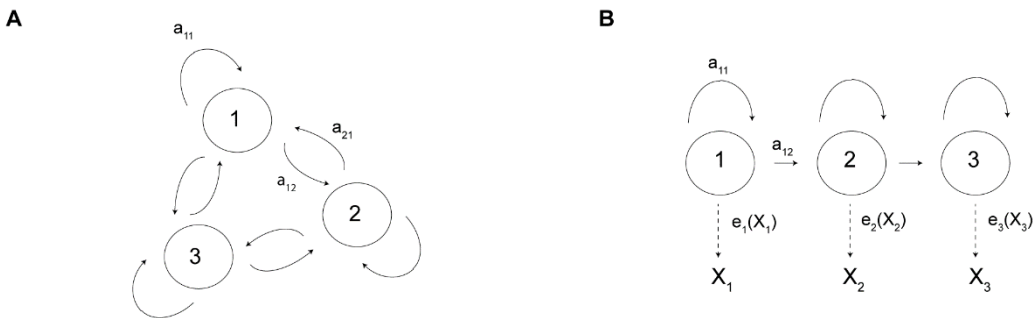
In a Hidden Markov Model, the states 1, 2, and 3 are invisible, or hidden (tutorial Rabiner, 1989). Instead, the stochastic observations or measurements X_1 , X_2 , and X_3 , which are influenced by the states are visible (**Figure 2.3B**), i.e. they are 'emitted'. The probability of observing X_n is described by an 'emission' probability distribution, $e(X_n)$. Similar to the Markov Model, a limitation of the Hidden Markov Model is that the chance to be in the same state is represented by a constant probability, e.g. a_{11} . The probability at a given time does not change depending on the time elapsed since entering that state ($a_{11, t=n} = a_{11, t=n+1}$). Thus, the overall probability to stay within a state over multiple consecutive time points decreases exponentially with time (a_{11}^t , $t = \text{time}$ and $0 < a < 1$). However, the state duration of processes is often better described using other distributions, e.g. a normal or poisson distribution.

A Hidden Semi Markov Model circumvents this limitation (reviewed in Yu, 2010). In contrast to a constant probability, the state duration (D) is described by a probability distribution, $p(D)$ (**Figure 2.3C**). The probability distribution describes how the probability of being in the current state changes over the time that passed from the moment of going into that state. Here, we used an HSMM to find the most likely sequence of states, i.e. the developmental stages, given the observed data, i.e. the luminescence levels (**Figure 2.3C**). In other words, we annotated the molts and intermolts in the luminescence traces, using a HSMM.

We determined the parameters of the HSMM by evaluating the performance of the model on a set of luminescence traces obtained from WT animals, before applying the model to the traces of RNAi-treated animals. In principle, the parameters of the duration probability distribution describe how likely it is to find a molt with a certain duration. Since we were interested in finding subtle differences that we could not readily identify from the heatmaps, we designed the distributions in such a way that small changes in

stage durations between mutants and wildtype are much more likely than big changes, which rapidly decay to zero.

Once our HSMM annotated the molts and the intermolts in the luciferase traces, we aimed to confirm that the developmental stages were reliably identified. To this end, we aligned the luminescence traces with the HSMM-based annotation to a single reference trace which we annotated manually using the graphical user interface as described before (Meeuse et al., 2019). If molts were to be annotated correctly by the HSMM (**Figure 2.4A**, RNAi trace 1), the low luminescence intensities corresponding to the molts would align with those of the reference trace. Hence, the dark intensities would fall in vertical columns, set by the alignment boundaries. However, if a molt is extended too much, i.e. the probability of the duration is zero or close to zero, the model annotates a ‘molt’ that is shorter than the actual molt (**Figure 2.4A**, RNAi trace 2, molt 4). As a result, after the alignment, the luminescence intensities of the actual molt fall outside of the alignment boundaries. Thus, the molt duration is longer than the parameters of the model allow. Indeed, hatch and molts fall in vertical columns for animals treated with mock RNAi (**Figure 2.4B**). In contrast, molt 4 of *nhr-25(RNAi)* failed to align, as L4 duration was extended more than the probability distribution permitted (**Figure 2.4C**). Likewise, the genes we identified at first instance (**GRH-1 manuscript**), i.e. by visual inspection of the heatmap, failed to align (data not shown) and were omitted from the analysis. Given that we specifically aimed to quantify more subtle changes and designed the probability distributions of the HSMM according to this, these observations were not unexpected.



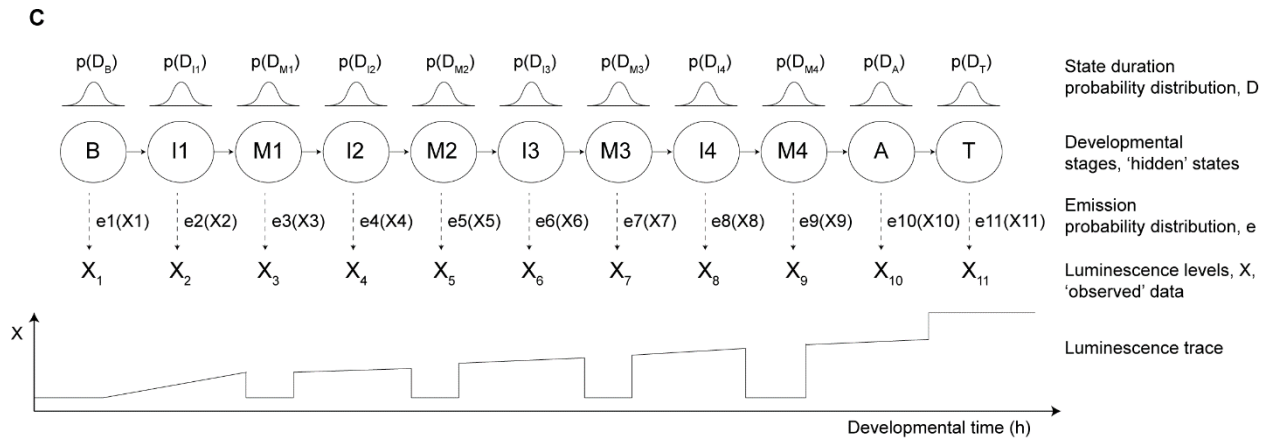


Figure 2.3: The Markov Model and its extensions

A, Example of a Markov Chain. States (1, 2, 3) and state transition probabilities (a_{11} , a_{12} , a_{21}) are indicated.

B, Example of a Hidden Markov Model. Hidden states (1, 2, 3), observations (X_1 , X_2 , X_3), state transition probabilities (a_{11} , a_{12}) and emission probabilities (e_1 , e_2 , e_3) are indicated. Emission probabilities are described by a probability distribution, which is a function of X .

C, Hidden Semi Markov Model describing the developmental stages as hidden states, and the luminescence traces as observations. Before hatch (B), intermolt n (In, with $n=1,2,3,4$), molt n (Mn, with $n=1,2,3,4$), adults (A) and an arbitrary terminal state (T) are indicated. State duration probability distributions $p(D_n)$ are described with a Poisson-shift distribution and emission probability distributions are described with a normal distribution.

Based on (Hayashi et al., 2017)

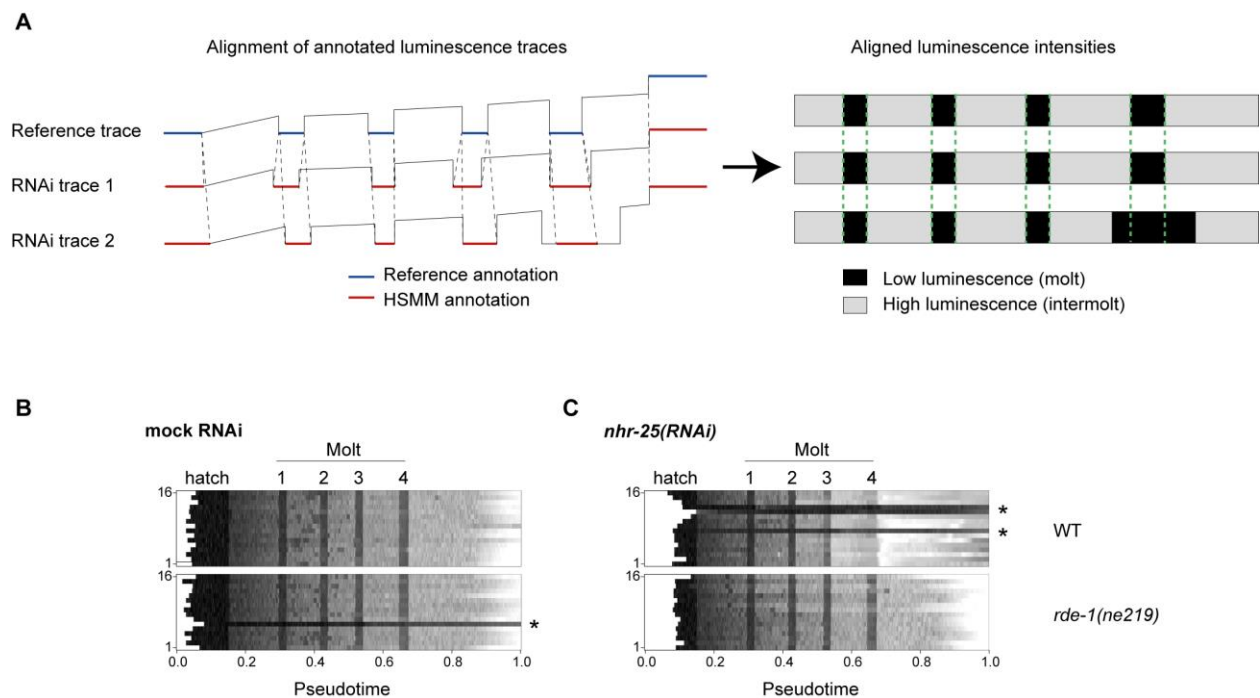


Figure 2.4: HSMM allows annotation of molts in luciferase traces

A, Cartoon of alignment of HSMM-annotated (red) luminescence traces to manually annotated (blue) reference trace (left). Cartoon of aligned luminescence intensities (right), in which black corresponds to low luminescence (molt) and grey high luminescence (intermolt). Alignment boundaries are indicated with green dashed lines.

B-C, Heatmaps of luminescence traces of mock RNAi (B) and *nhr-25(RNAi)* (C) in WT and RNAi deficient (*rde-1(ne219)*) animals aligned to reference trace. One horizontal line represents one animal. Dark grey corresponds to low luminescence and is associated with the hatch and molts respectively. Wells without a developing animals are indicated with *. Note that alignment works reliably in mock RNAi for both strain and *nhr-25(RNAi)* in (*rde-1(ne219)*) animals, but not in *nhr-25(RNAi)* in WT animals.

2.3.4 *ztf-6(RNAi)* reveals lengthening of intermolts

To identify transcription factors whose depletion caused subtle phenotypes, we quantified the durations of developmental stages and plotted the directed p-value in \log_{10} in a heatmap (**Figure 2.5A**). Hierarchical clustering of the directed p-values for each gene revealed no consistent lengthening or shortening of development over time. Moreover, mock RNAi conditions did not cluster together, suggesting that the differences we observed represent the variability in the data independent of transcription factor knock-down. We reasoned that RNAi effects might become visible only in later stages. To test this notion, we quantified the duration of L3 and L4 together (**Figure 2.5B**). We observed lengthening of L3-L4 in 'WBGene00012317', which corresponds to *ztf-6*, a transcription factor implicated in the control of dopaminergic neuron production (Doitsidou et al., 2018). Using manual annotation of the molts (as described in methods of (Meeuse et al., 2019)), we confirmed that I3 and I4, but not M3 and M4 are extended in *ztf-6(RNAi)* (**Figure 2.5C,D**). Thus, the method we present here reliably identified more subtle changes in stage durations and identified, besides *blmp-1*, *bed-3*, *grh-1*, *myrf-1*, *nhr-23*, and *nhr-25*, the zinc finger transcription factor *ztf-6* as a factor required for normal duration of intermolts.

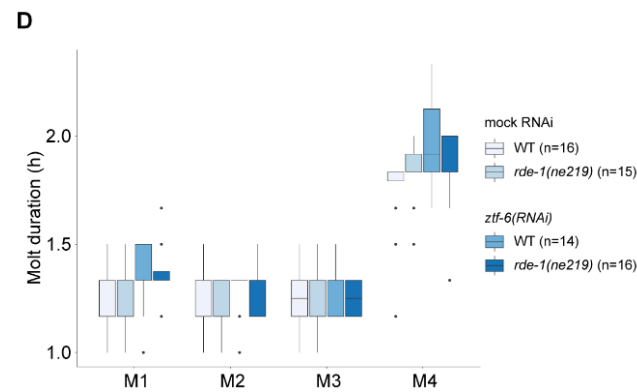
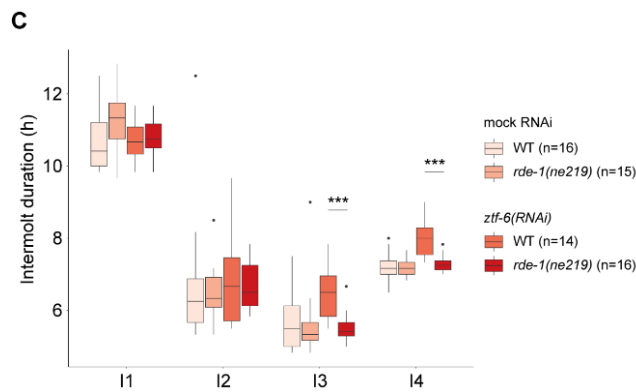
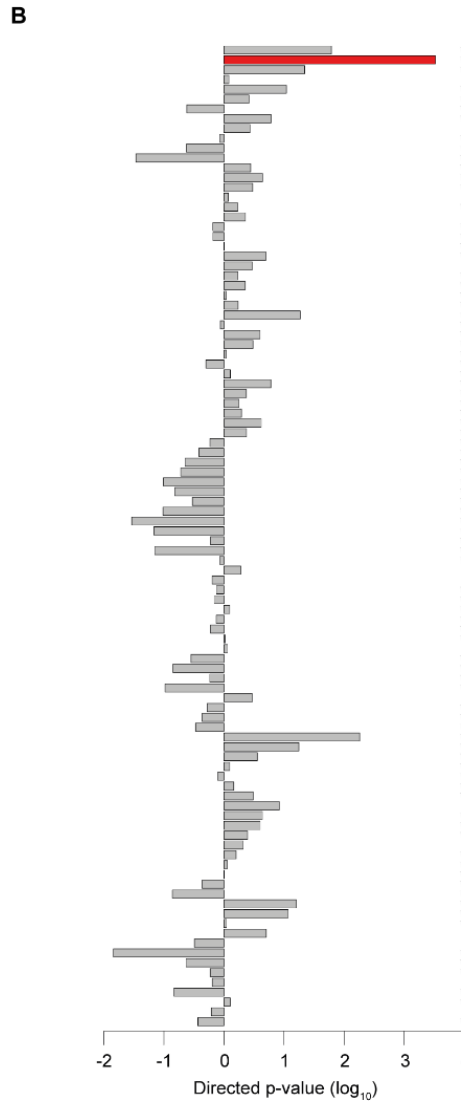
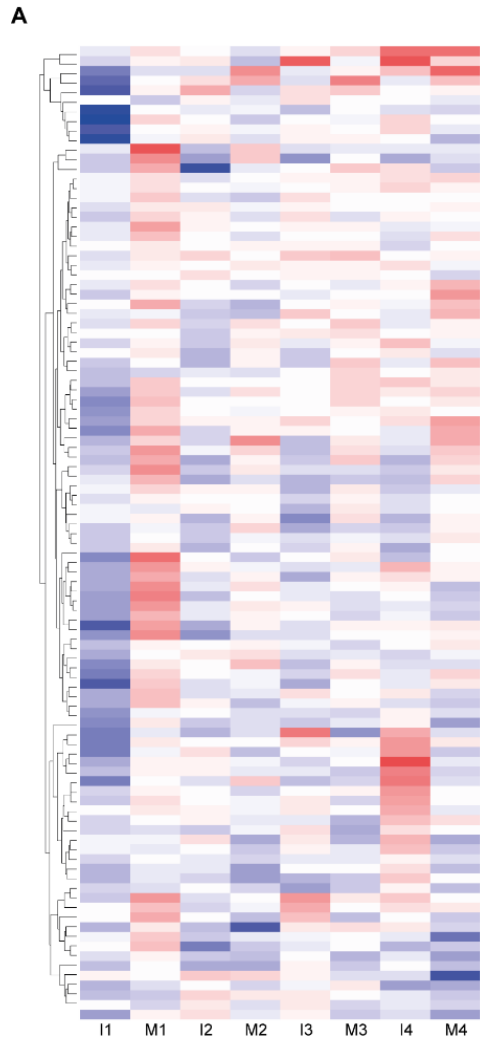


Figure 2.5: HSMM-based identification of subtle *ztf-6(RNAi)* phenotype

A, Heatmap of directed \log_{10} – transformed p-value of each developmental stage in WT animals relative to RNAi deficient animals. Red corresponds to lengthening and blue corresponds to shortening of developmental stages. Data is hierarchically clustered over developmental time. P-values are obtained by a paired t-test.

B, Barplot of directed \log_{10} – transformed p-value of L3-L4 stage in WT animals relative to RNAi deficient animals. Data is sorted as in B. Red bar indicates significant lengthened L3-L4 stage in *ztf-6(RNAi)*. P-values are obtained by a paired t-test.

C-D, Quantification of intermolt (C) and molt (D) in WT and RNAi deficient (*rde-1(ne219)*) animals in the presence of mock RNAi, and *ztf-6(RNAi)*. Boxes extend from first to third quartile, horizontal line indicates the median and dots indicate outliers. Significant differences between WT and *rde-1(ne219)* are indicated (***) $p < 0.001$, ns: not significant, Welch two sample t-test).

2.4 Manuscript: Control of oscillatory gene expression and molting through the transcription factor GRH-1

Kathrin Braun imaged the N2 molt. Anca Neagu generated the SWI strains and dissected the grh-1 promoter. MM performed the experiments and analyzed all the data. Michael Stadler conceived the differential expression analysis. HG and MM conceived the project and wrote the manuscript.

Control of oscillatory gene expression and molting through the Grainyhead/LSF transcription factor GRH-1

Authors: Milou W.M. Meeuse^{1,2}, Michael Stadler^{1,3}, Kathrin Braun¹, Anca Neagu¹, Helge Großhans^{1,2,4}

Affiliations: ¹ Friedrich Miescher Institute for Biomedical Research (FMI), Maulbeerstrasse 66, CH-4058 Basel

² University of Basel, Petersplatz 1, CH-4001 Basel

³ Swiss Institute for Bioinformatics, Basel

⁴ Correspondence to: helge.grosshans@fmi.ch

Abstract

Molting is a recurring process of cuticle synthesis and shedding in nematodes. As a cyclical process, it appears tightly coupled to massive gene expression oscillations seen for thousands of genes in *C. elegans*. However, specific transcriptional molting programs and mechanisms of their presumed rhythmic execution are unknown. Here, we identified the Grainyhead/LSF protein GRH-1 as a transcription factor important for molting and gene expression oscillations in *C. elegans*. Oscillatory activity of GRH-1 is required for proper rhythmic expression of a large group of oscillating genes encoding various structural components of the cuticle and ECM regulators as well as other factors including GRH-1 itself. Hence, in the absence of GRH-1, a timely completion of the molt fails and the integrity of the cuticle is compromised to the extent that the cuticle ruptures and animals die. These results identify GRH-1 as a key factor for molting programs and a putative component of the *C. elegans* developmental oscillator. Thus, they provide a basis for further dissection of the oscillator's architecture and molecular as well as developmental function.

Introduction

Various repetitive developmental processes, such as somitogenesis in vertebrates and branching of lateral roots in plants, are driven by gene expression oscillations. An extreme case is observed in *C. elegans* larvae, where ~3700 genes produce transcripts undergoing >2-fold changes from peak to trough levels (Meeuse et al., 2019). Mechanistically, mRNA level oscillations in *C. elegans* appear to arise from rhythmic transcription, as pre-mRNA expression patterns oscillate and precede rhythmic mRNA accumulation at the global level (Hendriks et al., 2014). 92 transcription factors were found to oscillate on the mRNA level (Hendriks et al., 2014). However, whether and how these transcription factors drive oscillatory gene expression in *C. elegans* remains to be determined.

Oscillations peak once during each of the four larval stages, L1 – L4, but peak-phases are widely distributed (Hendriks et al., 2014; Meeuse et al., 2019), suggesting a role of oscillations in diverse processes. Notably, however, oscillations appear tightly coupled to the molting cycle (Meeuse et al., 2019), exhibiting phase locking to all four molts, M1 – M4 despite variations in the duration of the individual larval stages. Hence, it seems likely that the developmental ‘oscillator’ in *C. elegans* serves to time molting and potentially other developmental processes.

Molting is fundamental to the development of *C. elegans* and indeed nematodes more generally. Nonetheless, the molecular mechanisms that control molting are poorly understood. *C. elegans* molting is characterized by a period of behavioral quiescence (lethargus) in which the exoskeleton, called the cuticle, is renewed. The *C. elegans* cuticle is a multi-layered extracellular matrix (ECM) consisting of protein, lipids and carbohydrates. The predominant class of structural proteins are collagens, which are produced by the underlying epidermis, also referred to as hypodermis. The cuticular collagens are encoded by ~170 genes and previous global analysis revealed their enrichment among oscillating genes (Hendriks et al., 2014). Before cuticle synthesis, connections between the old cuticle and the underlying epidermis are severed, first at the head and tail region and later at the central body, a phase called apolysis (Singh and Sulston, 1978). Following synthesis of the new cuticle, the old cuticle is removed. In a process termed ecdysis, animals undergo a series of stereotypic movements, i.e. rotating around the body axis and spontaneous back-and-forth motions. Breakage of the cuticle occurs at the head region, after which the worm escapes from the old cuticle and resumes feeding (Singh and Sulston, 1978). Although one would postulate that specific transcriptional programs play a role in timing and coordination of ECM remodeling, only a few transcription factors have been implicated in molting (Frand et al., 2005; Gissendanner and Sluder, 2000; Gissendanner et al., 2004; Kostrouchova et al., 1998; Russel et al., 2011) and the molecular programs that they control, and thus the molecular architecture that drives molting remains largely unexplored.

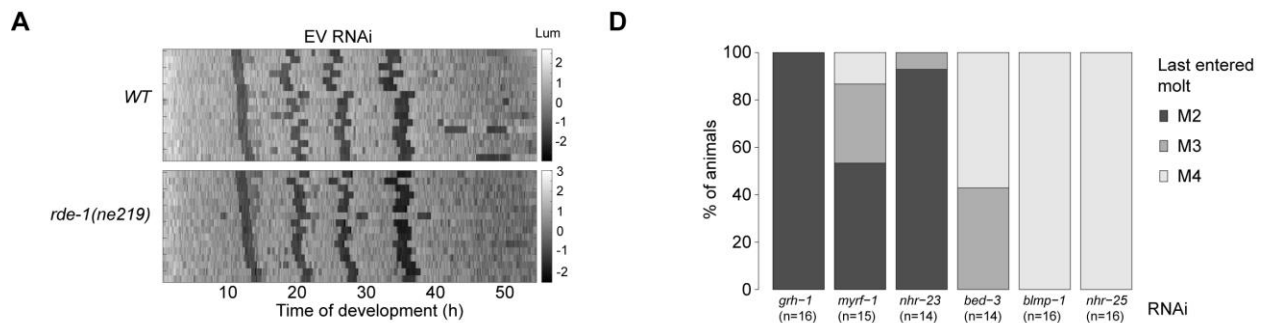
Here, we screened ‘oscillating’ transcription factors for their role in molting and we report the identification and characterization of a putative component of the *C. elegans* oscillator. Our characterization reveals that GRH-1, the sole *C. elegans* member of the conserved LSF/Grainyhead transcription factor family, is essential for the integrity of the cuticle. The majority of the genes affected by depletion of GRH-1 are oscillating genes, among them numerous structural components of the cuticle and ECM regulators. We find that rhythmic activity of GRH-1 is required not only for completion of the molt as such but also for its duration, suggesting an important role in epidermal remodeling. A negative transcriptional feedback loop controls rhythmic accumulation of GRH-1, a hallmark of an oscillator. Hence, our finding that GRH-1 is a key factor for the molting cycle and a potential oscillator component, will facilitate the characterization of the network that drives molting and oscillatory gene expression in *C. elegans*. Moreover, as *Drosophila* Grainyhead and the three mammalian Grainyhead-like factors (Grhl) play major roles in epithelial development and maintenance (Almeida and Bray, 2005; Boglev et al., 2011; Bray and Kafatos, 1991; Hemphälä et al., 2003; Lee and Adler, 2004; Rifat et al., 2010; Wilanowski et al., 2002; Yu et al., 2006), a phylogenetically conserved role of Grainyhead transcription factors in providing temporal coordination to epidermal programs seems possible.

Results

*Identification of *grh-1* in an RNAi screen for ‘oscillating’ transcription factors that affect molting*

Our previous study hinted towards rhythmic transcription as the predominant driver of mRNA transcript oscillations during larval development (Hendriks et al., 2014). To find transcription factors that drive oscillatory gene expression, we performed an RNAi screen targeting 92 transcription factors that exhibit oscillatory mRNA levels, according to our previous annotation (Hendriks et al., 2014). Given that our previous study revealed a tight coupling between gene expression oscillations and molting cycles (Meeuse et al., 2019), we screened for mutants with aberrant duration or progression of molting. To obtain such information, we examined luciferase activity in animals that express a luciferase transgene and are grown in the presence of D-luciferin (Meeuse et al., 2019; Olmedo et al., 2015). This assay detects, at the level of individual animals, periods of reduced feeding, related to the molts, by a drop in luminescence. We depleted 92 transcription factors by feeding animals on RNAi-expressing bacteria. To control for differences in larval growth among RNAi conditions unrelated to target protein depletion, we performed the experiment in parallel on RNAi deficient (*rde-1(ne219)*) animals (**Figure 1A**).

To detect mutants with aberrant molting, we plotted the luminescence intensities sorted by entry into the first molt in a heatmap (**Figure 1B,C**). Thus, we identified six genes of which the depletion caused abnormal progression through development following atypical molts (*nhr-23*, *myrf-1* and *grh-1*) (**Figure 1B,C, Figure S1**), or aberrant duration of molts (*blmp-1*, *bed-3* and *nhr-25*) (**Figure 1B,C,D, Figure S2**). In the remainder of this paper, we focus on validating and characterizing a role of one of these, *grh-1*, in regulating oscillatory gene expression.



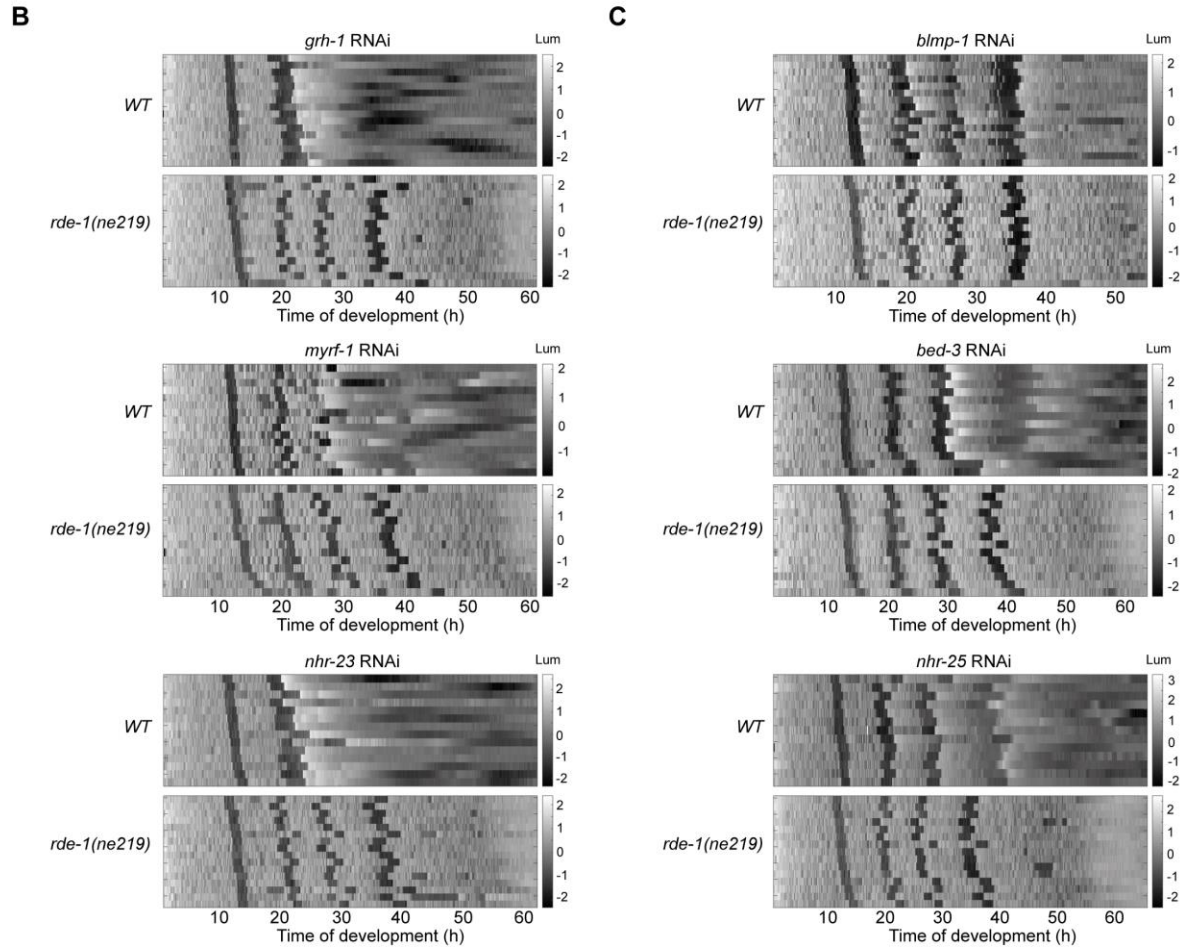


Figure 1: RNAi screen for ‘oscillating’ transcription factors revealed aberrant duration or progression of molting

A, Heatmap showing trend-corrected luminescence (Lum) of wild-type (WT, top) and RNAi-deficient (*rde-1(ne219)*, bottom) animals expressing luciferase from the *eft-3* promoter grown on mock (empty vector) RNAi in a temperature-controlled incubator set to 20 °C. Each line represents one animal. Hatch is set to $t = 0$ hours and traces are sorted by entry into the first molt. Darker color corresponds to low luminescence and is associated with the molt.

B, Heatmap showing trend-corrected luminescence (Lum) as in A, for indicated RNAi conditions causing cessation of development.

C, Heatmap showing trend-corrected luminescence (Lum) as in A, for RNAi indicated conditions causing extension of molt duration.

D, Quantification of the percentage of animals in last molt that they entered on indicated RNAi conditions in wildtype animals.

Loss of GRH-1 causes cuticle rupturing at the head during ecdysis

We aimed to validate our findings of the RNAi screen using an independent approach. Since *grh-1(0)* mutants died as embryos (data not shown), we used the auxin inducible degradation (AID) system (Zhang

et al., 2015) to degrade GRH-1 rapidly and conditionally. To this end, we tagged *grh-1* endogenously with *degron::3xflag* to generate allele *grh-1(xe135)*, and expressed the plant specific F-box protein TIR-1 as a transgene. In the presence of the plant hormone auxin, we observed rapid degradation of GRH-1, as shown below (**Figure S9A**). When we plated synchronized L1 *grh-1::aid::3xflag* animals on auxin-containing plates, we observed a lethality phenotype at the end of the first molt. The lethality was fully penetrant for high auxin concentrations (≥ 400 nM), and decreased in a dose-dependent manner (**Figure S3A**). At concentrations ≥ 1 mM, addition of auxin caused non-specific defects, independent of the presence of a degron on GRH-1 (**Figure S3B,C**).

To investigate the lethality during the molt in more detail, we first imaged molting in wild-type animals. We used time-lapse DIC imaging on L1 animals placed on an agar pad in a drop of M9, which allowed them to move. We could readily identify loosened cuticles at the tip of the head (**Figure S4**), indicating that apolysis occurred. After loosening the cuticle around the tip of the head, animals made spontaneous back-and-forth movements and the pharynx contracted rapidly (**Figure S4**). We observed animals in which the pharyngeal lining broke and the mouth plug was expelled before the animals escaped from the cuticle (**Figure S4A**), and animals in which the cuticle broke first and the pharyngeal lining with the mouth plug was expelled afterwards (**Figure S4B**). Our live imaging observations are consistent with previous observations (Singh and Sulston, 1978).

As observed in wild-type animals, loosening of the cuticle in the head region (**Figure 2A**) was followed by rapid back-and forth movements in animals depleted of GRH-1 (**Figure 2B**). However, the cuticle became looser and inflated in the head region (**Figure 2C**) and vesicles started to appear in the cavity underneath the loosened cuticle (**Figure 2D**). Finally, the cuticle broke in the head region and the underlying tissue was extruded (**Figure 2E,F**). The process from loosened cuticle until rupturing of the cuticle took roughly 5 to 10 minutes. We conclude that depletion of GRH-1 during L1 impairs the integrity of the newly forming cuticle.

GRH-1 phenotype occurs every larval stage

We wondered whether this phenotype was specific to L1. To test whether we could induce lethality and molting defects in every larval stage, we depleted GRH-1 by addition of auxin at the beginning of each larval stage and investigated the appearance of larval death using the luciferase assay (**Figure 2G,H,I,J**). Indeed, we observed lethality in M1, M2, M3 and M4, when auxin was present in L1, L2, L3 and L4 stage respectively. In conclusion, activity of GRH-1 is repetitively required for normal completion of molts.

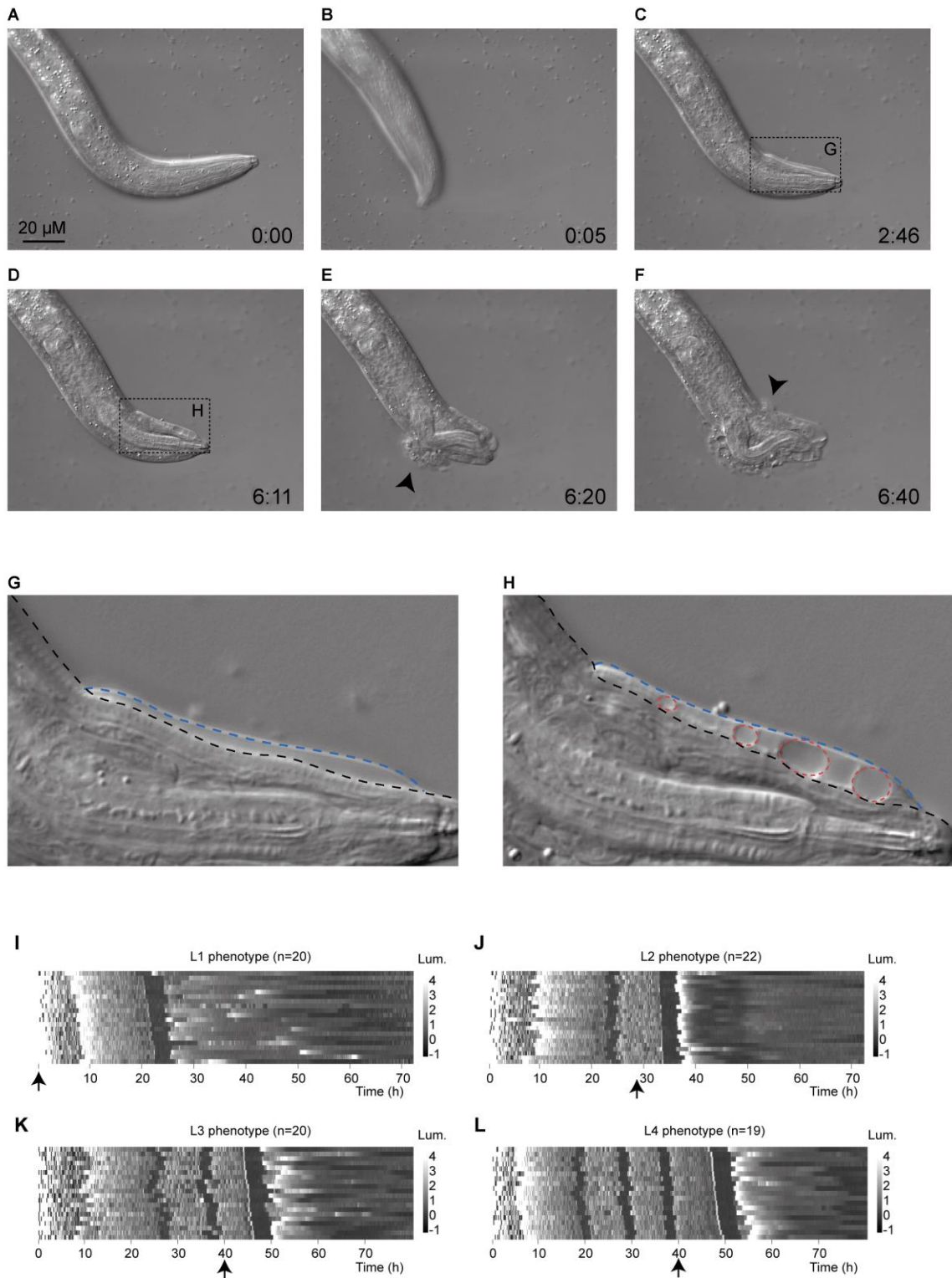


Figure 2: GRH-1 degradation leads to rupturing of the cuticle in the head region in M1 and subsequent molts

A-F, Image sequence of L1 synchronized *grh-1(xe135); pef-3::tir-1* animal (HW2418) plated on 250 μ M auxin-containing plates, grown at 20°C. Animals were transferred to an agar-pad containing microscopy slide and images were collected every 1 sec, using DIC, 100x magnification. Selected images are shown. Time stamp (min:sec) is

indicated. Arrows indicate phenotypic features: A. Loosening of the cuticle, B. Back-and-forth movements, C. Inflation of the cuticle, D. Vesicles underneath loosened cuticle, E and F. Rupturing of the cuticle.

G-H, Zoom in of C and D.

I-L, Heatmap showing trend-corrected luminescence (Lum) of *grh-1(xe135); peft-3::luc; peft-3::tir-1* animals (HW2434). L1 (I), L2 (J), L3 (K) and L4 (L) phenotypes are shown. $t = 0\text{h}$ corresponds to time of plating. Arrow indicates time point when 250 μM auxin was added at the beginning of each larval stage. Note that in L1, auxin was present at $t=0\text{h}$, before animals hatched.

GRH-1 protein levels oscillate and peak shortly before molt entry

Since GRH-1 seemed to be required for proper execution of recurring molts, and its mRNA levels oscillate (Hendriks et al., 2014; Meeuse et al., 2019), we wondered whether GRH-1 protein accumulation is also rhythmic. To this end, we sampled a synchronized population of animals expressing endogenously 3xFLAG-tagged GRH-1 (*grh-1(xe135)*), from M1 until M2. A qualitative analysis using western blotting revealed oscillatory accumulation of GRH-1 protein with its peak shortly before molt entry (**Figure 3A**).

Next, we performed time-lapse microscopy of single animals grown in micro-chambers as described previously (Meeuse et al., 2019), to investigate the GRH-1 levels in single animals and with high temporal resolution. By acquiring in parallel fluorescence and bright-field images, we could simultaneously quantify GRH-1::GFP level changes and developmental progression for the same animal to relate GRH-1 peak levels more accurately to the time of molting. As GFP intensities did not suffice for quantification using our previously published pipeline (Meeuse et al., 2019), we manually selected hypodermal cells and quantified the maximum intensity (**Figure 3B,C, Figure S6**). Although GRH-1 levels fall during the trough below the level of detection, preventing amplitude quantification, these data clearly reveal that GRH-1 accumulation peaks before molt entry (**Figure 3B,C, Figure S6**), confirming the western blot analysis (**Figure 3A**).

A



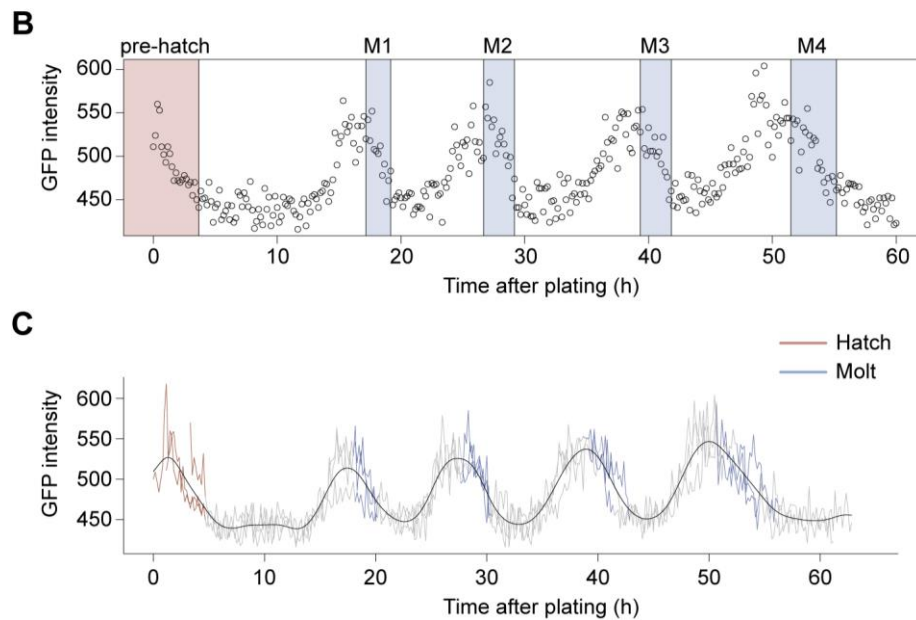


Figure 3: GRH-1 accumulation oscillates with its peak at molt entry

A, Western blot analysis of *grh-1(xe135); peft-3::luc; peft-3::tir-1* animals (HW2434) using anti-FLAG antibody. ACT-1 was used as loading control. Time points represent time of development of a synchronized population in liquid culture at 20°C with start of the culture at $t = 0$ h. Molts were determined by luciferase assays (**Figure S5**).

B, Quantification of GFP intensities at the peak of GRH-1::GFP expression in a single animal (HW2603) grown in micro-chambers. GFP intensity was determined by manual selection of a hypodermal cell for each time point and quantification of the maximum intensity. Specifically, we randomly selected a hypodermal cell in the mid-body of the worm, for which GFP intensity was among the brightest. Given that GFP intensities could not be distinguished from background in the trough of the oscillation, we cannot quantify amplitudes. $t = 0$ h corresponds to the time of plating. Pre-hatch (red) and molts (blue) are indicated.

C, Quantification of GFP intensities in three animal expressing GRH-1::GFP (HW2603) grown in micro-chambers (grey) (**Figure S6**). Black line represents a smoothed spline. GFP intensity was determined as in B. $t = 0$ h corresponds to the time of plating of the animal with the longest pre-hatch period. Animals are synchronized at hatch. Pre-hatch (red) and molts (blue) are indicated.

Molting requires oscillatory GRH-1 activity

Both the rhythmic accumulation of GRH-1 and a recurring requirement for GRH-1 for each molt provide circumstantial evidence for a rhythmic activity of GRH-1. If this were true, the consequences of perturbing GRH-1 should depend on when, during a given larval stage, the perturbation occurs. To test this prediction, we initiated GRH-1 degradation at variable times in L3 by adding auxin and monitored developmental progression using the luciferase assay. Plotting luminescence traces by the time when the animals entered molt 3 (M3 entry) in a heatmap (**Figure 4A**) revealed a striking cutoff on the onset of lethality: addition of auxin up to 3 hours before the M3 was sufficient for phenotypic onset at the end of M3 (**Figure 4A,B**,

blue), whereas animals receiving auxin later showed the phenotype one stage later (Figure 4A,B, red). Hence, initiation of GRH-1 depletion in the time window ranging from 3 hours before M3 until M3 is not sufficient for lethality at M3. We observed similar results when auxin was added in L2 (Figure S7). As we will show below (Figure S9A), our treatment depletes GRH-1 rapidly (< 1h) to levels below the normal trough level, revealing that this time window is not explained by the time it takes to deplete GRH-1 sufficiently. Hence, GRH-1 is iteratively needed during larval development for progression through molts, but its activity is dispensable during part of each larval stage. In other words, and as we had hypothesized, GRH-1 exhibits rhythmic activity during larval development.

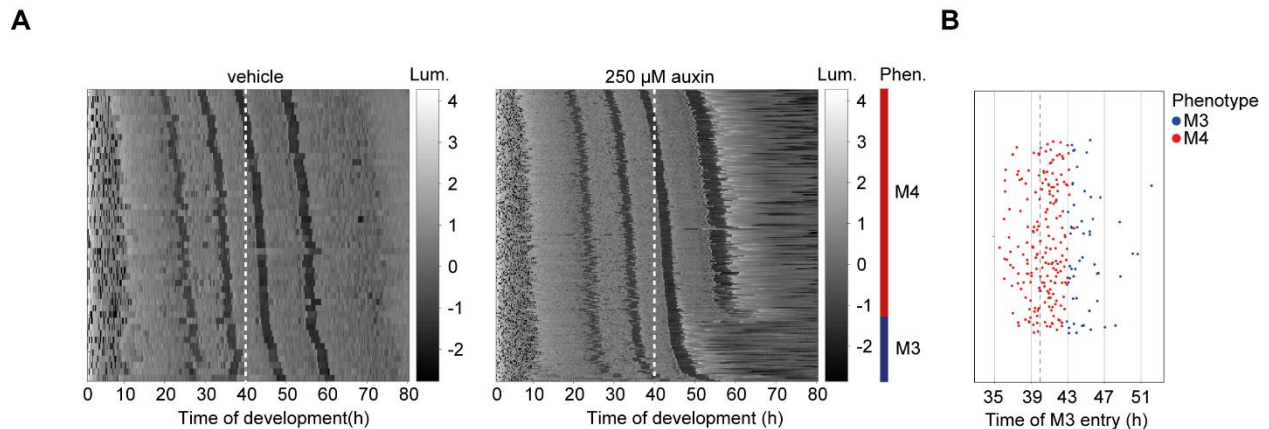


Figure 4: Lethality is dependent on the time of GRH-1 depletion

A, Heatmap showing trend-correct luminescence (Lum) of *grh-1(xe135); peft-3::luc; peft-3::tir-1* animals (HW2434) treated with vehicle (0.25% ethanol, left panel) or 250 μ M auxin (right panel) at 40 hours (white dashed line). Black corresponds to low luminescence occurring during lethargus (molt). Embryos of various stages were left to hatch and develop during the assay. Luminescence traces are sorted by entry into molt 3 (M3) so that traces of early hatched animals are on top and those of late hatched animals are at the bottom. Auxin-treated animals were categorized as “M3 phenotype” (blue bar) or “M4 phenotype” (red) depending on the last observed molt in the luminescence trace.

B, Quantification of time at which animals enter molt 3 (M3 entry). Dots (jittered in y) represent individual animals and are colored according to phenotype determined in A. Dotted line indicates when auxin was added.

Loss of GRH-1 reveals a long-molt phenotype

Given that long-period and short-period mutants have been identified in other oscillators, we wondered whether loss of GRH-1 reveals such phenotypes. To this end, we quantified the molt durations in wild-type animals and *degtron::grh-1* expressing animals exposed to auxin during the L3 stage. We observed a lengthening of the molt in GRH-1-depleted relative to wild-type animals (Figure 5A), whereas the duration of the preceding intermolt was not affected (Figure S8A). This result was qualitatively similar in animals that were exposed to auxin early in L3, and thus exhibited an M3 phenotype, and those that received auxin only late in L3, and thus exhibited an M4 phenotype (Figure 5A, Figure S8A). We conclude that loss of

GRH-1 results in extensive lengthening of the molt. In fact, we may even underestimate this effect since cuticle rupturing, used as a proxy for molt exit in GRH-1-depleted animals, occurs before the completion of ecdysis.

We wondered whether the extension of molt duration was connected to the lethality of GRH-1 depletion. To investigate this possibility, we took two approaches to attempt to uncouple the two phenotypes. First, we titrated the concentration of auxin and quantified the duration of larval stages. For animals that completed M1 normally, we quantified the duration of I1 and M1. We found that the period of molting was lengthened in an auxin dose-dependent manner (**Figure 5B**), whereas the duration of the intermolt did not change (**Figure S8B**). Even in the high auxin conditions where the phenotype was observed in M1, the length of I1 was not affected (**Figure S8C**). As numerous animals in the lowest concentrations (53 nM, 79 nM and 119 nM) entered all four molts, we quantified the durations of M1-3 and I1-3 in these animals. (We omitted M4 from this analysis as it was not always clear whether M4 lethality occurred within the time window of the experiment). We observed the dose-dependent lengthening not only in M1, but also in M2 and M3 (**Figure 5C**). In line with our observations in intermolt 1, effects appeared to be largely restricted to molt, with little or no extension of subsequent intermolts (**Figure S8D**).

Second, we investigated how the time of GRH-1 depletion affected the molt duration. To this end, we selected animals in which depletion of GRH-1 was initiated before the molt but did not result in cuticle rupturing. We quantified the duration of M3 in M4 phenotype animals (**Figure 4A**) and observed a relationship between M3 lengthening and M3 entry, i.e. the earlier animals received auxin relative to M3 entry, the longer the M3 period (**Figure 5D**). By contrast, in vehicle-treated animals, the M3 period did not change over time (**Figure 5D**). (M3 entry and duration of I3 were weakly correlated for both auxin- and vehicle-treated animals and similar correlations occurred in all stages (**Figure S8E,F**); hence, this effect was not linked to GRH-1 depletion.) We cannot, without further information about the dynamics of GRH-1 depletion, distinguish between the effects of timely depletion and GRH-1 levels on molt lengthening. Nevertheless, and in contrast to the cut-off we observed for the lethality (**Figure 4A**), the effects we observe on molt extension are gradual. Moreover, the results we present here reveal a time window in which GRH-1 is required for temporal control of the molt. In conclusion, depletion of GRH-1 caused lengthening of the molting period, which appears to persist throughout development. Thus, GRH-1 is repetitively required for normal duration of the molt.

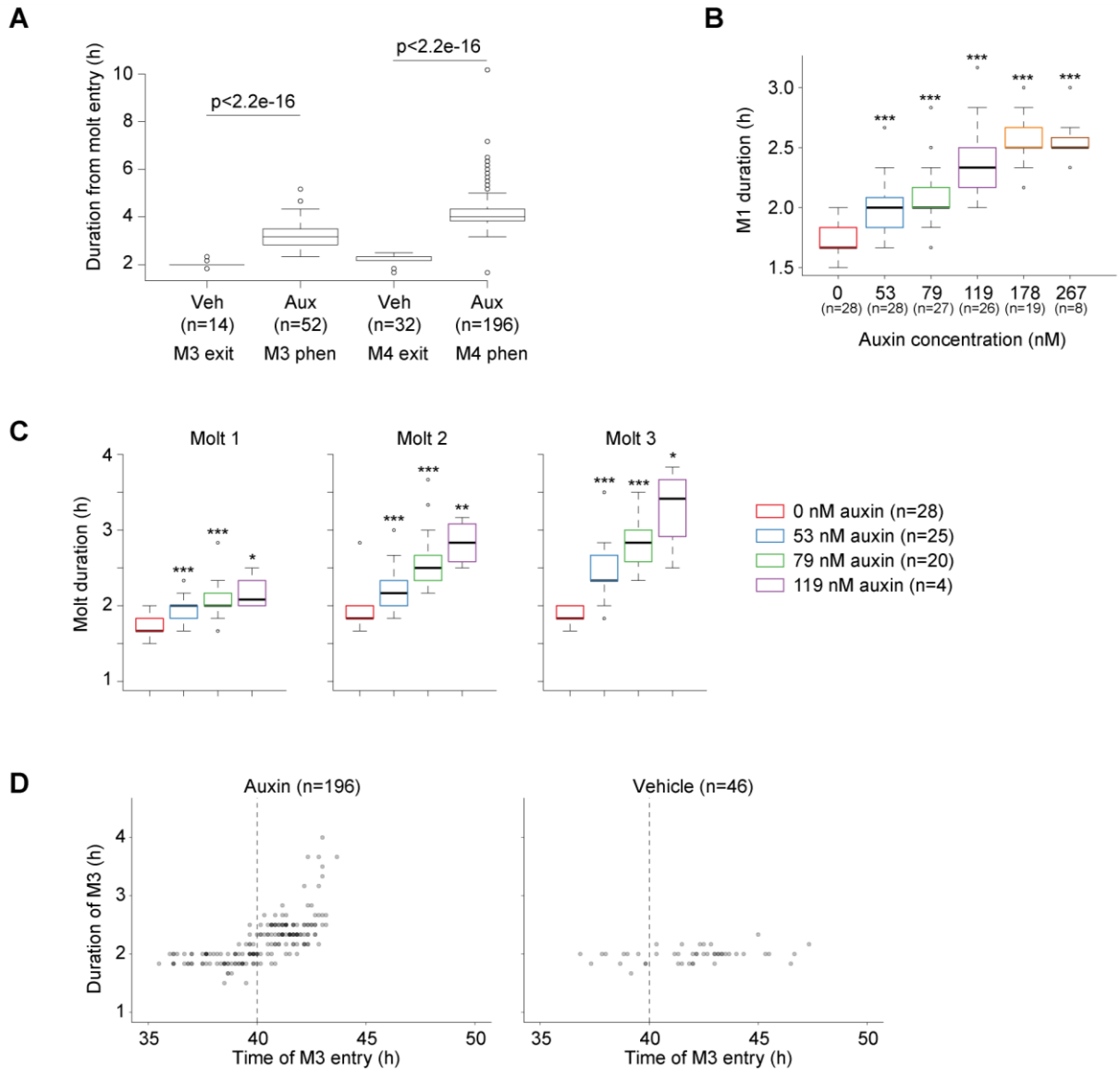


Figure 5: GRH-1 depletion causes lengthening of the molt

A, Quantification of molt duration for vehicle-treated animals (Veh) and auxin-treated animals (Aux). As cuticle rupturing occurs before completing ecdysis for auxin-treated animals, the molt duration might be under-estimated. Data for auxin-treated animals dying during M3 ecdysis and M4 ecdysis, respectively, (as explained in **Figure 4**) are shown separately. To resemble life history, vehicle-treated animals with M3 entry > 43h were selected for M3 quantification and animals with M3 entry \leq 43h were selected for M4 quantification. P-values are indicated.

B, Boxplot showing the duration of the first molt of animals treated with indicated concentrations of auxin. Animals that died during M1 were excluded. Significant differences relative to 0 nM auxin are indicated.

C, Boxplot showing the duration of M1, M2 and M3 of animals treated with indicated concentrations of auxin. Animals that revealed lethality at M1, M2 or M3 were excluded. Significant differences relative to 0 nM auxin are indicated.

D, Quantification of durations of M3 over the time of entering M3 respectively. Data is shown for ‘M4 phenotype’ animals and all vehicle-treated animals from **Figure 4**. Dashed line indicates treatment with 250 μ M auxin or vehicle at 40 hours after plating.

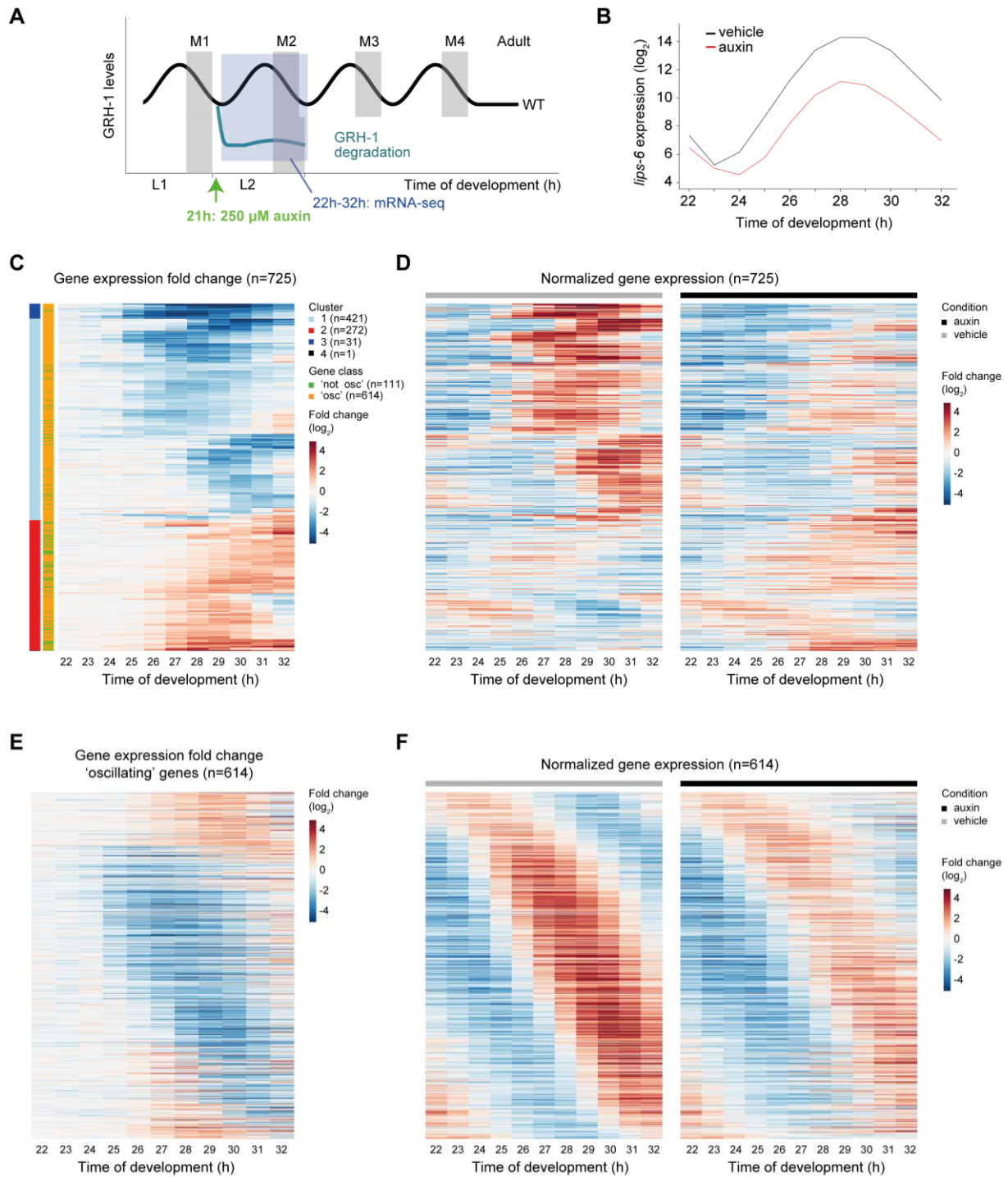
P-values were determined by Welch two-sample, two-sided t-test. * $p < 0.05$, ** $p < 0.01$, *** $p < 0.001$.

GRH-1 controls expression of a subset of 'oscillating' genes

To gain insight into the molecular functions of GRH-1, we investigated the gene expression changes upon GRH-1 degradation. To this end, we cultured a population of synchronized animals in liquid medium at 20°C. At 21 hours, when animals were in the early L2 stage, we added auxin (**Figure 6A, Figure S9**), to achieve a penetrant M2 defect. We sampled animals hourly from 22 hours until 32 hours, where after animals started dying (**Figure S9B**) and performed mRNA sequencing. We identified 725 genes ('hits') that differed significantly in their expression over time between vehicle and auxin conditions (**Figure 6B,C,D, methods**). These included genes that were upregulated in auxin-treated relative to vehicle-treated animals (**Figure 6C**; cluster 2 and 4, n=273) and downregulated genes (**Figure 6C**; cluster 1 and 3, n=452).

Strikingly, 'oscillating' genes were strongly enriched among the 'hits', i.e. 85% compared to 24% of all expressed genes, according to our previous annotation (Meeuse et al., 2019). To investigate whether 'oscillating hits' share similar gene expression patterns, we sorted them by their previously determined peak phase (Meeuse et al., 2019) and plotted the gene expression fold changes (**Figure 6E**) and mean-normalized expression in both conditions (**Figure 6F**) in heatmaps. We observed that genes with similar peak phases also tended to show similar changes in expression levels with regard to directionality of the pattern, fold changes, and the pattern of change over time (**Figure 6E,F**). This suggested to us that GRH-1 depletion affects genes in a peak-phase specific manner. To investigate this relationship further, we used the annotated peak phases (Meeuse et al., 2019) to quantify peak phase enrichment of 'oscillating hits' over the total of oscillating genes in 20° bins. We performed this analysis for upregulated (**Figure 6G**, red) and downregulated genes (**Figure 6G**, blue) separately. Strikingly, clear and opposing patterns emerged for the two groups: Downregulated genes were enriched for peak phases around molt entry (-30° to 70°), and depleted for opposite peak phases (130° to -90°) (**Figure 6G**). In contrast, upregulated genes were depleted for peak phases around molt entry (-50° to 70°) and enriched for opposite peak phases (150° to -90°) (**Figure 6G**). In other words, genes with expression peaks shortly before or during early stages of the molt failed to be upregulated upon GRH-1 depletion, whereas genes with expression troughs during the molt failed to be down-regulated during the molt. Although we cannot, at this point, discriminate primary from secondary targets, these phase-specific effects agree well with the phenotypic data and provide further evidence for the notion of a rhythmic GRH-1 activity.

To further investigate the functional relevance of GRH-1, we sought to examine in which tissues the genes affected by GRH-1 depletion are expressed, using a recently published tissue annotation (Cao et al., 2017). In agreement with the molting phenotype, we found that genes expressed in the hypodermis were strongly enriched in our data set (**Figure 6H**).



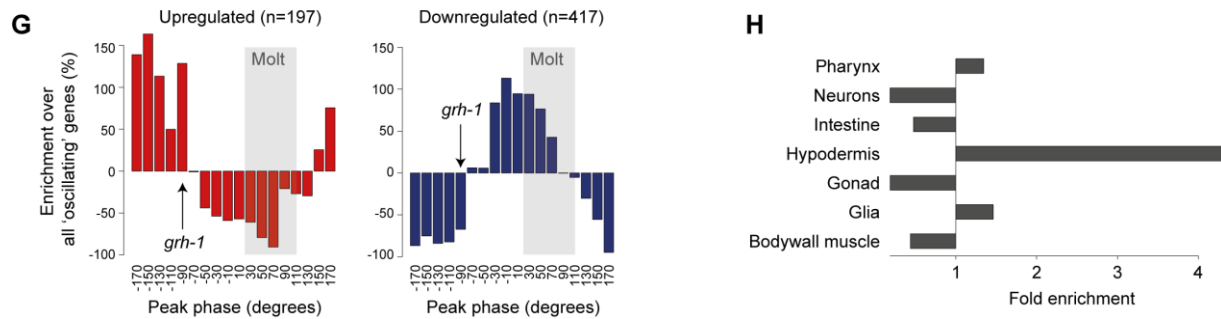


Figure 6: Degradation of GRH-1 affects expression of 614 ‘oscillating’ genes in a phase-specific manner

A, Schematic overview of experimental design. L1 synchronized *grh-1(xe135); peft-3::luc; peft-3::tir-1* animals (HW2434) were cultured in liquid at 20°C. After 21 hours, when animals reached early L2 stage, 250 μM auxin or an equivalent amount of vehicle was added to the culture. We sampled hourly from 22 hours until 32 hours and performed mRNA-sequencing and Western blotting (**Figure S9A**). Extension of molt 2 (M2) and cessation of M3 and M4 was confirmed using the luciferase assay (**Figure S9B**).

B, Expression of *lips-6* in \log_2 . Vehicle (black) and auxin (red) expression patterns are shown.

C, Heatmap of fold change between gene expression in 250 μM auxin and in vehicle conditions. Expression fold change is hierarchically clustered for significantly changing genes (n=725), ordered by mean expression and plotted in \log_2 . First vertical bar indicates four clusters obtained after hierarchical clustering. Cluster 2 (n=272) and cluster 4 (n=1) consist of genes mostly upregulated over time following auxin addition. Cluster 1 (n=421) and cluster 3 (n=31) consist of genes mostly downregulated. A second vertical bar indicates whether a gene is ‘oscillating’ (‘osc’) or ‘not oscillating’ (‘not osc’) in its expression patterns according to a previous annotation (Meeuse et al., 2019).

D, Gene expression heatmaps in auxin-treated (black) and control (grey) animals for significantly changing genes (n=725). Gene expression was mean-centered over both conditions, sorted according to C and plotted in \log_2 .

E, Heatmap of gene expression fold change for ‘oscillating’ genes (n=614) among significantly changing genes (n=725). Expression fold change is sorted by peak phase as previously determined (Meeuse et al., 2019) and plotted in \log_2 .

F, Gene expression heatmaps in auxin-treated (black) and control (grey) animals for ‘oscillating’ genes (n=614). Gene expression was mean-centered over both conditions, sorted as in E and plotted in \log_2 .

G, Barplot showing peak phase enrichment of ‘oscillating hits’ (this time course) over all ‘oscillating’ genes (Meeuse et al., 2019) for ‘upregulated’ genes (n=197) in red and ‘downregulated’ genes (n=417) in blue. Annotation of upregulated and downregulated genes according to C. Peak phases are sorted in 20° bins. The peak phase of *grh-1* mRNA is -90°(arrow) and the molt occurs roughly between 20° and 110° (grey box), as previously determined (Meeuse et al., 2019).

H, Barplot showing enrichment of indicated tissues in ‘all hits’ over genes with tissue annotation according to (Cao et al., 2017). Fold enrichment was calculated using a pseudocount of 12.

Cuticle rupturing results from loss of collagen expression

Given the hypodermal enrichment in our dataset, we sought to examine the molecular function of these genes. Hence, we used the recently published annotation of the *C. elegans* extracellular matrix, or matrisome (Teuscher et al., 2019) to identify ‘matrisome’ genes in our dataset. We found moderate and strong enrichment for ‘ECM regulators’ and ‘cuticular collagens’ respectively (**Figure 7A**). Enrichment

was maintained when focusing only on the oscillating genes or the downregulated genes, whereas enrichment was lost in the non-oscillating genes and also in the upregulated genes (**Figure 7A**). In agreement with rupturing of the cuticle upon GRH-1 depletion, it seems likely that downregulation of ‘oscillating’ matrisome genes accounts for this phenotype.

Next, we sought to further investigate this class of genes in single animals. To this end, we expressed a destabilized *gfp* from different promoters and investigated their expression in L3 stage in vehicle and auxin-treated single animals using time-lapse microscopy of single animals grown in micro-chambers as described previously (Meeuse et al., 2019). We investigated GFP levels driven by *col-41* and *col-146*, two structural components of the cuticle. According to our RNA-seq data, they are expressed with different peak phases and their expression peak is reduced by loss of GRH-1 (**Figure 7B,D**). We also included *qua-1* (Meeuse et al., 2019), whose mRNA accumulation appeared unaffected by GRH-1 degradation (**Figure 7H**).

Consistent with the RNA sequencing data, we detected oscillations of all reporters in L3 stage in vehicle-treated animals (**Figure 7C,E,I**). In auxin-treated animals that exhibited an M3 phenotype, we observed massive loss of peak expression for the *col-41* and *col-146* reporters (**Figure 7C,E**). GFP oscillations driven by the *qua-1* reporter were not, or only minimally, affected by GRH-1 degradation (**Figure 7I**). Similar results were obtained in independent replicates (**Figure S10, S11**). Thus, extensive loss of oscillatory collagen expression is likely to contribute to the phenotype.

GRH-1 controls its transcription via a negative feedback loop

Given that a negative feedback loop is one of the requirements for biochemical oscillations (Novák and Tyson, 2008), we investigated whether GRH-1 exhibits this characteristic. To this end, we examined how GRH-1 levels affect its gene expression, using a *pgrh-1::gfp-h2b-pest* reporter. In contrast to vehicle-treated animals, where GFP levels peak before and decline during the molt, in auxin-treated animals, GFP levels failed to decrease during the molt and continued to increase almost linearly (**Figure 7G**). Similar results were observed in an independent replicate (**Figure S11**), and in the RNA sequencing data (**Figure 7F**), although the increase was less strong at the mRNA level. Thus, our results indicate that oscillatory accumulation of GRH-1 is controlled by a negative transcriptional feedback loop.

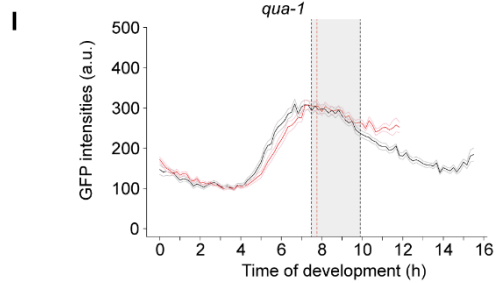
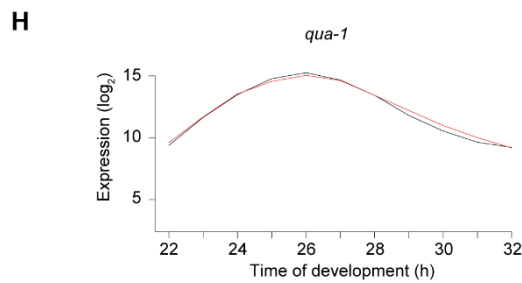
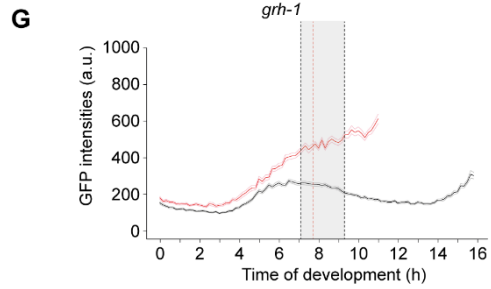
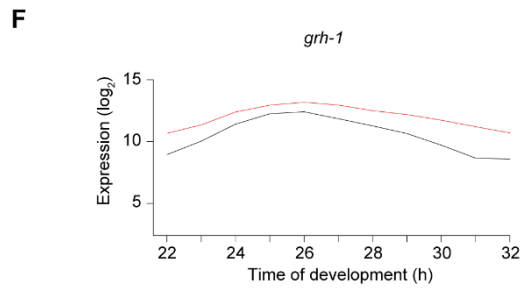
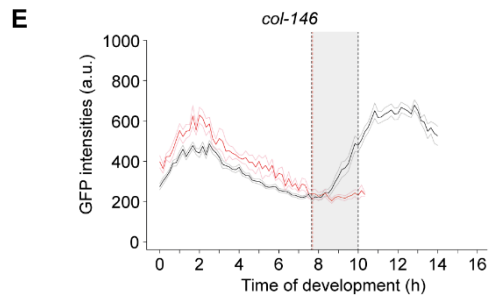
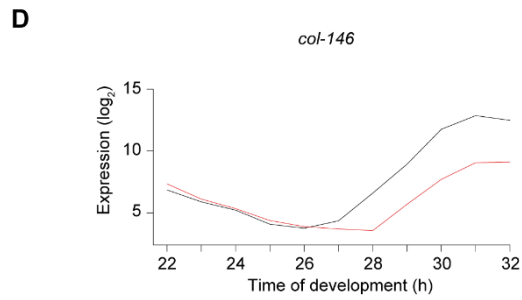
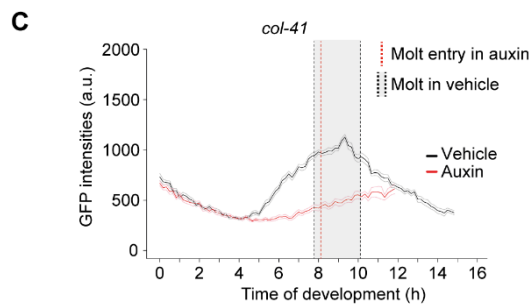
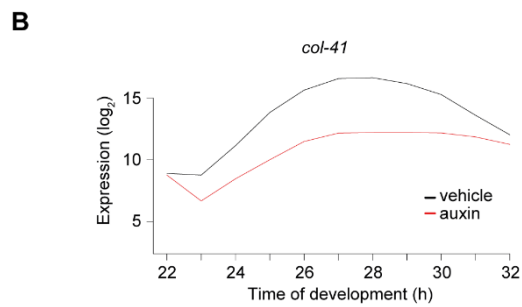
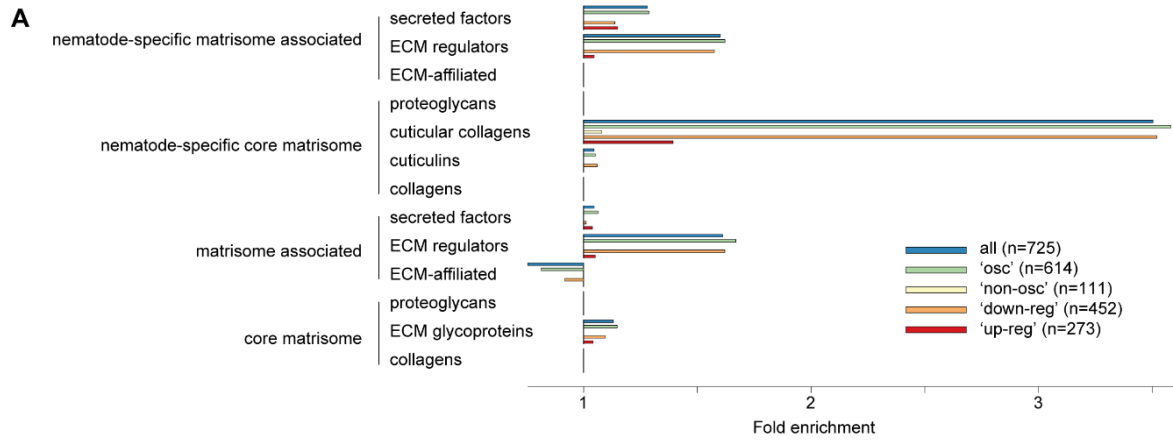


Figure 7: Depletion of GRH-1 results in downregulation of ‘oscillating’ components of the cuticle and upregulation of its own transcription

A, Barplot showing fold enrichment of indicated matrixome gene classes. Fold enrichment is shown for ‘all’ genes affected by GRH-1 depletion or an indicated subset of those. Fold enrichment was calculated using a pseudocount of 12.

B,D,F,H, Expression changes of indicated genes (B: *col-41*, D: *col-146*, F: *grh-1*, H: *qua-1*) in vehicle (black) and auxin treated (red) animals, obtained from time course in **Figure 6**.

C,E,G,I, Quantification of background subtracted GFP intensity of single animals over L3 stage, starting from M2 exit (t = 0h). Animals express *gfp::h2b::pest::unc-54 3'utr* from the indicated promoters (C: *col-41*, E: *col-146*, G: *grh-1*, I: *qua-1*) in the *grh-1::degron* background. Mean (black line) and SEM (grey lines) for time point with more than 5 vehicle-treated animals are shown. Mean (red line) and SEM (pink lines) for time points with more than 5 auxin treated (250 μ M) animals are shown. GFP intensities after the appearance of the phenotype in auxin-treated animals are not shown. GFP intensities ≤ 50 , which reflect segmentation errors, were omitted from mean and SEM. Mean molt 3 entry and mean molt 3 exit in vehicle-treated (grey box) and mean molt 3 entry in auxin-treated (red dotted line) animals are indicated. Traces of individual animals are shown in **Figure S10** and **Figure S11**.

Discussion

C. elegans larvae exhibit large-scale mRNA level oscillations that appear coupled to molting (Hendriks et al., 2014; Kim et al., 2013; Meeuse et al., 2019). However, the relevant gene expression programs and the transcription factors that shape either process have remained largely elusive so that we do not understand their regulatory logic or mechanistic underpinnings, nor the extent and means by which they are coupled. Here, we have begun to fill this gap in our understanding of the fundamental biology of *C. elegans* by identifying and characterizing the transcription factor GRH-1 as a factor important for both oscillatory gene expression and molting.

Our findings support a dual, and connected, role of GRH-1 in molting and gene expression oscillations: First, animals lacking GRH-1 fail to complete the molt and instead die by cuticular rupturing during ecdysis. Second, GRH-1 is required for every larval molt, but cuticular rupturing requires GRH-1 depletion at least 3 h before molt entry. Together with rhythmic accumulation of both GRH-1 mRNA and protein, these data are consistent with an oscillatory activity of GRH-1. The inferred window of activity fits well with a peak of GRH-1 protein levels shortly (roughly 1-2 hours) before molt entry, particularly when considering that GRH-1 may be functional at levels below the peak concentration and that its depletion, although rapid (<1 h to below trough levels) may yet take some time to occur. Third, GRH-1 depletion lengthens molting substantially. This occurs under conditions of extensive depletion, when animals burst during ecdysis but at a time much later than completion of ecdysis in wild-type animals. This is also true under more modest depletion, which avoids cuticle rupturing and yet delays ecdysis relative to wild-type animals. Fourth, depletion of GRH-1 predominantly affects the expression of oscillating genes, which account for >80 % of significantly mis-expressed genes. From these findings, we conclude that rhythmic GRH-1 activity is essential for oscillatory genes expression and molting. Moreover, the fact that oscillating genes dysregulated upon GRH-1 depletion are enriched for genes encoding structural components of the cuticle and ‘ECM regulators’ suggests that GRH-1 connects these two processes, i.e., that GRH-1 promotes oscillatory gene expression and thereby choreographs the complex molting process.

Although GRH-1 depletion massively perturbs oscillatory gene expression, less than 20% of all annotated oscillating genes (Meeuse 2019) are significantly affected. Moreover, the affected subset is enriched for certain peak phases, epidermal expression, and specific, i.e., molting-related, functions. These features do not necessarily exclude a function of GRH-1 as part of a core oscillator, since it is currently unknown whether gene expression oscillations in *C. elegans* involve one or several oscillators. Indeed, a core oscillator function fits well with our finding that degradation of GRH-1 increases *grh-1* mRNA levels as such a negative feedback is a key design principle of oscillator networks (Novák and Tyson, 2008). GRH-1-depleted animals may then behave as long-molt mutants, similar to long-period mutants of core

components of the circadian oscillator (Takahashi, 2004). Nonetheless, an alternative, more parsimonious explanation is that GRH-1 is required for a specific output of a more general oscillator, e.g., by coupling a “molting module” to the oscillator. Irrespective of which scenario applies, our discovery of an essential function of GRH-1 for oscillatory gene expression of a large group of genes provides a starting point for a molecular dissection of the core oscillator, e.g., by enabling identification of oscillator components through genetic modifier screens.

What is the cause of lethality in GRH-1 depleted animals? When combining the immediate phenotype, rupturing of the cuticle in the head, with the identity of the down-regulated genes as discussed above, it seems a consequence of a cuticle formation defect that impairs cuticular integrity. During ecdysis, the worm is transiently ensheathed by two cuticles, a newly formed one below the old one. In other words, rupturing occurs when a newly formed cuticle first becomes the outermost “shell” of the animal. This interpretation is in agreement with the fact that rupturing occurs during ecdysis but never before and that tissue extrusion occurred in-between the two cuticles. Although it remains possible that inappropriate proteolytic activities during ecdysis might additionally damage the newly formed cuticle, the interpretation that rupturing is a consequence of impaired cuticle formation is also consistent with cuticle defects in GRH-1-depleted *C. elegans* embryos, which do not undergo ecdysis (Venkatesan et al., 2003).

Soft, thin and granular cuticles, prone to rupturing, are also a hallmark of *Drosophila* Grainyhead mutant animals (Bray and Kafatos, 1991; Nüsslein-Volhard et al., 1984). With roles of Grhl1-3 in development and maintenance of epithelial tissues in mammals, i.e. epithelial differentiation (Yu et al., 2006), wound healing, eye lid closure (Boglev et al., 2011), and formation of hair coat (Wilanowski et al., 2002), our findings agree with a fundamental, evolutionarily conserved role of Grainyhead proteins in epidermis and ECM development and remodeling. Although individual Grhl targets of relevance have been described for these processes, e.g. transglutaminase 1, the enzyme essential for cross-linking structural components of the epidermis (Ting et al., 2005), and Desmoglein-1, Cadherin-1, Claudin 4, among other epithelial cell interaction genes (Wilanowski et al., 2008, Varma et al., 2012; Werth et al., 2010), we propose that also in other animals Grainyhead proteins may have a broader function in orchestrating epidermal and ECM development and remodeling programs. Indeed, given the overt similarities of Grainyhead protein functions across animals it appears that *C. elegans* molting could serve as an powerful genetically accessible, model of animal skin and ECM development and remodeling.

In summary, we propose that in this study we have identified and characterized a number of factors linked to a molting cycle oscillator that may have a functional correspondence in other animals, and that their further dissection provides a path to a molecular-mechanistic and systems understanding of gene expression oscillations in *C. elegans*.

Acknowledgements

We thank Iskra Katic, and Lan Xu for help in generating transgenic strains, Eliza Pandini Figueiredo Moreno and the FMI Functional Genomics Facility for RNA sequencing, Yannick Hauser and Laurent Gelman for help with imaging, Benjamin Titze, Jan Eglinger and Yannick Hauser for help with the KNIME workflow and Dimos Gaidatzis for conceiving the analysis that lead to the identification of the transcription factors.

Funding

M.W.M.M received a Boehringer Ingelheim Fonds PhD fellowship. This work is part of a project that has received funding from the European Research Council (ERC) under the European Union's Horizon 2020 research and innovation programme (Grant agreement No. 741269, to H.G.). The FMI is core-funded by the Novartis Research Foundation.

Author contributions

K.B imaged the N2 molt. A.N. generated the GFP reporter strains and dissected the *grh-1* promoter. M.W.M.M performed the remaining experiments and analyzed all the data. M.S. conceived the differential expression analysis. H.G. and M.W.M.M conceived the project and wrote the manuscript.

References

- Almeida, M.S., and Bray, S.J. (2005). Regulation of post-embryonic neuroblasts by *Drosophila* Grainyhead. *Mech. Dev.* *122*, 1282–1293.
- Arribere, J.A., Bell, R.T., Fu, B.X.H., Artiles, K.L., Hartman, P.S., and Fire, A.Z. (2014). Efficient marker-free recovery of custom genetic modifications with CRISPR/Cas9 in *Caenorhabditis elegans*. *Genetics* *198*, 837–846.
- Au, K.F., Jiang, H., Lin, L., Xing, Y., and Wong, W.H. (2010). Detection of splice junctions from paired-end RNA-seq data by SpliceMap. *Nucleic Acids Res* *38*, 4570–4578.
- Boglev, Y., Wilanowski, T., Caddy, J., Parekh, V., Auden, A., Darido, C., Hislop, N.R., Cangkrama, M., Ting, S.B., and Jane, S.M. (2011). The unique and cooperative roles of the Grainy head-like transcription factors in epidermal development reflect unexpected target gene specificity. *Dev. Biol.* *349*, 512–522.
- Bray, S.J., and Kafatos, F.C. (1991). Developmental function of Elf-1: an essential transcription factor during embryogenesis in *Drosophila*. *Genes Dev.* *5*, 1672–1683.
- Cao, J., Packer, J.S., Ramani, V., Cusanovich, D.A., Huynh, C., Daza, R., Qiu, X., Lee, C., Furlan, S.N., Steemers, F.J., et al. (2017). Comprehensive single-cell transcriptional profiling of a multicellular organism. *Science* *357*, 661–667.
- Frand, A.R., Russel, S., and Ruvkun, G. (2005). Functional Genomic Analysis of *C. elegans* Molting. *PLOS Biology* *3*, e312.
- Fraser, A.G., Kamath, R.S., Zipperlen, P., Martinez-Campos, M., Sohrmann, M., and Ahringer, J. (2000). Functional genomic analysis of *C. elegans* chromosome I by systematic RNA interference. *Nature* *408*, 325–330.
- Frøkjær-Jensen, C., Davis, M.W., Ailion, M., and Jorgensen, E.M. (2012). Improved Mos1-mediated transgenesis in *C. elegans*. *Nat. Methods* *9*, 117–118.
- Gaidatzis, D., Lerch, A., Hahne, F., and Stadler, M.B. (2015). QuasR: quantification and annotation of short reads in R. *Bioinformatics* *31*, 1130–1132.
- Gaujoux, R., and Seoighe, C. (2010). A flexible R package for nonnegative matrix factorization. *BMC Bioinformatics* *11*, 367.
- Gibson, D.G., Young, L., Chuang, R.-Y., Venter, J.C., Hutchison, C.A., and Smith, H.O. (2009). Enzymatic assembly of DNA molecules up to several hundred kilobases. *Nat. Methods* *6*, 343–345.
- Gissendanner, C.R., and Sluder, A.E. (2000). *nhr-25*, the *Caenorhabditis elegans* ortholog of *ftz-f1*, is required for epidermal and somatic gonad development. *Dev. Biol.* *221*, 259–272.
- Gissendanner, C.R., Crossgrove, K., Kraus, K.A., Maina, C.V., and Sluder, A.E. (2004). Expression and function of conserved nuclear receptor genes in *Caenorhabditis elegans*. *Dev. Biol.* *266*, 399–416.
- Hemphälä, J., Uv, A., Cantera, R., Bray, S., and Samakovlis, C. (2003). Grainy head controls apical membrane growth and tube elongation in response to Branchless/FGF signalling. *Development* *130*, 249–258.

- Hendriks, G.-J., Gaidatzis, D., Aeschmann, F., and Großhans, H. (2014). Extensive oscillatory gene expression during *C. elegans* larval development. *Mol. Cell* *53*, 380–392.
- Kamath, R.S., Fraser, A.G., Dong, Y., Poulin, G., Durbin, R., Gotta, M., Kanapin, A., Le Bot, N., Moreno, S., Sohrmann, M., et al. (2003). Systematic functional analysis of the *Caenorhabditis elegans* genome using RNAi. *Nature* *421*, 231–237.
- Katic, I., Xu, L., and Ciosk, R. (2015). CRISPR/Cas9 Genome Editing in *Caenorhabditis elegans*: Evaluation of Templates for Homology-Mediated Repair and Knock-Ins by Homology-Independent DNA Repair. *G3 (Bethesda)* *5*, 1649–1656.
- Kim, D. hyun, Grün, D., and van Oudenaarden, A. (2013). Dampening of expression oscillations by synchronous regulation of a microRNA and its target. *Nat. Genet.* *45*, 1337–1344.
- Kostrouchova, M., Krause, M., Kostrouch, Z., and Rall, J.E. (1998). CHR3: a *Caenorhabditis elegans* orphan nuclear hormone receptor required for proper epidermal development and molting. *Development* *125*, 1617–1626.
- Lee, H., and Adler, P.N. (2004). The grainy head transcription factor is essential for the function of the frizzled pathway in the *Drosophila* wing. *Mech. Dev.* *121*, 37–49.
- Meeuse, M.W.M., Hauser, Y.P., Hendriks, G.-J., Eglinger, J., Bogaarts, G., Tsiairis, C., and Großhans, H. (2019). State transitions of a developmental oscillator. *BioRxiv* 755421.
- Novák, B., and Tyson, J.J. (2008). Design principles of biochemical oscillators. *Nat Rev Mol Cell Biol* *9*, 981–991.
- Nüsslein-Volhard, C., Wieschaus, E., and Kluding, H. (1984). Mutations affecting the pattern of the larval cuticle in *Drosophila melanogaster*. *Wilhelm Roux' Archiv* *193*, 267–282.
- Olmedo, M., Geibel, M., Artal-Sanz, M., and Merrow, M. (2015). A High-Throughput Method for the Analysis of Larval Developmental Phenotypes in *Caenorhabditis elegans*. *Genetics* *201*, 443–448.
- Rifat, Y., Parekh, V., Wilanowski, T., Hislop, N.R., Auden, A., Ting, S.B., Cunningham, J.M., and Jane, S.M. (2010). Regional neural tube closure defined by the Grainy head-like transcription factors. *Dev. Biol.* *345*, 237–245.
- Rual, J.-F., Ceron, J., Koreth, J., Hao, T., Nicot, A.-S., Hirozane-Kishikawa, T., Vandenhoute, J., Orkin, S.H., Hill, D.E., van den Heuvel, S., et al. (2004). Toward improving *Caenorhabditis elegans* phenome mapping with an ORFeome-based RNAi library. *Genome Res.* *14*, 2162–2168.
- Russel, S., Frand, A.R., and Ruvkun, G. (2011). Regulation of the *C. elegans* molt by *pqn-47*. *Dev. Biol.* *360*, 297–309.
- Singh, R.N., and Sulston, J.E. (1978). Some Observations On Moulting in *Caenorhabditis Elegans*. *Nematologica* *24*, 63–71.
- Takahashi, J.S. (2004). Finding new clock components: past and future. *J. Biol. Rhythms* *19*, 339–347.

Ting, S.B., Caddy, J., Hislop, N., Wilanowski, T., Auden, A., Zhao, L.-L., Ellis, S., Kaur, P., Uchida, Y., Holleran, W.M., et al. (2005). A homolog of *Drosophila* grainy head is essential for epidermal integrity in mice. *Science* 308, 411–413.

Varma, S., Cao, Y., Tagne, J.-B., Lakshminarayanan, M., Li, J., Friedman, T.B., Morell, R.J., Warburton, D., Kotton, D.N., and Ramirez, M.I. (2012). The transcription factors Grainyhead-like 2 and NK2-homeobox 1 form a regulatory loop that coordinates lung epithelial cell morphogenesis and differentiation. *J. Biol. Chem.* 287, 37282–37295.

Venkatesan, K., McManus, H.R., Mello, C.C., Smith, T.F., and Hansen, U. (2003). Functional conservation between members of an ancient duplicated transcription factor family, LSF/Grainyhead. *Nucleic Acids Res* 31, 4304–4316.

Werth, M., Walentin, K., Aue, A., Schönheit, J., Wuebken, A., Pöde-Shakked, N., Vilianovitch, L., Erdmann, B., Dekel, B., Bader, M., et al. (2010). The transcription factor grainyhead-like 2 regulates the molecular composition of the epithelial apical junctional complex. *Development* 137, 3835–3845.

Wilanowski, T., Tuckfield, A., Cerruti, L., O’Connell, S., Saint, R., Parekh, V., Tao, J., Cunningham, J.M., and Jane, S.M. (2002). A highly conserved novel family of mammalian developmental transcription factors related to *Drosophila* grainyhead. *Mechanisms of Development* 114, 37–50.

Wilanowski, T., Caddy, J., Ting, S.B., Hislop, N.R., Cerruti, L., Auden, A., Zhao, L.-L., Asquith, S., Ellis, S., Sinclair, R., et al. (2008). Perturbed desmosomal cadherin expression in grainy head-like 1-null mice. *EMBO J.* 27, 886–897.

Yu, Z., Lin, K.K., Bhandari, A., Spencer, J.A., Xu, X., Wang, N., Lu, Z., Gill, G.N., Roop, D.R., Wertz, P., et al. (2006). The Grainyhead-like epithelial transactivator Get-1/Grhl3 regulates epidermal terminal differentiation and interacts functionally with LMO4. *Dev. Biol.* 299, 122–136.

Zhang, L., Ward, J.D., Cheng, Z., and Dernburg, A.F. (2015). The auxin-inducible degradation (AID) system enables versatile conditional protein depletion in *C. elegans*. *Development* 142, 4374–4384.

Methods

Transgenic animals

HW1939: *EG6699, xeSi296 [Peft-3::luc::gfp::unc-54 3'UTR, unc-119(+)] II* (Meeuse et al., 2019)

HW1949: *EG8080, xeSi301 [Peft-3::luc::gfp::unc-54 3'UTR, unc-119(+)] III* (this study)

HW2665: *rde-1(ne219) V* (gift from Gasser Lab)

HW2150: *EG6699, xeSi296 [Peft-3::luc::gfp::unc-54 3'UTR, unc-119(+)] II; rde-1(ne219) V* (this study)

CA1200: *ieSi57 [Peft-3::TIR1::mRuby::unc-54 3'UTR, cb-unc-119(+)] II* (Zhang et al., 2015)

HW1984: *ieSi57 [Peft-3::TIR1::mRuby::unc-54 3'UTR, cb-unc-119(+)] II; EG8080, xeSi301 [Peft-3::luc::gfp::unc-54 3'UTR, unc-119(+)] III* (this study)

HW2079: *EG8080, xeSi376 [Peft-3::TIR1::mRuby::unc-54 3'UTR, cb-unc-119(+)] III* (this study)

HW2418: *grh-1(xe135(grh-1::degron::3xFLAG)) I; EG8080, xeSi376 [Peft-3::TIR1::mRuby::unc-54 3'UTR, cb-unc-119(+)] III* (this study)

HW2434: *grh-1(xe135(grh-1::degron::3xFLAG)) I; EG6699, xeSi296 [Peft-3::luc::gfp::unc-54 3'UTR, unc-119(+)] II; EG8080, xeSi376 [Peft-3::TIR1::mRuby::unc-54 3'UTR, cb-unc-119(+)] III* (this study)

SWI reporters:

HW2814: *EG6699, xeSi482 [Pgrh-1::pest-gfp-h2b::unc-54 3'UTR, unc-119(+)] II* (this study)

HW2824: *grh-1(xe135(grh-1::degron::3xFLAG)) I; EG6699, xeSi482 [Pgrh-1::pest-gfp-h2b::unc-54 3'UTR, unc-119(+)] II; EG8080, xeSi376 [Peft-3::TIR1::mRuby::unc-54 3'UTR, cb-unc-119(+)] III* (this study)

HW2825: *EG6699, xeSi483 [Pcol-41::pest-gfp-h2b::unc-54 3'UTR, unc-119(+)] II* (this study)

HW2854: *grh-1(xe135(grh-1::degron::3xFLAG)) I; EG6699, xeSi483 [Pcol-41::pest-gfp-h2b::unc-54 3'UTR, unc-119(+)] II; EG8080, xeSi376 [Peft-3::TIR1::mRuby::unc-54 3'UTR, cb-unc-119(+)] III* (this study)

HW2826: *EG6699, xeSi484 [Pcol-146::pest-gfp-h2b::unc-54 3'UTR, unc-119(+)] II* (this study)

HW2855: *grh-1(xe135(grh-1::degron::3xFLAG)) I*; EG6699, *xeSi484 [Pcol-146::pest-gfp-h2b::unc-54 3'UTR, unc-119(+)] II*; EG8080, *xeSi376 [Peft-3::TIR1::mRuby::unc-54 3'UTR, cb-unc-119(+)] III* (this study)

HW2523: EG6699, *xeSi437 [Pqua-1::pest-gfp-h2b::unc-54 3'UTR, unc-119(+)] II* (Yannick Hauser, unpublished)

HW2856: *grh-1(xe135(grh-1::degron::3xFLAG)) I*; EG6699, *xeSi437 [Pqua-1::pest-gfp-h2b::unc-54 3'UTR, unc-119(+)] II*; EG8080, *xeSi376 [Peft-3::TIR1::mRuby::unc-54 3'UTR, cb-unc-119(+)] III* (this study)

HW2603: *grh-1(syb616(grh-1::GFP::3xFLAG)) I* (PHX616, three times backcrossed) (this study; custom-made by SunyBiotech)

Generation of transgenic animals

Endogenous degron-3XFLAG tagging *grh-1* by CRISPR/Cas9-mediated editing was performed using the previously published *dpy-10(cn64)* co-conversion protocol (Arribere et al., 2014). For the sgRNA plasmid, we inserted the sgRNA sequence (5' agagtttactctcatgagt 3') into NotI-digested pIK198 (Katic et al., 2015) by Gibson assembly (Gibson et al., 2009) with hybridized MM116 (5' AATTGCAAATCTAAATGTTTtagagtttactctcatgagtGTTTAAGAGCTATGCTGGAA 3') and MM117 (5' TTCCAGCATAGCTCTTAAACcactcatgagagtaaactctAAACATTTAGATTTGCAATT 3'). A degron-linker-3XFLAG-linker cassette was synthesized as gBlocks® Gene Fragments (Integrated DNA Technologies) with 50 bp homology arms to the *grh-1* locus before the stopcodon: 5' CCACGTTAATCGAGGTGGCTCCCACCAATCCAAACTCGTATTCCAACCTCAATGCCTAAAGAT CCAGCCAAACCTCCGGCCAAGGCACAAGTTGTGGGATGGCCACCGGTGAGATCATACCGGA AGAACGTGATGGTTTCCTGCCAAAAATCAAGCGGTGGCCCGGAGGCGGCGGCGTTCGTGAA GAGTACCTCAGGCGGCTCGGGTGGTACTGGCGGCAGCGACTACAAAGACCATGACGGTGAT TATAAAGATCATGACATCGATTACAAGGATGACGATGACAAGAGTACTAGCGGTGGCAGTG GAGGTACCGGCGGAAGCTGAGAGTAAACCTCTTTAGGTTCTTGTCTTAATTCTCTTAAAGGA GGACT 3'. Wildtype animals were injected with 10 ng/μL gBlock, 100 ng/μL sgRNA plasmid, 20 ng/μL AF-ZF-827 (Arribere et al., 2014), 50 ng/μL pIK155 (Katic et al., 2015) and 100 ng/μL pIK208 (Katic et al., 2015). Genome editing was confirmed by sequencing.

HW2079 animals were obtained by single copy-integration of pLZ31 (Zhang et al., 2015) into the universal MosSCI ttTi5605 site on chromosome III in EG8080 animals, using the published MosSCI protocol (Frøkjær-Jensen et al., 2012).

GFP reporters were constructed by amplifying the promoter from genomic DNA using the primers listed below and inserting them into *NheI*-digested pYPH0.14 as previously described (Meeuse et al., 2019). Transgenic animals were obtained by single copy-integration of the transgene into the *ttTi5605* locus (MosSCI site) on chromosome II in EG6699 animals, using the published MosSCI protocol (Frøkjær-Jensen et al., 2012).

AN153	CCATGGCTAAGTCTAGACATTCTGGAATGATAATTAATGATATAT TATTG	Pgrh-1 rv
AN154	gcgtgtcaataatcactcTGAAGGGGGGAGAAACC	Pgrh-1 fw
AN157	CCATGGCTAAGTCTAGACATtgctgagatgtgtcttcttc	Pcol-146 fw
AN158	gcgtgtcaataatcactcttgtgtggatcaccacctc	Pcol-146 rv
AN169	CCATGGCTAAGTCTAGACATcgttgagaacaatgttgtgt	Pcol-41 fw
AN170	gcgtgtcaataatcactcgtctcatttaattgtagtctatcg	Pcol-41 rv

RNAi screen

To knock-down 92 ‘oscillating’ transcription factors, we used the RNAi feeding method. *E. coli* HT115 bacteria carrying RNAi plasmids were obtained from either of the two libraries (Ahringer library (Fraser et al., 2000; Kamath et al., 2003), Vidal library (Rual et al., 2004)) or cloned (see generation of RNAi vectors).

For luciferase assays, bacteria were grown in 5 mL auto-induction medium (2 mM MgSO₄, 3.3 g/L (NH₄)₂SO₄, 6.8 g/LKH₂PO₄, 7.1 g/L Na₂HPO₄, 5 g/L glycerol, 0.5 g/L glucose, 2 g/L α -lactose, 100 ug/mL Amp in ZY medium (10 g/L tryptone, 5 g/L yeast extract)) at 37 °C. Bacteria were diluted in S-Basal medium (OD₆₀₀ = 0.45), with 100 uM Firefly D-luciferin (p.j.k., 102111) and 100 ug/mL Ampicillin. We used HW1939 animals that express luciferase from a constitutive and ubiquitous promoter, i.e. xeSi296 transgene. As a control strain, we used HW2150 animals expressing xeSi296 in an *rde-1(ne219)* background, which are RNAi deficient. For each RNAi condition we used 2 adjacent columns, i.e. 32 wells with 90 uL culture medium each. To avoid plate effects, the first 8 wells of the first column and the last 8 wells of the second column of the same RNAi condition were filled with an HW1939 animal and the remaining wells with an HW2150 animal.

Generation of RNAi vectors

For clones that were not available either of the two libraries, cDNA or genomic DNA was PCR amplified using the following primers:

locus	vector transformed	insert	Primer	Primer sequence
nhr-5	pMM012_R	Y73F8A.21a cDNA	MM070 MM071	ccaccggtccatggctagcTTCTGGCGGTAACAGTTCAA ttgatatcgaattctgcagGATGTGAGTATGGAATATTCGG
dmd-8	pMM013_R	T22H9.4 cDNA	MM076 MM077	ccaccggtccatggctagcCCCTGTCATCTTCTTCAAATGC ttgatatcgaattctgcagGTTTCAGCGCAGCTAATTGC
bcl-11	pMM014_R	F13H6.1a cDNA	MM078 MM079	ccaccggtccatggctagcAATAGAAACGTCTTCGGCGG ttgatatcgaattctgcagTTAACGTTGGTGTGACTGC
fkx-9	pMM015_R	K03C7.2b cDNA	MM080 MM081	ccaccggtccatggctagcGATTTGCTACGATCACCCAT ttgatatcgaattctgcagGGCCTTGATTGGAGAAAGTG
ztf-16	pMM016_R	R08E3.4a cDNA	MM082 MM083	ccaccggtccatggctagcCGACTACTGTATTTCCGAGTT ttgatatcgaattctgcagCAGTTAACGAAAGTGATGACTC
sem-2	pMM017_R	C32E12.5.1 cDNA	MM084 MM085	ccaccggtccatggctagcGATCTCCAAAAACCGCCCAA ttgatatcgaattctgcagTGCATCGCTCCATGGATAAT
grh-1	pMM018_R	Y48G8AR.1a cDNA	MM086 MM087	ccaccggtccatggctagcGAAGAAGTCCGACGGTGAAT ttgatatcgaattctgcagGAGTTTGGATTGGTGGGAGC
dmd-9	pMM019_R	Y67D8A.3 genomic DNA	MM088 MM089	ccaccggtccatggctagcCTTTGTTCCAGTTCAAACCAC ttgatatcgaattctgcagAGAGGGAAGGAACTGATAGAC
tbx-7	pMM020_R	ZK328.8.1 genomic DNA	MM090 MM091	ccaccggtccatggctagcCCTCATGACAGACAACTACT ttgatatcgaattctgcagCAACAAC TCCAAATCCACTT
M03D4.4b	pMM021_R	M03D4.4b cDNA	MM092 MM093	ccaccggtccatggctagcTCGGACACAGATTCATCACAAC ttgatatcgaattctgcagTCCGGTGTGCTGTATTTGTC
C08G9.2	pMM022_R	C08G9.2 cDNA	MM094 MM095	ccaccggtccatggctagcTACCGCAAGTGTACCAAAT ttgatatcgaattctgcagACCTTCACATGGATCTACACAA
nhr-112	pMM023_R	Y70C5C.6a cDNA	MM096 MM097	ccaccggtccatggctagcTTTTCCGCAGATTCTATCACTC ttgatatcgaattctgcagTATGATTCATCTCGCACACCA
ets-4	pMM024_R	F22A3.1a cDNA	MM098 MM099	ccaccggtccatggctagcATGCAATCTTCCAATCCAACC ttgatatcgaattctgcagAGGCAGGAATTTGTACACCA
ztf-14	pMM025_R	M163.2 genomic DNA	MM102 MM103	ccaccggtccatggctagcGCCGTCCCTGCATAACTACTC ttgatatcgaattctgcagAGAGAAGTGAGTTGCGGGAG
ztf-29	pMM026_R	Y66D12A.12 cDNA	MM104 MM105	ccaccggtccatggctagcCGTCACCGGCTCAACTTCCA ttgatatcgaattctgcagCATGTTCTCCTCCTTCGCTCT

PCR fragments were cloned into the RNAi feeding Pml1 and Sma1 digested L4440 vector (L4440 was a gift from Andrew Fire (Addgene plasmid # 1654 ; <http://n2t.net/addgene:1654> ; RRID:Addgene_1654)) using Gibson assembly (Gibson et al., 2009)) and transfected into *E. coli* HT115 bacteria.

Luciferase assays

Luciferase assays were performed as described before (Meeuse et al., 2019). In short, embryos were obtained from gravid adults by bleaching. Single embryos were transferred into a well of a white, flat-bottom, 384-well plate (Berthold Technologies, 32505) by pipetting. Animals were left to develop in 90 μ L S-Basal medium containing *E. coli* OP50 (OD₆₀₀ = 0.9) and 100 μ M Firefly D-Luciferin (p.j.k., 102111).

Plates were sealed with Breathe Easier sealing membrane (Diversified Biotech, BERM-2000). Luminescence was measured using a luminometer (Berthold Technologies, Centro XS3 LB 960) every 10 minutes for 0.5 sec for 72 hours in a temperature controlled incubator set to 20 degrees.

For auxin experiments, a 400x stock solution of 3-indoleacetic acid (auxin, Sigma Aldrich, I2886) in 100% ethanol was prepared. 1x Auxin was added to the culture medium at the start each experiment or at specific time points and in concentrations as indicated.

Luminescence data was analyzed using an automated algorithm to detect the hatch and the molts in MATLAB with the possibility to annotate molts manually, as described before (Meeuse et al., 2019). Completion of molts was scored by the presence of a drop in luminescence, followed by a period of stable and low luminescence and subsequent rise in luminescence.

RNA-seq time course

Synchronized L1 HW2434 worms were cultured in liquid culture (S-Basal supplemented with OP50, OD₆₀₀=3, 1000 animals/mL) in a temperature controlled incubator at 20°C with 120 rpm. After 21 hours of cultivation, the culture was split in two separate cultures and 250 µM auxin or 0.25% ethanol (vehicle), was added. We harvested hourly from 22 hours until 32 hours. At each time point 3000 animals and 10.000 animals were collected and washed three additional times with M9 buffer (42 mM Na₂HPO₄, 22 mM KH₂PO₄, 86 mM NaCl, 1 mM MgSO₄) for RNA extraction and Western Blotting respectively. To monitor developmental progression, bioluminescence of roughly 10 animals per well, collected at 21.5 hours and 25.5 hours, was recorded every 10 minutes for 0.5 sec in a temperature controlled incubator set to 20 degrees.

RNA extraction and sequencing library preparation

Pelleted animals were resuspended in Tri Reagent (MRC, TR118) and RNA was extracted using conventional phenol extraction, as described previously (Hendriks et al., 2014). Total RNA was DNase treated and libraries were prepared using the TruSeq Illumina mRNA-seq (stranded – high input) protocol. Libraries were sequenced using the Hiseq50 Cycle Single-end reads protocol on the HiSeq2500.

Processing of RNA-seq data

RNA-seq data was mapped to the *C. elegans* genome (ce10) using the qAlign function (splicedAlignment=TRUE, Rbowtie, version 1.22.0) from the QuasR package in R (Au et al., 2010; Gaidatzis et al., 2015) (version 1.22.0). Gene expression was quantified using qCount function from the QuasR package in R. Counts were scaled by total mapped library size for each sample. A pseudocount of

8 was added and counts were log₂-transformed. Genes that were not expressed, i.e. rowMeans=3, were excluded.

Differential expression analysis

To identify genes that change significantly, we calculated the fold change (FC) in gene expression between auxin (A) treated and control (C) animals (FC = A - C). As we expect most genes to be unchanged in the beginning of the time course, we used FC at t=22 hours as our null distribution. Since the null distribution is not normally distributed, we calculated the empirical cumulative distribution function ($\widehat{F}_n(x)$) of the absolute FC at t=22 hours, using the function `ecdf` of the package ‘stats’ in R (Version 3.5.1). Hence, we assumed noise to be undirected. Given that $\widehat{F}_n(x) = \widehat{P}_n(X \leq x)$, we calculated the probability of observing a FC at any given time point (X) larger than FC under the null distribution (x) as, $\widehat{P}_n(X > x) = 1 - \widehat{P}_n(X \leq x)$. We classified genes as ‘hits’ if the probability of FC of at least three time points was less than 10⁻³. Expression data was hierarchically clustered using the function `hclust` of the package `stats` in R and plotted in heatmaps using the function `aheatmap` of the package `NMF` in R (Gaujoux and Seoighe, 2010) (version 0.21.0). To generate the peak phase enrichment barplot, the fraction of ‘upregulated’ and ‘downregulated’ genes (according to **Figure 6C**) in each 20 degree phase bin was calculated by the number of genes in each 20 degree phase bin divided by the total number of genes. We calculated the peak phase enrichment by subtracting the fraction of all ‘oscillating’ genes from the fraction of ‘upregulated’ and ‘downregulated’ genes respectively and dividing this by the fraction of all ‘oscillating’ genes.

Western Blotting

Lysates were made by disruption (FastPrep-24, MP Biomedicals, 5 cycles, 25 sec on, 90 sec off), sonication (Biorupter, Diagnode, 10 cycles, 30 sec on, 60 sec off) and subsequent boiling. Proteins were separated by SDS-page and transferred to by semi-dry blotting. Antibodies were used at the following dilutions: mouse anti-FLAG-HRP (1:1000, A8592, Sigma Aldrich), mouse anti-Actin, clone C4 (1:5000, MAB1501, Millipore), mouse IgG HRP linked (1:7500, NXA931V, GE Healthcare). We used ECL Western Blotting detection reagent (RPN2232 and RPN2209, GE healthcare) and ImageQuant LAS 4000 chemiluminescence imager (GE Healthcare) for detection.

Phenotype imaging

For imaging phenotypes, HW2418 worms were mounted on a 2% (w/v) agarose pad with a drop of M9 buffer (42 mM Na₂HPO₄, 22 mM KH₂PO₄, 86 mM NaCl, 1 mM MgSO₄). *grh-1::degron* animals were imaged on a Axio Imager Z1 (Zeiss) microscope. We acquired Differential Interference Contrast (DIC) images using a 100x/1.4 oil immersion objective) and a TL Halogen Lamp (3.00 Volt, 900 ms exposure).

Images (1388x1040 pixels, 142.1 μm x 106.48 μm pixel size, 12 Bit) were acquired every second from the moment that the cuticle became loose around the tip of the head until after the worm bursted through the head, which took roughly 5 to 10 minutes. N2 animals were imaged on an Axio Imager Z2 (Zeiss) microscope. We acquired Differential Interference Contrast (DIC) images using a 63x/1.4 oil immersion objective) and a TL Vis-LED Lamp (5.74 Volt, 17 ms (**Figure S4A**) or 19 ms (**Figure S4B**) exposure). Images (1388x1040 pixels, 225.56 μm x 169.01 μm pixel size, 12 Bit) were acquired with 20 seconds ((**Figure S4A**) or 4 seconds (**Figure S4B**) intervals from the moment that the cuticle became loose around the tip of the head until the cuticle was shed.

Single worm imaging

Synchronized L1 animals expressing a transcriptional reporter in the HW2418 background (*grh-1(xe135(grh-1::degron::3xFLAG)) I; xeSi376 [Peft-3::TIR1::mRuby::unc-54 3'UTR, cb-unc-119(+)] III*) were grown on normal OP50-containing agar plates at 20°C for 26 hours until they reached late L2 stage. Single worm imaging chambers were prepared as previously described (Meeuse et al., 2019) with the adaptation that chambers were prepared from 4.5% agarose supplemented with 0.25% ethanol or 250 μM auxin while heating. L2 staged animals were placed in the chambers, covered with a glass cover slip and the imaging slides containing the chambers were prepared as described previously (Meeuse et al., 2019). We imaged the animals using a 2x sCMOS camera model (T2) CSU_W1 Yokogawa microscope with 20x air objective, NA = 0.8 in combination with a 50 μm disk unit and a 488 nm laser. The laser power was set to 70% and binning was set to 2. We used a motorized z-drive with 2 μm step size and 23 images per z-stack and took brightfield and fluorescent images in parallel with 10 min intervals in a ~21°C room.

Single worm imaging data analysis

GFP intensities were quantified using the previously published KNIME workflow (Meeuse et al., 2019). In short, worms are identified in the image by Illastik machine learning, straightened, and the GFP intensity of the worm was max projected to one pixel line for each time point. Background subtracted mean GFP intensities were determined from 20%-80% of the anterior-posterior axis for each time point and values were imported into R for further analysis.

Using ImageJ, we determine the time of molt entry by the first image in which the worm stopped pumping and are quiescent and the time of molt exit was determined by the first image in which the worms resumed pumping in a timeframe close to where the cuticle was shed (Meeuse et al., 2019). Finally, the time of phenotypic onset was scored by the first image in which the pharynx of the worm was bend, after which it usually did not take long before the cuticle was ruptured. We scored bending of the pharynx as the time frame of imaging was sometimes limiting or cuticle rupturing did not occur.

For visualization, GFP intensities were set to $t = 0$ hours at molt 2 exit. GFP intensities from the moment when the phenotype was observed were omitted from plotting. The mean and the SEM were calculated for time points at which the GFP intensities of more than 5 animals were recorded. GFP intensities ≤ 50 were omitted from the calculation of the mean and SEM, as we considered them segmentation errors.

Enrichment analysis

For enrichment of matrisome genes, the online Matrisome Annotator (http://ec2-3-120-159-30.eu-central-1.compute.amazonaws.com:3838/ubuntu/ecm_analyzer/) was used (access date: 18-09-2019). Fold enrichments were calculated in the following way: first, predicted number of ‘hits’ in a given category were calculated by: number of genes in a given category/total number of genes in the *C. elegans genome* * total number of ‘hits’. For simplicity we assume that the total number of genes is 20.000. Second a pseudocount of 12 was added to the predicted number of ‘hits’ and to the actual number of ‘hits’ in a given category. This was done to correct for large enrichments caused by categories with a small number of genes. Finally, the pseudocount corrected ‘hits’ was divided by the pseudocount corrected predicted ‘hits’.

For tissue enrichment, the previously published tissue annotation of (Cao et al., 2017) was used. Genes that are enriched at least 5-fold in a specific tissue compared to the second tissue were selected (ratio ≥ 5 and q-value < 0.05 , n=3926 genes). We calculated the enrichment of tissues in our ‘hits’ over the tissue-annotated genes (n=3926), using a pseudocount of 12.

Statistical analysis

Welch two-sample, two-sided t-tests were performed using the function `t.test (paired=TRUE)` of the package ‘stats’ in R (version 3.5.1).

Supplementary figures

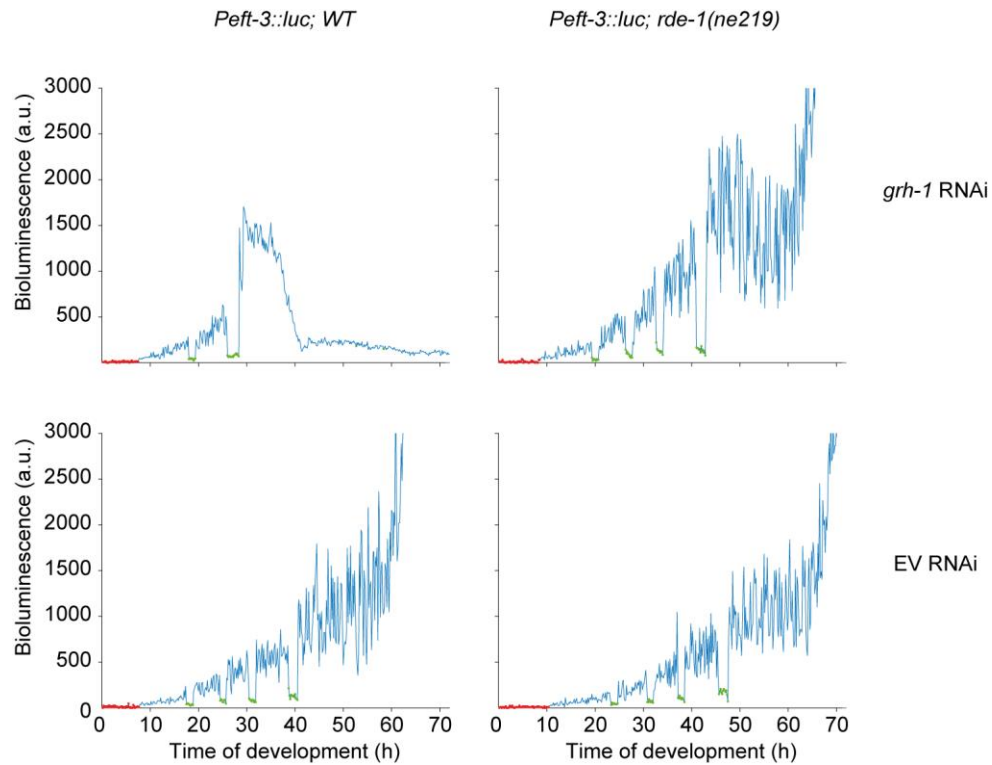
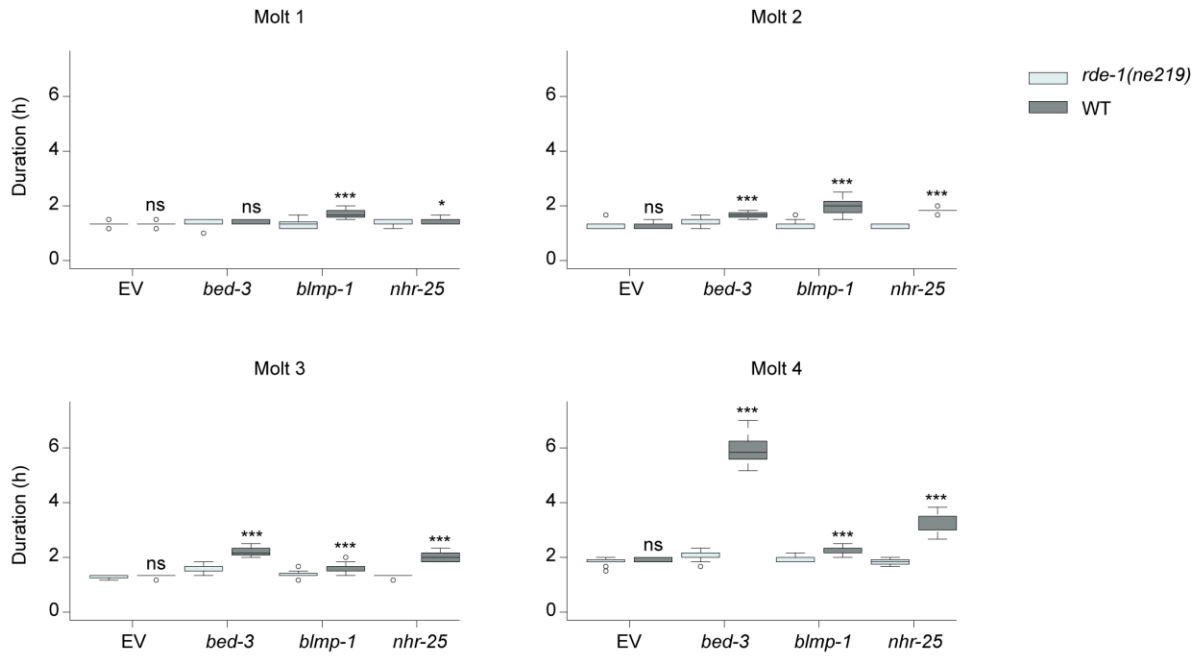


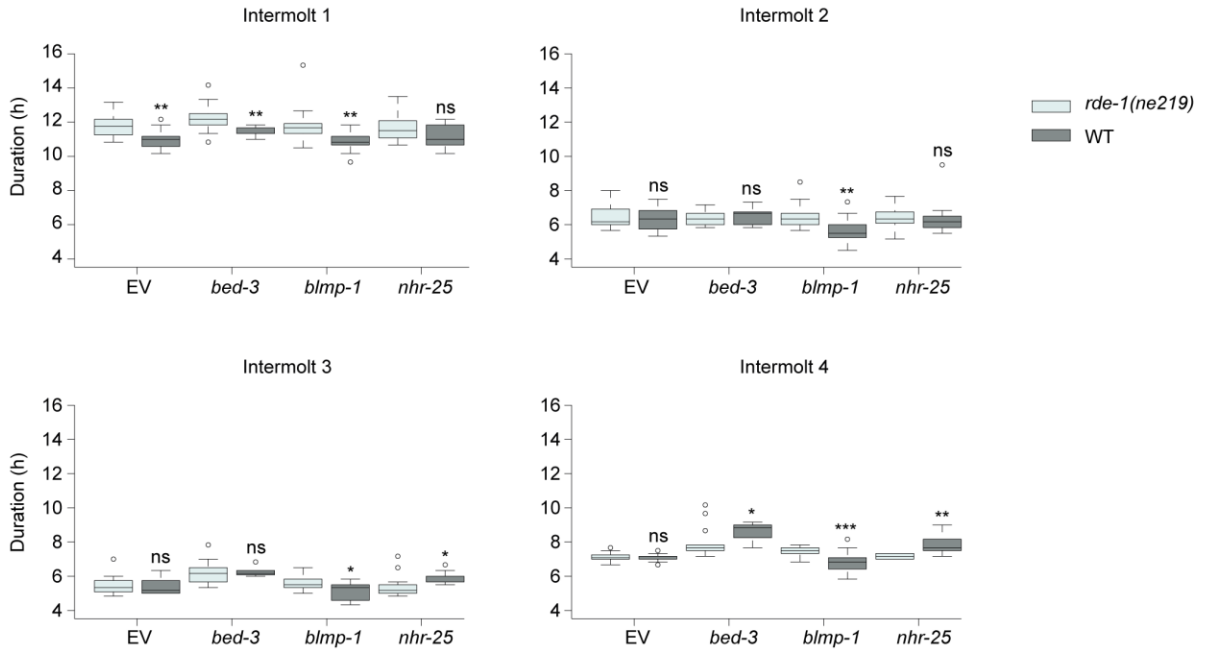
Figure S1: Related to Figure 1 – *grh-1* RNAi caused aberrant progression through development

Representative raw luminescence trace of single animals grown at 20°C for 72 hours. Left column showing wildtype animals and right column RNAi-deficient animals (*rde-1(ne219)*). Animals in upper panel were grown in the presence of *grh-1* RNAi and animals in the lower panel were grown in the presence of mock (empty vector) RNAi. Pre-hatch is indicated in red and molts in green.

A



B



C

	EV	<i>bed-3</i>	<i>blmp-1</i>	<i>nhr-25</i>
I1	0.94 (p=1.99E-03)	0.94 (p=8.52E-03)	0.92 (p=7.11E-03)	0.96 (p=1.07E-01)
M1	1.00 (p=1.00E+00)	1.02 (p=5.75E-01)	1.28 (p=2.09E-07)	1.08 (p=2.65E-02)
I2	0.98 (p=6.69E-01)	1.02 (p=6.22E-01)	0.87 (p=2.82E-03)	1.00 (p=9.37E-01)
M2	0.98 (p=6.18E-01)	1.20 (p=2.36E-04)	1.50 (p=8.86E-08)	1.44 (p=1.65E-13)
I3	0.99 (p=6.92E-01)	1.00 (p=9.05E-01)	0.92 (p=1.16E-02)	1.10 (p=1.28E-02)
M3	1.01 (p=6.81E-01)	1.38 (p=1.16E-06)	1.18 (p=1.42E-04)	1.57 (p=1.63E-10)
I4	1.00 (p=8.03E-01)	1.08 (p=4.85E-02)	0.92 (p=9.41E-04)	1.09 (p=1.25E-03)
M4	1.02 (p=2.81E-01)	2.95 (p=9.64E-08)	1.16 (p=7.04E-08)	1.74 (p=2.14E-09)

Figure S2: Related to Figure 1 – Quantification of candidate mutants showing aberrant duration of developmental stages

A, Quantification of molt durations in RNAi deficient (*rde-1(ne219)*) animals (light grey) and wildtype animals (dark grey) grown in the presence of mock, *bed-3*, *blmp-1* or *nhr-25* RNAi. Significant differences relative to *rde-1(ne219)* for each RNAi condition are indicated.

B, Quantification of intermolt durations in RNAi deficient (*rde-1(ne219)*) animals (light grey) and wildtype animals (dark grey) grown in the presence of *EV*, *bed-3*, *blmp-1* or *nhr-25* RNAi. Significant differences relative to *rde-1(ne219)* for each RNAi condition are indicated.

C, Fold change of mean stage durations and p-value in brackets in wildtype over RNAi-deficient animals.

ns: not significant, * p<0.05, ** p<0.01, *** p<0.001, Welch two-sample, two-sided t-test.

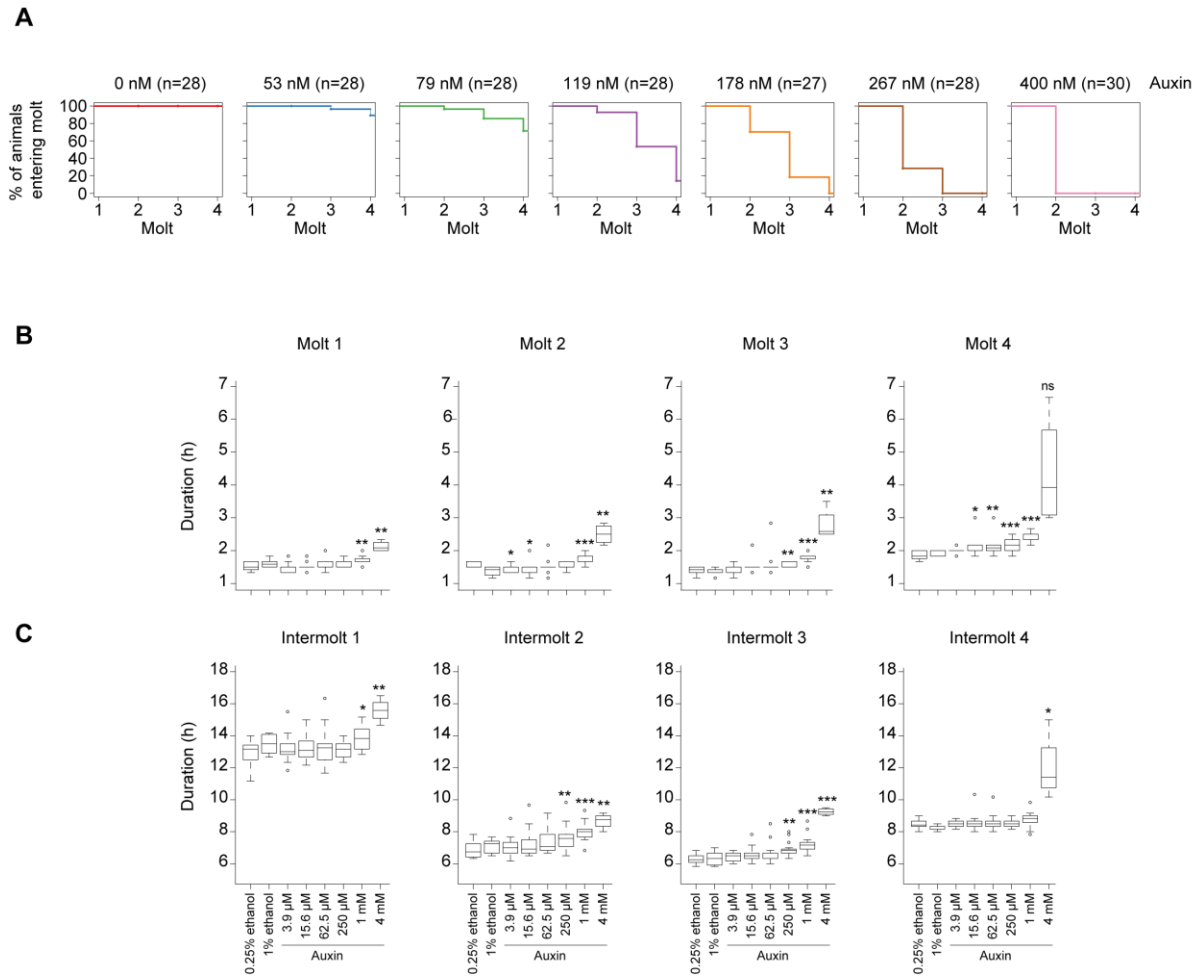


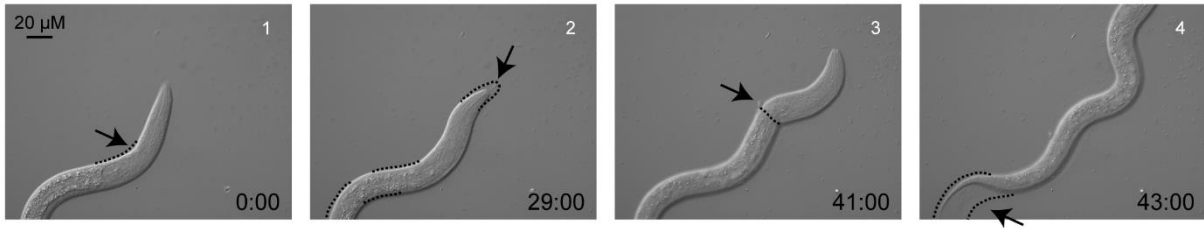
Figure S3: Related to Figure 2 – Lethality reveals dose-response effect on auxin and high auxin concentrations cause non-specific defects in strain without *grh-1::degron*

A, Quantification of the percentage of *grh-1(xe135); pef3::luc; pef3::tir-1* animals (HW2434) that enter each of four molts upon increasing indicated concentrations of auxin. Molts in single animals grown at 20 °C were determined as in **Figure S1**. For concentrations up to 250 μ M, similar results as for 400 nM were observed (data not shown).

B, Boxplots showing duration of each molt for indicated concentrations of auxin in *peft-3::tir-1; pef3::luc* animals (HW1984). Differences relative to 0.25% ethanol (0 nM auxin) for 3.9 μ M-1mM auxin and relative to 1% ethanol (0 nM auxin) for 4 mM auxin are indicated (ns: not significant, * $p < 0.05$, ** $p < 0.01$, *** $P < 0.001$, Welch two-sample, two-sided t-test).

C, Boxplots showing duration of each intermolt for indicated concentrations of auxin in *peft-3::tir-1; pef3::luc* animals (HW1984). Differences relative to 0.25% ethanol (0 nM auxin) for 3.9 μ M-1mM auxin and relative to 1% ethanol (0 nM auxin) for 4 mM auxin are indicated (ns: not significant, * $p < 0.05$, ** $p < 0.01$, *** $P < 0.001$, Welch two-sample, two-sided t-test).

A



B

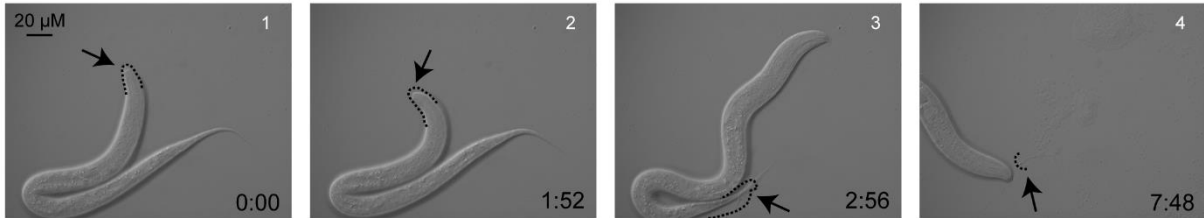


Figure S4: Related to Figure 2 – Molting in wildtype animals

Image sequence of N2 animal during M1. Animals were transferred to an agar-pad containing microscopy slide and images were collected using DIC, 63x magnification, Z2 microscope. Selected images are shown. Two different sequences of events were observed. In A, the pharyngeal lining is removed prior to ecdysis. In B, Pharyngeal lining is expelled after crawling out of the cuticle. Dashed lines indicate loosened cuticle. Arrows indicate specific features of the molt:

- A, 1. Loosened cuticle, 2. Detachment of pharyngeal lining, 3. Crawling out of cuticle, 4. Final crawling out of cuticle
B, 1. Loosened cuticle, 2. Back-and-forth movements, 3. Crawling out of cuticle with pharyngeal lining still attached, 4. Pharyngeal lining expelled.

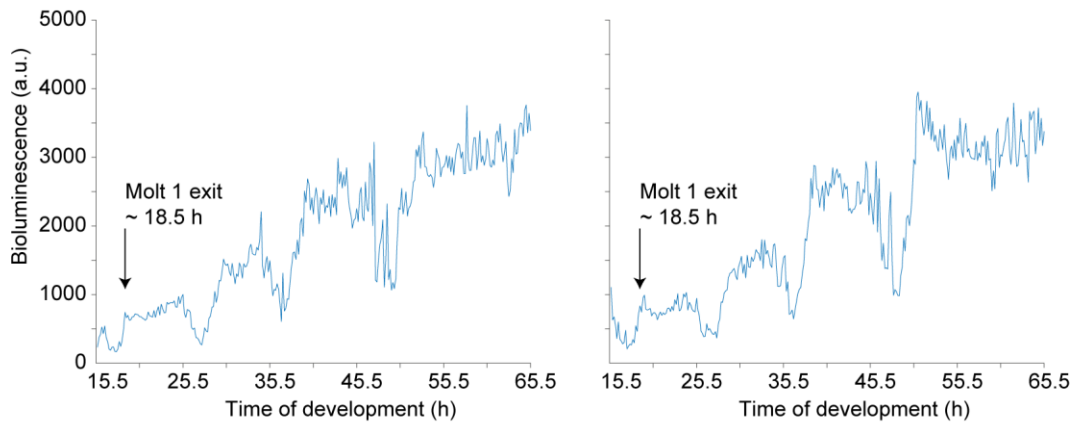
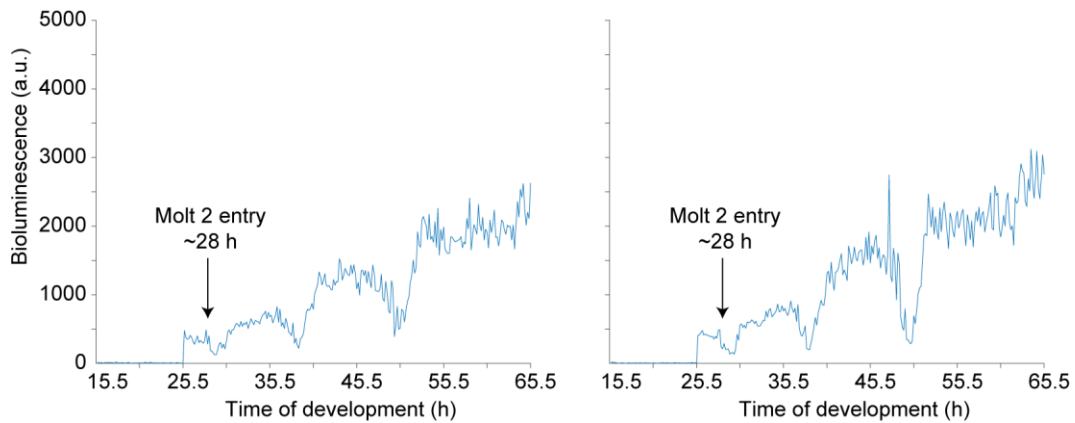
A**B**

Figure S5: Related to Figure 3 – Determination of molt occurrence by luciferase assay

Representative luminescence traces of a population of 5-10 HW2434 animals in duplicates. As a population of animals was used in this assay, note that the transitions between molt and intermolt are less sharp compared to single animal assays. As worms might develop differently in the luciferase assay compared to the liquid culture we used to obtain Western Blot samples (**Figure 3**), we consider only the first hours after starting the luciferase assay to be representative for developmental timing in the liquid culture. Hence, we sampled a small population of worms from the liquid culture at 15.5 hours (A), i.e. close to the first molt, and at 25.5 hours (B), i.e. close to the second molt, and left them to develop in the luminometer to detect the first molt and the second molt respectively.

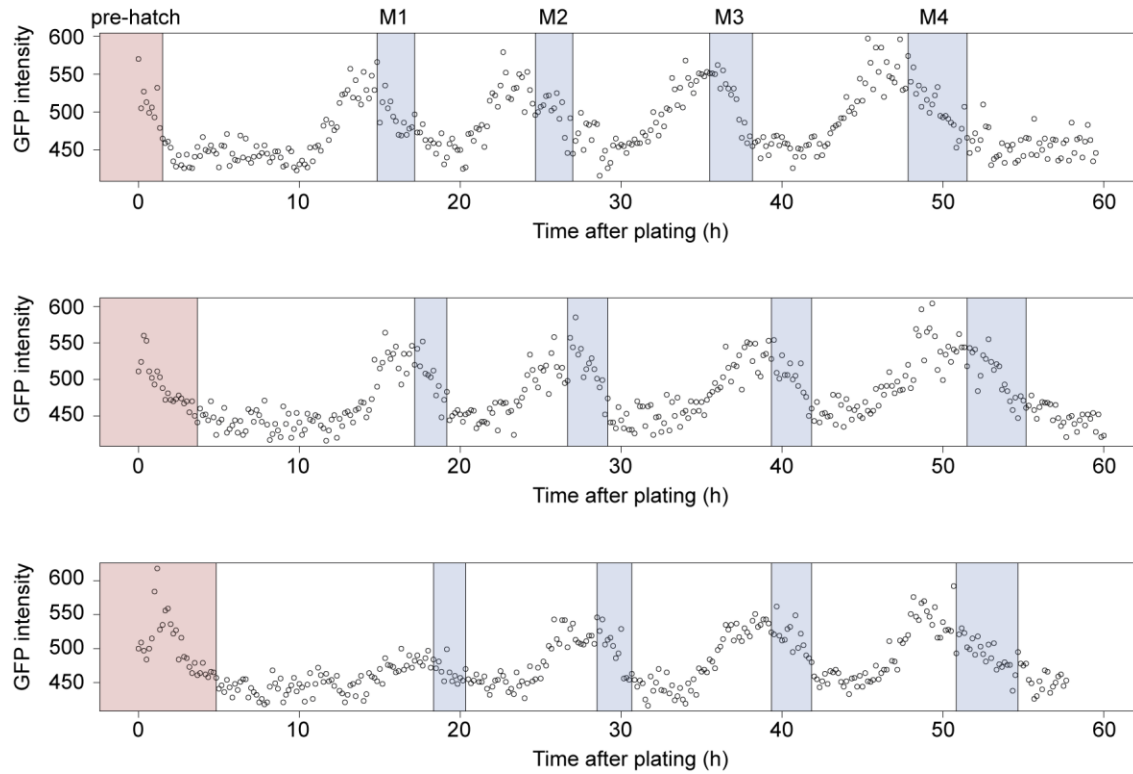


Figure S6: Related to Figure 3 – Quantification of GFP intensities of hypodermal cells in three individual animals

Quantification of GFP intensities in single animals expressing GRH-1::GFP (HW2603) grown in micro-chambers, shown in **Figure 3C**. GFP intensity was determined by manual selection of a hypodermal cell for each time point and quantification of the maximum intensity. T = 0h corresponds to the time of plating. Pre-hatch (red) and molts (blue) are indicated.

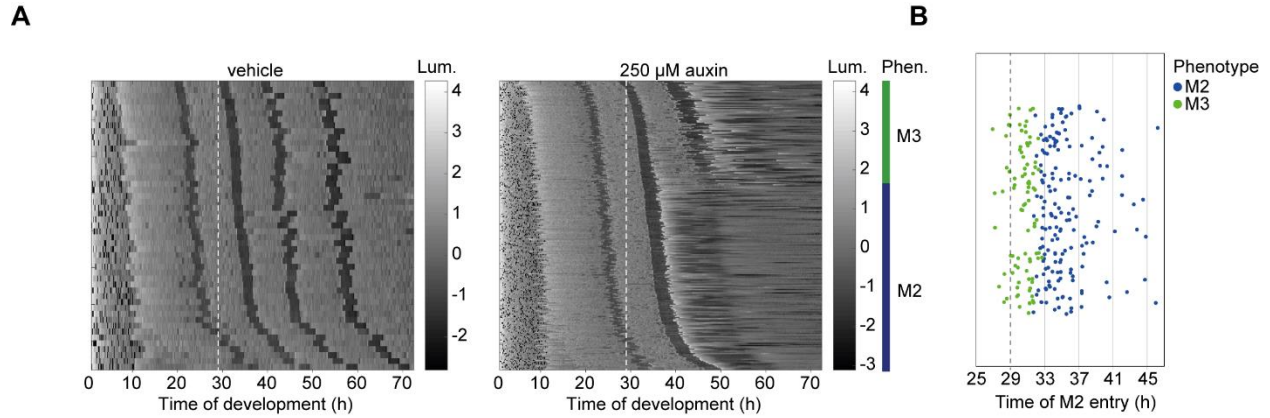


Figure S7: Related to Figure 4 - Lethality is dependent on the time of GRH-1 depletion

A, Heatmap showing trend-correct luminescence (Lum) of *grh-1(xe135); peft-3::luc; peft-3::tir-1* animals (HW2434) treated with vehicle (0.25% ethanol, left panel) or 250 μM auxin (right panel) at 29 hours (white dashed line). Luminescence traces are sorted by entry into M2. Black corresponds to low luminescence occurring during lethargus (molt). Embryos of various stages were left to hatch and develop during the assay. Note that early hatched animals are in top rows and late hatched animals are in bottom rows. Appearance of M3 phenotype (green bar) and M2 phenotype (blue bar) are indicated for auxin-treated animals. Animals were assigned to M2 phenotype when M2 was the last observed molt in the luminescence trace.

B, Quantification of time at which animals enter molt 2 (M2 entry). Dots (jittered in y) represent individual animals and are colored according to phenotype determined in A. Dotted line indicates when auxin was added.

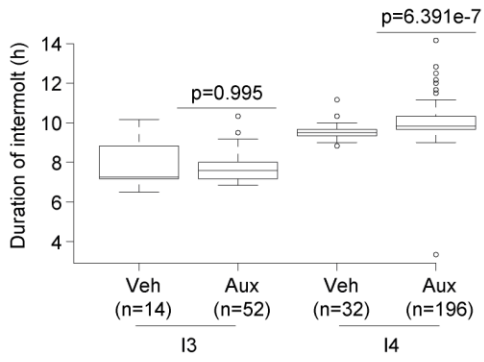
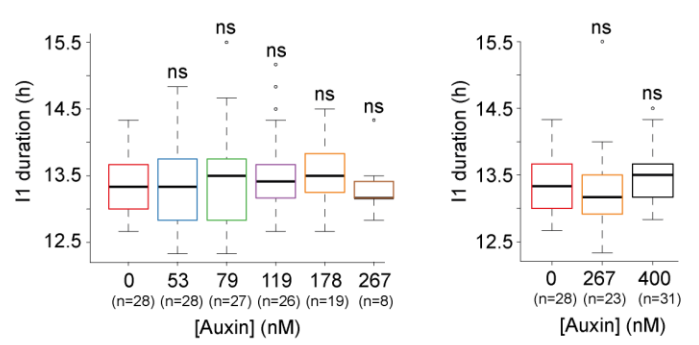
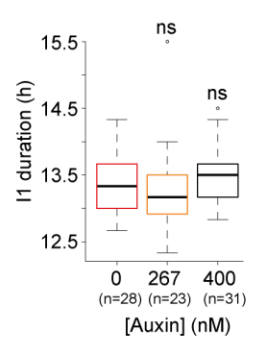
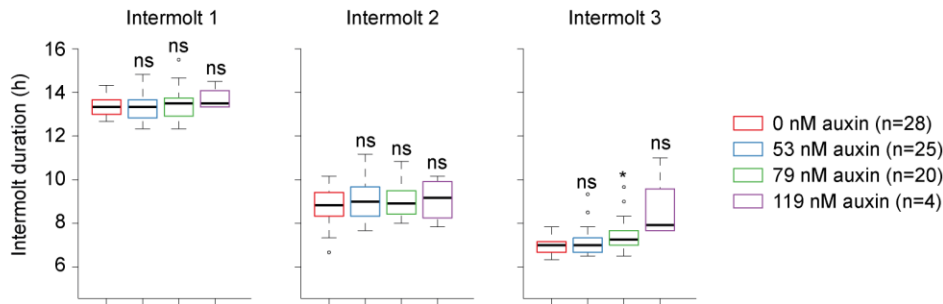
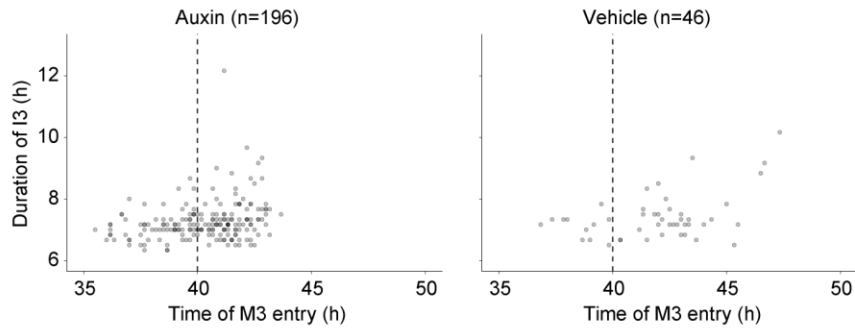
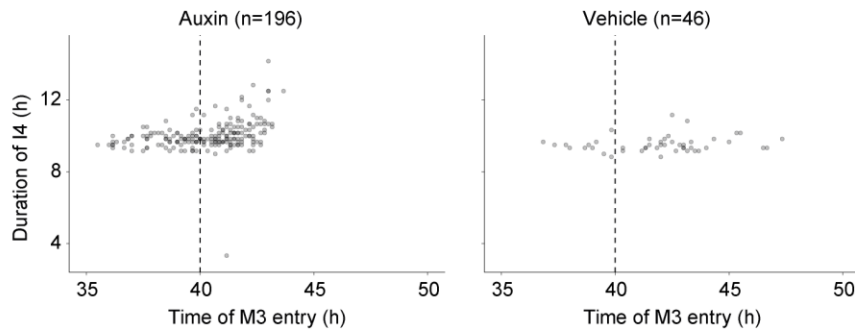
A**B****C****D****E****F**

Figure S8: Related to Figure 4 and 5 – Intermolt is not affected by timing or extend of GRH-1 depletion

A, Quantification of intermolt duration for vehicle treated animals (Veh) and auxin treated animals (Aux) from **Figure 4A,B** and **Figure 5A**. To resemble life history, vehicle-treated animals with M3 entry > 43h were selected for I3 quantification and animals with M3 entry \leq 43h were selected for I4 quantification. P-values are indicated.

B, Boxplot showing the duration of the first intermolt of animals treated with indicated concentrations of auxin (**Figure 5B**). Animals that revealed lethality at M1 were excluded. Significant differences relative to 0 nM auxin are indicated.

C, Boxplot showing duration of first intermolt for vehicle-treated animals and animals treated with 267 nM and 400 nM auxin (**Figure 5C**). For auxin-treated animals, only those who showed a phenotype at M1 were selected. Significant differences relative to 0 nM auxin are indicated.

D, Boxplot showing the duration of I1, I2 and I3 of animals treated with indicated concentrations of auxin (**Figure 5D**). Animals that revealed lethality at M1, M2 or M3 were excluded. Significant differences relative to 0 nM auxin are indicated.

E, Quantification of durations of I3 over the time of entering M3 respectively. Data is shown for ‘M4 phenotype’ animals and all vehicle-treated animals from **Figure 4A** and **Figure 5D**. Dashed line indicates treatment with 250 μ M auxin or vehicle at 40 hours after plating.

F, Quantification of durations of I4 over the time of entering M3 respectively. Data is shown for ‘M4 phenotype’ animals and all vehicle-treated animals from **Figure 4A** and **Figure 5D**. Dashed line indicates treatment with 250 μ M auxin or vehicle at 40 hours after plating.

P-values were determined by Welch two-sample, two-sided t-test. * $p < 0.05$, ** $p < 0.01$, *** $p < 0.001$

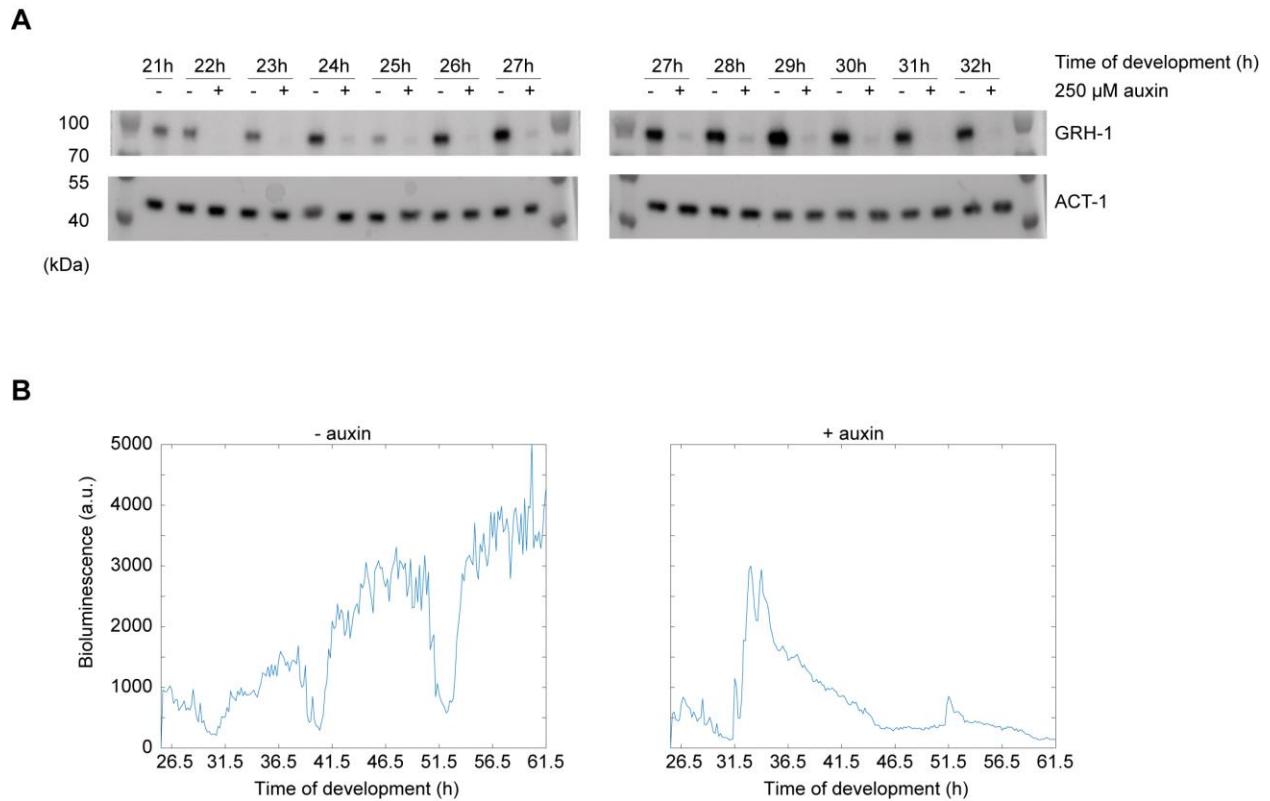


Figure S9: Related to Figure 6 – Degradation of GRH-1 in L2 and manifestation of M2 phenotype

A, Western blot analysis of HW2434 animals using anti-FLAG antibody. ACT-1 was used as loading control. Time points represent time of development of a synchronized population in liquid culture at 20°C with start of the culture at t=0 hours. After the first sample was taken at 21 hours, the culture was split and 250 μ M auxin (+ auxin) or 0.25% ethanol (-auxin, vehicle control) was added. Time point 27 hours was loaded on both gels.

B, Representative luminescence traces of a population of 5-10 HW2434 animals. As a population of animals was used in this assay, note that the transitions between molt and intermolt are less sharp compared to single animal assays. As worms might develop differently in the luciferase assay compared to the liquid culture we used to obtain sequencing samples (**Figure 6**) and Western blot samples (in A), we consider only the first hours after starting the luciferase assay to be representative for developmental timing in the liquid culture. Hence, we sampled a small population of worms from the liquid culture at 25.5 hours, i.e. close to the second molt, and left them to develop in the luminometer to detect the third molt respectively. We estimated the molt to occur between 29 and 31 hours of development.

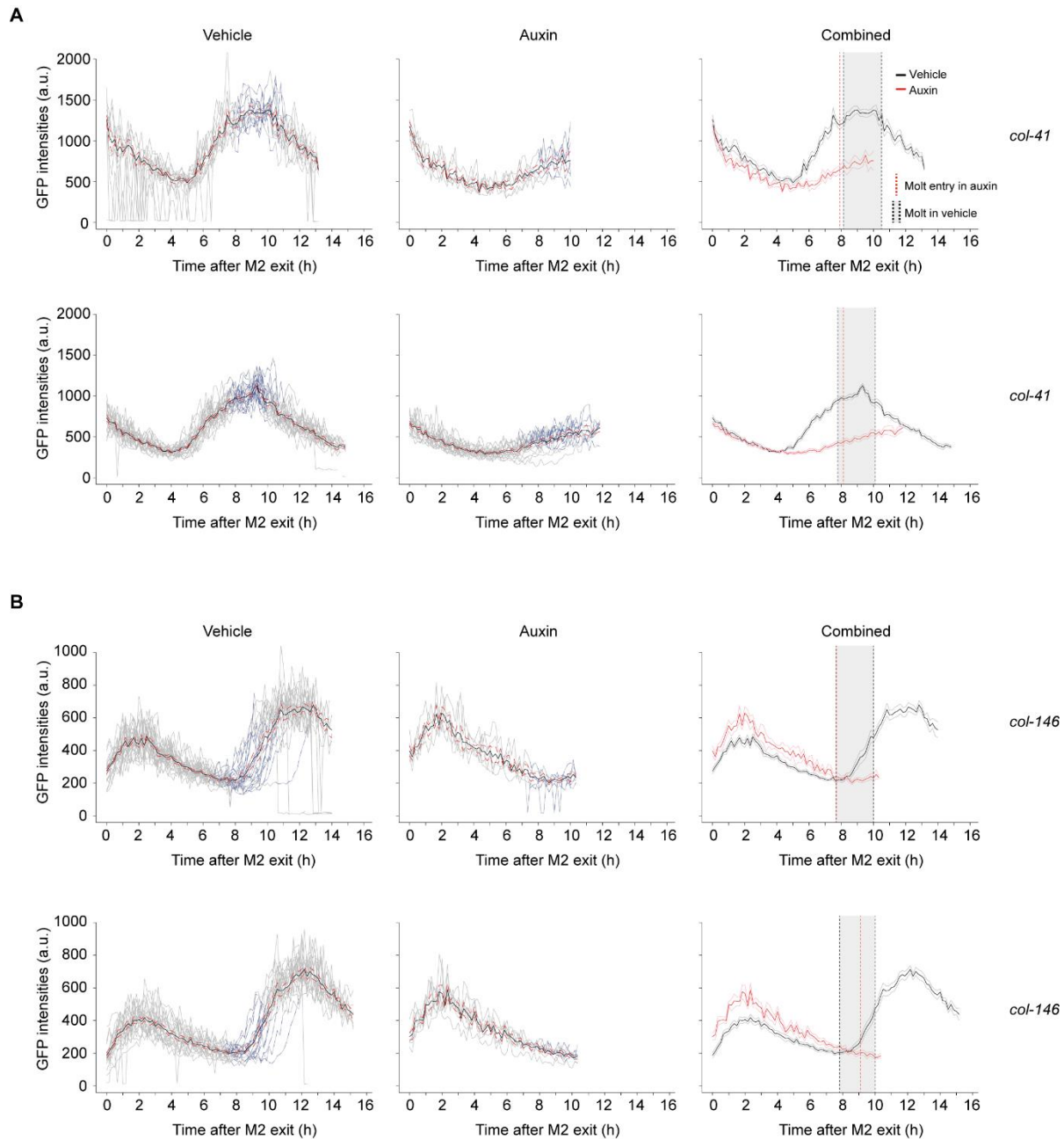


Figure S10: Related to Figure 7 – GFP intensities *col-41* and *col-146* reporters

Quantification of GFP intensity of single vehicle-treated ('vehicle') or 250 μ M auxin-treated ('auxin') animals over L3 stage, starting from M2 exit ($t = 0$ hours). Animals express GFP::H2B::PEST::UNC-54 3'UTR driven from the indicated promoters (A, *col-41*; B, *col-146*) in the *grh-1::aid* background. GFP intensity traces of single animals (grey), M3-entry to M3-exit (blue), mean (black) and SEM (red) are indicated. The panel 'combined' shows the mean and SEM for vehicle-treated (black) and auxin-treated (red) animals. Mean molt 3 entry and mean molt 3 exit in vehicle-treated (grey box) and mean molt 3 entry in auxin-treated (red dotted line) animals are indicated. Mean and SEM for time points with more than 5 animals are shown. GFP intensities after the appearance of the phenotype in auxin-treated animals are not shown. GFP intensities ≤ 50 were omitted from mean and SEM.

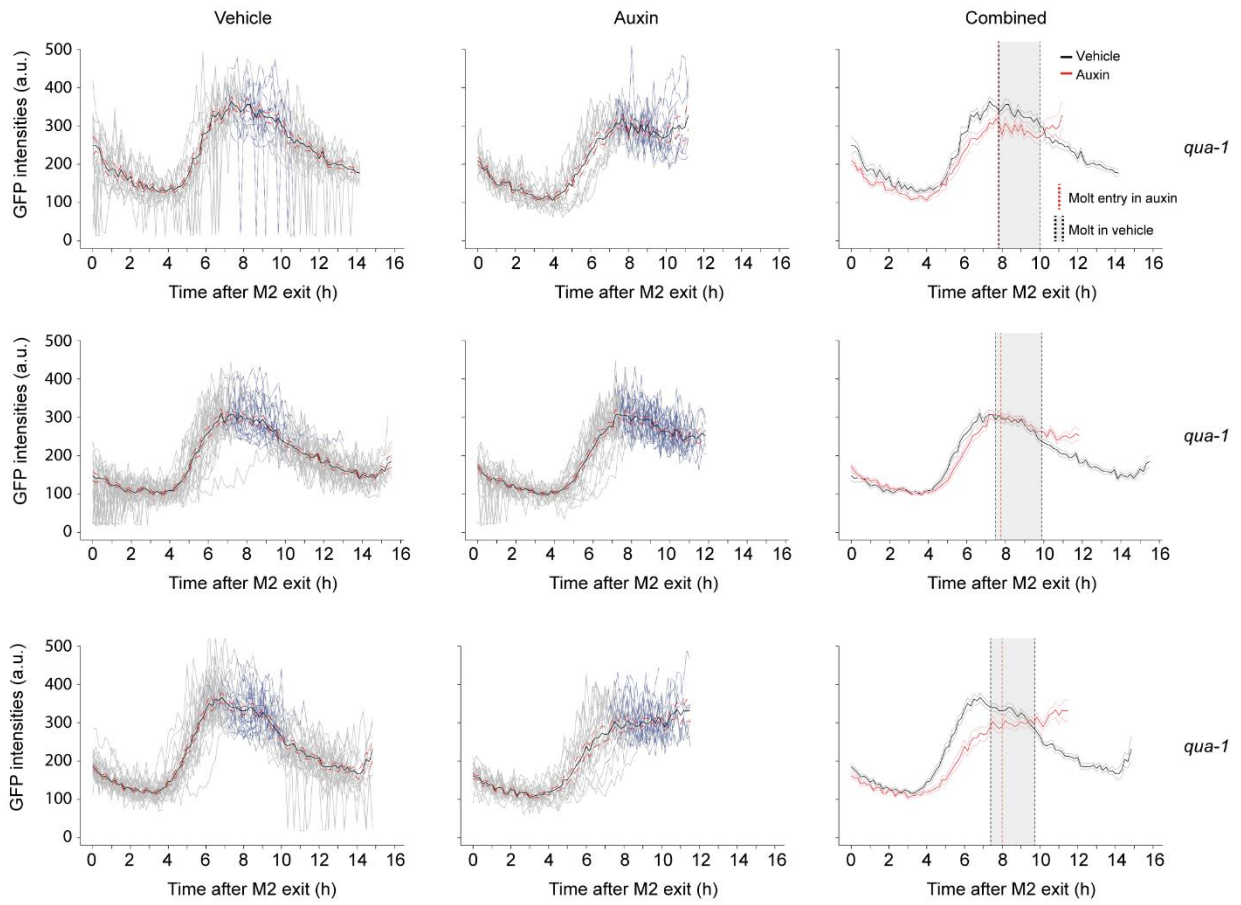
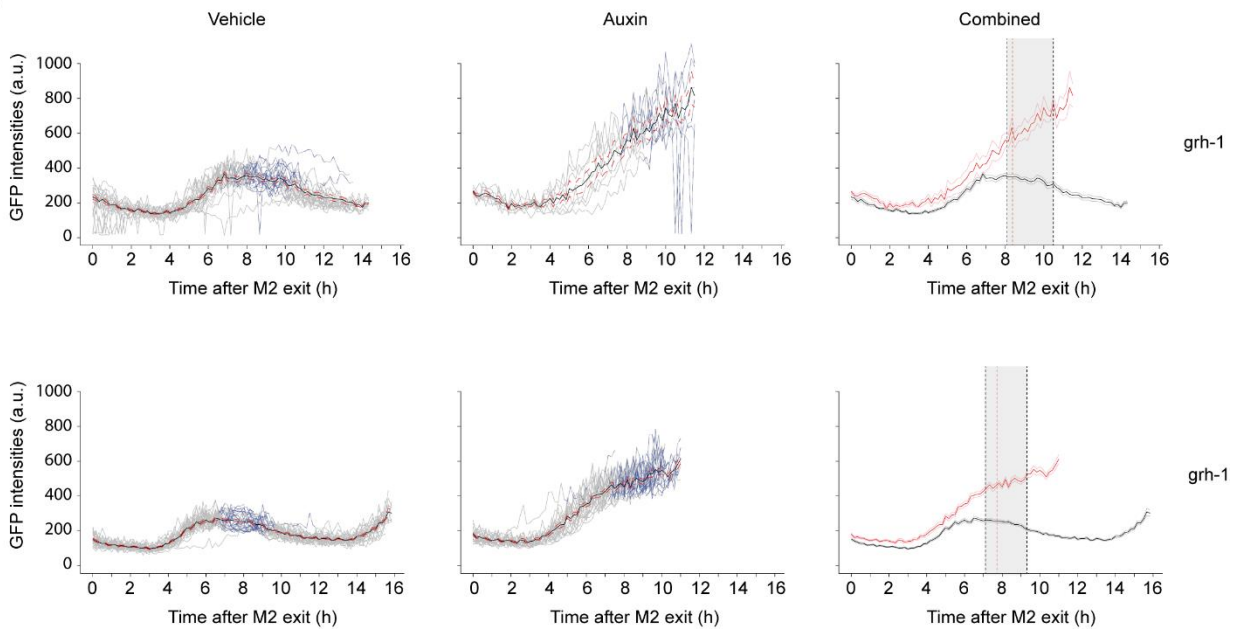
A**B**

Figure S11: Related to Figure 7 – GFP intensities *qua-1* and *grh-1* reporters

Quantification of GFP intensity of single vehicle-treated ('vehicle') or 250 μ M auxin-treated ('auxin') animals over L3 stage, starting from M2 exit ($t = 0$ hours). Animals express GFP::H2B::PEST::UNC-54 3'UTR driven from the indicated promoters (A, *qua-1*; B, *grh-1*) in the *grh-1::aid* background. GFP intensity traces of single animals (grey), M3-entry to M3-exit (blue), mean (black) and SEM (red) are indicated. The panel 'combined' shows the mean and SEM for vehicle-treated (black) and auxin-treated (red) animals. Mean molt 3 entry and mean molt 3 exit in vehicle-treated (grey box) and mean molt 3 entry in auxin-treated (red dotted line) animals are indicated. Mean and SEM for time points with more than 5 animals are shown. GFP intensities after the appearance of the phenotype in auxin-treated animals are not shown. GFP intensities ≤ 50 were omitted from mean and SEM.

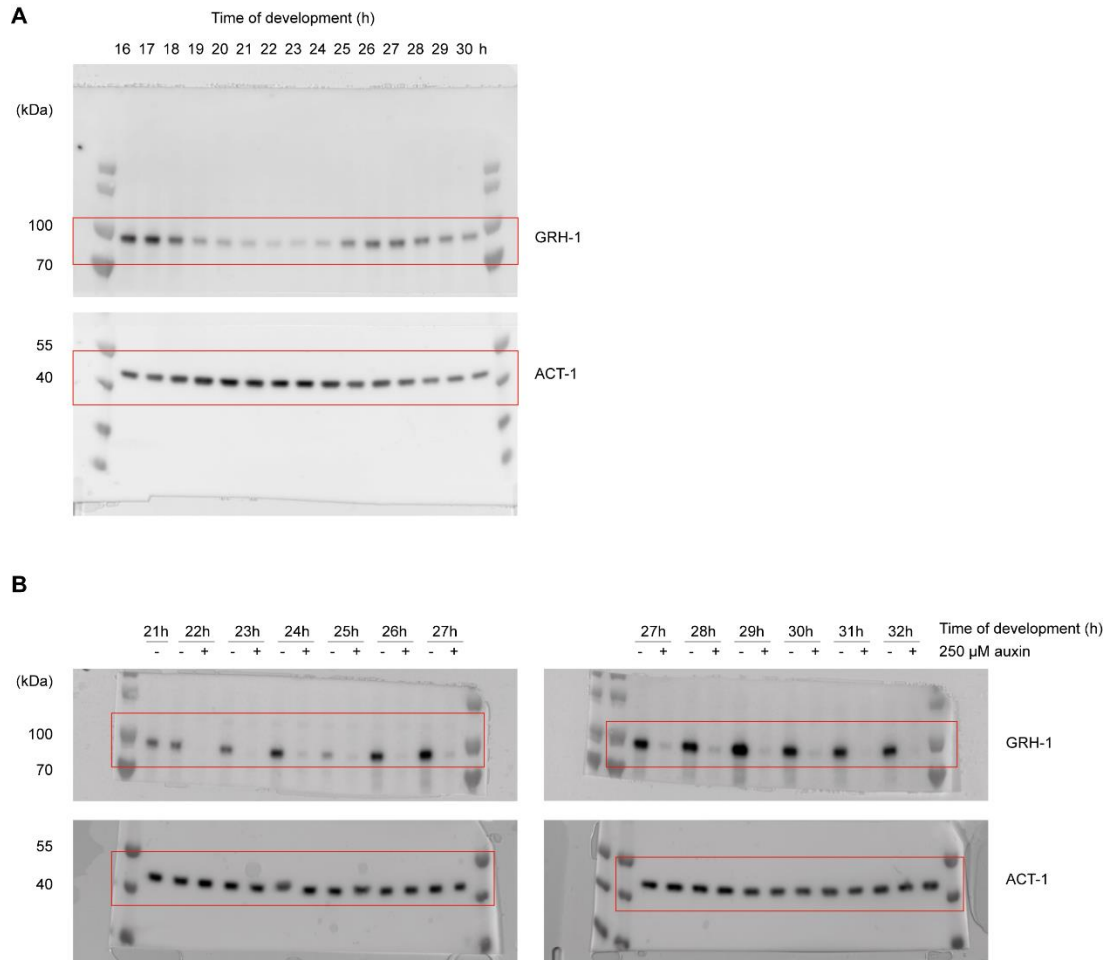


Figure S12: Uncropped Western blots

A, Uncropped Western blot of **Figure 3A**.

B, Uncropped Western blot of **Figure S9A**.

[end of manuscript]

2.5 Characterization of *myrf-1*, *nhr-25*, and *blmp-1*

Milou Meeuse and Helge Grosshans conceived the project. MM generated the strains, with help from Lan Xu and Iskra Katic with the microinjections. IK designed and generated the *blmp-1::degron* strain. MM performed the *nhr-25* and *blmp-1* luciferase experiments. Kathrin Braun performed the *myrf-1* experiments. The *blmp-1::degron* RNA-seq experiment was a joined effort of MM and Yannick Hauser. Dimos Gaidatzis performed the computational fusion of the *blmp-1::degron* time course which was sequenced in two batches. MM analyzed the experiments, under HG's supervision.

In addition to *grh-1*, we identified *myrf-1*, *nhr-23*, *nhr-25*, *bed-3*, *blmp-1* and *ztf-6* in our RNAi screen for aberrant progression or duration of developmental stages. These phenotypes may arise from stage-specific or more general developmental defects, or, alternatively, it is possible that these transcription factors are required for recurring developmental events. Although these transcription factors oscillate on the mRNA level (Hendriks et al., 2014), whether their activity is rhythmic and important for their function remains to be established. Moreover, whether and how they control repetitive developmental processes is unclear. Here, I aimed to address these questions in further detail for *myrf-1*, *nhr-25* and *blmp-1*. Hence, we performed experiments similar to those we have carried out for *grh-1* (see **GRH-1 manuscript**). Thus, we investigated the phenotypes resulting from partial and timed degradation of MYRF-1, NHR-25 and BLMP-1, using the auxin-inducible degradation system (AID). Whereas timed degradation may provide insight into whether and when the transcription factor is repetitively required, partial degradation may reveal additional phenotypes, which will help to better understand its functional relevance.

2.5.1 Loss of MYRF-1 prevents shedding of the cuticle in L1 stage

In our RNAi screen, we observed that RNAi against *myrf-1*, homolog of the transcription factor Myelin Regulatory Factor (Myrf), resulted in failure to complete larval development (**GRH-1 manuscript, Figure 1**). Specifically, 50% of the animals arrested at L2 stage and an additional 20% at L3 stage. A similar phenotype has been observed previously, i.e. homozygous progeny of a balanced *myrf-1(0)* strain revealed a fully penetrant L1 arrest (Russel et al., 2011, named *pqn-47*, later renamed to *myrf-1*). We suspected that RNAi was not strong enough to fully recapitulate the phenotype of the null mutant. Hence, I aimed to validate our results from the screen and the previously published phenotype (Russel et al., 2011) using an approach that allows the modulation of MYRF-1 levels. To this end, we degron-tagged *myrf-1* endogenously, and investigated its phenotype after MYRF-1 degradation mediated by auxin. Using DIC, we imaged the first molt of synchronized animals grown on auxin-containing plates (**Figure 2.6**).

Similar to previous observations in *myrf-1(0)* mutants, depletion of MYRF-1 resulted in an L1 arrest, followed by lethality. Similar to wild-type animals (**Figure S4 in GRH-1 manuscript**), behavioral quiescence was observed and apolysis occurred, hence MYRF-1-depleted animals entered the molting process normally (data not shown). Next, the cuticle became completely disconnected from the underlying tissue in the head (black arrows) and tail region (white arrows), which suggested to us that ecdysis was initiated (**Figure 2.6**). However, the cuticle did not break and animals failed to dislodge the pharyngeal lining (**Figure 2.6**, red arrows). Hence, they appear starved and eventually died from being trapped in the cuticle.

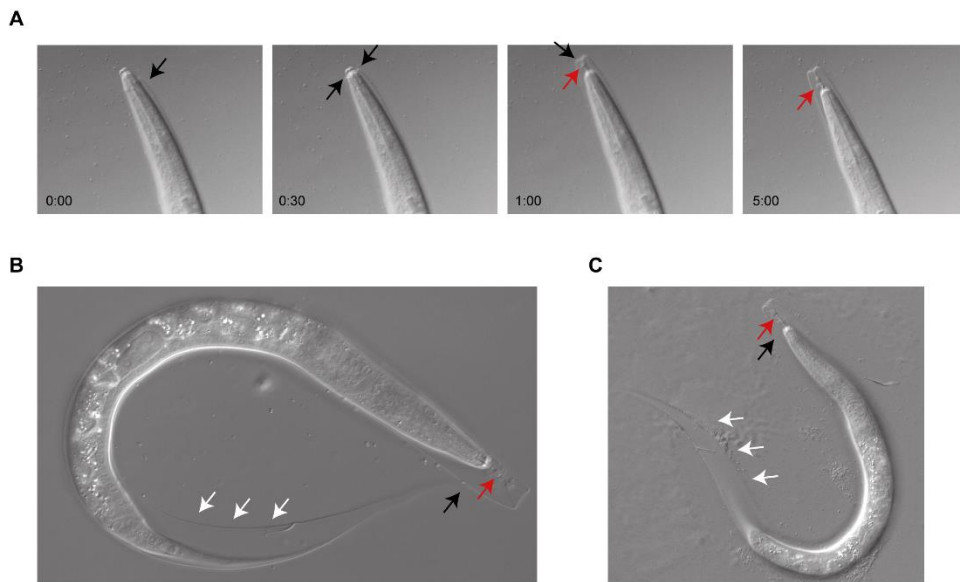


Figure 2.6: MYRF-1 depletions prevents dislodgement of pharyngeal lining and shedding of the cuticle

A, Image sequence of L1 synchronized *myrf-1(xe161); peft-3::tir-1; peft-3::luc* animal (HW2634) plated on 1 mM auxin-containing plates, grown at 20°C. Animals were transferred to an agar-pad containing microscopy slide and images were collected every 30 sec, using DIC, 63x magnification. Selected images are shown. Time min:sec is indicated.

B-C, Images of *myrf-1(xe161); peft-3::tir-1; peft-3::luc* animals (HW2634) grown under same conditions as in A. Animals were imaged using DIC, 63x magnification (B) and 40x magnification (C).

Black and white arrows indicate loose cuticle in head and tail region respectively. Red arrows indicate connected pharyngeal lining.

2.5.2 Activity of MYRF-1 is required in multiple larval stages

Given the L1 lethality, we wondered, on the one hand, whether lethality can be observed in other larval stages, and on the other hand, whether other phenotypes would arise, when MYRF-1 is depleted to a lesser extent. Hence, we added different concentrations of auxin and monitored developmental progression using the luciferase assay. We observed two distinct luciferase traces for high auxin concentrations (**Figure 2.7A**). In the one luciferase trace, we detected a prolonged L1, followed by a spike in luminescence (hereafter called type I traces). In the other luciferase trace, we could not observe a molt but a 'spiky' L1 stage instead (hereafter called type II traces). On lower concentrations of auxin, we also observed type I and type II traces, not only in L1, but also in L2 or L3 stage. If type I or type II traces were observed in L2 or in L3, the preceding stages in same animal appeared normal (**Figure 2.7A**). As luminescence levels can increase by other means than resumption of feeding, e.g. when the cuticle becomes penetrant for auxin, the spikes in luminescence may reflect cuticle defects.

Given that we observed high penetrance of the L1 arrest followed by lethality by visual inspection of animals grown on auxin-containing plates (**Figure 2.6**), we predict that both types of traces reflect dying worms, and we consider distinct phenotypes to be less likely. Hence, we quantified the lethality as the appearance of type I or type II traces upon different concentrations of auxin. We found that the appearance of the lethality was dependent on the concentration of auxin (**Figure 2.7B**). The fact that lethality appeared not only in L1, but also in L2 and L3 stages, suggests that MYRF-1 activity is not only required for the completion of L1 stage, but also for additional stages.

2.5.3 Larval stage durations were not affected on low auxin concentrations in *myrf-1::degron* animals

To investigate whether MYRF-1 depletion results in additional developmental phenotypes, we quantified the molt and intermolt durations in animals that did not arrested and died during any of the larval stages (**Figure 2.7B**, 'not'). We observed that molt and intermolt durations seemed not, or at most minimally, affected by MYRF-1 depletion (**Figure 2.7C,D**). It remains possible that MYRF-1 depletion was not sufficient in these animals to reveal additional developmental phenotypes. Alternatively, MYRF-1 might not be required for normal duration of larval stages. (The durations of larval stages in which lethality was observed was difficult to assess, because phenotypic traces were spiky and we failed to identify the molt in these traces. Hence, future experiments should address the question of whether the duration of the stage in which lethality is observed is affected in MYRF-1-depleted animals.)

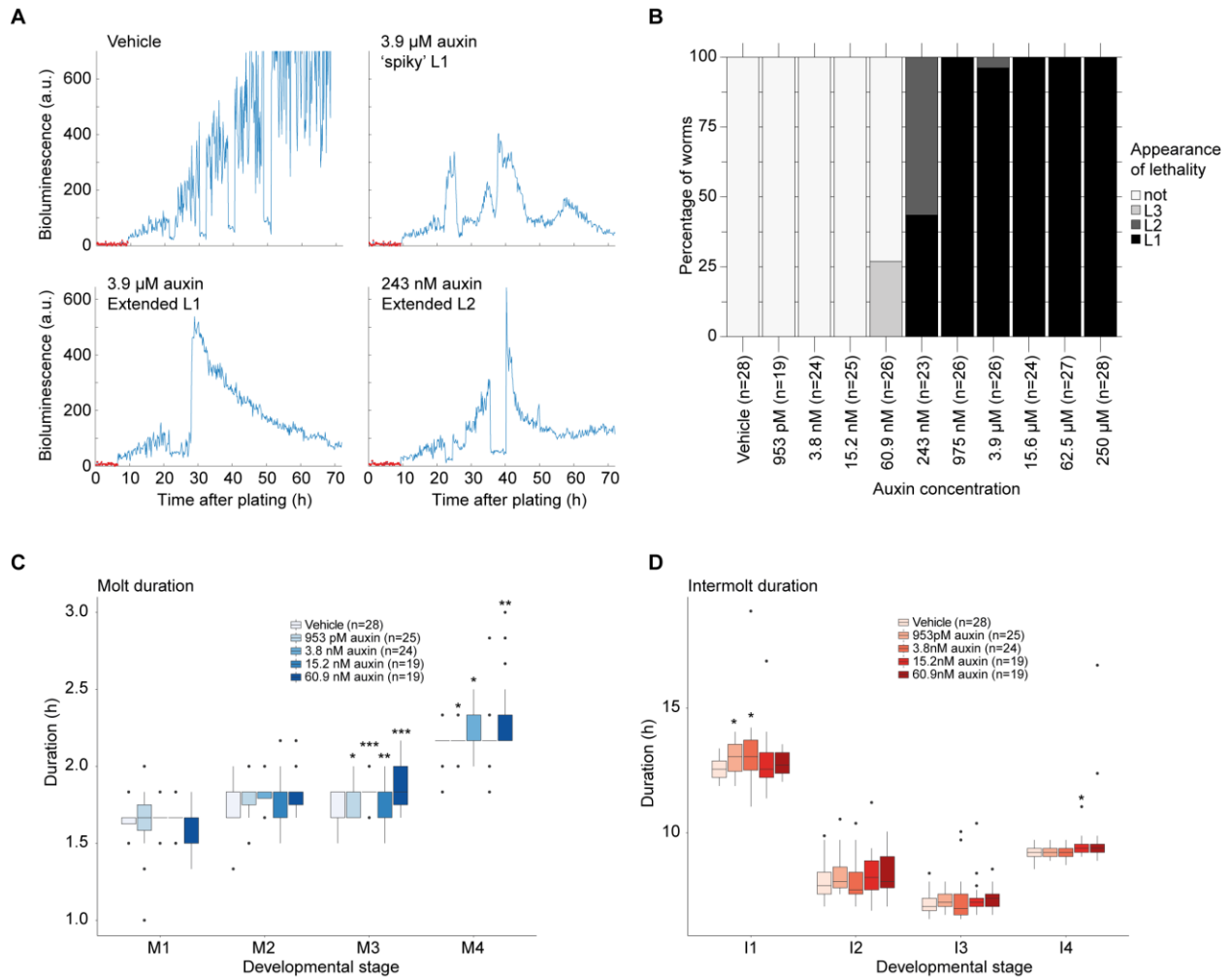


Figure 2.7: Lethality is dependent on the extent of MYRF-1 degradation

A, Representative luciferase traces of *myrf-1(xe161); peft-3::tir-1; peft-3::luc* animal (HW2634) treated with indicated concentrations of auxin.

B, Quantification of lethality on indicated auxin concentration range. Not: lethality is not observed, i.e. animals progressed through development completely. L3: normal development in L1 and L2 stage, followed by L3 lethality. L2: normal development in L1 stage, followed by L2 lethality. L1: L1 lethality.

C-D, Quantification of molt (C) and intermolt (D) duration of animals in B for which no lethality was observed ('not' in B) was observed. P-values were determined by Welch two-sample, two-sided t-test. * $p < 0.05$, ** $p < 0.01$, *** $p < 0.001$

2.5.4 Oscillatory MYRF-1 activity might be required for shedding the cuticle

Given that *myrf-1* oscillates on the mRNA level (Hendriks et al., 2014) and that MYRF-1 appears to be required not only for completion of L1, but also for other larval stages, I aimed to investigate whether its activity is also rhythmic. We expect that if activity of MYRF-1 were oscillating, MYRF-1 would be required for some and dispensable for other times within one larval stage. To this end, we used the *myrf-1::degron* strain to conditionally deplete MYRF-1. We initiated MYRF-1 degradation at variable times in L1 and L2 (**Figure 2.8A,B**), or L2 and L3 (**Figure 2.8D,E**) by adding auxin. We used an auxin concentration, i.e. 250 μ M, for which we observed fully penetrant lethality in L1 stage (**Figure 2.7B**). Sorting animals by entry of molt 1, we observed that onset of lethality was dependent on the time of auxin addition (**Figure 2.8A,D**). If auxin was added later than three hours after M1 exit, we never observed L2 lethality (**Figure 2.8C**). If auxin was added earlier than three hours after M1 exit, we observed mostly, but not always L2 lethality (**Figure 2.8C**). Thus, initiation of MYRF-1 depletion earlier than 3 hours after M1 exit is required to induce L2 lethality, whereas initiation of MYRF-1 depletion later than 3 hours after M1 is not sufficient to induce L2 lethality. Similar results were obtained when comparing the time of M2 exit with the onset of lethality in L3 and L4 stage (**Figure 2.8F**). (We note that we observed more, but not exclusively, type I traces in **Figure 2.8A**, whereas animals in **Figure 2.8D** revealed more, but not exclusively, type II traces. How the two types of luminescence traces arise in MYRF-1-depleted animals is unclear.) We consider two possible explanations. First, it is possible that MYRF-1 activity is required during the period leading up to the molt (3h after exit of the previous molt), but the onset of MYRF-1 degradation during this window was not sufficient to induce lethality. Alternatively, MYRF-1 activity is not required during the period leading up to the molt, and hence its depletion does not result in a phenotype. Given that the AID systems has been shown to rapidly degrade proteins (Zhang et al., 2015), and *myrf-1* accumulation peaks roughly at 2 hours after molt exit (Hendriks et al., 2014), our data is consistent with the first hypothesis. However, in the absence of further data, we can only speculate about a requirement for rhythmic activity of MYRF-1 in molting. Nevertheless, our results suggest that MYRF-1 is required during a specific time-window of multiple larval stages to prevent lethality in that specific stage, which is consistent with a model in which MYRF-1 is rhythmically active.

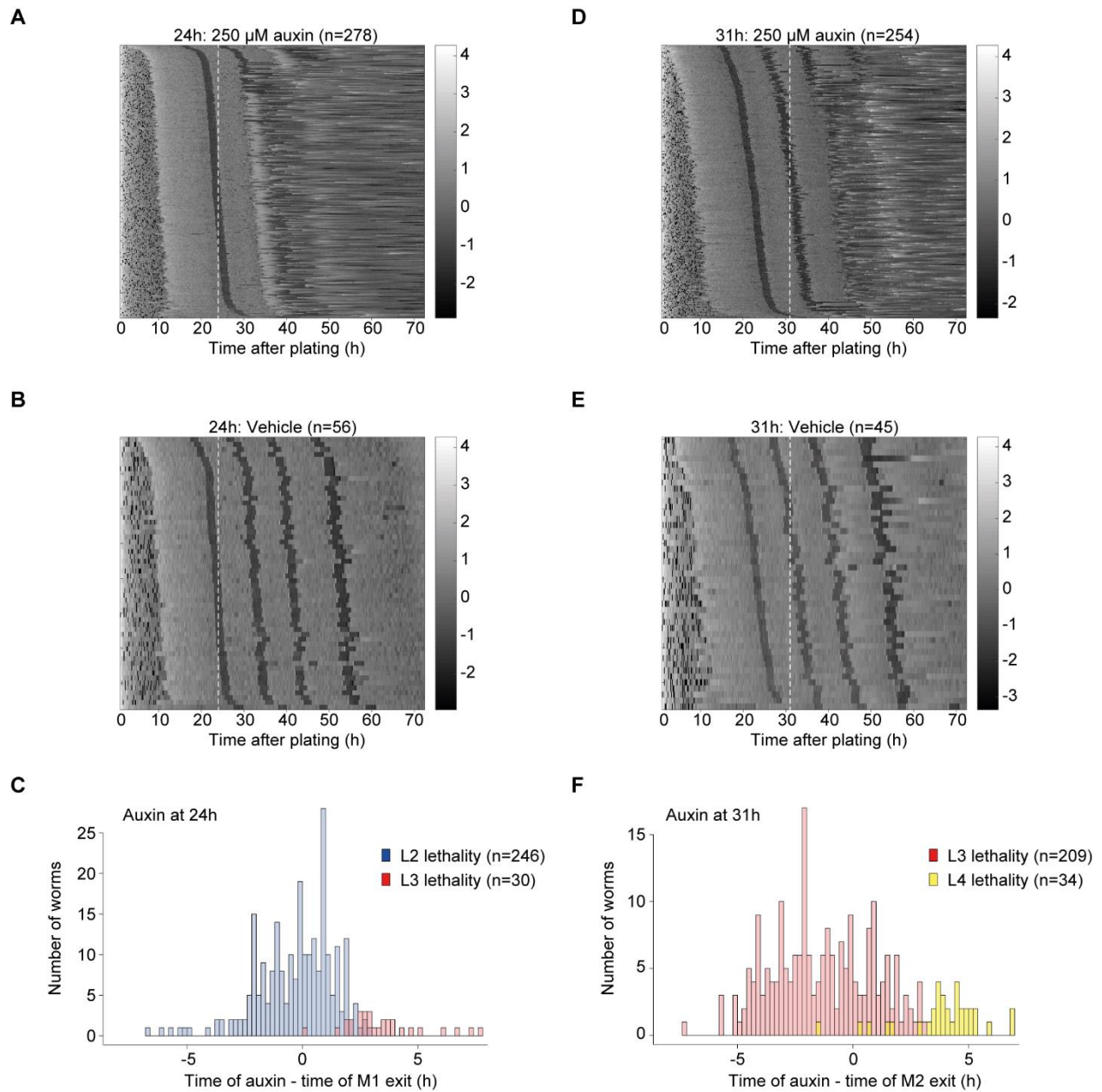


Figure 2.8: Time of MYRF-1 depletion determines the onset of lethality

A,B,D,E, Heatmap showing trend-correct luminescence (Lum) of *myrf-1(xe161); peft-3::tir-1;peft-3::luc* animal (HW2634) treated with vehicle (0.25% ethanol, B, E) or 250 μ M auxin (right panel, A,D) at 24 hours (A,B, white dashed line) or 31 hours (D,E, white dashed line). Luminescence traces are sorted by entry into molt 1. Black corresponds to low luminescence occurring during lethargus (molt). Embryos of various stages were left to hatch and develop during the assay. Note that early hatched animals are in top rows and late hatched animals are in bottom rows.

C,F, Quantification of the time at which auxin was added relative to M1 (C), or M2 (F) entry (time of auxin – time of M entry). Shown for appearance of lethality in L2 (blue), L3 (red), and L4 (yellow). Animals with phenotype in L1 (C, n=2) and L2 (F, n=11) were not included. Negative relative time indicates that auxin was added before M1 exit (C), or M2 exit (D). Positive relative time indicates that auxin was added after M1 exit (C), or M2 exit (D).

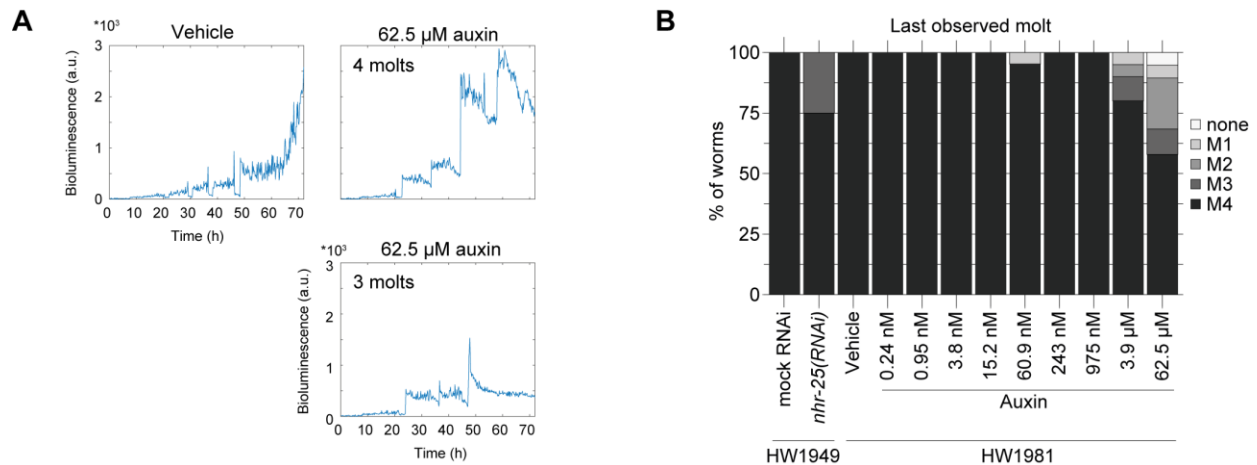
2.5.5 NHR-25 is required for completion and normal duration of development

nhr-25, ortholog of *Drosophila* Ftz-f1, revealed molting phenotypes (Asahina et al., 2000; Gissendanner and Sluder, 2000) and its mRNA expression peaks during the molt (Gissendanner et al., 2004; Hendriks et al., 2014). *nhr-25(RNAi)* animals showed lengthening of larval stages in our screen (**Figure S2 in GRH-1 manuscript**), and hence, I aimed to validate this phenotype and further investigate its role in development. To examine whether and how lengthening of larval stages is dependent on extent and timing of NHR-25 depletion, we used a previously published *nhr-25::degron* strain (Zhang et al., 2015). We depleted NHR-25 by auxin and monitored developmental progression by the luciferase assay. When we inspected the luminescence traces, we observed that luminescence levels were elevated during the molt and intermolt in NHR-25-depleted animals (**Figure 2.9A**). Given that *nhr-25(RNAi)* animals previously revealed disturbed integrity of the cuticle (Asahina et al., 2000; Gissendanner and Sluder, 2000) and that luminescence levels can rise by increased permeability of the cuticle, among other reasons, we propose that elevated luminescence levels reflect a defective cuticle, which we will further quantify below (**section 2.5.7**).

When titrating the concentration of auxin, we found that some animals receiving high concentrations of auxin failed to reach adulthood (**Figure 2.9B, Figure S1A (section 5)**). The number of molts that animals completed and the number of animals that reached a certain molt were dependent on the concentration of auxin (**Figure 2.9B, Figure S1A (section 5)**). Thus, NHR-25 is required for the completion of larval development. Moreover, we found a concentration-dependent lengthening of the molt and the intermolt (**Figure 2.9C, Figure S1B (section 5)**). We could recapitulate the results of the screen, as extension of molts and intermolts was similar to or even higher as those of *nhr-25(RNAi)* animals, at concentrations ≥ 62.5 μM (**Figure 2.9C, Figure S1B (section 5)**). We conclude that NHR-25 is needed not only for completion of larval development as such, but also for proper duration of the developmental stages.

2.5.6 Activity of NHR-25 is required in multiple larval stages

Given that RNAi and AID were initiated in embryos, it remains unclear whether NHR-25 is required in every larval stage, or whether NHR-25 is required only in a particular larval stage and lengthening of subsequent larval stages appears as a secondary effect. Hence, I aimed to investigate whether the time point of NHR-25 degradation is important for its function. To this end, we depleted NHR-25 by adding auxin at different times in L1 and L2 stage (**Figure 2.10A**) or in L2 and L3 stage (**Figure 2.10B**) and quantified the duration of molts and intermolts. When we added auxin in L2 stage, we observed a time-dependent lengthening of molt 2 and intermolt 3, i.e. the earlier NHR-25 degradation was initiated relative to M2 entry, the longer molt 2 and intermolt 3 (**Figure 2.10C**). In contrast, the duration of molt 3 was much less dependent on the onset of NHR-25 degradation (**Figure 2.10C**). Similar results were observed for molt 3, intermolt 4 and molt 4 respectively, when NHR-25 depletion was initiated in L3 stage (**Figure S2A (section 5)**). In the absence of further data on the dynamics of NHR-25 levels and activity, we cannot discriminate between a model in which NHR-25 is rhythmically active or constitutive active. Nevertheless, our results suggest NHR-25 is required in multiple larval stages to ensure their normal duration. Whether NHR-25 activity is rhythmic remains to be established.



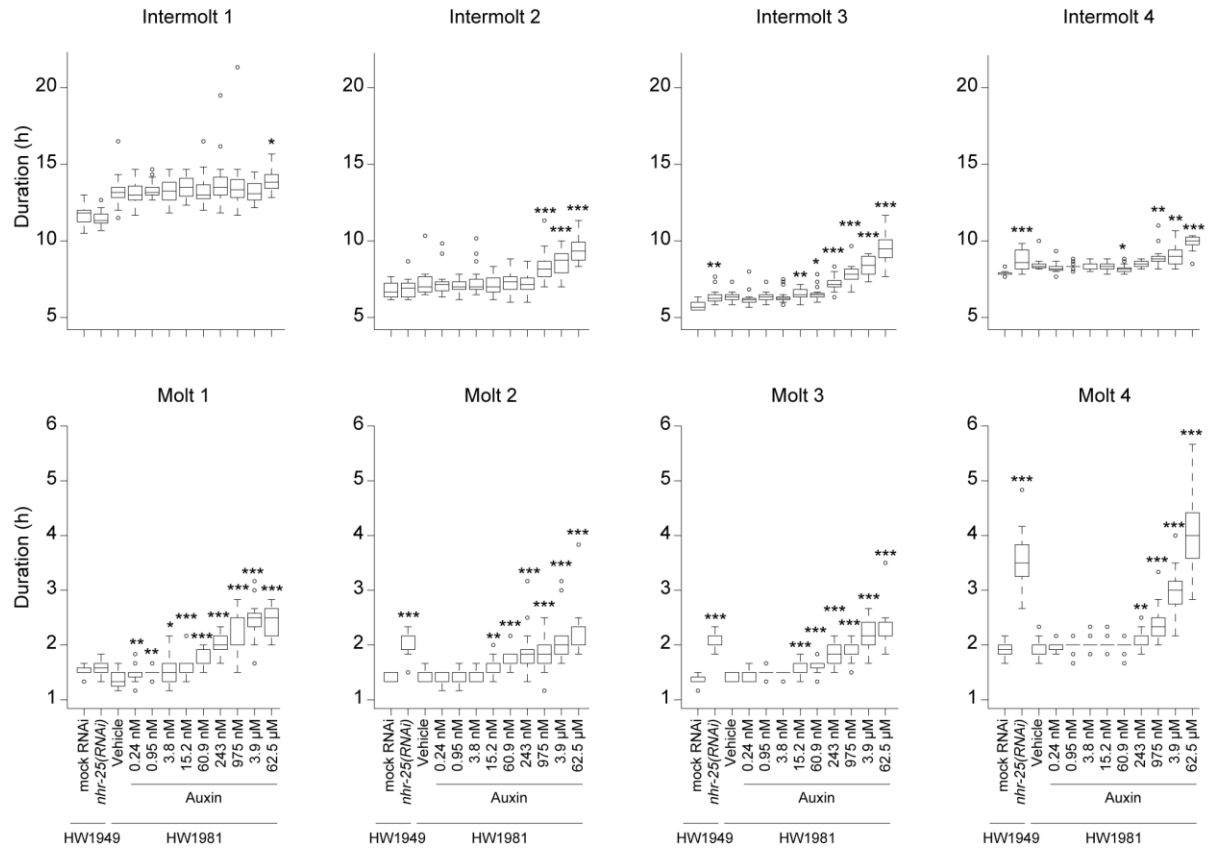
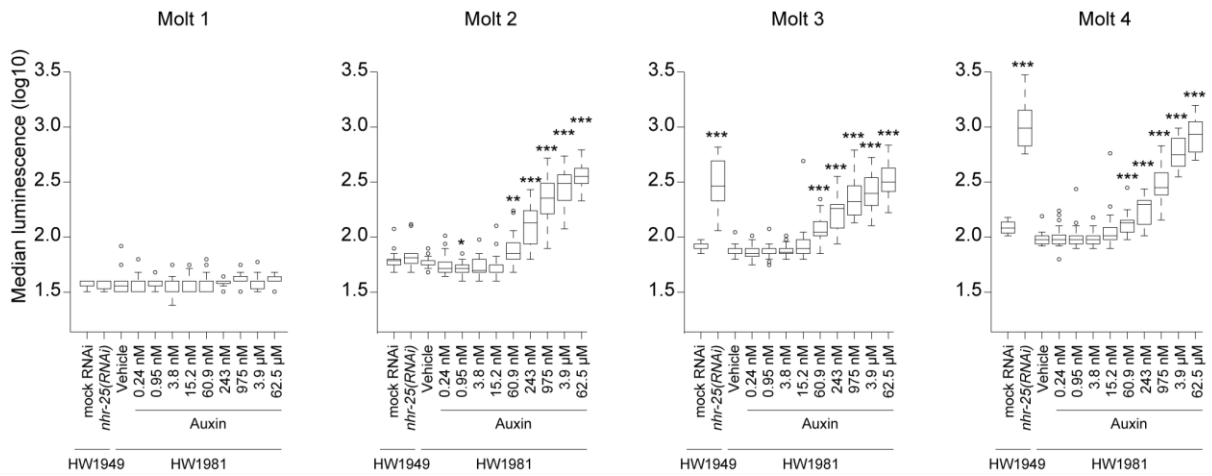
C**D**

Figure 2.9: Completion of molts, lengthening of stage durations and cuticle defects is dependent on the extent of NHR-25 depletion

A, Representative luminescence traces of a single *peft-3::TIR1; peft-3::luc, nhr-25::degron* (HW1981) animal treated with vehicle (0.25% ethanol) or 62.5 μ M auxin.

B, Quantification of the last observed molt in *peft-3::luc* (HW1949) animals treated with mock RNAi or *nhr-25* RNAi, and HW1981 animals treated with the indicated auxin concentrations.

C, Quantification of intermolt (top) and molt (bottom) durations in animals from B. Animals that did not complete 4 molts were excluded. Significant differences for *nhr-25(RNAi)* are relative to mock RNAi. Significant differences for auxin concentrations are relative to vehicle.

D, Quantification of median luminescence during the molt of animals in C. Significant differences for *nhr-25(RNAi)* are relative to mock RNAi. Significant differences for auxin concentrations are relative to vehicle.

P-values were determined by Welch two-sample, two-sided t-test. * $p < 0.05$, ** $p < 0.01$, *** $p < 0.001$

2.5.7 Loss of NHR-25 leads to defects in cuticle integrity

Given the increased luminescence in NHR-25-depleted compared to control animals (**Figure 2.9A**), we investigated whether and how luminescence levels were dependent on the extent and the time of NHR-25 depletion. We specifically focused on the luminescence during the molt, as we expect that the levels during the molt are less prone to changes in luminescence for reasons other than increased cuticle penetrance, e.g. increased feeding. When we quantified the luminescence levels during the molts, we found that the increase of the median luminescence during the molt was dependent on the concentration of auxin (**Figure 2.9D, S1C**). Thus, we conclude that NHR-25 is required for the integrity of the cuticle. Accordingly, the increase in the median luminescence during the molt was also dependent on the onset of NHR-25 degradation in L2 stage (**Figure 2.10D**) and L3 stage (**Figure S2B (section 5)**). In contrast to molt 2 extension, luminescence levels of molt 2 were not affected (**Figure 2.10D**). Increase in luminescence levels appeared for the first time in molt 3 and only when NHR-25 depletion was initiated long before entry into molt 2. The luminescence levels in molt 4 were mostly independent of the onset of NHR-25 degradation and were generally elevated (**Figure 2.10D**). We observed similar results for depletion of NHR-25 in L3 stage (**Figure S2B (section 5)**). During molting, the newly synthesized cuticle remains protected until the old cuticle is shed. Hence, if lengthening of a molt were to reflect synthesis of a defective cuticle, we would expect that increased permeability only arises in the subsequent stage. Our results are consistent with this idea, i.e. first, larval stages are increased in duration and defects in cuticle integrity arise in the subsequent stage. We conclude that NHR-25 is required for cuticle integrity.

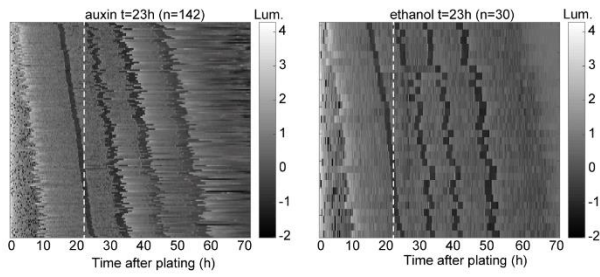
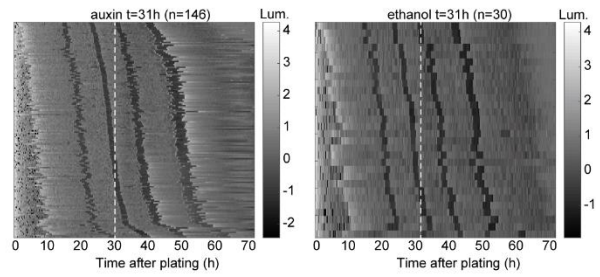
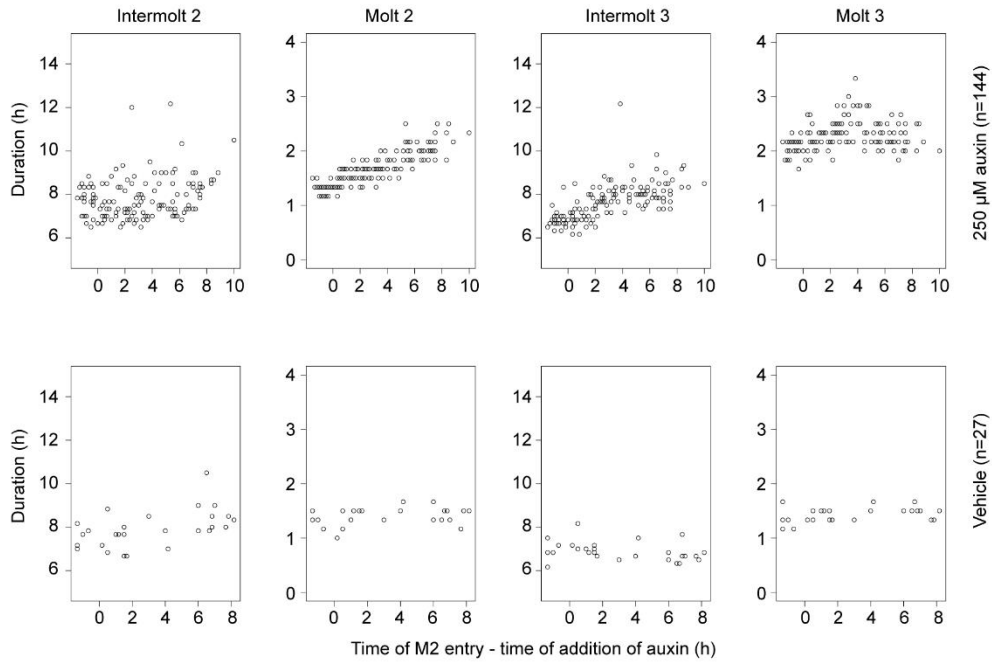
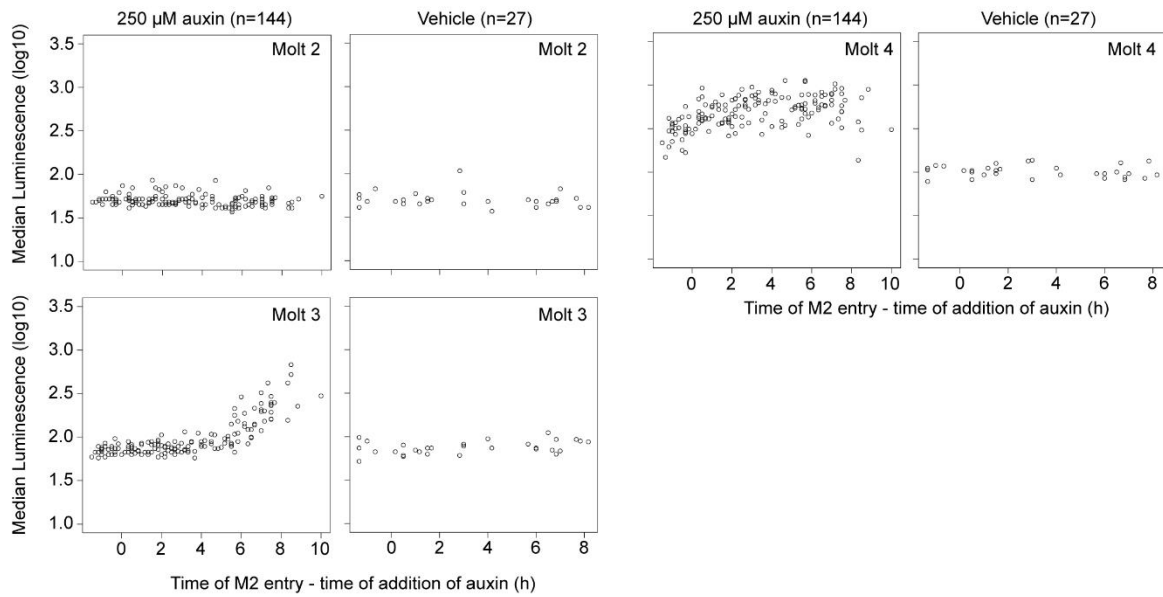
A**B****C****D**

Figure 2.10: Lengthening of larval development and cuticle integrity are dependent on the onset of NHR-25 degradation

A,B, Heatmap showing trend-correct luminescence (Lum) of *peft-3::TIR1; peft-3::luc, nhr-25::degron* (HW1981) animals treated with vehicle (0.25% ethanol, right) or 250 μ M auxin (left) at 23 hours (A, white dashed line) or 31 hours (B, white dashed line). Luminescence traces are sorted by entry into molt 1 (A) or molt 2 (B). Black corresponds to low luminescence occurring during lethargus (molt). Embryos of various stages were left to hatch and develop during the assay. Note that early hatched animals are in top rows and late hatched animals are in bottom rows.

C, Quantification of intermolt and molt durations over time of auxin or vehicle addition relative to time of M2 entry. Animals that receive auxin or vehicle in L2 stage from A and B were included, whereas animals that receive auxin or vehicle in other stages were excluded. Hence, negative values arise from receiving auxin or vehicle during molt 2.

D, Quantification of median luminescence during the molt over time of auxin or vehicle addition relative to time of M2 entry. Animals from A and B that received auxin or vehicle in L2 stage were included, whereas animals that receive auxin or vehicle in other stages were excluded. Hence, negative values arise from receiving auxin or vehicle during molt 2.

2.5.8 BLMP-1 controls the duration of molts

In our RNAi screen, we observed lengthening of molts in *blmp-1(RNAi)* animals, and interestingly, intermolts appeared to be shortened (**Figure S2 in GRH-1 manuscript**). To validate these results, we first repeated the RNAi experiment using more animals. Consistent with the results of the screen, *blmp-1(RNAi)* caused lengthening of molts (**Figure 2.11A,B,C**). In some of the RNAi experiments, and presumably depending on the extent of BLMP-1 depletion, overall larval stage durations remained largely unchanged, because lengthening of molts was accompanied by a shortening of intermolts (**Figure 2.11D,E, Figure S3 (section 5)**).

To further investigate whether the variability in our RNAi experiments resulted from differences in the extent of protein depletion by RNAi, we used the AID system to tune BLMP-1 levels. To this end, we degron-tagged *blmp-1* endogenously to allow conditional degradation of BLMP-1 upon addition of auxin. When we investigated the effect of different concentrations of auxin, we found that molts were extended with increasing auxin concentration (**Figure 2.11F**). Moreover, consistent with the results from *blmp-1(RNAi)*, intermolt durations were decreased at low auxin concentrations (**Figure 2.11G**), suggesting that extension of molts was compensated by shortening of intermolts. Instead, at high auxin concentrations, intermolt durations were extended (**Figure 2.11G**). We speculate that intermolts are lengthened as a secondary effect of the molts being extensively lengthened. These observations suggest a function of BLMP-1 in assuring proper duration of the molts.

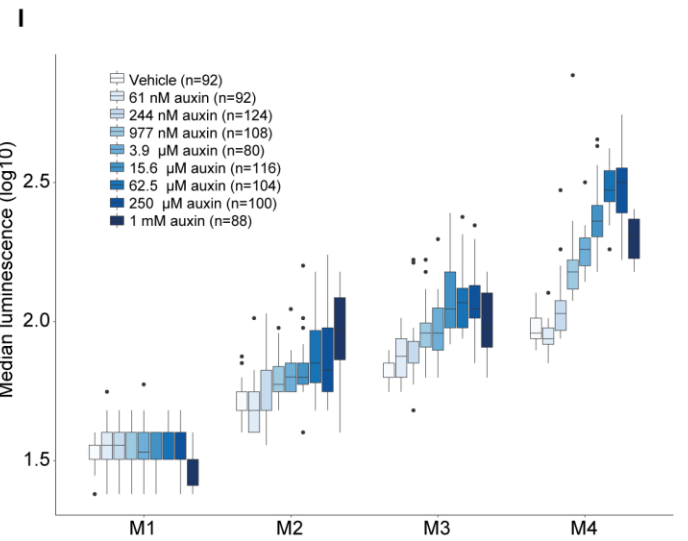
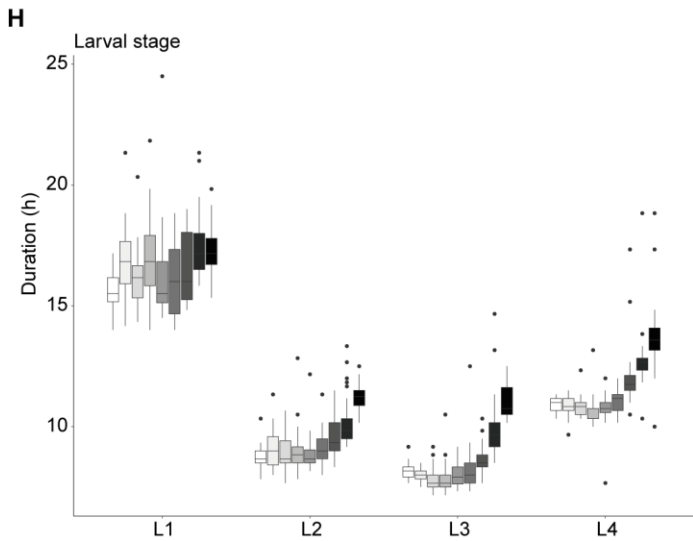
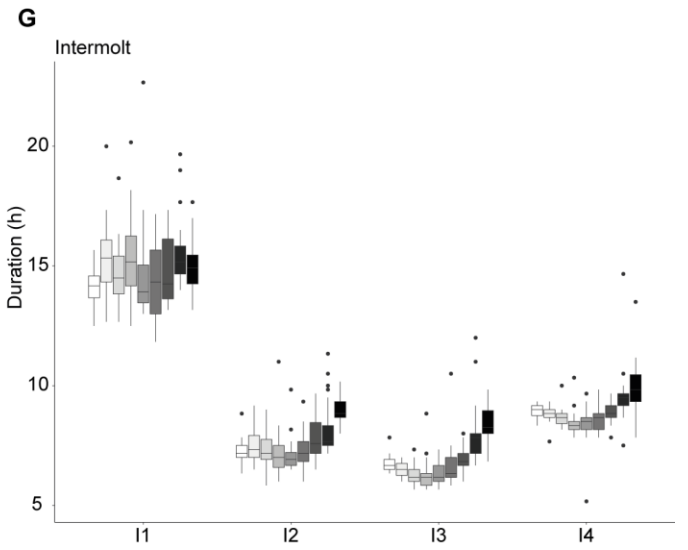
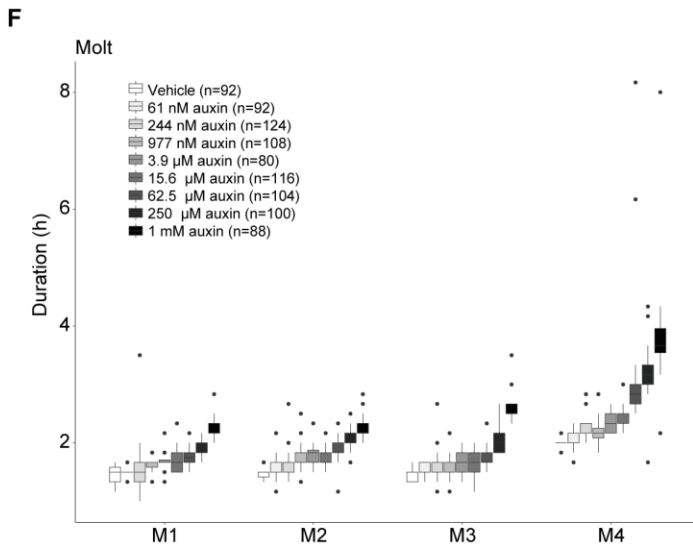
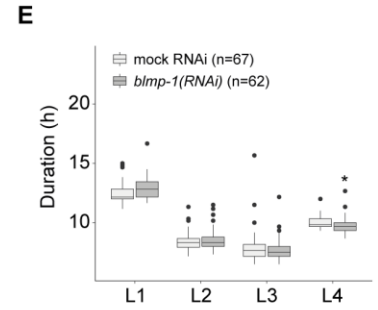
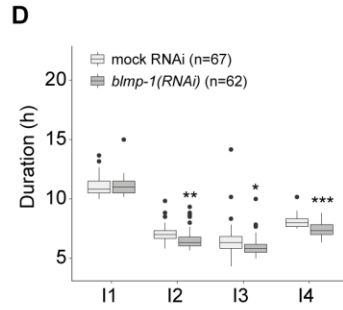
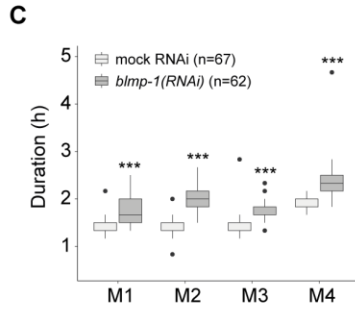
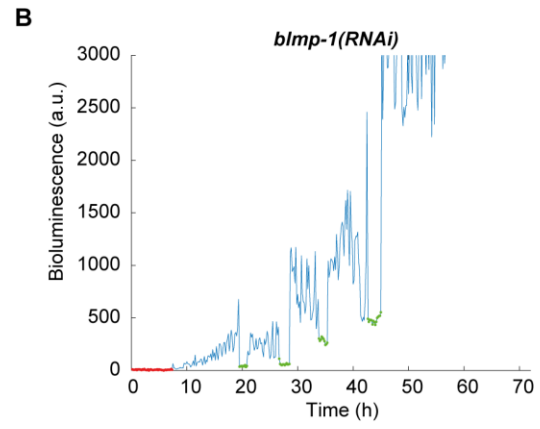
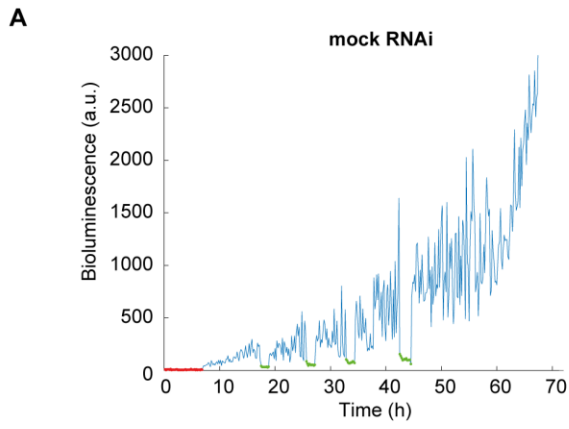


Figure 2.11: Lengthening of molts and cuticle defects are dependent on the extent of BLMP-1 depletion

A-B, Representative luminescence trace of a single animal (HW1939) expressing the *Peft-3::luciferase* transgene. Worms were grown on mock RNAi (A) or *blmp-1(RNAi)* (B).

C-E, Duration of molts (C), intermolts (D) and larval stages (E) for indicated RNAi conditions. Significant differences between mock RNAi and *blmp-1(RNAi)* are indicated (* $P < 0.05$, ** $P < 0.01$, *** $P < 0.001$, two-sided two-sample t-test)

F-H, Duration of molts (F), intermolts (G) and larval stages (H) for *blmp-1::degron; peft-3::luc, peft-3::TIR1* animals (HW2120) grown on indicated auxin concentrations. Dots represent outliers, and significant differences can be found in **Table S1**.

I, Quantification of median luminescence levels in \log_{10} during the molt for animals in F-H grown on indicated auxin concentrations. Dots represent outliers, and significant differences can be found in **Table S2**.

2.5.9 BLMP-1 activity is required during multiple stages to ensure proper molt durations

Similar to NHR-25, I aimed to investigate whether molt durations were dependent on the time of BLMP-1 depletion. On the one hand, I aimed to examine whether BLMP-1 is required in every larval stage. On the other hand, it remained unclear whether oscillatory activity if BLMP-1 is important for its function. To this end, we added auxin at different times in L2 (**Figure 2.12A**) and L3 stage (**Figure S4A (section 5)**) using high concentrations of auxin. The duration of M2 and I3 increased with the onset of BLMP-1 degradation in L2 stage (**Figure 2.12B**). Exposure to auxin in L2 did not affect I2 duration (**Figure 2.12B**). (We note that long I2 durations correspond to animals which received auxin in L1 stage). The length of M3 was generally extended relative to animals treated with vehicle control and much less dependent on the onset of BLMP-1 degradation in L2 (**Figure 2.12B**). We repeated this experiment by applying auxin in L3, and observed similar results (**Figure S4B (section 5)**).

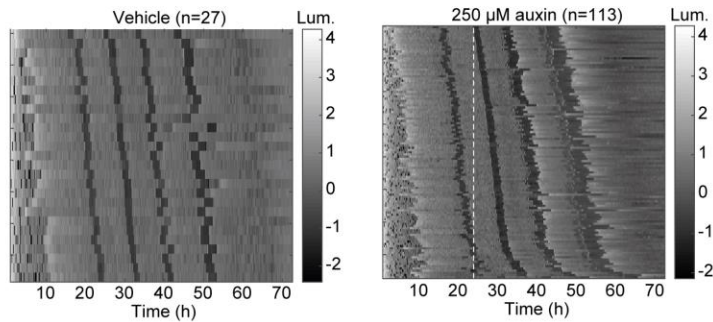
These results suggest a requirement of BLMP-1 in multiple larval stages to prevent extension of molt duration. Moreover and similar to NHR-25, we cannot exclude that BLMP-1 is constitutively active. However, it appears likely that BLMP-1 activity is rhythmic, as BLMP-1 levels oscillate (data not shown, Yannick Hauser, unpublished).

2.5.10 BLMP-1 is required for cuticle integrity

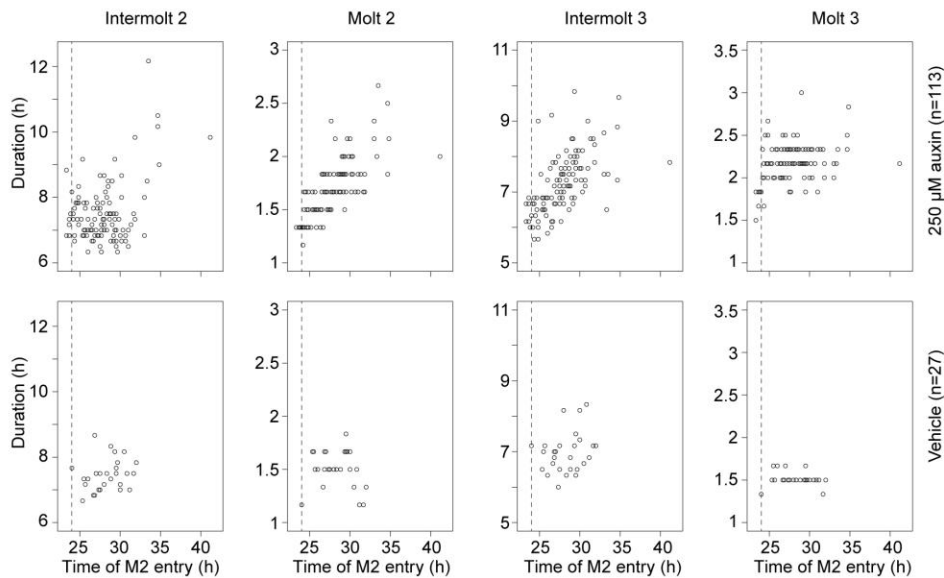
Luciferase traces of *blmp-1(RNAi)* animals revealed elevated luminescence levels (**Figure 2.11B**), similar to those observed in *nhr-25(RNAi)* animals. Hence, we quantified the median luminescence during the molt upon different concentrations of auxin. We observed that the increase in the luminescence during the molt is dependent on the concentration of auxin (**Figure 2.11I**), and on the onset of BLMP-1 depletion in L2 stage (**Figure 2.12C**). Luminescence appeared to be increased in molt 3 and molt 4 whereas molt extension was already observed in molt 2 (**Figure 2.12C**). We observed similar results when the onset of

BLMP-1 depletion occurred in L3 stage (**Figure S4C (section 5)**). In sum, and similar to NHR-25, lengthening of molt duration is followed by increased cuticle permeability in the subsequent stage, which is consistent with a model in which a defective cuticle is synthesized during the lengthened molt, but only becomes evident when the old cuticle is shed. We conclude that BLMP-1 is needed for cuticle integrity.

A



B



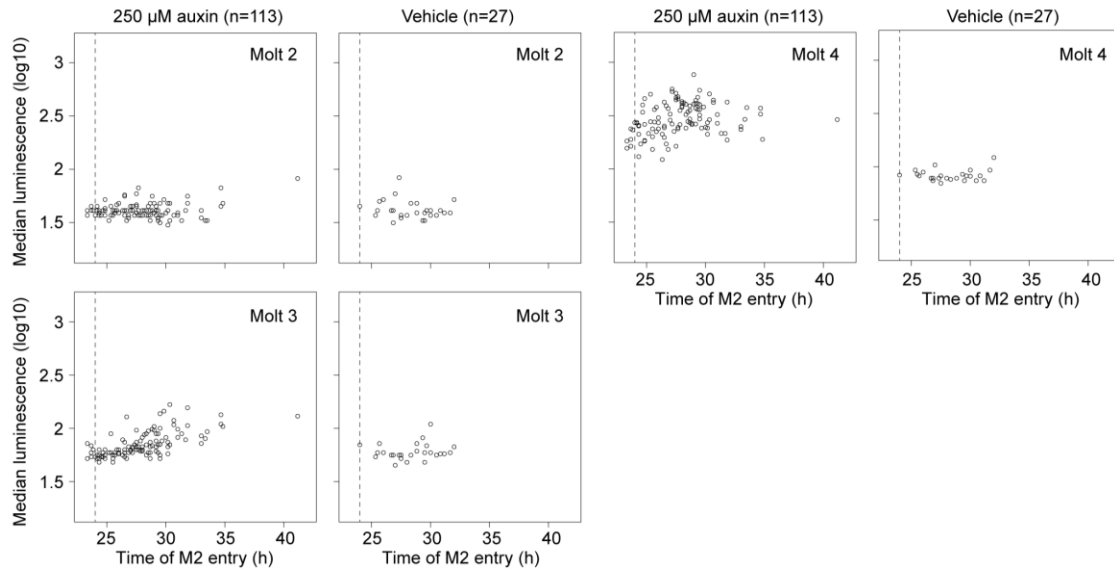
C

Figure 2.12: Lengthening of molts and cuticle defects are dependent on the onset of BLMP-1 depletion

A, Heatmaps showing trend-corrected luminescence (Lum.) traces of *blmp-1::degron*; *peft-3::luc*, *peft-3::TIR1* animals (HW2120); one animal per horizontal line. Vehicle (0.25% ethanol, left) or 250 μM auxin (right) were added at t=24h (dashed line). t=0 hours corresponds to start of the assay. Embryos hatch at different time points and traces are sorted by entry into M2.

B, Duration of I2, M2, I3 and M3 plotted over time at which single animals enter M2 in vehicle and auxin treated animals at t=24h (dashed line) shown in (A).

C, Quantification of median luminescence during the molt in log₁₀ over time of auxin addition relative to time of M2 entry. Data for molt 2, molt 3 and molt 4 is shown.

2.5.11 Identification of significantly changing genes using an Empirical Cumulative Distribution Function

To investigate the molecular function of BLMP-1, we wondered about the gene expression changes resulting from loss of BLMP-1. We performed a RNA-seq experiment, similar to that for GRH-1 (**GRH-1 manuscript, Figure 6**), i.e. we cultured a synchronized population of *blmp-1::degron* animals in liquid medium and initiated BLMP-1 degradation by addition of auxin at 20 hours, when animals were in early L2 stage. We selected auxin concentrations for which we observed lengthening of molts and intermolts (250 μM auxin, ++), and lengthening of molts, but shortening of intermolts (3.9 μM auxin, +) during the luciferase assay (**Figure 2.11F,G**). We harvested animals, every 30 minutes, from 20.5 until 49.5 hours, and performed mRNA sequencing. To identify differentially expressed genes, we used the same method as described in the GRH-1 manuscript, which we will explain in more detail here.

To identify genes whose expression changed in response to BLMP-1 degradation, we calculated the difference in expression for each gene at each time point between the conditions (the expression fold change). We expected gene expression to be unchanged, or at most minimally affected, at the first time point of harvesting (20.5 hours), shortly after auxin was added (20 hours). Scatter plots of – auxin over ++ auxin revealed that an increasing number of genes are changed in their expression over time (**Figure S5A (section 5)**). Moreover, the gene expression fold changes in the first two time points were not similarly distributed as observed in a quantile-quantile plot (**Figure S5B (section 5)**). Hence, we used the expression fold changes of the first time point (20.5 hours) as our null distribution. Although we did not collect replicates, this approach allowed us to investigate whether gene expression fold changes occurred over time, i.e. relative to the null distribution. Given that the expression fold changes at the first time point were not normally distributed (**Figure 2.13A**), we used an empirical cumulative distribution function (ECDF) as a probability model (**Figure 2.13B**). The ECDF is a non-parametric function which describes the distribution of empirical data (Cai, 2013), i.e. the probability distribution represents the observed data, not a predicted population. Given the total number of observations, n , each observation is given a probability of $1/n$. Next, the observations are ordered based on their values, from the smallest to the largest. Hence, for each subsequent observation, the probability increases with $1/n$, resulting in a step function. If n is sufficiently large, the ECDF describes the ‘true’ cumulative distribution function well. The ECDF is defined as:

$$\hat{F}(x) = \hat{P}(X \leq x).$$

$$\text{Thus, } \hat{P}(X > x) = 1 - \hat{F}(x).$$

Given that the distribution function is empirical in its nature, the probability of an observation in the first time point under the null distribution is uniform by definition, i.e. the number of genes in each bin was the same (**Figure 2.13C**). We note that many genes remained unchanged, as exemplified by the jump in the fraction of genes at fold change equals 0 (**Figure 2.13B**), hence the bin at $P = 1$ was overrepresented (**Figure 2.13C**). Significant changes in subsequent time points arise when the number of observation in the bin close to $P = 0$ increase, as exemplified for $t = 40\text{h}$ (**Figure 2.13D**, red bar).

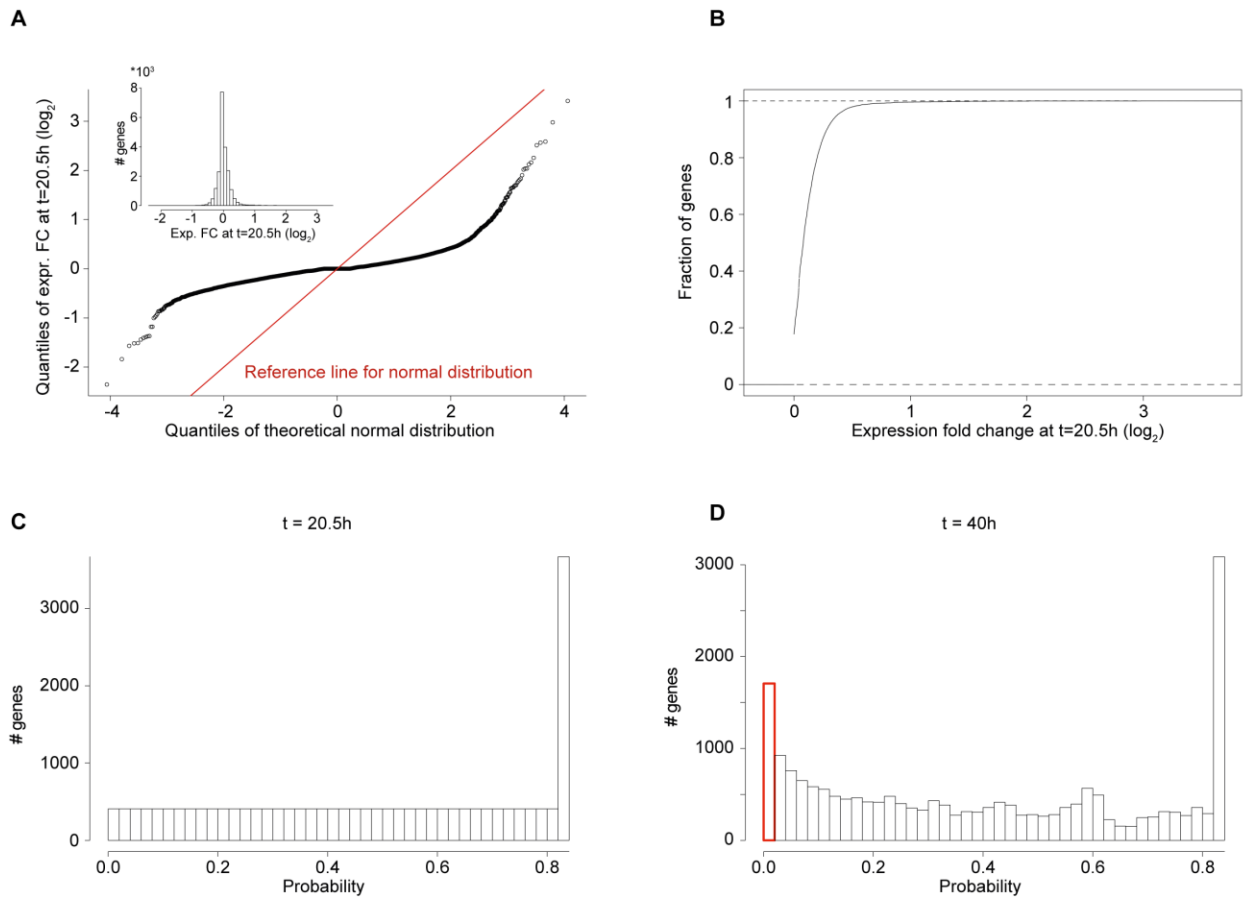


Figure 2.13: Describing the expression fold change with an ECDF allows the identification of significantly changed genes

A, QQ-plot showing the quantiles of the gene expression fold change (expr. FC) at the first time point ($t = 20.5h$) over quantiles of a theoretical normal distribution. If data were to be normally distributed, the quantiles would fall on the reference lines (red). Deviation from the reference line and histogram of the number of genes in each binned expression fold change value reveal that data is not normally distributed.

B, Empirical cumulative distribution function (ECDF) showing the fraction of genes over the expression fold change at the first time point ($t = 20.5h$).

C, Histogram plotting the number of genes over the probability at $t = 20.5h$. As the ECDF is empirical, the distribution is uniform per definition.

D, Histogram plotting the number of genes over the probability at $t = 40h$. The distribution deviates from a uniform distribution. The increase in the number of genes at a low probability (red bin) indicates genes that change significantly in their expression. Note that we used $P < 10^{-3}$ in at least 3 time points as selection criteria.

2.5.12 Loss of BLMP-1 results in global shifts in the peak of oscillatory gene expression

To identify significantly changing genes, we selected genes which revealed an expression fold change with a probability $P < 10^{-3}$ in at least 3 time points. We found 422 genes to be changed significantly in their expression, among them 354 oscillating genes (84%) (**Figure 2.14A**). Interestingly, many of the oscillating

genes were not, or at most minimally upregulated, downregulated, or changed in amplitude, (**Figure 2.14 A,B, Figure S6A,B,E,F (section 5)**) but instead, their expression fold change over time appeared to have a specific oscillatory pattern. This pattern became evident when we sorted the expression fold change by peak phase (**Figure S6A,B (section 5)**) according to our previous annotation (Meeuse et al., 2019). Given that amplitudes and mean expression levels remained largely unchanged in ++auxin compared to –auxin (**Figure S6E,F (section 5)**), one possible explanation of the oscillatory pattern in the expression fold change is a shift in the peak of gene expression between the different conditions. Indeed, we observed expression peaks for both + auxin and ++ auxin conditions to be shifted to earlier times, as exemplified for *B0034.1*, *col-149*, *jud-4* and *nlp-27*, whereas the time of the trough appeared to be unaffected (**Figure 2.14C**). We note that, although these effects were observed for the majority of the affected oscillating genes, visual inspection of the significantly changing genes revealed that a few genes exhibited other changes in their dynamics, e.g. dampening of amplitude (data not shown). Interestingly, affected oscillating genes appeared to have a peak phase preference during the beginning of the molt (**Figure 2.14D**), i.e. these peak phases were enriched over those of all oscillating genes, according our previous annotation (Meeuse et al., 2019). In contrast, opposite peak phases were depleted (**Figure 2.14D**).

Next, we wondered about the gene expression changes in the oscillating genes we did not identify as significantly changing. When we plotted their expression in heatmaps sorted by phase, according to our previous annotation (Meeuse et al., 2019), we found the patterns in the expression fold changes to be similar to those of the oscillating genes which we identified as significantly changing (compare **Figure S6A** with **Figure S6C (section 5)**). However and as expected, the expression fold changes were much smaller in magnitude in the ‘not-significantly changing oscillating’ genes (**Figure S6C (section 5)**). Moreover, when comparing the gene expression heatmaps of ‘significantly changing oscillating’ genes with those of ‘not-significantly changing’ genes, we observed a strong enrichment for high amplitude genes in the ‘significantly changing oscillating’ genes (compare **Figure S6B** with **Figure S6D (section 5)**). This is somewhat expected as a similar shift of the peak expression in time for a large amplitude gene and a small amplitude gene (which peak at the same time), would result in a larger expression fold change for the former. Given that not only the magnitude of the expression fold change, but also the extent of the shift could be biologically relevant, I aimed to quantify the shift in peak expression. To this end, we used a different method, as described in further detail below. Nevertheless, we conclude that the oscillating genes affected by loss of BLMP-1 appeared to peak at earlier times, among other dynamics changes. Hence, these observations are inconsistent with a model in which BLMP-1 is required for oscillatory gene expression as such, but rather suggests a more complex regulatory function.

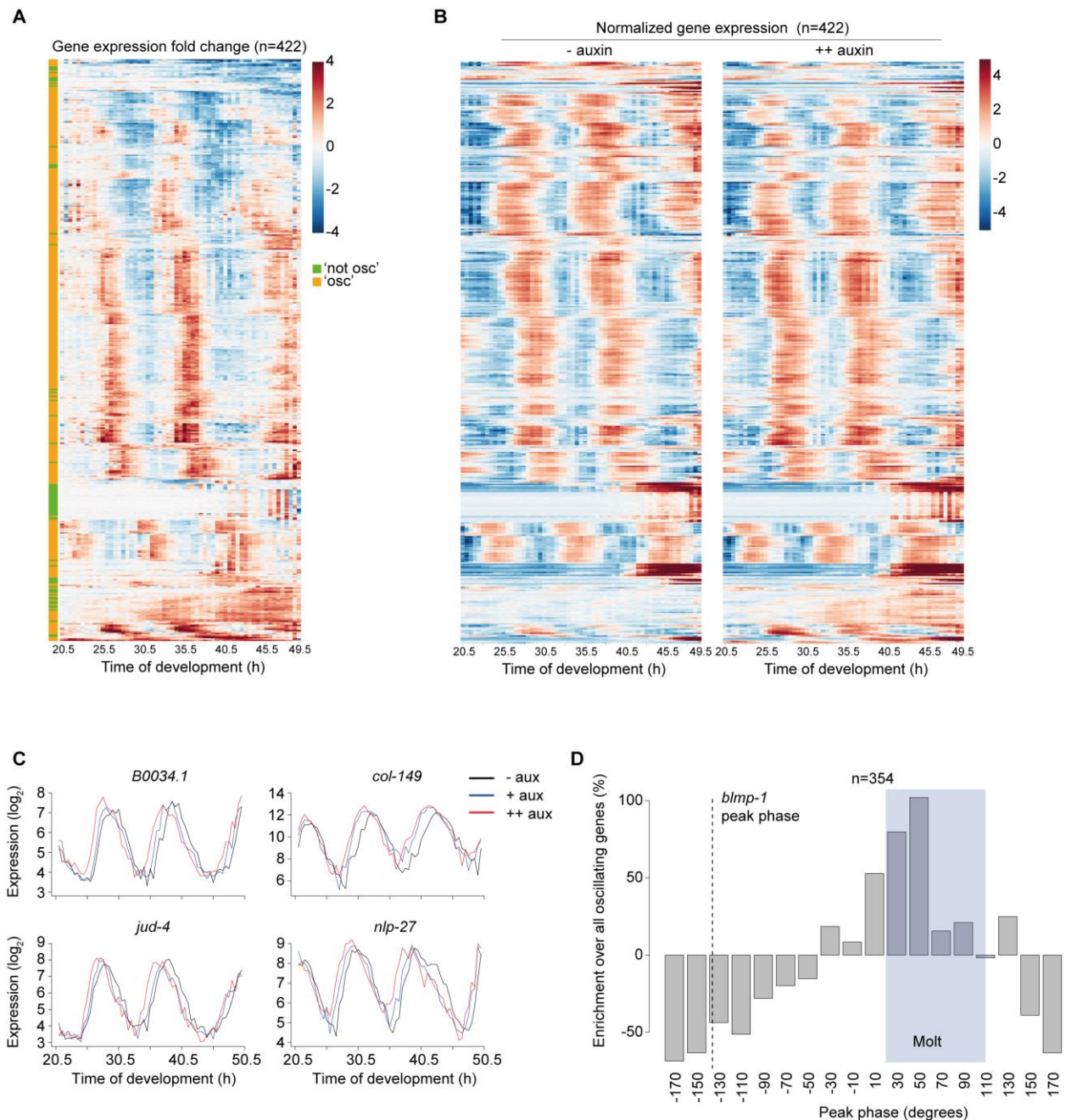


Figure 2.14: Expression fold change analysis reveals shifts in expression of oscillating genes upon loss of BLMP-1

A, Heatmap of fold change between gene expression in ++ auxin (250 μ M) and in - auxin (vehicle) conditions for significantly changing genes (n=422). Expression fold change is hierarchically clustered, ordered by mean expression and plotted in log₂. Vertical bar indicates whether a gene is 'oscillating' ('osc', orange) or 'not oscillating' ('not osc', green) in its expression according to a previous annotation (Meeuse et al., 2019).

B, Gene expression heatmaps in auxin-treated (++ auxin) and control (- auxin) animals for significantly changing genes (n=422). Gene expression was mean-centered over both conditions, sorted according to A and plotted in log₂.

C, Expression of *B0034.1*, *col-149*, *jud-4* and *nlp-27* in log₂. Vehicle (-auxin, black), + auxin (blue) and ++ auxin (red) expression patterns are shown.

D, Barplot showing peak phase enrichment of oscillating genes among genes in A (=354) over all 'oscillating' genes (Meeuse et al., 2019). Peak phases are sorted in 20° bins. The peak phase of *blmp-1* is -138°(dashed line) and the molt occurs roughly between 20° and 110° (blue box), as previously determined (Meeuse et al., 2019).

2.5.13 Identification of significant shifts in peak phase using cosine fitting and error propagation

To quantify the shift in peak phase between conditions, we applied cosine fitting on gene expression patterns of genes previously annotated as oscillating (Meeuse et al., 2019). Cosine fitting was performed as described in (Meeuse et al., 2019), which I will explain in more detail here. Cosine fitting is an extension of a linear model fit to the data, in which $\cos(\omega t)$ and $-\sin(\omega t)$ are used as regressors. ω is the angular frequency, which is equal to $\frac{2\pi}{\text{period}}$. A cosine can be described by the combination of the two regressors in the following way:

$$C \cdot \cos(\omega t + \varphi) = C \cdot \cos(\varphi) \cdot \cos(\omega t) - C \cdot \sin(\varphi) \cdot \sin(\omega t) = A \cdot \cos(\omega t) - B \cdot \sin(\omega t)$$

$$\text{Amplitude} = C = \sqrt{A^2 + B^2}$$

$$\text{Phase} = \varphi = \arctan(A, B)$$

By choosing a fixed ω , the regressors are only dependent on the time, t , and thus the model is linear. The coefficients A and B can be identified by fitting the linear model to the data. To choose a fixed ω which describes the data best, we fitted different linear models to the gene expression data, each with a different ω . To quantify how well the models fits the expression of each gene, we used the squared error, i.e. the square of the difference between the fitted values and the observed values. We found the best fit to occur at a period of 10.5 hours (**Figure 2.15A**). (We note that the time course was performed at 20°C and hence the period of the oscillation was increased compared to previous time courses performed at 25°C (Meeuse et al., 2019)). By fitting the linear model with $\omega = \frac{2\pi}{10.5h}$ to each gene individually, we determined the coefficients A and B and their standard errors. To identify genes that change significantly in peak phase between conditions, we calculated the confidence intervals of the phase shifts using error propagation on the standard errors of the coefficients. This because the uncertainties of the coefficients A and B are not linearly carried over to the phase shifts:

$$\begin{aligned} \text{phase shift} &= \text{peak phase}_{++\text{aux}} - \text{peak phase}_{--\text{aux}} \\ &= \arctan(A_{++\text{aux}}, B_{++\text{aux}}) - \arctan(A_{-\text{aux}}, B_{-\text{aux}}) \end{aligned}$$

To illustrate this with a simple example:

Let f be a linear combination of x and y , i.e. $f = x + y$

With standard deviations σ_x and σ_y

$$\text{Then } \sigma_f = \sqrt{\sigma_x^2 + \sigma_y^2}$$

For non-linear combinations, such as the phase shift we describe here, the combined uncertainty cannot be calculated and must be approximated. Here, we used Taylor expansion as part of an existing error propagation algorithm (**Methods**) to determine the confidence interval of the phase-shift. Obviously, a phase shift of 0 indicates no change in the peak phases between conditions. Hence, a confidence interval that includes 0 is not significant, whereas a confidence interval which is bigger (positive) or smaller (negative) than zero represents a significant and positive or negative phase shift respectively (**Figure 2.15B**).

2.5.14 BLMP-1 ensures that a subset of ‘molting’ genes peak at the right time

Using a 99% confidence interval (as determined by error propagation) and a phase shift of at least 36° , i.e. 10% of the period, as cut-offs, we found the peak phases of 594 genes to be significantly different between conditions (**Figure 2.15C,D**). Notably, only 91 genes of the 354 genes identified using the ‘expression fold change’ method, were found among the 594 genes identified here. Hence, using cosine fitting and error propagation, we were able to identify an additional set of genes that were strongly shifted in the time of their peak expression compared to the control. We speculate that both sets of genes might be relevant for the phenotypes we observed. To provide insight into the functional relevance, we combined the datasets and performed GO term analysis. We found the GO terms ‘cuticle development’ and ‘molting cycle’ to be strongly enriched (**Table S3**). Accordingly, we observed specific peak phases to be enriched during the molt and opposite peak phases to be depleted in the 594 genes compared to all oscillating genes (**Figure 2.15G**). We note that the peak phase enrichment is most prominent during the molt, but slightly shifted to later times compared to the peak phase enrichment of the 354 genes we identified above (compare **Figure 2.15G** with **Figure 2.14D**). Nevertheless, these results are consistent with a function of BLMP-1 in molting, and with a model in which BLMP-1 is rhythmically active. Moreover, the observation that many of the affected genes peak at earlier times, but the time of the trough remained unchanged compared to control animals, suggests that BLMP-1 ensures that the oscillatory expression of sets of genes occur in synchrony.

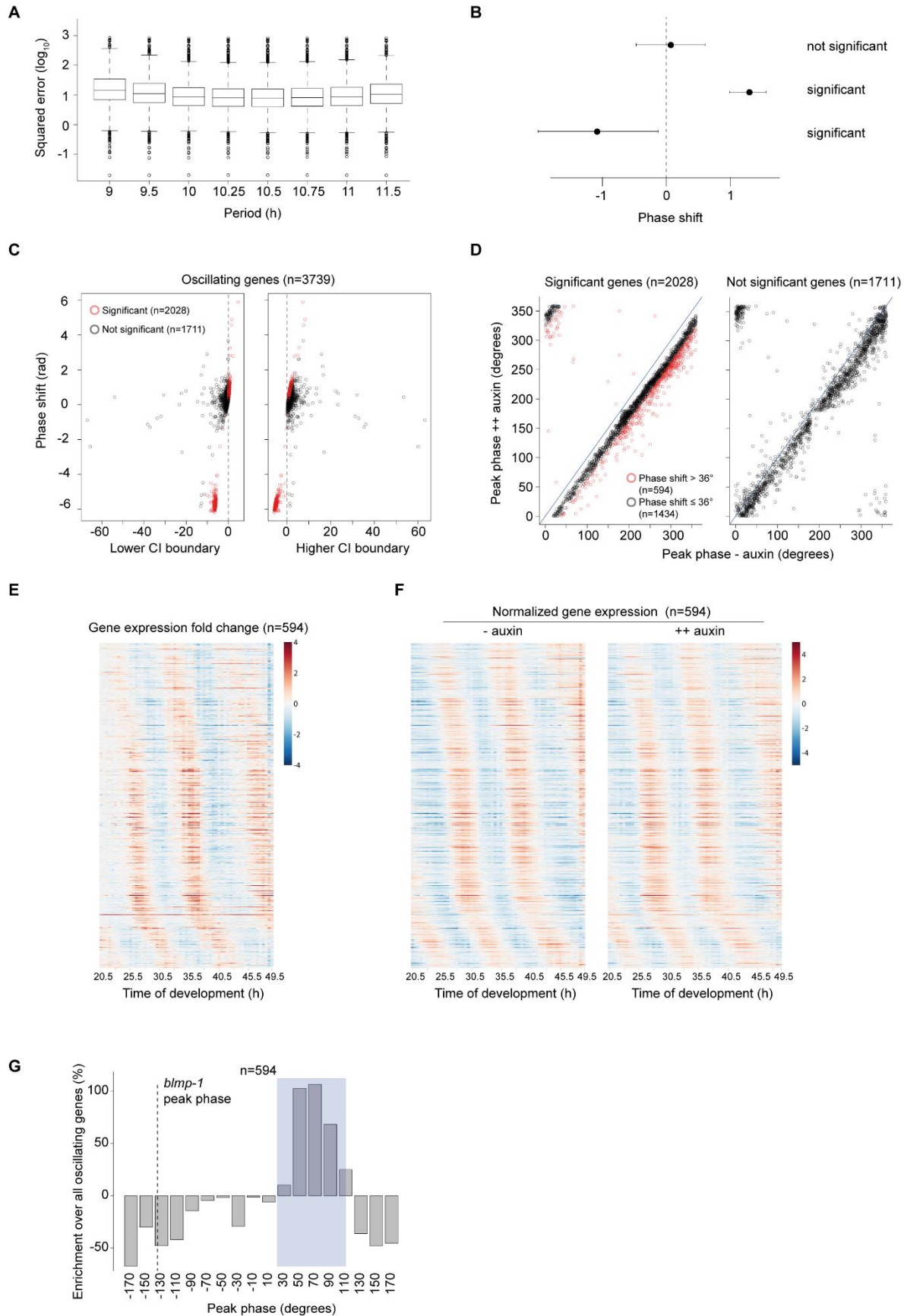


Figure 2.15: Quantification of phase shifts in expression of oscillating genes upon loss of BLMP-1 using cosine fitting

A, Boxplot showing the squared error (fitted – measured gene expression) in \log_{10} for each gene as determined by cosine fitting. Cosine fitting was performed on the previously annotated oscillating genes (Meeuse, Hauser) using the indicated periods.

B, Cartoon showing mean phase shifts (dots) with confidence intervals. A phase shift is considered significant if the confidence interval does not include 0. Note that confidence intervals of significant phase shifts can be larger than confidence intervals of non-significant phase shifts.

C, Scatterplot showing the phase shift in rad over the lower boundary of the confidence interval (CI) (left) and the higher boundary of the CI (right). Genes with significant (red) and not-significant (black) phase shift according to B are indicated.

D, Scatterplot showing the peak phase in degrees of ++ auxin (250 μ M) over – auxin (vehicle). Significantly changing genes (left) and not-significantly changing (right) genes as determined in C are indicated. Genes for which the phase shift is $> 36^\circ$ (red) and $\leq 36^\circ$ (black) are indicated.

E, Heatmap of fold change between gene expression in ++ auxin (250 μ M) and in - auxin (vehicle) conditions for significantly changing oscillating genes (n=594). Expression fold change is sorted by peak phase.

F, Gene expression heatmaps in auxin-treated (++ auxin) and control (- auxin) animals for significantly changing genes (n=594). Gene expression was mean-centered over both conditions, sorted according to A and plotted in \log_2 .

G, Barplot showing peak phase enrichment of significantly changed oscillating genes (n=594) over all ‘oscillating’ genes (Meeuse et al., 2019) Peak phases are sorted in 20° bins. The peak phase of *blmp-1* is -138° (dashed line) and the molt occurs roughly between 20° and 110° (blue box), as previously determined (Meeuse et al., 2019).

3. Discussion

Gene expression oscillations are wide-spread in biological systems. Whereas the molecular architecture, the functional relevance, and the systems properties have been investigated for some, they remain unclear for other biological oscillators. Here, I propose the *C. elegans* oscillator as a powerful tool to study genetic oscillations and provide insight into features that are unique, as well as those that might be shared between biological oscillators. In this work, we have described the *C. elegans* oscillator and investigated its system properties. We have identified putative components of the oscillator and provided insight into its functional relevance. Here, I will discuss these findings.

3.1 Identification of thousands of oscillating genes during *C. elegans* larval development

Previous mRNA-seq time courses did not cover all stages of *C. elegans* development or were not sufficient in temporal resolution to fully and accurately describe the *C. elegans* oscillator (Hendriks et al., 2014; Kim et al., 2013). Here, we collected precisely those data. Consistent with previous studies (Hendriks et al., 2014; Kim et al., 2013), we found that mRNA transcripts oscillate, peaking once every larval stage. We used these data to classify genes as ‘confidently oscillating’ or ‘not oscillating’. This expanded the number of oscillating genes from 2,718 (Hendriks et al., 2014) to 3,739 genes. We predict that the identification of oscillation genes improved by performing cosine fitting on L1-L3 stage, in which the oscillation period appeared stable. In our previous dataset covering L3 to young adult stages (Hendriks et al., 2014), the lengthening of the oscillation period in L4 and the genes which rise in their expression during late larval development might have hindered the detection of the additional 1240 genes we found here. For similar reasons, we expect that the 219 genes which we did not classify as ‘confidently oscillating’ here, are likely to be mis-classified before (Hendriks et al., 2014). We note that some of the 219 genes and other genes we classified as ‘not oscillating’ can show low amplitude or non-sinusoidal dynamics. Thus, the class of ‘not oscillating’ genes includes not only genes that lack oscillatory expression as such, but also genes for which we failed to identify high-amplitude and sinusoidal oscillations with high confidence using cosine fitting. Methods such as the Hilbert transform and the Wavelet transform, widely used in signal processing, can be applied to quantitatively describe the non-sinusoidal dynamics in gene expression. As most of the dynamic genes could be identified with ‘high confidence’ through cosine fitting and thus exhibit considerable sinusoidal oscillations, I considered the identification of genes with non-sinusoidal oscillations less of a priority for this thesis. Low-amplitude oscillations might still be relevant for the function of the oscillator, particularly, but not necessarily, because rhythmicity may arise at the level of protein accumulation or activity. However, the dynamics of low-amplitude oscillations might be difficult to confidently quantify across experiments and especially in mutants. Hence, the comprehensive set of

genes we present here, which oscillate ‘confidently’ and with high amplitudes (>2-fold between peak and trough), will help to unravel the transcriptional network of the oscillator and its system properties.

3.2 Developmental stage transitions reveal properties of the *C. elegans* oscillator

In this work, we used the set of oscillating genes to investigate how the oscillator behaves during stages of the *C. elegans* life cycle. We found the oscillation amplitudes to be stable during L2-L4 stage (amplitudes in L1 stage were difficult to assess, see (Meeuse et al., 2019)), and the period to be constant during L1-L3, but increased during L4. Moreover, our observation that oscillations are absent in newly hatched larvae, developmentally arrested dauer larvae and post-developmental adults, allowed us to characterize the behavior of the oscillator in response to its transition between oscillatory and stable states. This so-called bifurcation analysis has been performed extensively in systems which adopt oscillatory and stable behavior depending on input signals, such as electrical spiking in neurons (Izhikevich, 2000; Saggio et al., 2017) and genetic dynamics in cellular circuits (Conrad et al., 2008; Guantes and Poyatos, 2006). However, bifurcations in oscillators that act at the organism level have remained difficult to investigate, especially those occurring naturally. Here, we revealed a quantitative characterization of the natural and induced bifurcations of the *C. elegans* oscillator. In newly hatched larva, dauer larvae and adults, the oscillator appeared to be arrested in a specific phase rather than adopting a different, completely unrelated state. Interestingly, the specific phase of the oscillator at the stable regime corresponded to molt exit. Given that freshly hatched larvae, dauer exit and molt exit are sensitive to feeding, we propose that food is informative for the state of the oscillator, a hypothesis I will address in different sections the discussion. However, first, I will discuss the system level properties that can be inferred from the characteristics of the oscillator during its oscillatory and stable states.

3.2.1 The *C. elegans* oscillator emerges as a rigid oscillator

Our findings are consistent with the characteristics of a rigid oscillator (Abraham et al., 2010), i.e. an oscillator that is robust to changes in amplitude when changing its period. Mathematical models revealed that rigidity is favored in oscillatory networks consisting of combined positive and negative feedback loops over networks that consist of a negative feedback loop only (Tsai et al., 2008). Moreover, rigidity was enhanced when oscillators were coupled to one another (Abraham et al., 2010). Although these design principles are not a prerequisite of rigid oscillators, we propose them to be important features to investigate when dissecting the *C. elegans* oscillator. The ability to allow variations in the oscillation period, but at the same time have robust amplitudes seems to be functionally relevant for developmental oscillators as they need to ensure faithful development across different conditions. Our findings are

consistent with a rigid oscillator under stable environmental conditions during which amplitudes remained stable and the period increased naturally during late larval development. Whether the amplitude of oscillations remains unchanged under changing environmental conditions, e.g. at lower temperatures when the duration of developmental stages and the oscillation period increase, remains to be established.

3.2.2 State transitions of the *C. elegans* oscillator resemble a SNIC bifurcation

The qualitative changes we observed in the dynamics of the oscillator during the transitions prompted us to investigate which type of bifurcation is consistent with our results. The stable amplitude, the increasing period and the arrest at a particular oscillator phase, which we observed here, are all in agreement with the characteristics of a SNIC bifurcation rather than a Hopf bifurcation. Although the type of bifurcation puts constraints on the design and the parameters of the network, SNIC bifurcations have been observed in different network designs (reviewed in Purcell et al., 2010). At the same time, a particular network design can reveal different types of bifurcations, depending on the parameters. In fact, network topologies consisting of positive and negative feedback loops revealed both Hopf and SNIC bifurcations (Conrad et al., 2008). Hence, we can only speculate about the architecture of the *C. elegans* oscillator, as it cannot be inferred directly from the notion that its transitions resemble a SNIC bifurcation.

3.2.3 What is the status of the core oscillator during the stable regimes?

The absence of oscillations in freshly hatched larva, dauer larvae and adults, allows to speculate about the status of the core oscillator. It is possible that the core oscillator is not functional, and hence, its output oscillations are absent in the stable regimes of the system. Alternatively, the core oscillator could still be active, but the output is not connected to the core oscillator. If the core oscillator would remain active through the *C. elegans* lifecycle, one would expect that oscillations can initiate at variable times depending on the phase of the oscillator when feeding is resumed. Although animals hatched at different times and are subsequently starved for different durations to synchronize L1 animals during our RNA-seq time courses, the onset of oscillations appeared synchronous among animals. On the one hand, it remains possible that the core oscillator is active, but resumption of feeding resets the phase of active oscillator, resulting in synchronous initiation of oscillations within a population. On the other hand, the core oscillator is initially quiescent, but becomes activated upon resumption of feeding. Identification of the core components of the *C. elegans* oscillator and their dynamics throughout the *C. elegans* life cycle will help to determine the status of the oscillator during the stable regimes.

3.2.4 Transition from a stable into an oscillatory regime during embryogenesis

To complete our description of the *C. elegans* oscillator, here, I will discuss our findings on the properties of the oscillator during embryogenesis. In contrast to the sudden onset and termination of oscillations in larvae and adults, respectively, the system appeared to be in a different state and more slowly approach an oscillatory state during early embryogenesis, before it transitioned into an oscillatory state later during embryogenesis. In contrast to the transitions we discussed above, our observations during embryogenesis are inconsistent with a SNIC bifurcation. We note that the correlations were lower in embryos compared to larvae, which might reflect embryo-specific transcriptional programs. Moreover, the first cuticle is synthesized but not shed during embryogenesis, which could suggest that, in embryos, only part of the oscillator functions or only part of the output is coupled to the oscillator. However, as data was collected from single embryos, the quality and the depth of the data was lower than in larvae. Hence, we speculate that a highly resolved RNA-seq time course covering embryogenesis, hatching and the first larval stages will provide insight not only into the type of bifurcation, but also whether the oscillator as such, or only a subset of the genes start oscillating in embryos. Hence, these studies will further address the question of whether certain oscillatory modules can be split from others, facilitating the dissection of the architecture of the oscillator.

3.3 A function of the *C. elegans* oscillator in repetitive developmental processes

Gene expression oscillators are often considered time-keeping mechanisms as they can determine time depending on the phase of their oscillation (Rensing et al., 2001). If the *C. elegans* oscillator were to ensure correct timing of developmental events, we would at least expect developmental stages to coincide with the oscillation period, although that does not directly imply functional coupling. Up to date, quantification of developmental progression and transcript dynamics simultaneously and with high temporal resolution has been lacking. Here, we collected those data and showed that oscillations are phase-locked to the molts (Meeuse et al., 2019). Although it remains possible that oscillations and development are timed very precisely but regulated through independent mechanisms, our error propagation analysis suggests that oscillations and development are tightly coupled. Hence, we propose that the oscillator acts as a mechanism which controls timely execution of repetitive developmental events. Given that cuticular components of the cuticle were enriched among oscillating genes (Hendriks et al., 2014), and that our results here suggest that GRH-1 acts as a key factor for molting and a putative component of the oscillator, a role of the oscillator in regulation molting seems very likely.

However, the functions of the oscillator do not appear to be restricted to molting, as peak phases of the oscillations are wide-spread (Hendriks et al., 2014). We propose that animals require sufficient resources and coordination of multiple developmental processes to faithfully execute a molt. Hence, the oscillator might control those processes already before the molt. We consider epidermal remodeling one of those processes. Indeed, we showed that the transition from a stable into an oscillatory state of the system during embryogenesis coincided with epidermal morphogenesis, and elongation, long before the first cuticle was synthesized. Moreover, mutations in factors which connect the cuticle, epidermis, basement membrane and muscle cells revealed molting phenotypes, suggesting that cuticle renewal requires remodeling of the underlying tissues (reviewed in Lažetić and Fay, 2017). Finally, repetitive seam cell proliferation and molting are coupled processes, but appear to be regulated by different mechanisms (Ruaud and Bessereau, 2006). Hence, we speculate that the *C. elegans* oscillator generally controls epidermal programs, possibly among other repetitive events.

Interestingly, recent studies showed that oscillations of lineage-specifying transcription factors keep stem cells in a proliferative and multipotent state, whereas constant expression coincided with cellular differentiation (Imayoshi et al., 2013; Kobayashi et al., 2009). It has been proposed that oscillations serve to give stem cells the opportunity to adopt different states, depending on the cues available at that time. Intriguingly, a function in cell differentiation appears to be shared by the homologs of the transcription factors we identified in this work. Myrf, the mammalian homolog of *myrf-1*, is a direct target of Sox10, which act together to activate the myelin-specific regulatory network during oligodendrocyte differentiation (Hornig et al., 2013). Blimp1, the mammalian homolog of *blmp-1*, is a master regulator of the B and T cell fates (reviewed in Nutt et al., 2007). Grainyhead and Grainy head like (Grhl) factors, the *Drosophila* and mammalian homologs of *grh-1* respectively, play a role in development and maintenance of epithelial tissues (reviewed in Wang and Samakovlis, 2012). NHR-25 controls cell fates of vulva precursor cells in *C. elegans* (Ward et al., 2013) and its homolog SF-1, plays a role in the differentiation of adrenal glands and gonads (Schimmer and White, 2010). Hence, it seems possible that the *C. elegans* oscillator can function to provide cells with a time-window in which specific developmental programs, e.g. cell fate choices and molting, can be executed. Consistent with this hypothesis, we found that oscillations ceased during the transition to post-developmental adults. The cues that could potentially define this time-window will be discussed in **section 3.7**.

3.4 Transcript oscillations arise from rhythmic transcription

Gene expression oscillations can result from rhythmic production, rhythmic degradation or a combination of these two. We previously found that pre-mRNA levels are rhythmic (Hendriks et al., 2014). Moreover, several transcriptional reporters, in which the promoter of an oscillating gene is fused to nuclear and destabilized GFP, recapitulated not only the oscillation as such but also the phase and the amplitude of the endogenous oscillating transcript (Hauser et al, unpublished), indicating that promoters are sufficient for oscillatory gene expression. In this work, we investigated this notion further and specifically asked at which step of transcription oscillatory regulation occurs. Our finding that RNAPII occupancy at the TSS of oscillating genes is rhythmic suggests that recruitment of RNAPII to the promoter occurs in an oscillatory manner. However, some genes that oscillate on the mRNA level do not exhibit detectable rhythmic RNAPII occupancy, which might reflect a contribution of transcriptional processes after RNAPII recruitment or rhythmic post-transcriptional regulation. In the circadian oscillator, only about 20% of transcript oscillations resulted from rhythmic transcription (Koike et al., 2012), and post-transcriptional regulation, e.g. transcription termination, alternative splicing, translation, miRNAs, polyadenylation and mRNA degradation, are known to modulate transcript oscillations in the circadian oscillator (reviewed in Lim and Allada, 2013). However, given that in our data RNAPII amplitudes appeared to be lower at a global level and specifically for the genes whose transcriptional reporter transgenes recapitulated the amplitude perfectly (Yannick Hauser, unpublished), we suspect the dynamic range of RNAPII-ChIP-seq to be lower than that of mRNA-seq. Although we cannot comment on the extent of rhythmic RNAPII occupancy for genes with insufficient ChIP-seq coverage and a contribution of post-transcriptional processes remains possible, we propose that the *C. elegans* gene expression oscillations emerge, to a large extent, from rhythmic transcription.

3.5 Finding components of the *C. elegans* oscillator

The work we present here provides evidence for rhythmic transcription in establishing mRNA level oscillations, suggesting a role of rhythmically active transcription factors. Although rhythmic activity of transcription factors can be achieved in various ways, e.g. subcellular localization, post-translational modifications, degradation, or accessibility of DNA-binding sites, the fact that 92 transcription factors oscillated on the mRNA level provided a good starting point to investigate the role of these transcription factors, with potentially rhythmic activity, in regulating transcript oscillations. Given the coupling to oscillations to larval development (Meeuse et al., 2019), we screened the 92 ‘oscillating’ transcription factors for aberrant progression through development. We expected to find lengthening, shortening and irregular development, as similar phenotypes arise for core clock mutants of the circadian rhythm

(Takahashi, 2004). Interestingly, irregular molts have been observed for mutants of *lin-42* (Monsalve et al., 2011). *lin-42* is the homolog of the core component of the circadian clock, Period, which inhibits CLOCK-BMAL1 in their function as activators of period transcription (**Figure 1.2**). Given its conservation and the role of Period as a co-factor, *lin-42* was not present in our screen. Although *lin-42* mRNA levels peak once per larval stage (Jeon et al., 1999), a role as a core component of the *C. elegans* oscillator has not established.

In our screen, we found lengthening of development (*nhr-25*, *ztf-6*, *bed-3*) and larval lethality (*nhr-23*, *grh-1*, and *myrf-1*), but failed to find mutants with irregular development. We only observed shortening of intermolts which was accompanied by lengthening of molts (*blmp-1*). Although the phenotypic effects of mutants of oscillating genes are not easily predicted by intuition, it remains possible that short-period and arrhythmic mutants would only be observed when over- or mis-expressing these genes.

Most transcription factors did not reveal any phenotype in our hands. We consider several explanations: i) Knock-down by RNAi was insufficient to reveal phenotypes. ii) Our assay is not sensitive enough to pick up very small changes. iii) The function of some factors might be redundant and hence only double mutants would show phenotypes. iv) Certain transcription factors might not act at the core, but more downstream, v) or act to couple oscillators. As the latter two types of transcription factors are not essential for generating oscillations as such or only control a small subset of oscillations respectively, they might not reveal strong phenotypes. Indeed, transcription factors that act in one of the feedback loops, or as input, or as output of the circadian clock have frequently shown mild or no phenotypes (reviewed in Takahashi, 2004). However, given their gene expression changes, and the strong phenotypes we find for *grh-1* and *blmp-1* depletion, indicate that such predictions do not always apply. vi) It is also plausible that transcription factors exhibit rhythmic activity without oscillations at the mRNA level, a class of transcription factors which were not included in our screen. vii) With the improved annotation of oscillating genes we presented here, the number of oscillating transcription factors increased from 92 (Hendriks et al., 2014) to 154 (Meeuse et al., 2019). Hence, we might simply have missed some important factors. Finally, viii) as other mechanisms might contribute to generating oscillations, components of the oscillator might include proteins other than transcription factors.

Nevertheless, the screen we performed here has been a great proof of principle and now provides us with a tool to more extensively screen the *C. elegans* genome for factors important for the functioning of the oscillator. In this work, we have identified a handful of interesting factors and we propose that they serve as a good starting point for dissecting the *C. elegans* oscillator (**section 3.6**).

3.6 Insights into the molecular architecture of the *C. elegans* oscillator

Perturbation of the oscillator followed by phenotypic and genetic characterization, has provided major insights into the architecture of the circadian and segmentation oscillator. In this work, we have characterized *nhr-25*, *blmp-1*, *myrf-1* and *grh-1* as putative components of the *C. elegans* oscillator and I will further discuss them below.

3.6.1 MYRF-1 and GRH-1 as putative components of the ‘molting oscillator’

Previously, *myrf-1(0)* mutants have been shown to die from being trapped in their cuticle in L1 stage, and hence, a role of *myrf-1* in regulating molting has been suggested (Russel et al., 2011, here named *pqn-47*, later renamed to *myrf-1*). Here, we observed the same phenotype. Additionally, our data suggest that the rhythmic activity of MYRF-1 might be required for shedding of the cuticle during multiple larval stages. Although the molecular mechanisms through which MYRF-1 functions in molting remains to be established, we expect that the oscillatory activity of MYRF-1 ensures the timely expression of genes required to break and escape from the cuticle. RNA-seq time course experiments in MYRF-1 depleted and control experiments would facilitate the identification of such genes. Interesting candidates could be genes of the *nekl-mlt* kinase pathway, as some of the null mutants also resulted in encasement by the old cuticle. Moreover, the *nekl-mlt* kinase pathway has been implicated in endocytosis, which has been suggested to account at least partially for the shedding defects (Lažetić and Fay, 2017b; Yochem et al., 2015). A role of endocytosis in molting has been proposed, as it may be important for the uptake and recycling of sterols and components of the cuticle (Lažetić and Fay, 2017a). Interestingly the *C. elegans* genome encodes *myrf-2*, the paralog of *myrf-1*. *myrf-1* and *myrf-2* act redundantly in synaptic rewiring of neurons, a L1-L2 stage specific function of *myrf-1* (Meng et al., 2017). Although *myrf-2* mRNA levels do not oscillate, at least not with fold-changes >2 (Meeuse et al., 2019), whether *myrf-2* exhibits rhythmic activity and acts together with *myrf-1* in ecdysis remains to be established.

In this work, we present a functional characterization of GRH-1 as a putative component of the ‘molting oscillator’. As our findings are discussed in depth in the manuscript, here I will summarize them. We found that depletion of GRH-1 resulted in a long-molt phenotype, a phenotype we expect from an oscillator component and rupturing of the cuticle, a phenotype that appears to be conserved in Grainyhead mutants in *Drosophila* (Bray and Kafatos, 1991; Nüsslein-Volhard et al., 1984b). Moreover, our results indicate that rhythmic activity of GRH-1 is important for its function and that GRH-1 controls its expression via a negative feedback loop, features required for generating oscillations (Novák and Tyson, 2008). Finally, loss of GRH-1 affected the expression of a subset of oscillating genes, which were enriched for structural components of the cuticle, for the hypodermis and for particular peak phase. Thus, our insights on GRH-

1 function are three-fold: i) although we cannot distinguish between it being a core component or acting more downstream of the (sub-) oscillator(s), GRH-1 appears to be an important factor of the *C. elegans* oscillator. ii) Given that the molecular mechanisms which regulate molting are not well understood, here we provide insight into those mechanisms and propose that GRH-1 acts to control molting in a timely manner. As the oscillating genes affected by GRH-1 depletion were also enriched for ‘ECM regulators’, we propose a broader role for GRH-1 in regulating epidermal remodeling. iii) Our data on GRH-1 provides further evidence for the hypothesis that the *C. elegans* oscillator and molting are functionally coupled. Hence, we propose that GRH-1 ensures temporal control of epidermal programs, a function which may be shared with Grainyhead proteins in other organisms.

3.6.2 NHR-25 and NHR-23 as potential sterol sensors in the *C. elegans* oscillator

In agreement with a proposed role of *nhr-23* and *nhr-25* in molting (Gissendanner and Sluder, 2000; Kostrouchova et al., 1998, 2001), we showed that NHR-25 depletion resulted in defects in cuticle integrity and a long-period phenotypes for molts and intermolts. We were able to induce these phenotypes in multiple developmental stages by conditional NHR-25 depletion. Similarly, NHR-23 is repetitively required for its function in molting (Kostrouchova et al., 2001). However, whether and how NHR-23 and NHR-25 act as core components of the *C. elegans* oscillator is unknown. One possible function of NHR-23 and NHR-25 could be sterol sensing, a function similar to that of their *Drosophila* orthologues Dhr3, an ecdysone-responsive gene and its downstream target Ftz-f1 respectively (Gissendanner and Sluder, 2000; Kostrouchova et al., 1998). It sounds appealing that sensing of food controls or provides input for the oscillator to ensure that development occurs only when favorable conditions are met. Consistent with this idea, our findings revealed that re-feeding dauer diapause animals as well as synchronized L1 larvae resulted in resumption of oscillations at a specific phase of the oscillator, which coincided with molt exit. However, a ligand of *nhr-23* or *nhr-25* and a sterol that regulates molting in *C. elegans* has not been identified yet.

3.6.3 BLMP-1 as a putative ‘coupling’ factor in the *C. elegans* oscillator

Although *blmp-1* mRNA levels oscillate, whether and how it functions in the *C. elegans* oscillator remained unclear. Our results suggest that BLMP-1 is required for proper duration of molts and for cuticle integrity. Surprisingly, loss of BLMP-1 did not result in loss of oscillatory gene expression as such, instead the dynamics of a subset of oscillations appears to be affected in diverse ways. Many, but not all, of the affected genes revealed a more rapid increase their expression upon loss of BLMP-1, such their peak expression appeared shifted to earlier times, but their trough occurred at the same time. Our observation that molts are lengthened and the expression of a subset of genes appear to peak earlier upon loss of

BLMP-1, are somewhat unexpected. It remains possible that BLMP-1 was not fully degraded in the ++auxin condition and hence extension of molts could be compensated by shortening of intermolts as observed in the +auxin condition. However, we validated the phase shifts of some genes by RT-qPCR (data not shown) and genome-wide using a *blmp-1(0)* mutant in a separate time-course (Yannick Hauser, data not shown, unpublished). Hence, we propose that molting and gene expression were uncoupled. Moreover, phase shifts did not become progressively worse over development, suggesting that BLMP-1 is repetitively required for the expression of a subset of genes at the right time. Although to a lesser extent, we also observed other changes in the dynamics of gene expression in BLMP-1 depleted animals. Taken together, our results are consistent with a model in which BLMP-1 ensures that oscillations occur in synchrony by controlling their dynamics. Although it remains to be established whether BLMP-1 activity is rhythmic, the affected genes were enriched for a particular peak phase and unpublished data from our lab showed that BLMP-1 level oscillate (Yannick Hauser). Hence, we speculate that rhythmic activity of BLMP-1 ensures coupling between oscillatory gene expression and repetitive events such as molting. Given that a subset of genes appeared affected in their dynamics, it is possible that BLMP-1 couples different oscillators with each other, or alternatively different output modules of the core oscillator. Moreover, and in line with the hypothesis that the *C. elegans* oscillator acts to time and synchronize repetitive developmental events, development among *blmp-1(0)* animals appeared to become less synchronous (Yannick Hauser, unpublished), a phenotype that we predicted for components of the oscillator (**section 3.5**). We note that we did not observe this phenotype during the RNAi screen, supporting the notion that RNAi was weak in this case, and potentially also for other transcription factors tested. Thus, we propose BLMP-1 as a ‘coupling’ factor’ in the *C. elegans* oscillator.

How is synchronization between oscillations achieved mechanistically? It seems likely that BLMP-1 should provide input for and at the same time receive input from the oscillations to be synchronized. The type of feedback between the synchronizer and the oscillations to be synchronized determines the properties of the coupling (Kim et al., 2010). For example, positive feedback loops appeared to result in more robust coupling with response to noise compared to negative feedback loops (**Figure 3.1A**). In contrast, coupling via positive feedback loops resulted in less robustness over a range of coupling strengths compared to coupling via negative feedback loops (**Figure 3.1B**). Synchronization of the zebrafish segmentation oscillator between cells has been proposed to occur by Delta-Notch signaling via positive feedback (as reviewed in Oates et al., 2012) (**Figure 3.1A**), ensuring robustness to noise (Kim et al., 2010), whereas coupling between neurons can occur via negative feedback (**Figure 3.1B**), ensuring robustness to varying signaling between the coupling factor and the oscillators (Kim et al., 2010). Although coupling of

oscillations has mostly been studied between different cells, we propose that similar network motifs may underlie the functioning of BLMP-1 in the *C. elegans* oscillator. However, whether and to what extent BLMP-1 synchronizes different oscillators, or outputs thereof and what the identity and function of these oscillators are, remains to be identified.

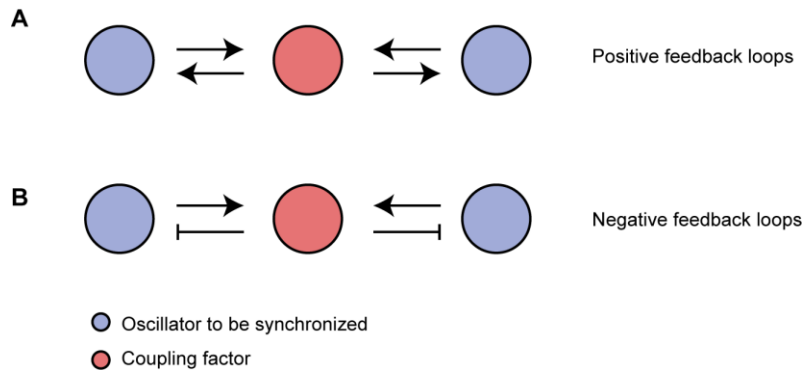


Figure 3.1: Schematic overview of coupled oscillators

Simplified cartoon of network motifs of coupled oscillators. A coupling factor (red) can synchronize two oscillators (purple) by positive feedback loops (A) or negative feedback loops (B). Based on (Kim et al., 2010).

3.7 Outlook and open questions

3.7.1 Do transcript oscillations arise solely from rhythmic transcription?

Although our data revealed rhythmic RNAPII occupancy at the promoter of oscillating genes, it remains unclear whether rhythmic transcription is the only mechanisms from which mRNA level oscillations emerge. Hence, it is unknown whether and to what extent post-transcriptional processes modulate rhythmic transcript accumulation.

Distinct modes of regulation can be inferred from differences in amplitudes and peak phases between mRNA production, and mRNA accumulation dynamics (Korenčič et al., 2012; Le Martelot et al., 2012). In principle, three different scenarios and their combinations exist: i) decreased amplitude in mRNA accumulation compared to mRNA production indicates stable and long-lived mRNAs. ii) Production and accumulation with similar amplitude and phases suggest short lived mRNA which are predominantly produced in a rhythmic manner. iii) Increased amplitude and often phase-shifted mRNA accumulation compared to production indicates a contribution of post-transcriptional processes. Hence, collecting temporally highly resolved mRNA production dynamics, e.g. RNAPII occupancy at the promoter, the gene body and the 3' end of the genes, together with mRNA accumulation dynamics across all larval stages will facilitate quantitative analysis of the amplitudes and peak phases. These datasets will not only provide

insight into the levels at which oscillations arise, but will also classify genes according to the different modes of regulation (discussed above), and hence, further facilitate the functional dissection of the *C. elegans* oscillator.

3.7.2 What is the molecular mechanism of GRH-1?

How exactly GRH-1 acts to control the expression of oscillatory genes remains unclear. The opposing phase enrichments for upregulated and downregulated oscillating genes upon GRH-1 depletion suggest that GRH-1 can act as a transcriptional activator and repressor. Interestingly, Grainyhead has been proposed as a pioneer transcription factor for epithelial genes in *Drosophila* (Jacobs et al., 2018), and its role as transcriptional activator and repressor may be explained by the fact that Grainyhead makes the DNA accessible for other transcription factors to bind. Whether GRH-1 acts as a pioneer transcription factor in *C. elegans* remains to be established. Studying chromatin accessibility and binding of GRH-1 to the DNA directly will help to distinguish primary from secondary targets of GRH-1 and provide insight into its mode of action.

Although our data is consistent with a model in which GRH-1 is rhythmically active, our experiments in which we initiated GRH-1 depletion at different times did not test this notion directly. Moreover, as we were limited by the time animals die during ecdysis, we may have underestimated the number of genes affected, and perhaps overestimated their phase enrichments in GRH-1 depleted animals. We propose that we can address both issues with the following experiments: targeted modulation of amplitude, peak phase and expression levels, rather than depleting GRH-1 as such in RNA-seq experiments and reporter assays. These experiments will not only reveal whether rhythmic activity of GRH-1 is required for its function, but also provide further insight into its molecular function. Additionally, these experiments will allow quantitative characterization of GRH-1 and facilitate mathematical modeling, which will help to better understand the dynamic functions of GRH-1 and how GRH-1 dynamics are regulated. Finally, screening for suppression or enhancement of the GRH-1 phenotype upon genome-wide mutagenesis will further aid the identification of the network that regulates its gene expression and its protein level activity.

3.7.3 Autonomous or forced oscillator?

Our observation that oscillations are absent in freshly hatched L1 larvae, dauer larvae and adults, suggest that the oscillator is quiescent. As discussed above, food may serve to initiate the oscillator. However, it remains unclear what mechanism ensures that the oscillator keeps running during development. Is the *C. elegans* oscillator an autonomous oscillator, similar to the circadian clock? Or is it a forced oscillator, i.e. does it require a trigger for each cycle? Given that the state of the oscillator at the moment of onset in L1

and dauer exit resembles that of the oscillator directly after molting, it seems possible that food not only acts to initiate, but also to trigger oscillations in each cycle. Interestingly, a recent study found that the absence of food in L3 and L4 stage directly after the molt resulted in developmental arrest. These time points appeared to act as developmental checkpoints and progression through them is regulated by hormone signaling (Schindler et al., 2014). These checkpoints ensure that development can only proceed when sufficient resources are available. Thus, a role of food-mediated hormone signaling in triggering the oscillator after molt exit, similar to the onset of oscillations in freshly hatched L1 and dauer animals seems likely. Alternatively, an autonomous oscillator might run continuously, and the absence of food might actively inhibit the oscillator. This mechanism would prevent that development continues when insufficient resources are available. Genetic perturbation, e.g. mis-expression, of the players in this pathway (Schindler et al., 2014), or induced starvation during the intermolt followed by mRNA sequencing will help to understand whether and how food triggers or inhibits the oscillator.

3.7.4 What is the topology of the oscillator at the molecular level?

Although our functional dissection of the *C. elegans* oscillator provides insight into its properties and putative components, the exact molecular architecture remains to be established. Our data on GRH-1 and BLMP-1 is consistent with the hypothesis that the oscillator controls different but synchronized developmental processes. On the one hand, the oscillator might comprise sub-oscillators, which are coupled but drive different processes. On the other hand, only one core oscillator might exist, which regulates well-separated but synchronized outputs. The topology of sub-oscillators we propose here shares similarities with that observed in somitogenesis, in which the oscillators of the Notch, FGF and Wnt signaling pathways are coupled. It is worth noting that it is unclear whether they represent the core oscillator or act as output of a core oscillator that remains to be identified (Dequéant and Pourquié, 2008). Although it may be difficult to directly infer the topology from mutants in which subsets of genes are affected, we propose GRH-1, for reasons mentioned in **section 3.6.1**, as a good starting point for dissecting the *C. elegans* oscillator. We expect that unraveling the molecular mechanisms important for the function of GRH-1 will also provide insight into the overall architecture of the oscillator.

It is likely that the complexity of the oscillators' architecture arises from the fact that multiple events need to be synchronized during *C. elegans* development. These events involve different repetitive processes, such as seam cell divisions and molting, which appear to be driven by different mechanisms (Ruaud and Bessereau, 2006), providing further support for the existence of coupled sub-oscillators or coupled outputs. Additionally, stage-specific events, such as the larval-to-adult transition, take place during *C.*

elegans development. The larval-to-adult transition in the skin of *C. elegans* is characterized by cessation of the molting cycle, seam cell exit of the cell cycle, terminal differentiation of the seam cells and synthesis of an adult instead of a larval cuticle (Sulston and Horvitz, 1977). To ensure that the repetitive developmental events cease upon adulthood, time-keeping mechanisms of rhythmic and linear processes need to be coordinated. At what level the linear timer interacts with the oscillator and how the linear timer ‘knows’ when to stop the activity of the oscillator is currently unknown.

3.7.5 What is the topology of the oscillator at the tissue level?

Above we focused on the molecular topology of the oscillator. However, the architecture of the oscillator at the tissue level also remains unclear. Given that mRNA-sequencing was performed on populations of whole animals, our sequencing data might not only be affected by population asynchrony, but also mask distinct dynamics between different tissues. We previously observed strong enrichment of the hypodermis for the expression of oscillating genes (Hendriks et al., 2014) and the transcriptional reporters we imaged so far are predominantly, but not exclusively expressed in the hypodermal cells (Meeuse et al., 2019, GRH-1 manuscript, Yannick Hauser unpublished). Hence, oscillations on the whole animal level might be dominated by hypodermal expression. Moreover, mRNA transcripts may oscillate with similar amplitudes but out of phase in different tissues, resulting in a composite phase at the whole animal level. Therefore, we might have misinterpreted the peak-phases and amplitudes. Finally, if oscillations were to oscillate in antiphase from one tissue to the other, the expression in different tissues could cancel each other out, and thus, we might have underestimated the extent of oscillations. Single cell sequencing will facilitate the identification of aberrant dynamics in tissues and provide insight into the tissue-level architecture of the oscillator.

The core of the circadian oscillator is shared among tissues, but the output is tissue-specific (Zhang et al., 2014). In *C. elegans*, it is unknown whether the same oscillator exists across different tissues and whether it drives the same or a tissue-specific output. Alternatively, it remains possible that different oscillators act in different tissues. Hence, tissue specific depletion of the components of the oscillator will provide insight into their relevance and functioning in different tissues. In any case, oscillations in different tissues must be synchronized to provide robust control over animal level processes, such as molting. In the circadian clock, entrainment of peripheral clocks involves neural control, hormonal control, temperature and local cues such as feeding and activity (Mohawk et al., 2012). Similarly and considering that they have been implicated in molting (reviewed in Lažetić and Fay, 2017a), nuclear hormone receptors and hedgehog signaling might be candidates for synchronizing oscillations across tissues in *C. elegans*.

4. Methods

ChIP-seq

For RNA polymerase II ChIP-sequencing, synchronized L1 wild-type (N2) worms were grown at 25°C on XL plates containing 2% NGM and concentrated OP50. Worms were collected hourly from 22 hrs (90.000 worms) until 33 hrs (46.000 worms) after plating. RNA polymerase II ChIP was performed as previously described (Miki et al., 2017). In short, worms were incubated in M9 with 2% Formaldehyde for 30 minutes at room temperature with gentle agitation to allow protein-DNA crosslinking. Worms were lysed with beads using the FastPrep-24 5G machine (MP Biomedicals, settings: 8 m/sec, 30 sec on, 90 sec off, 5 cycles). Lysates were sonicated using the Bioruptor Plus Sonication system (Diagenode, settings: 30 sec on, 30 sec off, 20 cycles). 250 µg sonicated chromatin was incubated with 10 µg mouse anti-RNA polymerase II CTD antibody (8WG16, Abcam) at 4°C for 2 hours with gentle agitation and subsequently with 45 µL Dynabeads Protein G (Thermo Fisher Scientific) at 4°C overnight with gentle agitation. Eluate was treated with 0.13 ug/uL RNase and 1 ug/uL Proteinase K. ChIP-seq libraries were prepared using NEBNext Ultra DNA Library Prep Kit for Illumina (New England Biolabs) and sequenced using the HiSeq 50 cycle single-end reads protocol on the HiSeq 2500 system.

Sequencing reads were mapped to the ce10 *C. elegans* genome using the qAlign function (default parameters, Rbowtie aligner version 1.12.0) from the QuasR package in R (Au et al., 2010; Gaidatzis et al., 2015; Kim et al., 2015; Langmead et al., 2009) (version 1.12.0). ChIP-seq counts within 1-kb windows, i.e. -500 bp to +500 bp around the annotated TSS (using WS220/ce10 annotations), were scaled by total mapped library size per sample and log₂-transformed after adding a pseudocount of 8. Genes with a mean scaled TSS window count of less than 8 across all samples were excluded. Log₂-transformed counts were then quantile-normalized using the normalize.quantiles function from the preprocessCore library in R (Bolstad et al., 2003). Finally, quantile-normalized values were row-centered.

For total RNA sequencing, worms were collected hourly from 22 hrs (10.000 worms) until 33 hrs (5.000 worms) after plating from the same plates as for ChIP sequencing. RNA was extracted in Tri Reagent and DNase treated as described previously (Hendriks et al., 2014). Total RNA-seq libraries were prepared using Total RNA-seq ScriptSeq Library Prep Kit for Illumina (New England Biolabs) and sequenced using the HiSeq 50 cycle single-end reads protocol on the HiSeq 2500 system.

RNA-seq data were mapped to the *C. elegans* genome (ce10) using the qAlign function (splicedAlignment=TRUE, Rbowtie aligner version 1.16.0) from the QuasR package in R (Au et al., 2010; Gaidatzis et al., 2015; Kim et al., 2015; Langmead et al., 2009) (version 1.16.0). Exonic and intronic

expression was quantified using qCount function from the QuasR package in R. For exonic expression, the exon annotation of the ce10 assembly (version WS220) was used. Genomic positions of introns were determined by gene body position (start of the first exon until end of the last exon) minus position of exons, which were extended with 10 nucleotides to ensure that reads close to the boundaries were not included in intronic counts. Counts were scaled by total mapped library size for each sample. A pseudocount of 8 was added and counts were \log_2 -transformed. Lowly expressed genes were excluded (maximum \log_2 -transformed exonic expression - ($\log_2(\text{gene width})$ - $\text{mean}(\log_2(\text{gene width}))$) ≤ 6). Of the previously annotated 'high-confidence-oscillating' genes ($n=3739$) (Meeuse et al., 2019), 2106 genes were sufficiently expressed on the exonic level. A reduction in the number of oscillating genes is likely due to reduced number of mapped reads. Oscillating genes were sorted by phase and mean-normalized expression was plotted in heatmaps.

Hidden Semi Markov Model

To determine the positions of the molts in the luminescence traces, we constructed a hidden semi-Markov model (HSMM) using the R package mhsmm (O'Connell and Højsgaard, 2011) (version 0.4.16). Before applying the model, the raw time course traces were processed as follows: First, we \log_2 transformed the raw intensity values after adding a pseudocount of 16 ($y=\log_2(x+16)$). Then we determined the noise floor of each experiment by calculating the median intensity of the first 20 time points (before the hatching). This was used to extend every trace at the beginning by 20 time points to ensure the correct detection of the hatch. After this, we performed a lowess regression with a smoother span of 0.2 using the R function 'lowess' from the package 'gplots' (Warnes et al.) to remove the overall trend of the traces. The resulting traces were used as an input to the HSMM. The HSMM was comprised of a total of 11 states connected in a linear fashion: B, I1, M1, I2, M2, I3, M3, I4, M4, A, T. B refers to the section before the hatch, I refers to intermolts, M refers to molts, A refers to adulthood and T refers to the termination state. T is a dummy state that ensures that the HSMM walks through the full time course until the end. This state is set to emit a very high value of 10, which is outside of the range of the data. By extending each trace by 100 time points with a value of 10, the HSMM is forced at the end to enter state 11 and emit the high values observed in T. The various parameters required by the HSMM were manually extracted from a set of 15 wildtype traces. The wildtype traces were collected from 3 independent experiments and molts were manually annotated using a graphical user interface in MATLAB (Meeuse et al., 2019). The means of the emission distributions were set to -0.5(B), 0.3(I), -2.0(M), 0.3(A) and 10(T). The standard deviations for the emission distributions were all set to 0.2. We used Poisson-shift as sojourn distributions with lambdas of 50(B), 40(I1), 2(M), 30(I2-I4), 30(A), 70(T) and shifts of 21(B), 50(I1), 5(M), 30(I2-I4), 30(A), 30(T). We

determined the most likely sequence of states given the observed data using the viterbi algorithm implemented in the function `predict` from the package 'raster' (Hijmans, 2019) in R. To investigate whether the states were properly annotated, we interpolated the \log_2 -transformed luminescence in annotated state for each worm to the corresponding state of a 'perfect' worm, i.e. a combination of state durations with the highest probability, using the function 'approx' from the package 'stats' (R Core Team) in R. We visualized alignment performance by plotting the interpolated \log_2 -transformed luminescence in heatmaps. To quantify the state durations, we excluded conditions for which molts could not be reliably annotated by visual inspection of the heatmap and traces with mean \log_2 -transformed luminescence ≤ 5.8 , referring to empty wells. Significant differences between WT and RNAi-deficient animals were calculated using `t.test(paired=TRUE)` from the package 'stats' (R Core Team) in R.

Transgenic worm strains

Luciferase strains

HW1939: *EG6699, xeSi296 [Peft-3::luc::gfp::unc-54 3'UTR, unc-119(+)] II* (Meeuse et al., 2019)

HW2150: *EG6699, xeSi296 [Peft-3::luc::gfp::unc-54 3'UTR, unc-119(+)] II; rde-1(ne219) V* (this study)

HW1949: *EG8080, xeSi301 [Peft-3::luc::gfp::unc-54 3'UTR, unc-119(+)] III* (this study)

HW1993: *EG8081, xeSi312 [Peft-3::luc::gfp::unc-54 3'UTR, unc-119(+)] IV* (this study)

AID strains

KRY85: *ieSi57 [Peft-3::TIR1::mRuby::unc-54 3'UTR, cb-unc-119(+)] II; nhr-25(nhr-25::degron-TEV-3xFLAG) X* (Zhang et al., 2015)

HW1981: *ieSi57 [Peft-3::TIR1::mRuby::unc-54 3'UTR, cb-unc-119(+)] II; EG8080, xeSi301 [Peft-3::luc::gfp::unc-54 3'UTR, unc-119(+)] III; nhr-25(nhr-25::degron-TEV-3xFLAG) X* (this study)

HW2079: *EG8080, xeSi376 [Peft-3::TIR1::mRuby::unc-54 3'UTR, cb-unc-119(+)] III* (GRH-1 manuscript)

HW2566: *myrf-1[(xe161)myrf-1::degron::3xFLAG] II* (this study)

HW2634: *myrf-1[(xe161)myrf-1::degron::3xFLAG] II; EG8080, xeSi376 [Peft-3::TIR1::mRuby::unc-54 3'UTR, cb-unc-119(+)] III; EG8081, xeSi312 [Peft-3::luc::gfp::unc-54 3'UTR, unc-119(+)] IV* (this study)

HW2078: *blmp-1[xe80(blmp-1::degron)] I* (this study)

HW2120: *blmp-1*[*xe80(blmp-1::degron)*] I; EG6699, *xeSi296* [*Peft-3::luc::gfp::unc-54 3'UTR, unc-119(+)*] II; EG8080, *xeSi376* [*Peft-3::TIR1::mRuby::unc-54 3'UTR, cb-unc-119(+)*] III (this study)

Generation of transgenic worm strains

Luciferase strains HW1949 and HW1993 were generated by single copy integration of the transgene into universal MosSCI sites in EG8080 and EG8081 animals respectively, by injecting pMM002 as previously described (Meeuse et al., 2019).

HW2079 animals were generated as described in the GRH-1 manuscript.

Endogenous degron-3XFLAG tagging of *myrf-1* and *blmp-1* by CRISPR/Cas9-mediated editing was performed as for *grh-1* (**GRH-1 manuscript**).

For *myrf-1*, we used the following hybridized primers for inserting the sgRNA sequence into pIK198 (Katic et al., 2015):

MM124 5' AATTGCAAATCTAAATGTTT GGATTGACTGCAGCAGTTCC GTTTAAGAGCTATGCTGGAA 3'

MM125 5' TTCCAGCATAGCTCTTAAAC GGAAGTCTGCAGTCAATCC AAACATTTAGATTTGCAATT 3'

A degron-linker-3XFLAG-linker cassette was synthesized as gBlocks® Gene Fragments (Integrated DNA Technologies) with 50 bp homology arms to the *myrf-1* locus right after **aa171**, similar to the position described before (Meng et al., 2017) :

5'
AAATGCAAAACATGAATGCTCCACAATTCTGGAGCCAACCGGAACT**GCT**atgcctaaagatccagccaaacctccggccaa
ggcacaagttgtgggatggccaccggtgagatcataccggaagaacgtgatggtttcctgccaaaaatcaagcgggtggcccgaggcgcggttc
gtgaagAGTACCTCAGGCGGCTCGGGTGGTACTGGCGGCAGCGACTACAAAGACCATGACGGTGATTATAAAGATC
ATGACATCGATTACAAGGATGACGATGACAAGAGTACTAGCGGTGGCAGTGAGGTACCGGCGGAAGCGCAGTC
AATCAACCTACAAACACCCTGGCTCAACTCAACCTTTTCAACAT 3'.

For *blmp-1*, the sgRNA sequence: 5' gccgaagagaacggtgccgg 3' was cloned into pIK198 (by Iskra Katic). A degron cassette was synthesized as gBlocks® Gene Fragments (Integrated DNA Technologies) with 65 bp homology arms to the *blmp-1* locus, 30 bp downstream of the **ATG** start codon.

5'
ttcgtatctattttaacaaaacctgtaaaaa**atg**GGTCAAGGAAGTGGGATGACGGTGTCCGatgcctaaagatccagccaaacc
tccggccaaggcacaagttgtgggatggccaccggtgagatcataccggaagaacgtgatggtttcctgccaaaaatcaagcgggtggcccgaggcg

cgggcgttcgtgaagCCGGCACCGTTCTCTTCGGCTGCTGCGGCAGCTCACTCACCTCATTCTCCCCTTTCTGTCGG
3'

Wildtype animals were injected with constructs as described in the GRH-1 manuscript and genome editing was confirmed by sequencing.

***blmp-1::degron* time course**

Synchronized L1 HW2120 animals were cultured in liquid medium (S-medium [1L S Basal [5.85 g NaCl, 1 g K₂ HPO₄, 6 g KH₂PO₄, 1 mL cholesterol (5 mg/ml in ethanol), in H₂O to 1L] , 10 mL 1 M potassium citrate pH 6, 10 mL trace metals solution [1.86 g disodium EDTA, 0.69 g FeSO₄ •7 H₂O, 0.2 g MnCl₂•4 H₂O, 0.29 g ZnSO₄ •7 H₂O, 0.025 g CuSO₄ •5 H₂O, in H₂O to 1L], 3 ml 1 M CaCl₂, 3 ml 1 M MgSO₄] supplemented with OP50, OD₆₀₀ = 3.5, 1000 worms/mL). Animals were grown in a temperature controlled incubator at 20°C, shaking at 240 rpm. After 20 hours, we harvested ~500 animals for RNA-seq. Subsequently, the culture was split in three separate cultures and 3.9 μM auxin, 250 μM auxin, or 0.25% ethanol (vehicle) was added. ~500 animals were harvested every 30 minutes from 20.5 hours until 49.5 hours. Animals were washed three times with M9 buffer and 200 μL Norgen lysis buffer (Norgen Single cell RNA purification kit, Cat. 51800) was added, separated over two 1.5 mL Eppendorf tubes and stored at -80 degree for further processing.

RNA isolation

To extract RNA, 5 freeze-thaw cycles were performed. RNA was isolated using the Norgen Single cell RNA purification kit (Cat. 51800, starting from step 2). Extracted RNA was DNase treated on columns (according to Norgen kit) and libraries were prepared using the TruSeq Illumina mRNA-seq (stranded – high input) protocol. Libraries were sequenced using the Hiseq50 Cycle Single-end reads protocol on the HiSeq2500.

Processing of RNA-seq data

The RNA-seq samples were mapped to the *C. elegans* genome (ce10) with the R package QuasR (Au et al., 2010; Gaidatzis et al., 2015; Kim et al., 2015; Langmead et al., 2009) using the spliced alignment algorithm SpliceMap (Au et al., 2010). The command used to perform the alignments was "proj <- qAlign("samples.txt", "BSgenome.Celegans.UCSC.ce10", splicedAlignment=TRUE)". The command used to create the expression count table was qCount(proj, exons, orientation="opposite"). For gene quantification, gene annotation from WormBase was used (WS220). To normalize for sequencing depth, each sample was divided by the total number of reads and multiplied by 1/4th of the average library size. This reduction by 1/4 was done to account for over-amplification observed in the data. The data was produced in two batches, the first one containing time points 20h-35.5h and the second one containing

time points 34h-49.5h. The time points 34h, 34.5h, 35h and 35.h were profiled in both batches and were used to fuse the two datasets into a single one. To do so, we first calculated the average \log_2 expression level of those common time points in the three conditions as well as for the two batches separately. Comparing the results from the two batches (from common time points) allowed us to calculate gene specific fold-changes, representing the differences between the batches caused by technical biases. We then corrected the original expression levels by adding half of the correction amount on the first batch and the other half on the second batch. This resulted in a configuration where the average expression level for each gene of the common time points in the first batch was identical to average expression level for each gene in the second batch. This correction was performed for the three conditions separately. This resulted in a batch-corrected expression count table that was further \log_2 transformed after the addition of a pseudocount of 8 in order to minimize large changes in expression caused by low count numbers. The differential expression analysis was performed as described in the GRH-1 manuscript. In short, the fold change was calculated between conditions over time. The fold change at the first time point $t=20.5h$ was used as null distribution and its empirical cumulative distribution function, $\hat{F}_n(x)$, was calculated using the function 'ecdf' of the package 'stats' in R (version 3.6.1). The probability of observing a fold change at any given time larger than the fold change x under the null distribution equals $1 - \hat{F}_n(x)$. We classified genes as significantly changing if the probability of the fold change of at least three time points was less than 10^{-3} .

Cosine fitting was performed using a linear model with $\cos(\omega t)$ and $\sin(\omega t)$ as regressors, as described in (Meeuse et al., 2019). The period of the cosine that fits the data best was determined by fitting a cosine to the data for each of the periods 9, 9.5, 10, 10.25, 10.5, 10.75, 11 and 11.5 hours. A minimum in the median squared error was found for 10.5 hours, and hence this period was used for cosine fitting. The coefficients of linear model with their corresponding standard errors were propagated using the function 'propagate' of the package 'propagate' (Spiess, 2018) using the function $\text{atan2}(B_{++aux}, A_{++aux}) - \text{atan2}(B_{-aux}, A_{-aux})$, which represents the phase shift between ++aux and -aux conditions. A and B are the coefficients of the cosine and the sine respectively. Genes were classified as significant if the obtained 99% confidence interval did not include 0 and the phase shift was bigger than 10% of the period (36°).

5. Supplement

Table S1: p-values of molt, intermolt and larval stage durations (**Figure 2.11F,G,H**)

	M1	M2	M3	M4	I1	I2	I3	I4	L1	L2	L3	L4
61 nM auxin	5.86E-01	2.16E-01	9.28E-04	1.87E-01	1.92E-03	2.33E-01	1.07E-02	2.08E-01	1.59E-03	1.83E-01	1.46E-01	5.29E-01
244 nM auxin	1.93E-01	8.09E-03	8.04E-03	1.47E-08	1.04E-01	7.19E-01	3.71E-05	3.77E-04	4.58E-02	2.28E-01	9.57E-03	6.04E-01
977 nM auxin	1.99E-04	4.51E-07	7.02E-05	1.43E-05	3.54E-03	9.21E-01	1.65E-03	1.46E-05	1.14E-03	1.85E-01	5.97E-02	1.54E-02
3.9 μ M auxin	8.67E-05	1.41E-06	1.71E-06	1.25E-10	2.94E-01	4.32E-01	3.55E-03	6.03E-03	1.58E-01	4.92E-01	2.51E-01	2.49E-01
15.6 μ M auxin	3.23E-05	2.01E-08	1.47E-06	4.27E-18	5.84E-01	9.28E-01	5.09E-01	6.12E-04	2.28E-01	9.16E-02	5.17E-01	8.37E-02
62.5 μ M auxin	8.78E-08	1.64E-09	4.28E-11	4.95E-05	5.85E-02	9.71E-03	1.82E-01	5.80E-01	9.02E-03	4.53E-05	7.37E-04	3.54E-04
250 μ M auxin	8.35E-14	8.68E-16	2.70E-16	1.29E-12	1.70E-04	3.13E-04	1.40E-04	1.39E-02	2.19E-06	6.07E-07	1.30E-06	7.28E-07
1 mM auxin	9.35E-18	2.43E-15	1.40E-17	2.58E-08	5.26E-03	1.15E-14	6.52E-11	6.81E-04	3.31E-06	3.93E-19	5.56E-17	1.13E-07

Table S2: p-values of median luminescence intensity (**Figure 2.11I**)

	M1	M2	M3	M4
61 nM auxin	4.45E-02	9.14E-01	6.38E-03	4.07E-01
244 nM auxin	3.48E-02	1.16E-01	3.20E-03	1.05E-02
977 nM auxin	1.08E-01	3.45E-04	3.90E-06	1.76E-03
3.9 μ M auxin	6.14E-02	8.82E-05	9.53E-05	1.90E-09
15.6 μ M auxin	1.81E-01	2.69E-04	3.75E-08	1.78E-12
62.5 μ M auxin	9.88E-02	3.96E-05	2.93E-08	5.57E-17
250 μ M auxin	2.07E-01	2.08E-04	4.45E-08	1.75E-11
1 mM auxin	7.70E-02	2.79E-06	4.62E-06	1.26E-13

Table S3: GO-term analysis of significantly changing oscillating genes identified by ‘expression fold change’ (Figure 2.14) and ‘cosine fitting’ (Figure 2.15) methods

GO biological process complete	total # genes in GO term	# hits in GO term	expected	Fold Enrichment	raw P value	FDR
cuticle development involved in collagen and cuticulin-based cuticle molting cycle	34	10	1.43	6.98	7.91E-06	1.45E-03
cuticle development	54	13	2.28	5.71	2.38E-06	5.31E-04
collagen and cuticulin-based cuticle development	50	12	2.11	5.69	5.96E-06	1.16E-03
molting cycle	113	27	4.76	5.67	1.17E-11	3.64E-08
molting cycle, collagen and cuticulin-based cuticle	110	26	4.64	5.61	3.44E-11	7.17E-08
extracellular matrix organization	61	14	2.57	5.44	1.60E-06	3.83E-04
extracellular structure organization	63	14	2.66	5.27	2.22E-06	5.13E-04
xenobiotic metabolic process	49	9	2.07	4.36	5.00E-04	4.46E-02
cellular response to xenobiotic stimulus	49	9	2.07	4.36	5.00E-04	4.40E-02
response to xenobiotic stimulus	50	9	2.11	4.27	5.69E-04	4.93E-02
defense response to other organism	291	42	12.27	3.42	6.63E-11	1.04E-07
response to external biotic stimulus	293	42	12.35	3.4	8.03E-11	1.00E-07
response to other organism	293	42	12.35	3.4	8.03E-11	8.36E-08
response to biotic stimulus	293	42	12.35	3.4	8.03E-11	7.16E-08
defense response	296	42	12.48	3.37	1.07E-10	7.40E-08
innate immune response	223	30	9.4	3.19	1.42E-07	4.23E-05
immune response	225	30	9.49	3.16	1.69E-07	4.81E-05
immune system process	230	30	9.7	3.09	2.59E-07	6.75E-05
endoplasmic reticulum unfolded protein response	157	20	6.62	3.02	3.39E-05	5.17E-03
response to unfolded protein	181	22	7.63	2.88	2.69E-05	4.43E-03
cellular response to unfolded protein	177	21	7.46	2.81	5.59E-05	7.94E-03
cellular response to topologically incorrect protein	188	21	7.93	2.65	1.22E-04	1.52E-02
response to topologically incorrect protein	197	22	8.31	2.65	8.50E-05	1.11E-02
response to endoplasmic reticulum stress	193	21	8.14	2.58	1.70E-04	2.04E-02
response to stress	965	81	40.69	1.99	1.80E-08	7.49E-06
response to external stimulus	573	46	24.16	1.9	7.11E-05	9.87E-03
cellular response to chemical stimulus	495	39	20.87	1.87	4.76E-04	4.31E-02
multi-organism process	589	45	24.84	1.81	2.92E-04	2.85E-02

Analysis Type: PANTHER Overrepresentation Test (Released 20190711)

Annotation Version and Release Date: GO Ontology database Released 2019-07-03

GO biological process complete

Figure S1: Related to figure 2.9 – Completion of molts, lengthening of stage durations and cuticle defects in high auxin concentration range

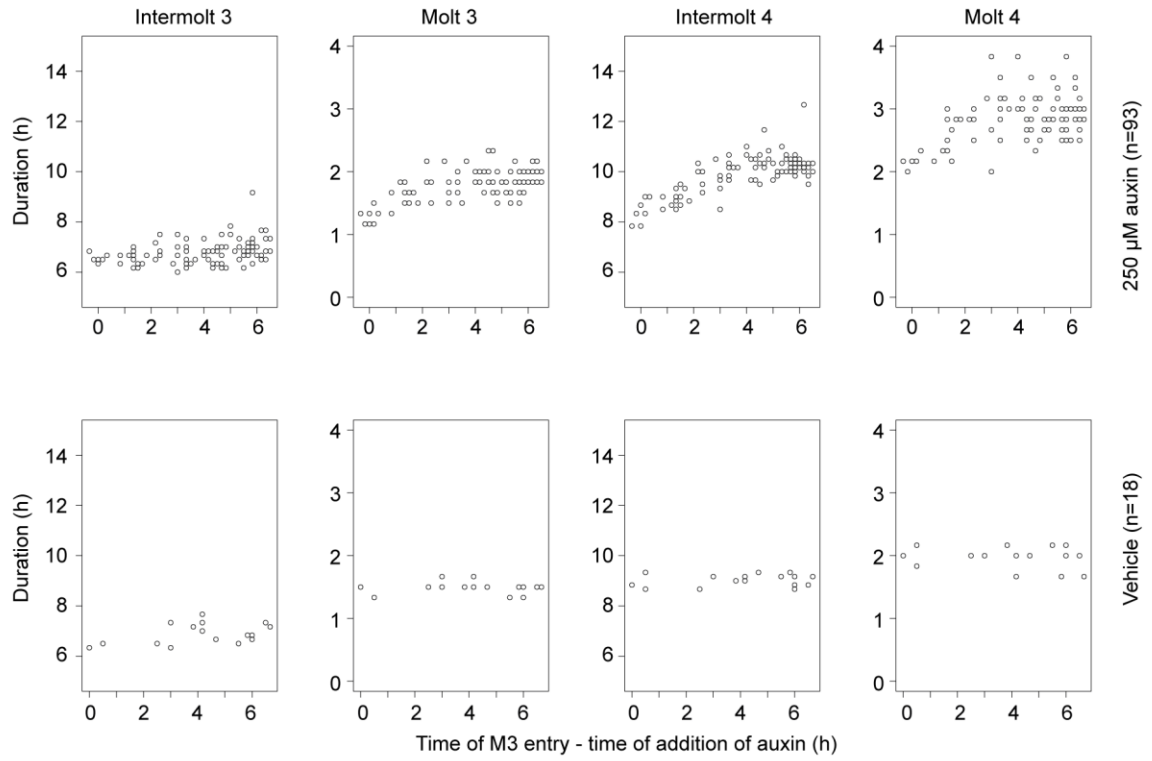
A, Quantification of the last observed molt in *peft-3::luc* (HW1949) animals treated with mock RNAi or *nhr-25* RNAi, and *peft-3::TIR1; peft-3::luc, nhr-25::degron* (HW1981) animals treated with the indicated auxin concentrations.

B, Quantification of intermolt (top) and molt (bottom) durations in animals from A. Animals that did not complete 4 molts were excluded. Significant differences for *nhr-25(RNAi)* are relative to mock RNAi. Significant differences for auxin concentrations are relative to vehicle.

C, Quantification of median luminescence in \log_{10} during the molt of animals in C. Significant differences for *nhr-25(RNAi)* are relative to mock RNAi. Significant differences for auxin concentrations are relative to vehicle.

P-values were determined by Welch two-sample, two-sided t-test. * $p < 0.05$, ** $p < 0.01$, *** $p < 0.001$

A



B

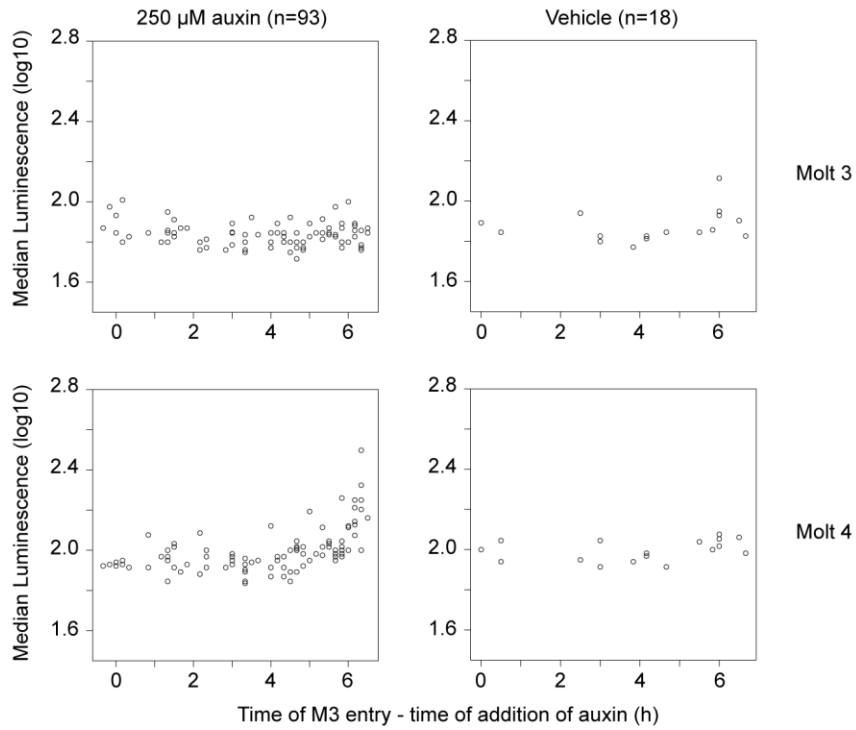


Figure S2: Related to figure 2.10 - Lengthening of larval development and cuticle integrity are dependent on the onset of NHR-25 degradation in L3 stage

A, Quantification of intermolt and molt durations over time of auxin addition relative to time of M3 entry. Animals that receive auxin in L3 stage from **Figure 2.10B** are shown.

B, Quantification of median luminescence during the molt over time of auxin addition relative to time of M3 entry. Animals that receive auxin in L3 stage from **Figure 2.10B** are shown.

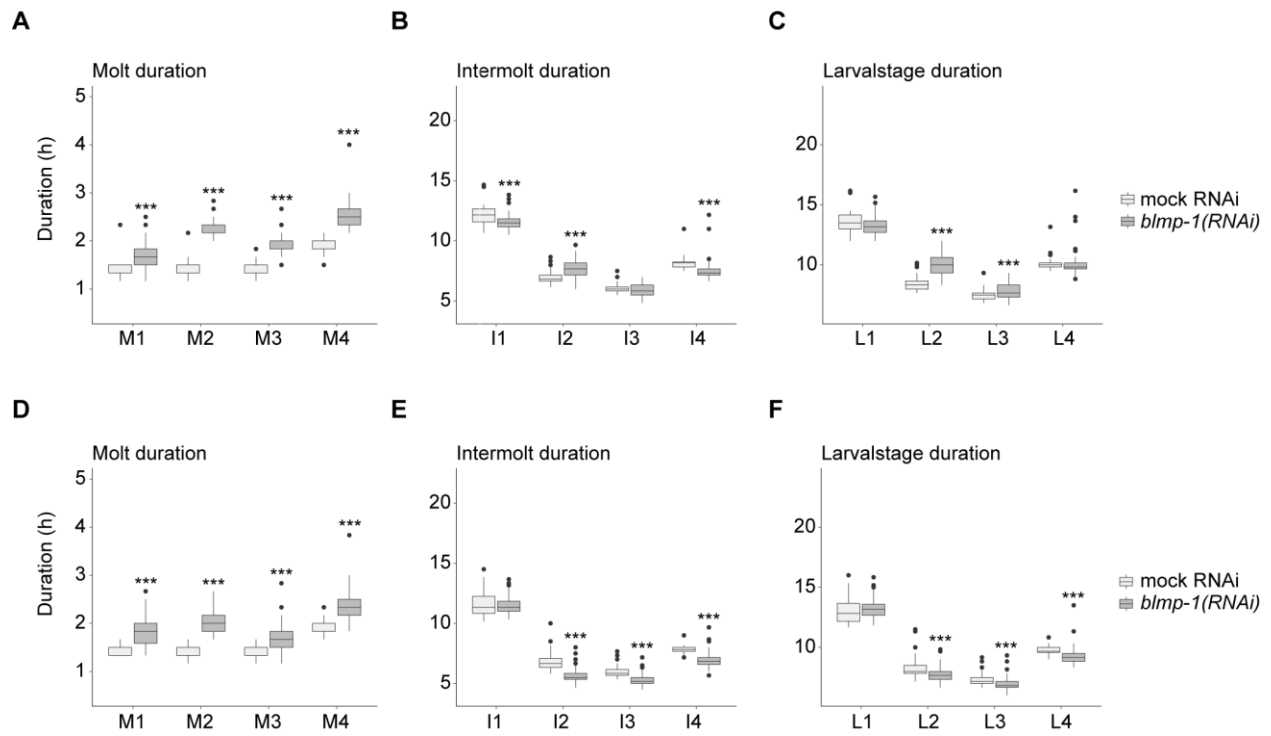


Figure S3: Related to Figure 2.11 - Lengthening of molts in *blmp-1(RNAi)* animals

Replicate experiments of the one shown in **Figure 2.11A-E**. Duration of molts (A,D), intermolts (B,E) and larval stages (C,F) for indicated RNAi conditions. Significant differences between mock RNAi and *blmp-1(RNAi)* are indicated (* P<0.05, ** P<0.01, *** P<0.001, two-sided two-sample t-test)

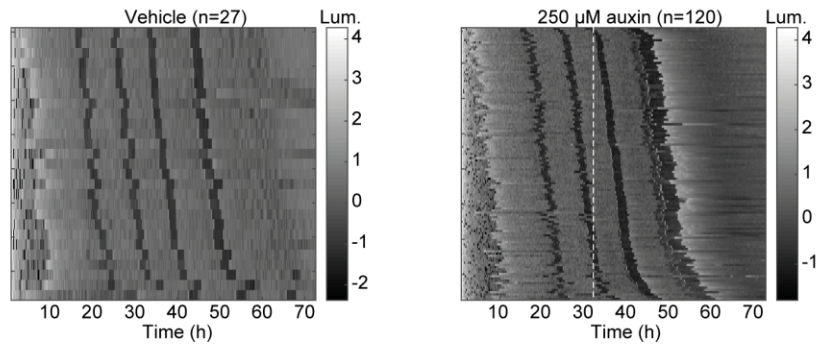
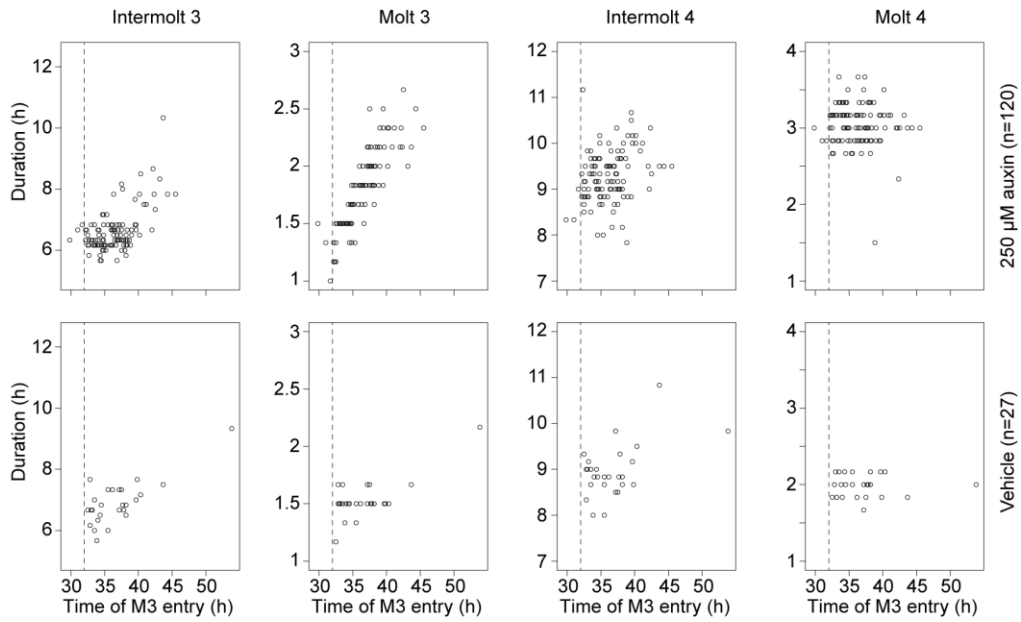
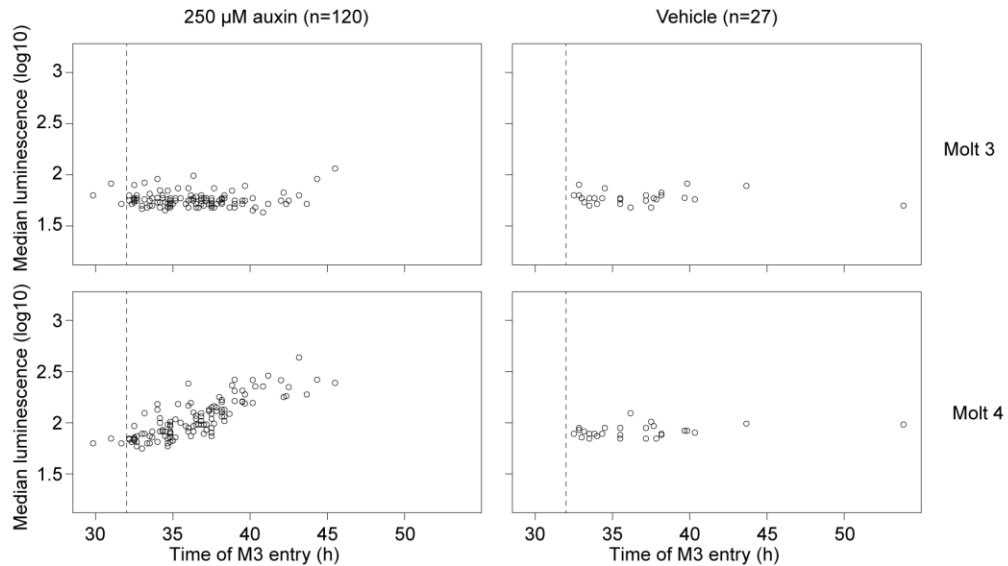
A**B****C**

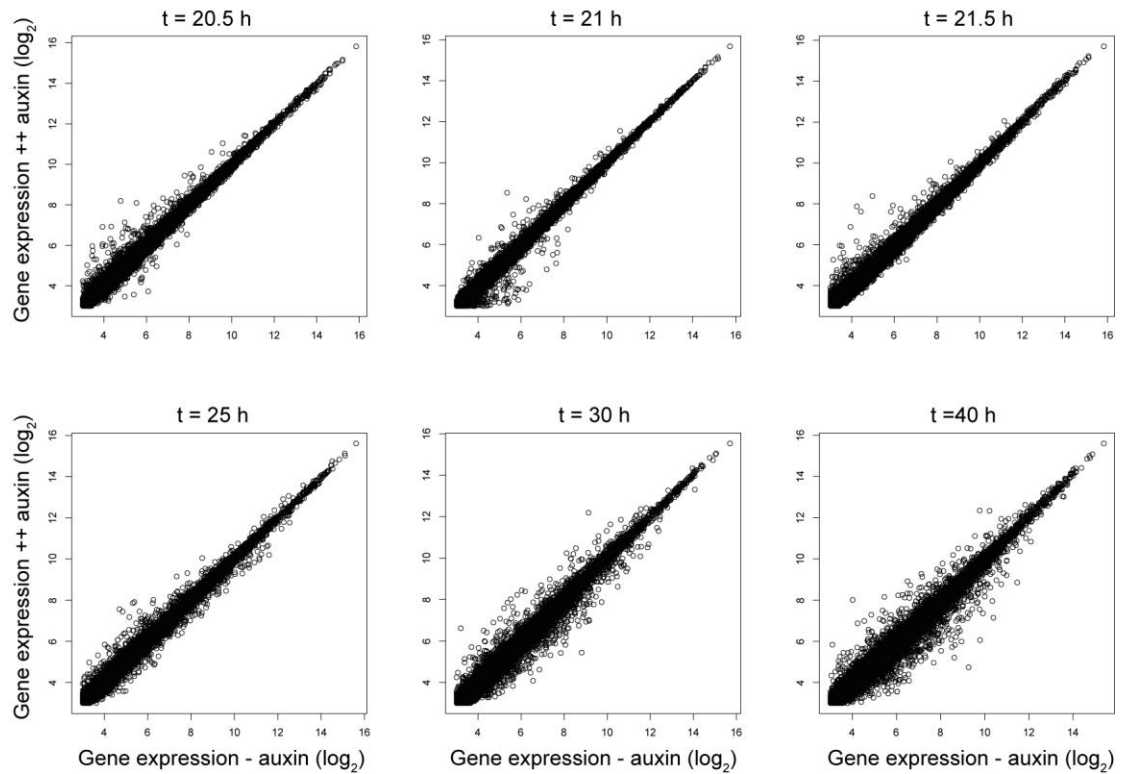
Figure S4: Related to figure 2.12 - Lengthening of molts and cuticle defects are dependent on the onset of BLMP-1 depletion in L3 stage

A, Heatmaps showing trend-corrected luminescence (Lum.) traces of *blmp-1::degron*; *peft-3::luc*, *peft-3::TIR1* animals (HW2120); one animal per horizontal line. Vehicle (0.25% ethanol, left) or 250 μ M auxin (right) were added at t=32h (dashed line). t=0 hours corresponds to start of the assay. Embryos hatch at different time points and traces are sorted by entry into M3.

B, Duration of I3, M3, I4 and M4 plotted over time at which single animals enter M3 in vehicle and auxin treated animals at t=32h (dashed line) shown in (A).

C, Quantification of median luminescence during the molt in log₁₀ over time of auxin addition relative to time of M3 entry. Data for molt 3 and molt 4 is shown.

A



B

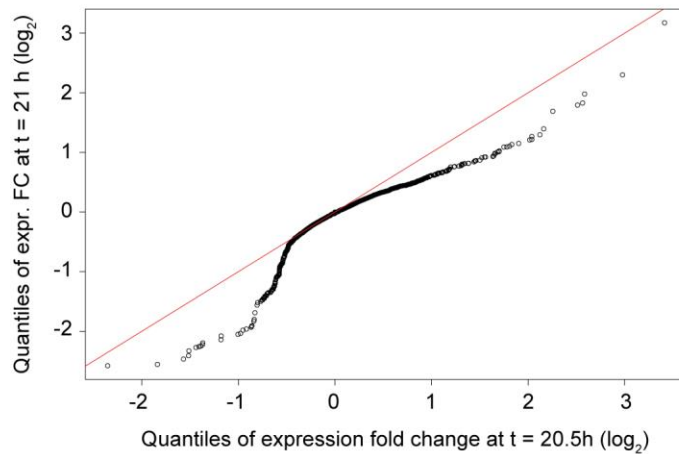


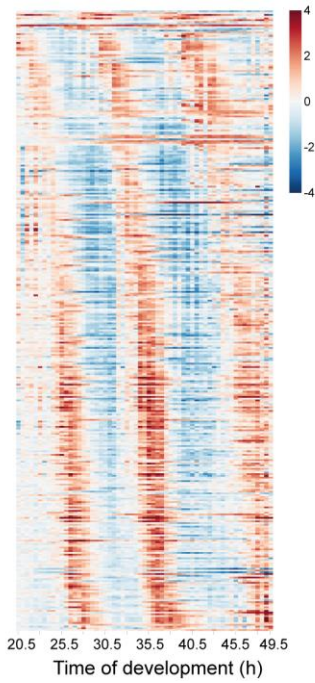
Figure S5: Related to figure 2.13 - Gene expression changes at different time points show distinct distributions

A, Scatterplot showing gene expression of ++ auxin (250 μ M) over – auxin (vehicle) for indicated time points.

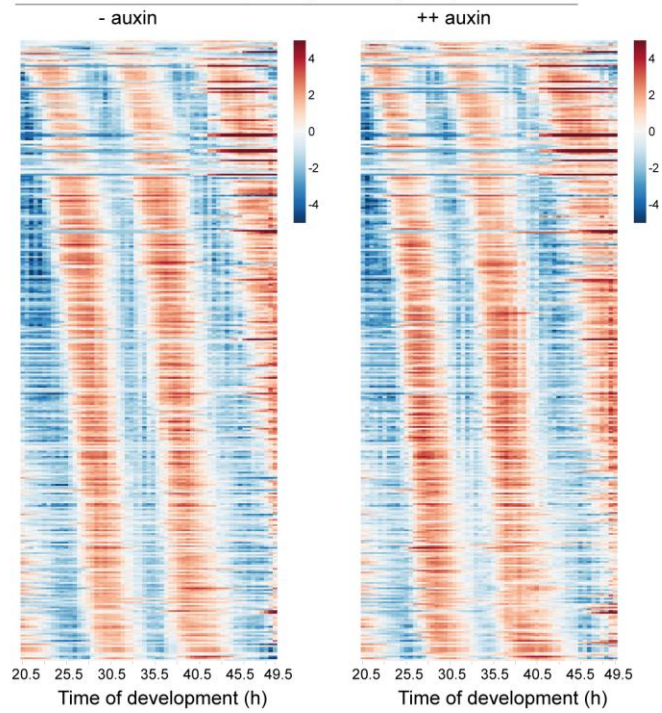
B, QQ-plot showing quantiles of expression fold change at t = 20.5 hours over t = 21 hours. Reference line (red) indicates equal distribution.

A

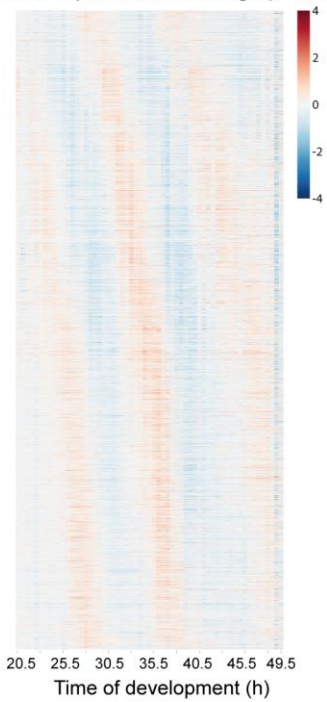
Expression fold change (n=354)

**B**

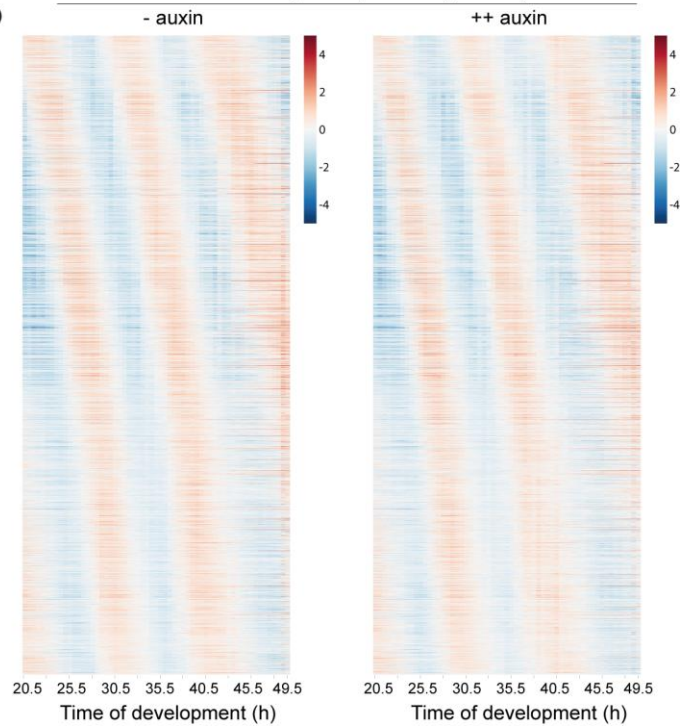
Normalized gene expression (n=354)

**C**

Gene expression fold change (n=3385)

**D**

Normalized gene expression (n=3385)



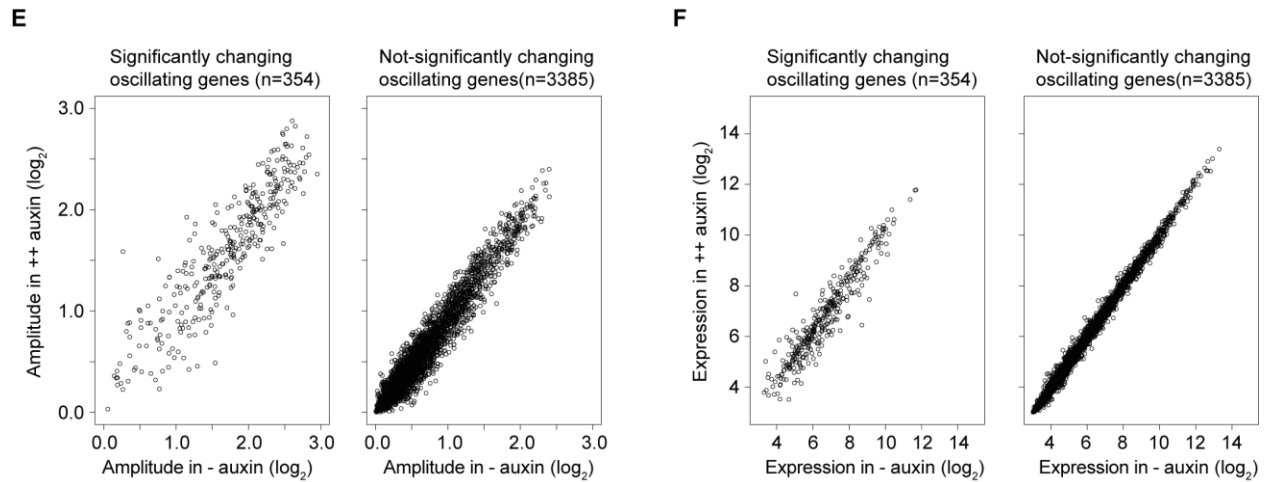


Figure S6: Related to Figure 2.14 - ‘Expression fold change’ method enriches for oscillating genes with high amplitudes

A, Heatmap of fold change between gene expression in ++ auxin (250 μ M) and in - auxin (vehicle) conditions for significantly changing oscillating genes (n=354). Genes are sorted by peak phase (Meeuse et al., 2019).

B, Gene expression heatmaps in auxin-treated (++) auxin) and control (- auxin) animals for significantly changing oscillating genes (n=354). Gene expression was mean-centered over both conditions, sorted according to A and plotted in \log_2 .

C, Heatmap of fold change between gene expression in ++ auxin (250 μ M) and in - auxin (vehicle) conditions for ‘not-significantly’ changing oscillating genes (n=3385). Genes are sorted by peak phase (Meeuse et al., 2019).

D, Gene expression heatmaps in auxin-treated (++) auxin) and control (- auxin) animals for ‘not-significantly’ changing oscillating genes (n=3385). Gene expression was mean-centered over both conditions, sorted according to C and plotted in \log_2 .

E, Scatterplot showing the amplitude of gene expression oscillations in auxin-treated (++) auxin) over control (-auxin) animals for significantly changing oscillating genes and not-significantly changing oscillating genes. Amplitudes were determined by cosine fitting in **Figure 2.15**.

F, Scatterplot showing the gene expression in auxin-treated (++) auxin) over control (-auxin) animals for significantly changing oscillating genes and not-significantly changing oscillating genes.

6. References

- Abraham, U., Granada, A.E., Westermarck, P.O., Heine, M., Kramer, A., and Herzog, H. (2010). Coupling governs entrainment range of circadian clocks. *Mol Syst Biol* 6, 438.
- Almeida, M.S., and Bray, S.J. (2005). Regulation of post-embryonic neuroblasts by *Drosophila* Grainyhead. *Mech. Dev.* 122, 1282–1293.
- Alon, U. (2007). Network motifs: theory and experimental approaches. *Nat Rev Genet* 8, 450–461.
- Ambros, V. (1989). A hierarchy of regulatory genes controls a larva-to-adult developmental switch in *C. elegans*. *Cell* 57, 49–57.
- Ambros, V., and Horvitz, H.R. (1984). Heterochronic mutants of the nematode *Caenorhabditis elegans*. *Science* 226, 409–416.
- Antebi, A. (2006). Nuclear hormone receptors in *C. elegans*. *WormBook* 1–13.
- Asahina, M., Ishihara, T., Jindra, M., Kohara, Y., Katsura, I., and Hirose, S. (2000). The conserved nuclear receptor Ftz-F1 is required for embryogenesis, moulting and reproduction in *Caenorhabditis elegans*. *Genes Cells* 5, 711–723.
- Aschoff, J. (1960). Exogenous and endogenous components in circadian rhythms. *Cold Spring Harb. Symp. Quant. Biol.* 25, 11–28.
- Aspöck, G., Kagoshima, H., Niklaus, G., and Bürglin, T.R. (1999). *Caenorhabditis elegans* has scores of hedgehog-related genes: sequence and expression analysis. *Genome Res.* 9, 909–923.
- Au, K.F., Jiang, H., Lin, L., Xing, Y., and Wong, W.H. (2010). Detection of splice junctions from paired-end RNA-seq data by SpliceMap. *Nucleic Acids Res* 38, 4570–4578.
- Auden, A., Caddy, J., Wilanowski, T., Ting, S.B., Cunningham, J.M., and Jane, S.M. (2006). Spatial and temporal expression of the Grainyhead-like transcription factor family during murine development. *Gene Expression Patterns* 6, 964–970.
- Aulehla, A., and Pourquié, O. (2010). Signaling gradients during paraxial mesoderm development. *Cold Spring Harb Perspect Biol* 2, a000869.
- Aulehla, A., Wehrle, C., Brand-Saberi, B., Kemler, R., Gossler, A., Kanzler, B., and Herrmann, B.G. (2003). Wnt3a plays a major role in the segmentation clock controlling somitogenesis. *Dev. Cell* 4, 395–406.
- Baugh, L.R., Demodena, J., and Sternberg, P.W. (2009). RNA Pol II accumulates at promoters of growth genes during developmental arrest. *Science* 324, 92–94.
- Benayoun, B.A., and Veitia, R.A. (2009). A post-translational modification code for transcription factors: sorting through a sea of signals. *Trends Cell Biol.* 19, 189–197.
- Biggin, M.D. (2011). Animal transcription networks as highly connected, quantitative continua. *Dev. Cell* 21, 611–626.
- Blumenthal, T. (2018). Trans-splicing and operons in *C. elegans* (*WormBook*).

- Boglev, Y., Wilanowski, T., Caddy, J., Parekh, V., Auden, A., Darido, C., Hislop, N.R., Cangkrama, M., Ting, S.B., and Jane, S.M. (2011). The unique and cooperative roles of the Grainy head-like transcription factors in epidermal development reflect unexpected target gene specificity. *Dev. Biol.* *349*, 512–522.
- Bolstad, B.M., Irizarry, R.A., Astrand, M., and Speed, T.P. (2003). A comparison of normalization methods for high density oligonucleotide array data based on variance and bias. *Bioinformatics* *19*, 185–193.
- Bray, S.J., and Kafatos, F.C. (1991). Developmental function of Elf-1: an essential transcription factor during embryogenesis in *Drosophila*. *Genes Dev.* *5*, 1672–1683.
- Bray, S.J., Burke, B., Brown, N.H., and Hirsh, J. (1989). Embryonic expression pattern of a family of *Drosophila* proteins that interact with a central nervous system regulatory element. *Genes Dev.* *3*, 1130–1145.
- Briscoe, J., and Théron, P.P. (2013). The mechanisms of Hedgehog signalling and its roles in development and disease. *Nature Reviews Molecular Cell Biology* *14*, 416–429.
- Brody, T., and Odenwald, W.F. (2000). Programmed transformations in neuroblast gene expression during *Drosophila* CNS lineage development. *Dev. Biol.* *226*, 34–44.
- Bujalka, H., Koening, M., Jackson, S., Perreau, V.M., Pope, B., Hay, C.M., Mitew, S., Hill, A.F., Lu, Q.R., Wegner, M., et al. (2013). MYRF is a membrane-associated transcription factor that autoproteolytically cleaves to directly activate myelin genes. *PLoS Biol.* *11*, e1001625.
- Bürglin, T.R., and Kuwabara, P.E. (2006). Homologs of the Hh signalling network in *C. elegans* (WormBook).
- C. elegans* Sequencing Consortium (1998). Genome sequence of the nematode *C. elegans*: a platform for investigating biology. *Science* *282*, 2012–2018.
- Cai, E. (2013). *Exploratory Data Analysis: Conceptual Foundations of Empirical Cumulative Distribution Functions*.
- Cassada, R.C., and Russell, R.L. (1975). The dauerlarva, a post-embryonic developmental variant of the nematode *Caenorhabditis elegans*. *Dev. Biol.* *46*, 326–342.
- Cenci, C., and Gould, A.P. (2005). *Drosophila* Grainyhead specifies late programmes of neural proliferation by regulating the mitotic activity and Hox-dependent apoptosis of neuroblasts. *Development* *132*, 3835–3845.
- Chambers, I., Silva, J., Colby, D., Nichols, J., Nijmeijer, B., Robertson, M., Vrana, J., Jones, K., Grotewold, L., and Smith, A. (2007). Nanog safeguards pluripotency and mediates germline development. *Nature* *450*, 1230–1234.
- Chen, B., Zhu, Y., Ye, S., and Zhang, R. (2018). Structure of the DNA-binding domain of human myelin-gene regulatory factor reveals its potential protein-DNA recognition mode. *J. Struct. Biol.* *203*, 170–178.
- Chen, Z., Eastburn, D.J., and Han, M. (2004). The *Caenorhabditis elegans* nuclear receptor gene *nhr-25* regulates epidermal cell development. *Mol. Cell. Biol.* *24*, 7345–7358.
- Chepyala, S.R., Chen, Y.-C., Yan, C.-C.S., Lu, C.-Y.D., Wu, Y.-C., and Hsu, C.-P. (2016). Noise propagation with interlinked feed-forward pathways. *Sci Rep* *6*.
- Chisholm, A.D., and Hardin, J. (2005). *Epidermal morphogenesis* (WormBook).
- Conrad, E., Mayo, A.E., Ninfa, A.J., and Forger, D.B. (2008). Rate constants rather than biochemical mechanism determine behaviour of genetic clocks. *J R Soc Interface* *5*, S9–S15.

- Cooke, J., and Zeeman, E.C. (1976). A clock and wavefront model for control of the number of repeated structures during animal morphogenesis. *J. Theor. Biol.* *58*, 455–476.
- Corsi, A.K., Wightman, B., and Chalfie, M. (2015). A Transparent Window into Biology: A Primer on *Caenorhabditis elegans*. *Genetics* *200*, 387–407.
- Cox, G.N., Staprans, S., and Edgar, R.S. (1981a). The cuticle of *Caenorhabditis elegans*: II. Stage-specific changes in ultrastructure and protein composition during postembryonic development. *Developmental Biology* *86*, 456–470.
- Cox, G.N., Kusch, M., and Edgar, R.S. (1981b). Cuticle of *Caenorhabditis elegans*: its isolation and partial characterization. *J. Cell Biol.* *90*, 7–17.
- Cramer, P. (2019). Organization and regulation of gene transcription. *Nature* *573*, 45–54.
- Cristo, I., Carvalho, L., Ponte, S., and Jacinto, A. (2018). Novel role for Grainy head in the regulation of cytoskeletal and junctional dynamics during epithelial repair. *J Cell Sci* *131*, jcs213595.
- Davis, M.W., Birnie, A.J., Chan, A.C., Page, A.P., and Jorgensen, E.M. (2004). A conserved metalloprotease mediates ecdysis in *Caenorhabditis elegans*. *Development* *131*, 6001–6008.
- Dequéant, M.-L., and Pourquié, O. (2008). Segmental patterning of the vertebrate embryonic axis. *Nat. Rev. Genet.* *9*, 370–382.
- Dibner, C., Schibler, U., and Albrecht, U. (2010). The mammalian circadian timing system: organization and coordination of central and peripheral clocks. *Annu. Rev. Physiol.* *72*, 517–549.
- Doitsidou, M., Minevich, G., Kroll, J.R., Soete, G., Gowtham, S., Korswagen, H.C., Sebastiaan van Zon, J., and Hobert, O. (2018). A *Caenorhabditis elegans* Zinc Finger Transcription Factor, ztf-6, Required for the Specification of a Dopamine Neuron-Producing Lineage. *G3 (Bethesda)* *8*, 17–26.
- Dubrulle, J., McGrew, M.J., and Pourquié, O. (2001). FGF signaling controls somite boundary position and regulates segmentation clock control of spatiotemporal Hox gene activation. *Cell* *106*, 219–232.
- Dynlacht, B.D., Attardi, L.D., Admon, A., Freeman, M., and Tjian, R. (1989). Functional analysis of NTF-1, a developmentally regulated *Drosophila* transcription factor that binds neuronal cis elements. *Genes Dev.* *3*, 1677–1688.
- Edens, W.A., Sharling, L., Cheng, G., Shapira, R., Kinkade, J.M., Lee, T., Edens, H.A., Tang, X., Sullards, C., Flaherty, D.B., et al. (2001). Tyrosine cross-linking of extracellular matrix is catalyzed by Duox, a multidomain oxidase/oxidase with homology to the phagocyte oxidase subunit gp91phox. *J Cell Biol* *154*, 879–892.
- Elowitz, M.B., and Leibler, S. (2000). A synthetic oscillatory network of transcriptional regulators. *Nature* *403*, 335–338.
- Emery, B., Agalliu, D., Cahoy, J.D., Watkins, T.A., Dugas, J.C., Mulinyawe, S.B., Ibrahim, A., Ligon, K.L., Rowitch, D.H., and Barres, B.A. (2009). Myelin gene regulatory factor is a critical transcriptional regulator required for CNS myelination. *Cell* *138*, 172–185.
- Ferrell, J.E. (2002). Self-perpetuating states in signal transduction: positive feedback, double-negative feedback and bistability. *Curr. Opin. Cell Biol.* *14*, 140–148.
- Forman, B.M., and Samuels, H.H. (1990). Interactions among a subfamily of nuclear hormone receptors: the regulatory zipper model. *Mol. Endocrinol.* *4*, 1293–1301.

- Frand, A.R., Russel, S., and Ruvkun, G. (2005). Functional Genomic Analysis of *C. elegans* Molting. *PLOS Biology* 3, e312.
- Frisch, S.M., Farris, J.C., and Pifer, P.M. (2017). Roles of Grainyhead-like transcription factors in cancer. *Oncogene* 36, 6067–6073.
- Gaidatzis, D., Lerch, A., Hahne, F., and Stadler, M.B. (2015). QuasR: quantification and annotation of short reads in R. *Bioinformatics* 31, 1130–1132.
- George-Raizen, J.B., Shockley, K.R., Trojanowski, N.F., Lamb, A.L., and Raizen, D.M. (2014). Dynamically-expressed prion-like proteins form a cuticle in the pharynx of *Caenorhabditis elegans*. *Biol Open* 3, 1139–1149.
- Gill, H.K., Cohen, J.D., Ayala-Figueroa, J., Forman-Rubinsky, R., Poggioli, C., Bickard, K., Parry, J.M., Pu, P., Hall, D.H., and Sundaram, M.V. (2016). Integrity of Narrow Epithelial Tubes in the *C. elegans* Excretory System Requires a Transient Luminal Matrix. *PLOS Genetics* 12, e1006205.
- Gissendanner, C.R., and Sluder, A.E. (2000). *nhr-25*, the *Caenorhabditis elegans* ortholog of *ftz-f1*, is required for epidermal and somatic gonad development. *Dev. Biol.* 221, 259–272.
- Gissendanner, C.R., Crossgrove, K., Kraus, K.A., Maina, C.V., and Sluder, A.E. (2004). Expression and function of conserved nuclear receptor genes in *Caenorhabditis elegans*. *Dev. Biol.* 266, 399–416.
- Gomez, C., and Pourquié, O. (2009). Developmental control of segment numbers in vertebrates. *J Exp Zool B Mol Dev Evol* 312, 533–544.
- Gomez, C., Özbudak, E.M., Wunderlich, J., Baumann, D., Lewis, J., and Pourquié, O. (2008). Control of segment number in vertebrate embryos. *Nature* 454, 335–339.
- Guantes, R., and Poyatos, J.F. (2006). Dynamical principles of two-component genetic oscillators. *PLoS Comput. Biol.* 2, e30.
- Hall, D.H., Herndon, L.A., and Altun, Z. (2017). Introduction to *C. elegans* Embryo Anatomy. (In *WormAtlas*).
- Hall, D.H., Herndon, L.A., and Altun, Z. Introduction to *C. elegans* Embryo Anatomy. (In *WormAtlas*).
- Hao, L., Aspöck, G., and Bürglin, T.R. (2006). The hedgehog-related gene *wrt-5* is essential for hypodermal development in *Caenorhabditis elegans*. *Dev. Biol.* 290, 323–336.
- Hashmi, S., Zhang, J., Oksov, Y., and Lustigman, S. (2004). The *Caenorhabditis elegans* cathepsin Z-like cysteine protease, *Ce-CPZ-1*, has a multifunctional role during the worms' development. *J. Biol. Chem.* 279, 6035–6045.
- Hayashi, T., Watanabe, S., Toda, T., Hori, T., Roux, J.L., and Takeda, K. (2017). Duration-Controlled LSTM for Polyphonic Sound Event Detection. *IEEE/ACM Transactions on Audio, Speech, and Language Processing* 25, 2059–2070.
- Hayes, G.D., Frand, A.R., and Ruvkun, G. (2006). The *mir-84* and *let-7* paralogous microRNA genes of *Caenorhabditis elegans* direct the cessation of molting via the conserved nuclear hormone receptors *NHR-23* and *NHR-25*. *Development* 133, 4631–4641.
- Hemphälä, J., Uv, A., Cantera, R., Bray, S., and Samakovlis, C. (2003). Grainy head controls apical membrane growth and tube elongation in response to Branchless/FGF signalling. *Development* 130, 249–258.

- Hendriks, G.-J., Gaidatzis, D., Aeschmann, F., and Großhans, H. (2014). Extensive oscillatory gene expression during *C. elegans* larval development. *Mol. Cell* 53, 380–392.
- Herrgen, L., Ares, S., Morelli, L.G., Schröter, C., Jülicher, F., and Oates, A.C. (2010). Intercellular coupling regulates the period of the segmentation clock. *Curr. Biol.* 20, 1244–1253.
- Hijmans, R.J. (2019). raster: Geographic Data Analysis and Modeling.
- Hirano, A., Fu, Y.-H., and Ptáček, L.J. (2016). The intricate dance of post-translational modifications in the rhythm of life. *Nat. Struct. Mol. Biol.* 23, 1053–1060.
- Horn, M., Geisen, C., Cermak, L., Becker, B., Nakamura, S., Klein, C., Pagano, M., and Antebi, A. (2014). DRE-1/FBXO11-dependent degradation of BLMP-1/BLIMP-1 governs *C. elegans* developmental timing and maturation. *Dev. Cell* 28, 697–710.
- Hornig, J., Fröb, F., Vogl, M.R., Hermans-Borgmeyer, I., Tamm, E.R., and Wegner, M. (2013). The transcription factors Sox10 and Myrf define an essential regulatory network module in differentiating oligodendrocytes. *PLoS Genet.* 9, e1003907.
- Huang, T.-F., Cho, C.-Y., Cheng, Y.-T., Huang, J.-W., Wu, Y.-Z., Yeh, A.Y.-C., Nishiwaki, K., Chang, S.-C., and Wu, Y.-C. (2014). BLMP-1/Blimp-1 regulates the spatiotemporal cell migration pattern in *C. elegans*. *PLoS Genet.* 10, e1004428.
- Imayoshi, I., Isomura, A., Harima, Y., Kawaguchi, K., Kori, H., Miyachi, H., Fujiwara, T., Ishidate, F., and Kageyama, R. (2013). Oscillatory control of factors determining multipotency and fate in mouse neural progenitors. *Science* 342, 1203–1208.
- Isomura, A., and Kageyama, R. (2014). Ultradian oscillations and pulses: coordinating cellular responses and cell fate decisions. *Development* 141, 3627–3636.
- Isshiki, T., Pearson, B., Holbrook, S., and Doe, C.Q. (2001). *Drosophila* neuroblasts sequentially express transcription factors which specify the temporal identity of their neuronal progeny. *Cell* 106, 511–521.
- Izhikevich, E.M. (2000). Neural excitability, spiking and bursting. *Int. J. Bifurcation Chaos* 10, 1171–1266.
- Jacobs, J., Atkins, M., Davie, K., Imrichova, H., Romanelli, L., Christiaens, V., Hulselmans, G., Potier, D., Wouters, J., Taskiran, I.I., et al. (2018). The transcription factor Grainy head primes epithelial enhancers for spatiotemporal activation by displacing nucleosomes. *Nature Genetics* 50, 1011.
- Jeon, M., Gardner, H.F., Miller, E.A., Deshler, J., and Rougvie, A.E. (1999). Similarity of the *C. elegans* developmental timing protein LIN-42 to circadian rhythm proteins. *Science* 286, 1141–1146.
- Johnson, W.A., McCormick, C.A., Bray, S.J., and Hirsh, J. (1989). A neuron-specific enhancer of the *Drosophila* dopa decarboxylase gene. *Genes Dev.* 3, 676–686.
- Johnstone, I.L., and Barry, J.D. (1996). Temporal reiteration of a precise gene expression pattern during nematode development. *EMBO J* 15, 3633–3639.
- Jovine, L., Darie, C.C., Litscher, E.S., and Wassarman, P.M. (2005). Zona pellucida domain proteins. *Annu. Rev. Biochem.* 74, 83–114.

- Kamath, R.S., Fraser, A.G., Dong, Y., Poulin, G., Durbin, R., Gotta, M., Kanapin, A., Le Bot, N., Moreno, S., Sohrmann, M., et al. (2003). Systematic functional analysis of the *Caenorhabditis elegans* genome using RNAi. *Nature* *421*, 231–237.
- Katic, I., Xu, L., and Ciosk, R. (2015). CRISPR/Cas9 Genome Editing in *Caenorhabditis elegans*: Evaluation of Templates for Homology-Mediated Repair and Knock-Ins by Homology-Independent DNA Repair. *G3 (Bethesda)* *5*, 1649–1656.
- Kelley, M., Yochem, J., Krieg, M., Calixto, A., Heiman, M.G., Kuzmanov, A., Meli, V., Chalfie, M., Goodman, M.B., Shaham, S., et al. (2015). FBN-1, a fibrillin-related protein, is required for resistance of the epidermis to mechanical deformation during *C. elegans* embryogenesis. *Elife* *4*.
- Kim, D., Langmead, B., and Salzberg, S.L. (2015). HISAT: a fast spliced aligner with low memory requirements. *Nat. Methods* *12*, 357–360.
- Kim, D. hyun, Grün, D., and van Oudenaarden, A. (2013). Dampening of expression oscillations by synchronous regulation of a microRNA and its target. *Nat. Genet.* *45*, 1337–1344.
- Kim, J.-R., Shin, D., Jung, S.H., Heslop-Harrison, P., and Cho, K.-H. (2010). A design principle underlying the synchronization of oscillations in cellular systems. *J Cell Sci* *123*, 537–543.
- Kimble, J., and Hirsh, D. (1979). The postembryonic cell lineages of the hermaphrodite and male gonads in *Caenorhabditis elegans*. *Dev. Biol.* *70*, 396–417.
- Kobayashi, T., Mizuno, H., Imayoshi, I., Furusawa, C., Shirahige, K., and Kageyama, R. (2009). The cyclic gene *Hes1* contributes to diverse differentiation responses of embryonic stem cells. *Genes Dev.* *23*, 1870–1875.
- Koenning, M., Jackson, S., Hay, C.M., Faux, C., Kilpatrick, T.J., Willingham, M., and Emery, B. (2012). Myelin gene regulatory factor is required for maintenance of myelin and mature oligodendrocyte identity in the adult CNS. *J. Neurosci.* *32*, 12528–12542.
- Koike, N., Yoo, S.-H., Huang, H.-C., Kumar, V., Lee, C., Kim, T.-K., and Takahashi, J.S. (2012). Transcriptional Architecture and Chromatin Landscape of the Core Circadian Clock in Mammals. *Science* *338*, 349–354.
- Kondratov, R.V., Chernov, M.V., Kondratova, A.A., Gorbacheva, V.Y., Gudkov, A.V., and Antoch, M.P. (2003). BMAL1-dependent circadian oscillation of nuclear CLOCK: posttranslational events induced by dimerization of transcriptional activators of the mammalian clock system. *Genes Dev.* *17*, 1921–1932.
- Korenčič, A., Bordyugov, G., Košir, R., Rozman, D., Goličnik, M., and Herzog, H. (2012). The Interplay of cis-Regulatory Elements Rules Circadian Rhythms in Mouse Liver. *PLOS ONE* *7*, e46835.
- Kostrouchova, M., Krause, M., Kostrouch, Z., and Rall, J.E. (1998). CHR3: a *Caenorhabditis elegans* orphan nuclear hormone receptor required for proper epidermal development and molting. *Development* *125*, 1617–1626.
- Kostrouchova, M., Krause, M., Kostrouch, Z., and Rall, J.E. (2001). Nuclear hormone receptor CHR3 is a critical regulator of all four larval molts of the nematode *Caenorhabditis elegans*. *Proc. Natl. Acad. Sci. U.S.A.* *98*, 7360–7365.
- Kouns, N.A., Nakielna, J., Behensky, F., Krause, M.W., Kostrouch, Z., and Kostrouchova, M. (2011). NHR-23 dependent collagen and hedgehog-related genes required for molting. *Biochem. Biophys. Res. Commun.* *413*, 515–520.

- Kuwabara, P.E., and Labouesse, M. (2002). The sterol-sensing domain: multiple families, a unique role? *Trends in Genetics* *18*, 193–201.
- Kuwabara, P.E., Lee, M.H., Schedl, T., and Jefferis, G.S. (2000). A *C. elegans* patched gene, *ptc-1*, functions in germline cytokinesis. *Genes Dev.* *14*, 1933–1944.
- Langmead, B., Trapnell, C., Pop, M., and Salzberg, S.L. (2009). Ultrafast and memory-efficient alignment of short DNA sequences to the human genome. *Genome Biol.* *10*, R25.
- Laskowski, M., and Tusscher, K.H. ten (2017). Periodic Lateral Root Priming: What Makes It Tick? *The Plant Cell* *29*, 432–444.
- Lažetić, V., and Fay, D.S. (2017a). Molting in *C. elegans*. *Worm* *6*, e1330246.
- Lažetić, V., and Fay, D.S. (2017b). Conserved Ankyrin Repeat Proteins and Their NIMA Kinase Partners Regulate Extracellular Matrix Remodeling and Intracellular Trafficking in *Caenorhabditis elegans*. *Genetics* *205*, 273–293.
- Le Martelot, G., Canella, D., Symul, L., Migliavacca, E., Gilardi, F., Liechti, R., Martin, O., Harshman, K., Delorenzi, M., Desvergne, B., et al. (2012). Genome-wide RNA polymerase II profiles and RNA accumulation reveal kinetics of transcription and associated epigenetic changes during diurnal cycles. *PLoS Biol.* *10*, e1001442.
- Lee, H., and Adler, P.N. (2004). The grainy head transcription factor is essential for the function of the frizzled pathway in the *Drosophila* wing. *Mech. Dev.* *121*, 37–49.
- Lee, C., Etchegaray, J.-P., Cagampang, F.R.A., Loudon, A.S.I., and Reppert, S.M. (2001). Posttranslational Mechanisms Regulate the Mammalian Circadian Clock. *Cell* *107*, 855–867.
- Levine, J.H., Lin, Y., and Elowitz, M.B. (2013). Functional roles of pulsing in genetic circuits. *Science* *342*, 1193–1200.
- Lewis, J. (2003). Autoinhibition with transcriptional delay: a simple mechanism for the zebrafish somitogenesis oscillator. *Curr. Biol.* *13*, 1398–1408.
- Li, Z., Park, Y., and Marcotte, E.M. (2013). A Bacteriophage tailspike domain promotes self-cleavage of a human membrane-bound transcription factor, the myelin regulatory factor MYRF. *PLoS Biol.* *11*, e1001624.
- Lim, C., and Allada, R. (2013). Emerging roles for post-transcriptional regulation in circadian clocks. *Nat. Neurosci.* *16*, 1544–1550.
- Lück, S., Thurley, K., Thaben, P.F., and Westermark, P.O. (2014). Rhythmic degradation explains and unifies circadian transcriptome and proteome data. *Cell Rep* *9*, 741–751.
- Mace, K.A., Pearson, J.C., and McGinnis, W. (2005). An epidermal barrier wound repair pathway in *Drosophila* is mediated by grainy head. *Science* *308*, 381–385.
- Magnúsdóttir, E., Kalachikov, S., Mizukoshi, K., Savitsky, D., Ishida-Yamamoto, A., Panteleyev, A.A., and Calame, K. (2007). Epidermal terminal differentiation depends on B lymphocyte-induced maturation protein-1. *Proc. Natl. Acad. Sci. U.S.A.* *104*, 14988–14993.
- Mancuso, V.P., Parry, J.M., Storer, L., Poggioli, C., Nguyen, K.C.Q., Hall, D.H., and Sundaram, M.V. (2012). Extracellular leucine-rich repeat proteins are required to organize the apical extracellular matrix and maintain epithelial junction integrity in *C. elegans*. *Development* *139*, 979–990.

- Mavroudis, P.D., DuBois, D.C., Almon, R.R., and Jusko, W.J. (2018). Daily variation of gene expression in diverse rat tissues. *PLoS One* *13*.
- Maxwell, C.S., Kruesi, W.S., Core, L.J., Kurhanewicz, N., Waters, C.T., Lewarch, C.L., Antoshechkin, I., Lis, J.T., Meyer, B.J., and Baugh, L.R. (2014). Pol II docking and pausing at growth and stress genes in *C. elegans*. *Cell Rep* *6*, 455–466.
- McMahon, L., Legouis, R., Vonesch, J.L., and Labouesse, M. (2001). Assembly of *C. elegans* apical junctions involves positioning and compaction by LET-413 and protein aggregation by the MAGUK protein DLG-1. *J. Cell. Sci.* *114*, 2265–2277.
- McMahon, L., Muriel, J.M., Roberts, B., Quinn, M., and Johnstone, I.L. (2003). Two Sets of Interacting Collagens Form Functionally Distinct Substructures within a *Caenorhabditis elegans* Extracellular Matrix. *Mol Biol Cell* *14*, 1366–1378.
- Meeuse, M.W.M., Hauser, Y.P., Hendriks, G.-J., Eglinger, J., Bogaarts, G., Tsiairis, C., and Großhans, H. (2019). State transitions of a developmental oscillator. *BioRxiv* 755421.
- Meng, J., Ma, X., Tao, H., Jin, X., Witvliet, D., Michell, J., Zhu, M., Dong, M.-Q., Zhen, M., Jin, Y., et al. (2017). Myrf ER-bound transcription factors drive *C. elegans* synaptic plasticity via cleavage-dependent nuclear translocation. *Dev Cell* *41*, 180-194.e7.
- Merris, M., Wadsworth, W.G., Khamrai, U., Bittman, R., Chitwood, D.J., and Lenard, J. (2003). Sterol effects and sites of sterol accumulation in *Caenorhabditis elegans*: developmental requirement for 4alpha-methyl sterols. *J. Lipid Res.* *44*, 172–181.
- Miki, T.S., Carl, S.H., and Großhans, H. (2017). Two distinct transcription termination modes dictated by promoters. *Genes Dev.*
- Ming, Q., Roske, Y., Schuetz, A., Walentin, K., Ibraimi, I., Schmidt-Ott, K.M., and Heinemann, U. (2018). Structural basis of gene regulation by the Grainyhead/CP2 transcription factor family. *Nucleic Acids Res.* *46*, 2082–2095.
- Mohawk, J.A., Green, C.B., and Takahashi, J.S. (2012). CENTRAL AND PERIPHERAL CIRCADIAN CLOCKS IN MAMMALS. *Annu Rev Neurosci* *35*, 445–462.
- Mönke, G., Cristiano, E., Finzel, A., Friedrich, D., Herzel, H., Falcke, M., and Loewer, A. (2017). Excitability in the p53 network mediates robust signaling with tunable activation thresholds in single cells. *Sci Rep* *7*, 46571.
- Monsalve, G.C., Van Buskirk, C., and Frand, A.R. (2011). LIN-42/PERIOD controls cyclical and developmental progression of *C. elegans* molts. *Curr. Biol.* *21*, 2033–2045.
- Moreno-Risueno, M.A., Van Norman, J.M., Moreno, A., Zhang, J., Ahnert, S.E., and Benfey, P.N. (2010). Oscillating gene expression determines competence for periodic Arabidopsis root branching. *Science* *329*, 1306–1311.
- Nevil, M., Bondra, E.R., Schulz, K.N., Kaplan, T., and Harrison, M.M. (2017). Stable Binding of the Conserved Transcription Factor Grainy Head to its Target Genes Throughout *Drosophila melanogaster* Development. *Genetics* *205*, 605–620.
- Niederreither, K., McCaffery, P., Dräger, U.C., Chambon, P., and Dollé, P. (1997). Restricted expression and retinoic acid-induced downregulation of the retinaldehyde dehydrogenase type 2 (RALDH-2) gene during mouse development. *Mech. Dev.* *62*, 67–78.

- Niwa, Y., Masamizu, Y., Liu, T., Nakayama, R., Deng, C.-X., and Kageyama, R. (2007). The initiation and propagation of Hes7 oscillation are cooperatively regulated by Fgf and notch signaling in the somite segmentation clock. *Dev. Cell* *13*, 298–304.
- Novák, B., and Tyson, J.J. (2008). Design principles of biochemical oscillators. *Nat Rev Mol Cell Biol* *9*, 981–991.
- Novelli, J., Ahmed, S., and Hodgkin, J. (2004). Gene interactions in *Caenorhabditis elegans* define DPY-31 as a candidate procollagen C-proteinase and SQT-3/ROL-4 as its predicted major target. *Genetics* *168*, 1259–1273.
- Nüsslein-Volhard, C., Wieschaus, E., and Kluding, H. (1984a). Mutations affecting the pattern of the larval cuticle in *Drosophila melanogaster*. *Wilhelm Roux' Archiv* *193*, 267–282.
- Nüsslein-Volhard, C., Wieschaus, E., and Kluding, H. (1984b). Mutations affecting the pattern of the larval cuticle in *Drosophila melanogaster*. *Wilhelm Roux' Archiv* *193*, 267–282.
- Nutt, S.L., Fairfax, K.A., and Kallies, A. (2007). BLIMP1 guides the fate of effector B and T cells. *Nat. Rev. Immunol.* *7*, 923–927.
- Oates, A.C., Morelli, L.G., and Ares, S. (2012). Patterning embryos with oscillations: structure, function and dynamics of the vertebrate segmentation clock. *Development* *139*, 625–639.
- O'Connell, J., and Højsgaard, S. (2011). Hidden Semi Markov Models for Multiple Observation Sequences: The mhsmm Package for R. *Journal of Statistical Software* *39*, 1–22.
- Olmedo, M., Geibel, M., Artal-Sanz, M., and Merrow, M. (2015). A High-Throughput Method for the Analysis of Larval Developmental Phenotypes in *Caenorhabditis elegans*. *Genetics* *201*, 443–448.
- Page, A.P., and Johnstone, I.L. (2007). The cuticle (WormBook).
- Palmeirim, I., Henrique, D., Ish-Horowicz, D., and Pourquié, O. (1997). Avian hairy gene expression identifies a molecular clock linked to vertebrate segmentation and somitogenesis. *Cell* *91*, 639–648.
- Pomerening, J.R., Sontag, E.D., and Ferrell, J.E. (2003). Building a cell cycle oscillator: hysteresis and bistability in the activation of Cdc2. *Nat. Cell Biol.* *5*, 346–351.
- Porrúa, O., and Libri, D. (2015). Transcription termination and the control of the transcriptome: why, where and how to stop. *Nat. Rev. Mol. Cell Biol.* *16*, 190–202.
- Priess, J.R., and Hirsh, D.I. (1986). *Caenorhabditis elegans* morphogenesis: the role of the cytoskeleton in elongation of the embryo. *Dev. Biol.* *117*, 156–173.
- Prokop, A., Bray, S., Harrison, E., and Technau, G.M. (1998). Homeotic regulation of segment-specific differences in neuroblast numbers and proliferation in the *Drosophila* central nervous system. *Mechanisms of Development* *74*, 99–110.
- Purcell, O., Savery, N.J., Grierson, C.S., and di Bernardo, M. (2010). A comparative analysis of synthetic genetic oscillators. *J R Soc Interface* *7*, 1503–1524.
- Purvis, J.E., and Lahav, G. (2013). Encoding and decoding cellular information through signaling dynamics. *Cell* *152*, 945–956.
- R Core Team R: A language and environment for statistical computing.

- Rabiner, L.R. (1989). A tutorial on hidden Markov models and selected applications in speech recognition. *Proceedings of the IEEE* 77, 257–286.
- Rensing, L., Meyer-Grahe, U., and Ruoff, P. (2001). Biological timing and the clock metaphor: oscillatory and hourglass mechanisms. *Chronobiol. Int.* 18, 329–369.
- Rifat, Y., Parekh, V., Wilanowski, T., Hislop, N.R., Auden, A., Ting, S.B., Cunningham, J.M., and Jane, S.M. (2010). Regional neural tube closure defined by the Grainy head-like transcription factors. *Dev. Biol.* 345, 237–245.
- Roberts, B., Clucas, C., and Johnstone, I.L. (2003). Loss of SEC-23 in *Caenorhabditis elegans* Causes Defects in Oogenesis, Morphogenesis, and Extracellular Matrix Secretion. *Mol Biol Cell* 14, 4414–4426.
- Rossant, J., Zirngibl, R., Cado, D., Shago, M., and Giguère, V. (1991). Expression of a retinoic acid response element-hsp β transgene defines specific domains of transcriptional activity during mouse embryogenesis. *Genes Dev.* 5, 1333–1344.
- Ruaud, A.-F., and Bessereau, J.-L. (2006). Activation of nicotinic receptors uncouples a developmental timer from the molting timer in *C. elegans*. *Development* 133, 2211–2222.
- Russel, S., Frand, A.R., and Ruvkun, G. (2011). Regulation of the *C. elegans* molt by pqn-47. *Dev. Biol.* 360, 297–309.
- Saga, Y., Hata, N., Koseki, H., and Taketo, M.M. (1997). Mesp2: a novel mouse gene expressed in the presegmented mesoderm and essential for segmentation initiation. *Genes Dev.* 11, 1827–1839.
- Saggio, M.L., Spiegler, A., Bernard, C., and Jirsa, V.K. (2017). Fast–Slow Bursters in the Unfolding of a High Codimension Singularity and the Ultra-slow Transitions of Classes. *J Math Neurosci* 7.
- Schimmer, B.P., and White, P.C. (2010). Minireview: steroidogenic factor 1: its roles in differentiation, development, and disease. *Mol. Endocrinol.* 24, 1322–1337.
- Schindler, A.J., Baugh, L.R., and Sherwood, D.R. (2014). Identification of late larval stage developmental checkpoints in *Caenorhabditis elegans* regulated by insulin/IGF and steroid hormone signaling pathways. *PLoS Genet.* 10, e1004426.
- Schröter, C., Ares, S., Morelli, L.G., Isakova, A., Hens, K., Soroldoni, D., Gajewski, M., Jülicher, F., Maerkl, S.J., Deplancke, B., et al. (2012). Topology and Dynamics of the Zebrafish Segmentation Clock Core Circuit. *PLOS Biology* 10, e1001364.
- Sentenac, A. (1985). Eukaryotic RNA polymerases. *CRC Crit. Rev. Biochem.* 18, 31–90.
- Shimojo, H., Ohtsuka, T., and Kageyama, R. (2008). Oscillations in notch signaling regulate maintenance of neural progenitors. *Neuron* 58, 52–64.
- Šilhánková, M., Jindra, M., and Asahina, M. (2005). Nuclear receptor NHR-25 is required for cell-shape dynamics during epidermal differentiation in *Caenorhabditis elegans*. *J Cell Sci* 118, 223–232.
- Singh, R.N., and Sulston, J.E. (1978). Some Observations On Moulting in *Caenorhabditis Elegans*. *Nematologica* 24, 63–71.
- Smale, S.T., and Kadonaga, J.T. (2003). The RNA polymerase II core promoter. *Annu. Rev. Biochem.* 72, 449–479.

- Sonnen, K.F., Lauschke, V.M., Uraji, J., Falk, H.J., Petersen, Y., Funk, M.C., Beaupeux, M., François, P., Merten, C.A., and Aulehla, A. (2018). Modulation of Phase Shift between Wnt and Notch Signaling Oscillations Controls Mesoderm Segmentation. *Cell* *172*, 1079-1090.e12.
- Spiess, A.-N. (2018). propagate: Propagation of Uncertainty.
- Stricker, J., Cookson, S., Bennett, M.R., Mather, W.H., Tsimring, L.S., and Hasty, J. (2008). A fast, robust and tunable synthetic gene oscillator. *Nature* *456*, 516–519.
- Strogatz, S.H. (2015). *Nonlinear Dynamics and Chaos: With Applications to Physics, Biology, Chemistry, and Engineering*, Second Edition (Boulder, CO: Westview Press).
- Sulston, J.E., and Horvitz, H.R. (1977). Post-embryonic cell lineages of the nematode, *Caenorhabditis elegans*. *Dev. Biol.* *56*, 110–156.
- Sulston, J.E., Schierenberg, E., White, J.G., and Thomson, J.N. (1983). The embryonic cell lineage of the nematode *Caenorhabditis elegans*. *Dev. Biol.* *100*, 64–119.
- Suzuki, M., Sagoh, N., Iwasaki, H., Inoue, H., and Takahashi, K. (2004). Metalloproteases with EGF, CUB, and thrombospondin-1 domains function in molting of *Caenorhabditis elegans*. *Biol. Chem.* *385*, 565–568.
- Takahashi, J.S. (2004). Finding new clock components: past and future. *J. Biol. Rhythms* *19*, 339–347.
- Takahashi, J.S. (2017). Transcriptional architecture of the mammalian circadian clock. *Nat Rev Genet* *18*, 164–179.
- Teuscher, A.C., Jongsma, E., Davis, M.N., Statzer, C., Gebauer, J.M., Naba, A., and Ewald, C.Y. (2019). The in-silico characterization of the *Caenorhabditis elegans* matrisome and proposal of a novel collagen classification. *Matrix Biology Plus* *1*, 100001.
- Thacker, C., Peters, K., Srayko, M., and Rose, A.M. (1995). The *bli-4* locus of *Caenorhabditis elegans* encodes structurally distinct *kex2*/subtilisin-like endoproteases essential for early development and adult morphology. *Genes Dev.* *9*, 956–971.
- Thein, M.C., Winter, A.D., Stepek, G., McCormack, G., Stapleton, G., Johnstone, I.L., and Page, A.P. (2009). Combined extracellular matrix cross-linking activity of the peroxidase MLT-7 and the dual oxidase BLI-3 is critical for post-embryonic viability in *Caenorhabditis elegans*. *J. Biol. Chem.* *284*, 17549–17563.
- Ting, S.B., Caddy, J., Hislop, N., Wilanowski, T., Auden, A., Zhao, L.-L., Ellis, S., Kaur, P., Uchida, Y., Holleran, W.M., et al. (2005). A homolog of *Drosophila* grainy head is essential for epidermal integrity in mice. *Science* *308*, 411–413.
- Todeschini, A.-L., Georges, A., and Veitia, R.A. (2014). Transcription factors: specific DNA binding and specific gene regulation. *Trends Genet.* *30*, 211–219.
- Tsai, T.Y.-C., Choi, Y.S., Ma, W., Pomerening, J.R., Tang, C., and Ferrell, J.E. (2008). Robust, Tunable Biological Oscillations from Interlinked Positive and Negative Feedback Loops. *Science* *321*, 126–129.
- Turner, C.A., Mack, D.H., and Davis, M.M. (1994). Blimp-1, a novel zinc finger-containing protein that can drive the maturation of B lymphocytes into immunoglobulin-secreting cells. *Cell* *77*, 297–306.
- Varma, S., Cao, Y., Tagne, J.-B., Lakshminarayanan, M., Li, J., Friedman, T.B., Morell, R.J., Warburton, D., Kotton, D.N., and Ramirez, M.I. (2012). The transcription factors Grainyhead-like 2 and NK2-homeobox 1 form a regulatory loop that coordinates lung epithelial cell morphogenesis and differentiation. *J. Biol. Chem.* *287*, 37282–37295.

- Venkatesan, K., McManus, H.R., Mello, C.C., Smith, T.F., and Hansen, U. (2003). Functional conservation between members of an ancient duplicated transcription factor family, LSF/Grainyhead. *Nucleic Acids Res* 31, 4304–4316.
- Veronico, P., Gray, L.J., Jones, J.T., Bazzicalupo, P., Arbucci, S., Cortese, M.R., Di Vito, M., and De Giorgi, C. (2001). Nematode chitin synthases: gene structure, expression and function in *Caenorhabditis elegans* and the plant parasitic nematode *Meloidogyne artiellia*. *Mol. Genet. Genomics* 266, 28–34.
- Vuong-Brender, T.T.K., Ben Amar, M., Pontabry, J., and Labouesse, M. (2017a). The interplay of stiffness and force anisotropies drives embryo elongation. *ELife* 6, e23866.
- Vuong-Brender, T.T.K., Suman, S.K., and Labouesse, M. (2017b). The apical ECM preserves embryonic integrity and distributes mechanical stress during morphogenesis. *Development* 144, 4336–4349.
- Wang, S., and Samakovlis, C. (2012). Grainy head and its target genes in epithelial morphogenesis and wound healing. *Curr. Top. Dev. Biol.* 98, 35–63.
- Ward, J.D., Bojanala, N., Bernal, T., Ashrafi, K., Asahina, M., and Yamamoto, K.R. (2013). Sumoylated NHR-25/NR5A Regulates Cell Fate during *C. elegans* Vulval Development. *PLOS Genetics* 9, e1003992.
- Warnes, G.R., Bolker, B., Bonebakker, L., Gentleman, R., Liaw, W.H.A., Lumley, T., Maechler, M., Magnusson, A., Moeller, S., Schwartz, M., et al. *gplots: Various R Programming Tools for Plotting Data* version 3.0.1.1 from CRAN.
- Webb, A.B., and Oates, A.C. (2016). Timing by rhythms: Daily clocks and developmental rulers. *Dev. Growth Differ.* 58, 43–58.
- Welsh, D.K., Takahashi, J.S., and Kay, S.A. (2010). Suprachiasmatic nucleus: cell autonomy and network properties. *Annu. Rev. Physiol.* 72, 551–577.
- Werth, M., Walentin, K., Aue, A., Schönheit, J., Wuebken, A., Pode-Shakked, N., Vilianovitch, L., Erdmann, B., Dekel, B., Bader, M., et al. (2010). The transcription factor grainyhead-like 2 regulates the molecular composition of the epithelial apical junctional complex. *Development* 137, 3835–3845.
- Wilanowski, T., Caddy, J., Ting, S.B., Hislop, N.R., Cerruti, L., Auden, A., Zhao, L.-L., Asquith, S., Ellis, S., Sinclair, R., et al. (2008). Perturbed desmosomal cadherin expression in grainy head-like 1-null mice. *EMBO J.* 27, 886–897.
- Winter, A.D., and Page, A.P. (2000). Prolyl 4-Hydroxylase Is an Essential Procollagen-Modifying Enzyme Required for Exoskeleton Formation and the Maintenance of Body Shape in the Nematode *Caenorhabditis elegans*. *Mol Cell Biol* 20, 4084–4093.
- Xuan, W., Audenaert, D., Parizot, B., Möller, B.K., Njo, M.F., De Rybel, B., De Rop, G., Van Isterdael, G., Mähönen, A.P., Vanneste, S., et al. (2015). Root Cap-Derived Auxin Pre-patterns the Longitudinal Axis of the Arabidopsis Root. *Curr. Biol.* 25, 1381–1388.
- Yamanaka, N., Rewitz, K.F., and O'Connor, M.B. (2013). Ecdysone control of developmental transitions: lessons from *Drosophila* research. *Annu. Rev. Entomol.* 58, 497–516.
- Yeung, J., Mermet, J., Jouffe, C., Marquis, J., Charpagne, A., Gachon, F., and Naef, F. (2017). Transcription factor activity rhythms and tissue-specific chromatin interactions explain circadian gene expression across organs. *Genome Res.*
- Yochem, J., Tuck, S., Greenwald, I., and Han, M. (1999). A gp330/megalyn-related protein is required in the major epidermis of *Caenorhabditis elegans* for completion of molting. *Development* 126, 597–606.

Yochem, J., Lažetić, V., Bell, L., Chen, L., and Fay, D. (2015). *C. elegans* NIMA-related kinases NEKL-2 and NEKL-3 are required for the completion of molting. *Dev. Biol.* *398*, 255–266.

Yu, S.-Z. (2010). Hidden semi-Markov models. *Artificial Intelligence* *174*, 215–243.

Yu, Z., Lin, K.K., Bhandari, A., Spencer, J.A., Xu, X., Wang, N., Lu, Z., Gill, G.N., Roop, D.R., Wertz, P., et al. (2006). The Grainyhead-like epithelial transactivator Get-1/Grhl3 regulates epidermal terminal differentiation and interacts functionally with LMO4. *Dev. Biol.* *299*, 122–136.

Zhang, L., Ward, J.D., Cheng, Z., and Dernburg, A.F. (2015). The auxin-inducible degradation (AID) system enables versatile conditional protein depletion in *C. elegans*. *Development* *142*, 4374–4384.

Zhang, R., Lahens, N.F., Ballance, H.I., Hughes, M.E., and Hogenesch, J.B. (2014). A circadian gene expression atlas in mammals: implications for biology and medicine. *Proc. Natl. Acad. Sci. U.S.A.* *111*, 16219–16224.

Zugasti, O., Rajan, J., and Kuwabara, P.E. (2005). The function and expansion of the Patched- and Hedgehog-related homologs in *C. elegans*. *Genome Res.* *15*, 1402–1410.

7. Acknowledgements

I would like to thank my supervisor Helge for introducing me the exciting research on gene expression oscillations. Thank you for the excellent guidance, for teaching me how to write papers, for your positive attitude no matter what happens, for the freedom you gave me, for the trust you had in me and for the ability to dive into the world of data analysis.

I want to thank my thesis committee members Andy Oates and Erik van Nimwegen for their input and fruitful discussions during our yearly meetings. Andy, thank you for inviting me in Lausanne and giving me the opportunity to present and discuss my work in your lab.

Thank you, Kathrin and Anca for making the lab such a well-organized and tidy place to be, but I am most grateful for your great experimental support during the final stages of my PhD. An extra thank you goes to Kathrin for fun we had during in preparing the cakes for the Xmas cake competition and the prizes we shared. I am very thankful to Yannick, which whom I shared ups and downs as our joined projects evolved, but who was always there for me. Chiara, thank you for always being next to me in the lab, for learning me Italian swearing words, for listening to me and for an occasional hug when I really needed them. Thanks you, Gert-Jan for introducing me to the project and handing it over to me. Ben, thank you for our scientific input and teaching me how to be a critical scientist. Thank you Rajani for sharing your enthusiasm for hiking with me. Thomas, Thomas, Thomas, thank you for your positive energy in our office and the lab. Giovanna for giving me advice on so many different aspects of life. I would like to thank Jun for sharing his fun facts, Takashi for scientific discussions, Flo for our occasional bike rides, and interns Andrea and Carolin for their effort in the lab. Jana, I admire your commitment, thanks for sharing that with me. Thank you, Smita and Maike for organizing an amazing lab retreat during the time when I really needed a break from writing. Saheli, Marit, Michaela, thank you for following up on the oscillation projects in the lab. I am pretty sure we are going to find interesting things! I am very grateful to Iskra and Lan for their constant support in generating worm strains. I would like to thank Yannick, Chiara and Lucas for reading and providing input on earlier versions of my thesis. Thank you, Dimos, Michael, Sarah, Foivos and Lucas, for teaching me a lot about writing code, data analysis and modelling. Also a big thanks to Jimmy our pink fluffy lab mascot who makes me smile when I enter the lab. Thank you Grosshans Lab for the great time!

Thank you Tsiairis lab for the interesting discussions on oscillations. I would like to thank Eliza, and Sebastien of the genomics facility, for their great support in sequencing my samples. Thanks also to Laurent, Steve, Jan and Benjamin from FAIM for helping me with microscopy and data analysis. I would like to thank the media kitchen for preparing all the reagents I used throughout my PhD. Elida, thank you so much for answering all my burning questions, even before I started my PhD.

I would like to thank the student representatives for organizing events with me and learning skills that I would have never learned on the bench. Piera, thank you so much for supporting me personally and the reps as a group.

I am grateful to BIF for funding my PhD project and for giving me the opportunity to meet great people. Thank you Nina, for sharing your passion for sports with me and showing me around in wonderful Copenhagen.

I want to thank my previous supervisors, Ludwig, Sarah, Jan-Willem and Xiaoqing for introducing me to a career in science and teaching me experiments and scientific thinking.

A big thank you to Laura for the great time we spent together. Also the other girls of the cooking group, Lara, Lea, Dilek for making such delicious meals from all around the world together. I would like to thank the guys from the Basel Pharma Ride group for the hard but fun rides and Avoras Racing team for supporting my athletic ambitions.

Johannes, ik wil je bedanken voor de ontspanning en gezelligheid tijdens de fiets en hardlooptrainingen, die toch af en toe ook wel zwaar waren ;). De mooie tochten in de Alpen vergeet ik niet meer. Helaas woon je niet meer in Basel, maar ik wil jou, Anais en Charlotte bedanken dat we op bezoek mogen komen, hopelijk snel in jullie nieuwe huis! Nel en Nancy, dankjulliewel voor onze vriendschap en alle leuke dingen die we hebben meegemaakt in Leiden, Delft en daarna. Al reikt de magische driehoek nu wel heel erg ver (Canada, Nederland en Basel), ik denk dat ie altijd zal blijven bestaan. Nancy, ik wens je heel veel success met het afronden van jouw PhD en Nel, met alle uitdagingen die je nog als docente te wachten staan. Dankjewel, Charlotte, voor onze wekelijkse 'beesten' trainingen, die theebezoekjes werden nadat ik naar Basel vertrok, maar hopelijk trekken de mega Mindies er nog eens op uit! Sarah, ik wil je bedanken voor de etentjes, de MTB tochtjes en de gezelligheid in het lab tijdens mijn stage tijd in Maastricht. We komen snel eens op kraamvisite in Wageningen! Lieve Yvonne, dankjewel voor je steun, je medeleven en je luisteren. Ik bewonder je doorzettingsvermogen en je inzet en heb daar veel van geleerd. Ik betwijfel niet dat we elkaar nog veel meer zullen leren.

Ik wil André, Hanneke, Pauke, Marc, Roel, Florieke en Timo bedanken omdat jullie me zo warm hebben opgevangen in de familie. Dankjulliewel voor jullie interesse, jullie medeleven en de gezellige verjaardagen, feestdagen en bezoeken in Basel.

Lieve Milan, bedankt voor de fijne tijd die we altijd samen hebben doorgebracht. Ik kan me voorstellen dat mensen op vakantie gedacht hebben dat wij een tweeling waren ;). Ik ben ontzettend trots op je dat je nu je eigen leven hebt opgebouwd in Antwerpen samen met Kristina, dat je het naar je zin hebt als architect en dat je je energie nu in het bolderen kwijt kunt. Bedankt voor je steun en de belletjes als het even tegen zat. Kristina, ačiū, voor je wijze levenslessen en de gezelligheid!

Lieve papa en mama, bedankt voor alle steun en liefde die jullie me altijd gegeven hebben. Ik bewonder jullie toewijding en trots voor Milan en mij enorm. Ik weet dat jullie enorm met me meegeleefd hebben in de afgelopen 4 jaar en dat het moeilijk moet zijn geweest dat ik zo ver weg woon, maar dat maakt de band alleen maar sterker. En, zo kunnen we samen langlaufen, mountainbiken en naar cross wedstrijden gaan in het mooie Zwitserland!

Tot slot, allerliefste Guy, ik kan me een leven zonder jou in Basel al niet meer voorstellen. Bedankt dat je me achterna bent gekomen naar Zwitserland en dat je alles voor me over hebt en me steunt in alles wat ik doe. Ik ben trots dat je je draai in Basel gevonden hebt en dat je zo ongedwongen en positief door het leven gaat. Bedankt voor de ontzettend mooie, gezellige, zware avonturen op de racefiets, de MTB, de crossfiets, de langlaufskies en de wandelschoenen. Ik kijk uit naar alle dingen die nog op ons pad gaan komen.

8. Curriculum vitae

MILOU MEEUSE, PHD

milou_meeuse@msn.com | +31648202130 | Bürklinstrasse 7 | 4127 Birsfelden, Switzerland | C-permit

ABOUT ME

I am an enthusiastic and motivated PhD graduate in Molecular and Computational Biology with experience in designing, performing and analyzing genomics experiments, supervising students and laboratory technicians, presenting my research to diverse audiences and writing a research proposal and scientific papers. I enjoy searching creative and analytical solutions to complex problems and approach them systematically and with perseverance. I am committed to learning new skills and setting up effective collaborations to achieve goals. In my role as one of 6 student representatives and as PhD student working on multidisciplinary research projects, I demonstrated effective communication and teamwork skills.

PROFESSIONAL EXPERIENCE

Dec 2019 - now **Postdoc | Grosshans Lab, Friedrich Miescher Institute (FMI), Basel, CH**

- Finalizing manuscripts from PhD for submission
- Performing ChIP-seq analysis to identify targets of oscillatory transcription factors
- Improving a GUI in MATLAB to visualize data and automatically annotate features of time series experiments
- Mentoring two new PhD students to continue my projects

2015 - 2019 **PhD Molecular and Computational Biology | Grosshans Lab, FMI, Basel, CH**

- Investigated function and molecular mechanisms of oscillatory gene expression in *C. elegans* using wet-lab and computational approaches, resulting in 3 manuscripts
- Analysis of time course RNA-seq sets in R (quasR, edgeR) and integration of scRNA-seq data
- Ensured fulfilment of laboratory work by technical associates
- Received prestigious Boehringer Ingelheim Fonds PhD Fellowship (written proposal)

2017 – 2019 **Elected student representative | FMI, Basel, CH**

- Elected as representative by students in 2017/2018 and 2018/2019
- Taking decisions on budget and strategy
- Organizing 3-day FMI student retreat 2019
- Developed and conducted a survey to evaluate student satisfaction

EDUCATION

2015 – 2019 **PhD Molecular and Computational Biology | University Basel, CH**

- Graduated Summa Cum Laude, on December 13, 2019
- Thesis title: Functional characterization of a gene expression oscillator in *C. elegans*

2013 – 2015 **Master Biomedical Sciences | University Maastricht, NL**

- Graduated with Highest Honors, ranked among top-3 in class
- Master thesis in cancer genetics: The role of AMPK in cellular adaptation to metabolic stress. Department of Molecular Genetics, Maastricht University
- Master Internship in cancer biomarkers: SLC16A12, a potential biomarker for the efficacy of CAIX inhibition in cancer cells. Maastro Lab, University hospital Maastricht

2010 – 2013 **Bachelor Life Science and Technology | University Leiden, NL**

- Graduated with Highest Honors, ranked #1 in class
- Taught fellow students that had to retake Calculus exams
- Bachelor internship: Characterization of HGF- and collagen-induced morphology of colorectal cancer organoids and the role of Matrix MetalloProteinases, Hubrecht Institute, Utrecht, Netherlands

PRIZES AND HONORS

- 2020 Ed Fischer Prize for best PhD thesis 2019, Friedrich Miescher Institute, Basel, Switzerland
- 2015 1st prize Poster, Mosa Biomedical Conference, Maastricht, Netherlands
- 2015 1st prize Master Thesis, Faculty of Health, Medicine and Life Sciences, Maastricht University, Netherlands
- 2010 St. Jozef Prize for best high school thesis on RNA interference in *C. elegans*, Trevianum High School, Sittard, Netherlands

OTHER ACHIEVEMENTS

2010 – 2015 **Independent tutor of high school students | NL**

- Coached 3 high school students for 2 - 5 years in Biology, Mathematics, and Physics
- Supervised them in preparing for exams, which they passed successfully
- Devised methods of teaching according to students needs

2009 – now **Elite cyclist | Avoras Racing Team, CH**

- Received sponsorship from Giant Store Sittard-Geleen (NL, 2013-2015) and from Avoras Racing team (CH, 2019-now) to participate in (inter-)national cyclocross races
- Top-3 in national races and top-15 in international races

LANGUAGES Dutch (mother tongue), English (fluent), German (basics)

CONFERENCE PRESENTATIONS

- 2016 Protein-DNA interaction workshop, GENiE, Sevilla, SP, oral presentation
- 2017 International Chronobiology Meeting, Gordon Research Conference, Stowe (VT), USA, selected oral presentation
- 2017 Summer School Epigenetics meets mathematics, Berlin, DE, oral presentation
- 2018 Metazoan Systems Biology Workshop, Bordeaux, FR, poster
- 2018 Biological Oscillators, EMBO Symposium, Heidelberg, DE, poster
- 2018 Basel Worm Meeting, Basel, CH, selected oral presentation
- 2020 Systems Biology: Global Regulation of Gene Expression, Cold Spring Harbor, New York, USA, poster

PUBLICATIONS

Milou W.M. Meeuse*, Yannick P. Hauser*, Lucas J. Morales Moya, Gert-Jan Hendriks, Jan Eglinger, Guy Bogaarts, Charisios Tsiairis, Helge Großhans, Developmental function and state transitions of a gene expression oscillator in *C. elegans*, MSB, 2020

Milou W.M. Meeuse, Michael Stadler, Kathrin Braun, Anca Neagu, Helge Großhans, Control of oscillatory gene expression and molting through the Grainyhead/LSF transcription factor GRH-1 (in preparation)

Yannick P. Hauser*, Milou W.M. Meeuse*, Jan Eglinger, Helge Großhans, The BLMP-1 transcription factor supports coupling of oscillatory gene expression with development (in preparation)